Title

Development and Utilization of Piezoelectric Scaffold Systems for the Modulation of the Physico-Chemical Microenvironment of the Cells to Enhance Their Regenerative Behaviors

Author

Ico, Gerardo

Publication Date

2018

UNIVERSITY OF CALIFORNIA
RIVERSIDE

Development and Utilization of Piezoelectric Scaffold Systems for the Modulation of the Physico-Chemical Microenvironment of the Cells to Enhance Their Regenerative Behaviors

A Dissertation submitted in partial satisfaction
of the requirements of for the degree of

Doctor of Philosophy

in

Bioengineering

by

Gerardo Rene Ico

December 2018

Dissertation Committee:
Dr. Jin Nam, Chairperson
Dr. Nosang V. Myung
Dr. William Grover

The Dissertation of Gerardo Rene Ico is approved:

____

____

____

Committee Chairperson

University of California, Riverside

ACKNOWLEDGEMENTS

The text of this dissertation, in part or in full, is a reprint of the material as it appears in Size-dependent piezoelectric and mechanical properties of electrospun P(VDF-TrFE) nanofibers for enhanced energy harvesting, *Journal of Materials Chemistry A* (2016) and Transformative piezoelectric enhancement of P(VDF-TrFE) synergistically driven by nanoscale dimensional reduction and thermal treatment, *Nanoscale* (2018). The co-author, Jin Nam, listed in these publications directed and supervised the research which forms the basis for this dissertation.

Additionally, I would like to thank Adam Showalter and Austin Myung for their assistance in conducting experiments for the data generated in these publications; Wayne Bosze for his expertise and guidance in design of experiments, Shannon C. Gott and Masaru P. Rao for providing patterned silicon substrates used in determining the mechanical properties of the material used; Bum Sung Kim and Nosang V. Myung for their expertise in electrical measurements techniques.

DEDICATION

This dissertation and all the work gone into it is, first and foremost, dedicated to my parents, Dora and Hector Ico. Their support and belief in me since my first day in school and their exemplification of hard work has instilled in me the same values towards achieving my goals. Secondly, I would like to thank my wife for her unconditional support. The sacrifice she made in waiting for me to finish my Ph.D. will indeed pay off in the future for the both of us. Her family's support is also appreciated. Finally, my friends who have always tried including me in outings even though I most likely declined due to focusing on my research.

ABSTRACT OF THE DISSERTATION

Development and Utilization of Piezoelectric Scaffold Systems for the Modulation of the Physico-Chemical Microenvironment of the Cells to Enhance Their Regenerative Behaviors

by

Gerardo Rene Ico

Doctor of Philosophy, Graduate Program in Bioengineering
University of California, Riverside, December 2018
Dr. Jin Nam, Chairperson

Piezoelectric polymer, poly(vinylidene-trifluoroethylene) (P(VDF-TrFE)), exhibits excellent characteristics, such as flexibility and biocompatibility, for various biological applications that utilize energy conversion between mechanical strain and electric potentials. However, its typically low piezoelectric properties have limited its use as an effective piezoelectric platform. To address this, electrospinning was utilized as a method to manipulate the nanostructure of P(VDF-TrFE) nanofibers to engineer a high-performing piezoelectric material. More specifically, we show that the piezoelectric performance of P(VDF-TrFE) is size dependent; by dimensional reduction to the nanoscale (30 nm), a transformative enhancement in piezoelectric performance was achieved by the synergistic effects of flexoelectricity materialization and enhanced dipole domain alignment. The electrospun P(VDF-TrFE) at this size scale exhibits an exceptional piezoelectric coefficient, d_{33}, at -108 pm V^{-1}, approaching the same magnitude of more traditional inorganic materials, while maintaining its flexibility.

We exploit these high performing P(VDF-TrFE) nanofibers for specific biological applications. In one aspect, the large surface area-to-volume ratio inherent to nanomaterials, together with the transformative piezoelectric properties, allowed us to use the material as an ultrasensitive, acoustic-responsive, drug delivery platform driven by the direct piezoelectric effect. The intrinsic negative zeta potential was utilized to electrostatically load cationic drug molecules. We show that the drug release sensitivity of the P(VDF-TrFE) nanofibers depends on the fiber diameter, thus piezoelectric properties. We further showed that the drug release quantity can be tuned by applied acoustic pressure or number of acoustic doses for specific tissue applications.

Additionally, through the direct piezoelectric effect, we also demonstrated the utility of P(VDF-TrFE) nanofibers with an aligned morphology in neural tissue engineering. We demonstrate that the piezoelectric P(VDF-TrFE) nanofibers provide a means to culture neural stem cells while electrically stimulating the cells by acoustic actuation of the scaffold, generating electric potentials that were utilized to modulate the cellular behaviors. The electrical stimulation of neural stem cells resulted in neural stem cell differentiation towards different phenotypes, including neurons, oligodendrocytes, and astrocytes, demonstrating the potential utility of the piezoelectric scaffolds for engineering neural tissues composed of multiple cell phenotypes.

Finally, a proof-of-concept cell culture platform that can modulate the mechanical properties of cell culture scaffolds on demand, was devised based on the indirect piezoelectric effect. Microfabricated interdigitated electrodes were designed, via computational simulations, to act as an electric field-generating substrate for the P(VDF-TrFE) scaffold. We showed that the stiffness of the P(VDF-TrFE) nanofibers electrospun onto such interdigitated electrodes can be precisely controlled by modulating the applied electric fields across the electrodes. The results demonstrate the significant potential of electrospun piezoelectric nanofibers for a cell culture substrate with an on-demand change of the physical cellular microenvironment.

Table of Contents

List of Figures

List of Tables

1. Introduction

1.1 Piezoelectricity

Piezoelectricity is an electromechanical phenomenon which allows for the direct conversion of mechanical energy to electrical energy. This conversion is known as the direct piezoelectric effect. Conversely, the conversion of electrical energy to a mechanical response yields the indirect piezoelectric effect. Piezoelectricity was discovered in 1880 by French physicists Jacques and Pierre Curie who hypothesized and proved that materials with certain crystal asymmetries would give rise to an electric potential under a mechanical strain (the Greek origin of the root of piezoelectric, piezen, meaning to press). The strongest conversion at that time came from quartz and Rochelle salt.[1] The indirect effect was set forth a year later, first when mathematician Gabriel Lippman gave mathematical proof that application of an electric field to these materials should cause a mechanical deformation, and later tested successfully by the Curie brothers.[2, 3]

More recently, the use of piezoelectricity has emerged in various applications such as force transducers and actuators governed by the direct and indirect piezoelectric effect, respectively. Examples of the former include, automotive knock sensors that detect vibrations and adjust engine parameters to prevent catastrophic failure when uncontrolled detonation of air and fuel mixtures occur,[4] piezoelectric microphones to transduce acoustical waves to electrical signal,[5] and piezoelectric igniters used in push-button gas grills and lighters.[6, 7] The mechanical to electrical conversion has also enabled the harvesting of wasted mechanical energy for powering low-power devices.[8, 9] For the latter, fuel injectors for combustible engines utilize piezoelectric elements to precisely introduce fuel via injection needles,[10] inkjet printers that work on the principle of piezoelectric-driven volume reduction in reservoirs to expel ink,[11] and speaker technology including equipment buzzers and audio headphones.[12, 13]

In the field of medicine, micro tweezers utilize both the direct and indirect piezoelectric effects for force sensitive and spatially precise surgical tools.[14, 15] Sleep apnea detection bands work through the direct piezoelectric effect to record abnormal respiration waveforms.[16, 17] The use of piezoelectric elements in ultrasound transducers has revolutionized the field of real-time biomedical imaging. [18, 19] In cardiology, echocardiograms diagnose and manage common heart diseases,[20] otolaryngology utilizes ultrasound imaging to reveal the internal structures of the neck such as the thyroid or lymph nodes and diagnose associated diseases,[21, 22] and in ophthalmology, it has allowed doctors to detect tumors or make assessments of hidden posterior segment lesions in cases of pre-operative cataract.[23-25] Perhaps the most famous use of this imaging modality, utilizing piezoelectric elements, involves monitoring the health and development of a fetus throughout pregnancy in the field of obstetrics.[26] Through a similar principle, use of focused, directional, extracorporeal shockwaves have been utilized to fragment hardened biological deposits such as gallstones, kidney stones, and plaque buildup in arteries.[27-29]

This dissertation begins with a brief introduction on the theory of piezoelectricity. The basis and comparison of the materials science between inorganic- and organic-based piezoelectric materials is then discussed to reveal the properties responsible for piezoelectricity. Next, a discussion of naturally occurring biological piezoelectric materials and the effects of endogenous and exogenous electrical stimulation reveals the importance of the advancement of engineered biocompatible piezoelectric materials for bioengineering applications. In the proceeding chapters, the work conducted to contribute to the science of piezoelectricity and field of bioengineering is presented, first through the optimization of a biocompatible piezoelectric platform by dimensional reduction and proper thermal conditions, and secondly demonstrated by the applications of drug delivery and cell-culture scaffolds, respectively.

1.1.1. Fundamentals of piezoelectricity

The governing physical aspect driving piezoelectricity is the non-centrosymmetric nature of a material. There exist 32 classes of crystals for which 21 of them fall into the category satisfying asymmetry. Of those, only 20 are considered piezoelectric in the sense of the direct piezoelectric effect and further still, only 10 of the 20 can exhibit ferroelectricity due to the spontaneous polarization of the unit cell. For the former, the electric displacement in response to a mechanical stress due to its asymmetry is what leads to the direct effect and the indirect effect only in the presence of a mechanical stress that initially converts the asymmetrical non-polarized material into a net polarized material. For the latter, the spontaneous polarization does not necessitate a pre-stress to elicit the indirect effect. Additionally, both the direct and indirect effect in this case manifests from the change in polarization magnitude and/or direction.

Physical constants of the material such as electric susceptibility (χ_e) which relates to the relative permittivity (ε_r) by,

$$\epsilon_r = \chi_e + 1 \tag{1.1}$$

quantifies how susceptible a material is in terms of polarization to an applied external electric field (**ϕ**), which influence the electric displacement of the material by

$$\boldsymbol{D} = \boldsymbol{\phi}\varepsilon_0\varepsilon_r \tag{1.2}$$

where ε_0 is the permittivity of free space. Other physical constants such as the elastic constants (s) (e.g., Young's Modulus (**E**), Bulk Modulus, Shear Modulus) relate how a material responds mechanically to an applied physical stress (**σ**). For example, the change in deformation, or strain (S), of a material induced by a stress is given by,

$$S = \frac{\boldsymbol{\sigma}}{\boldsymbol{E}} \tag{1.1}$$

By means of the Linear Theory of Piezoelectricity the coupling between these constants (electrostatic and elastic) is presented in the two constitutive equations of piezoelectricity, of which there are four forms, where each constitutive equation describes either the direct or indirect piezoelectric effect through the use of the piezoelectric coefficients (*d*, *e*, *g*, *h*; depending on which forms of the constitutive equations are used) (**Figure 1.1a**). Throughout this dissertation the strain-charge form (red arrows in **Figure 1.1a**) with the following constitutive equations is used,

$$D_i = d_{ikl}T_{kl} + \varepsilon_{ik}^{T}\phi_k, \tag{1.4}$$

and

$$S_{ij} = d_{kij}\phi_k + s_{ijkl}^{\phi}T_{kl} \tag{1.5}$$

where d is the piezoelectric charge coefficient with units of m V^{-1} or C N^{-1}. **Equation 1.4** describes the direct piezoelectric effect that is used for sensing applications such as force transduction and energy harvesting. The resulting electric displacement is directly proportional to the applied stress, *T*, by a factor of the piezoelectric coefficient of the material. The second term on the right-hand side of the equation goes to zero in cases where an external electric field is absent or otherwise contributes to the electric displacement in the presence of an electric field proportional to the dielectric constant of the material at a constant stress (T superscript). **Equation 1.5** describes the indirect piezoelectric effect used in fields of actuators such as micro positioners and acoustics. The strain induced by an applied electric field is proportional, again, to the piezoelectric coefficient while the second term can go to zero for some materials that do not require an external pre-stress (i.e., ferroelectric materials exhibiting spontaneous polarization) or proportional to the external stress by the elastic constant (s) at a constant electric field (ϕ superscript). Material characterization in either the direct or indirect effect is directly transferable to the other effect since the piezoelectric coefficient is present in both cases.

The tensor notation presented in **Equations 1.4** and **1.5** can be compressed into matrix notation, to present the elastic (S_{ij} and s_{ijk}) and piezoelectric (d_{ikl} and d_{kij}) as matrix arrays, such that *ij* or *kl* are replaced by *p* or *q*. In this way *i,j,k,l* can be assigned values of 1,2, or 3 and *p* and *q* can be assigned values of 1,2,3,4,5, or 6. Rewriting **Equations 1.4** and **1.5** with this new notation produces,

$$D_i = d_{iq}T_q + \varepsilon_{ik}^{T}\phi_k, \tag{1.6}$$

and

$$S_p = d_{kp}\phi_k + s_{pq}^{\phi}T_q. \tag{1.7}$$

The numbering is useful when describing the associated directionality of piezoelectric materials (**Figure 1.1b**). By convention, the polarization direction of the material is designated as the z- axis of the piezoelectric material and is indicated by the number 3 and the longitudinal and lateral direction as 1 and 2 respectively. The shear components about the 1, 2, and 3 axis are designated as 4, 5, and 6, respectively. For example, a stress, T_3, imparted on the faces in the plane perpendicular to the polarization axis can induce an electric displacement, D_3, on the same faces, coupled by the piezoelectric coefficient, d_{33}. Similarly, a stress, T_1, imparted on the faces in the plane parallel to the polarization axis can induce an electric displacement, D_3, on the faces in the plane perpendicular to the polarization axis, by the coupling piezoelectric coefficient, *d*$_{31}$. Thus, the matrix form of **Equations 1.6** and **1.7** are,

$$\begin{bmatrix} D_1 \\ D_2 \\ D_3 \end{bmatrix} = \begin{bmatrix} d_{11} & d_{12} & d_{13} & d_{14} & d_{15} & d_{16} \\ d_{21} & d_{22} & d_{23} & d_{24} & d_{25} & d_{26} \\ d_{31} & d_{32} & d_{33} & d_{34} & d_{35} & d_{36} \end{bmatrix} \begin{bmatrix} T_1 \\ T_2 \\ T_3 \\ T_4 \\ T_5 \\ T_6 \end{bmatrix} + \begin{bmatrix} \varepsilon_{11}^T & \varepsilon_{12}^T & \varepsilon_{13}^T \\ \varepsilon_{21}^T & \varepsilon_{22}^T & \varepsilon_{23}^T \\ \varepsilon_{31}^T & \varepsilon_{32}^T & \varepsilon_{33}^T \end{bmatrix} \begin{bmatrix} \phi_1 \\ \phi_2 \\ \phi_3 \end{bmatrix} \tag{1.8}$$

and

$$\begin{bmatrix} S_1 \\ S_2 \\ S_3 \\ S_4 \\ S_5 \\ S_6 \end{bmatrix} = \begin{bmatrix} d_{11} & d_{12} & d_{13} \\ d_{21} & d_{22} & d_{23} \\ d_{31} & d_{32} & d_{33} \\ d_{41} & d_{42} & d_{43} \\ d_{51} & d_{52} & d_{53} \\ d_{61} & d_{62} & d_{63} \end{bmatrix} \begin{bmatrix} \phi_1 \\ \phi_2 \\ \phi_3 \end{bmatrix} + \begin{bmatrix} s_{11}^\phi & s_{12}^\phi & s_{13}^\phi & s_{14}^\phi & s_{15}^\phi & s_{16}^\phi \\ s_{21}^\phi & s_{22}^\phi & s_{23}^\phi & s_{24}^\phi & s_{25}^\phi & s_{26}^\phi \\ s_{31}^\phi & s_{32}^\phi & s_{33}^\phi & s_{34}^\phi & s_{35}^\phi & s_{36}^\phi \\ s_{41}^\phi & s_{42}^\phi & s_{43}^\phi & s_{44}^\phi & s_{45}^\phi & s_{46}^\phi \\ s_{51}^\phi & s_{52}^\phi & s_{53}^\phi & s_{54}^\phi & s_{55}^\phi & s_{56}^\phi \\ s_{61}^\phi & s_{62}^\phi & s_{63}^\phi & s_{64}^\phi & s_{65}^\phi & s_{66}^\phi \end{bmatrix} \begin{bmatrix} T_1 \\ T_2 \\ T_3 \\ T_4 \\ T_5 \\ T_6 \end{bmatrix}, \tag{1.9}$$

which, depending on the macroscopic symmetry of the material, can allow for most of the piezoelectric, elastic, and dielectric components to go to zero.

1.1.2. Ceramic-based piezoelectric materials

One major type of piezoelectric crystal structure for ceramic based materials is the perovskite structure both of which lead zirconate titanate ($Pb[Zr_xTi_{1-x}]O_3$ ($0 \le X \le 1$); PZT) and barium titanate ($BaTiO_3$) are (**Figure 1.2a**). Both materials' chemical composition are in the form $A^{2+}B^{4+}X^{2-}_3$ where the A atom sits on the four corners of the unit cell, the B atoms on the faces of the unit cell in an octahedral from, and the X atom within the octahedral center. An intrinsic displacement of the X atom parallel to the *c-axis* gives rise to the tetragonal structure resulting in a dipole across the unit cell and subsequently giving rise to piezo- and ferroelectric properties of these materials. The other major type of crystal structure for ceramic based materials are wurtzite structures in which zinc oxide (ZnO) configures towards (**Figure 1.2b**). In this chemical form, $A^{Y+}B^{Y-}$, both the cation and anion are centered in a tetrahedral cage of the opposite atom of equal charge. As a hexagonal crystal, all atoms are tetrahedrally coordinated with a dipole formed along the *c-axis* under stimulation.

Typical processing of ceramic piezoelectric materials begins with oxidation of the proper precursors under high temperatures. The result is a polycrystalline structure, which for the case of ferroelectric materials, produces grains each with their own polarization orientation known as domains. Thus, the electromechanical response depends strongly on the mode of stimulation and most importantly the post-processing conditions. For a tetragonal structure-based material, the displacement of the metal ion centered in the oxygen octahedral can be towards the six faces of the unit cell. The relative polarity direction of each domain for a tetragonal structure can exist at 180° or at 90° for which the boundary between the differently oriented domains is known as a domain wall. Domain re-orientation and growth can be induced by a strong electric field or stress, giving rise to the expansion or the generation of surfaces charges on the surface of the material. Specialized processing conditions may induce a monocrystalline structure where the entire material exists as a single domain. Typical applications for this special type of ferroelectric material are non-volatile memory applications where inducing a controllable remnant polarization can act as binary code for system applications. However, the 100% crystallinity of these materials limits their use in applications requiring flexible materials.

1.1.3. Polymer-based piezoelectric materials

The mechanism behind the piezoelectric properties of polymer-based materials remains the same as ceramic-based materials where the presence of a net dipole across the material drives the piezoelectric response. However, because the polymer chain is flexible compared to a 100% crystalline ceramic, the polymer can exist in an amorphous state where the chains are randomly oriented from one another. In other areas of the material, there can exist an ordered packing of the chains that give rise to a crystalline state within the material. Both physical states are not mutually exclusive thus giving rise to the semi-crystalline characteristic that is often present in piezoelectric polymers.

Moreover, as seen in ceramics that there exists distinct phases that are responsible for the net dipole across an asymmetric crystal (e.g., tetragonal, wurtzite) in comparison to symmetric phases (e.g., cubic), polymers too exist in different phases that give the material the ability to exhibit piezoelectricity. Most piezoelectric polymers are based on polyvinylidene fluoride (PVDF) $[-(-C_2H_2F_2)_n-]$ which can exist in a few phases, including the α-,γ-, and β-phase. In a typical PVDF granule or film that has undergone no special processing, the most energetically favorable phase for formation is the α-phase in which the chain exists in a trans/gauche (TGTG’) linkage which situates the pair of fluorine atoms on both sides of the polymer chain (**Figure 1.3a**). The γ- (TTTGTTTG’) and β-phase (TTTT) (**Figure 1.3b**) contain trans linkages which situates most and all of the fluorine atoms on one side of the chain, respectively. Thus, due to the electronegativity of the fluorine atoms and their concentration on a single side of the chain, chains existing in these two phases contain a dipole moment across the polymer chain that is otherwise nullified in the α-phase. As a result, it is these two electroactive phases that are primarily responsible for the piezoelectricity on PVDF based polymers.

The secondary factor responsible for the piezoelectric nature of these polymers is the crystalline state in which these electroactive phases exist in. An amorphous state (random flowing red lines in **Figure 1.3c**) of the electroactive phases will result in nullification of the net dipole of the molecular chains in a similar way that the trans/gauche configuration of the α-phase nullifies the dipole created by the electronegativity of the fluorine atoms. Thus, a macroscale ordered organization of the electroactive chains that give rise to a net dipole across several of these chains (crystalline domains; ordered red lines within cubes in **Figure 1.3c**) is crucial towards the bulk piezoelectricity of the material. Moreover, there is a need of alignment of these randomly oriented macroscopic polarized domains within the material for the bulk material to exhibit both piezoelectric effects (**Figure 1.3c**).

As a result, typical processing of PVDF precursor into a piezoelectric structure involves the sophisticated manipulation of the phases and alignment of the crystalline domains into an ordered bulk material.[30] To achieve this, stretching allows for the molecular chain to transition from a random amorphous state to a more ordered structure of a crystalline domain while at the same time providing part of the energy to transform the α-phase into the electroactive phases. The remainder of the energy required for such transformation comes from a poling process, that is either concurrently or subsequently conducted with stretching, which favors a re-orientation of the atomic, molecular, and crystalline structures along the same path as the applied electric field. Usually the process is conducted at elevated temperatures and maintained while cooled through the Curie transition point so that the resulting net polarization of the material is locked into the less energetically stable electroactive phases.

Various methods exist that employ the strategies of stretching and poling with additional methods to promote higher number molecular phase transitions and higher content crystallinity. For example, casted films by a method similar to blade coating can form the β-phase only when processed in this manner at elevated temperatures[30]. Spin-coated and quenched samples, to temperatures below room temperature, enable the synthesis of films with high β-phase content compared to when the same processing is quenched at elevated temperatures.[31] Special attention has also been given to the rate of solvent evaporation for spin-coated films. Employing rapid thermal annealing at a temperature ramp rate of 30 °C min^{-1} has been shown to promote directional solvent removal along the normal of the film. This directionality gives rise to ordering of the molecular chain parallel to the substrate into the β-phase crystallites.[32] Uniaxial stretching of PVDF films have shown that the rate of stretching ratio, stretching temperature, and stretching rate has a strong influence on the β-phase content and the profile of the polarization hysteresis loops.[33, 34] Subsequent poling of stretched films shows an increase transformation from the α-phase to the β-phase while simultaneously promoting a re-orientation of the dipoles to create effective PVDF-based sensors and actuators.[35]

Another method to promote the formation of the electroactive phases is by making the α-phase the less energetically stable state. PVDF copolymers created with monomers such as tetrafluoroethylene (TFE) or, more popularly, trifluoroethylene (TrFE) introduce molarity composition-dependent, periodic units that create steric hindrance within the molecular chain (**Figure 1.4**). As a result, incorporation of these bulky monomers creates an energetically favorable configuration of the molecular chain into the electroactive phases. This allows for less processing steps to promote a piezoelectric molecular structure and more attention to increasing the crystallinity and polarity of the material. Typical degree of crystallinity values for P(VDF-TrFE) films range from 65-80% compared to PVDF of 45-60%.[36, 37] Though the addition of more fluorine atoms is responsible for the phase stabilization by incorporating TrFE, the presence of their electronegativity on both sides of the molecular chain induces a smaller dipole across the TrFE monomer (5.7×10^{-30} C m)[38] compared to the VDF monomer in the β-phase ($\sim 7.5 \times 10^{-}$

^{30} C m).[38, 39] Thus, even though the intrinsic piezoelectric coefficients of PVDF copolymers are not as large as the homopolymer, the improved processability, degree of crystallinity, and temperature stability make it an attractive material for different applications.[40] In this regard, the performance of P(VDF-TrFE) can be tuned accordingly by adjusting the ratio of VDF to TrFE. For example, the Curie Point can be varied from 80 °C to 140 °C by changing the content of TrFE from 35% to 22%.[41] However, too high of a content can prove detrimental to the overall polarity and piezoelectricity of the polymer.

1.1.4. Piezoelectric micro- and nanofibers synthesized by electrospinning

The development of the electrospinning process has proven a facile method to create structures of polymeric or inorganic fibers with their dimensions in the nanometer and micrometer range.[42, 43] The technique involves the electrification of a charged jet of polymeric solution, by a high voltage source and typically dispensed at a fixed flow rate through a syringe via a syringe pump, to be collected on a grounded substrate some distance away. Opposing forces between electrostatic repulsion and surface tension are balanced until a critical voltage is applied to induce a large enough electrostatic repulsion to break the surface of the solution into a thin jet known as the Taylor cone (**Figure 1.5**). This jet further stretches and whips as it is attracted towards the grounded collector all while the solutions' solvent evaporates due to the rapid thinning of the charged jet solution. The resulting collected sample is composed of dry polymeric fibers whose diameters can range from a few nanometers to several microns. The fiber diameter is dependent upon, first and foremost, on solution properties such as viscosity, electrical conductivity, and surface tension, secondly, electrospinning conditions including, flow rate, applied voltage and tip-to-collector distance, and finally environmental conditions such as temperature and absolute humidity. The versatility of this technique has allowed its applicability in various fields including tissue engineering,[44] water remediation, [45] and gas sensing technologies.[46] In the case of inorganic-based piezoelectric fibers, typical synthesis requires the mixing of the oxide precursors, such as barium acetate and titanium isopropoxide as the starting ingredients for $BaTiO_3$, together with a polymer carrier during electrospinning.[47] Subsequent calcination to burn-off the polymer carrier leaves behind the proper chemistry of oxide which can then be annealed to create the proper crystal structure to induce piezoelectricity in the remaining fibers.[48]

In contrast to the multi-step process of synthesizing inorganic-based piezoelectric fibers, creating polymeric fibers by electrospinning can be limited to one step. In this context, the ability to draw and stretch polymeric materials using electric field-induced attraction from the syringe to collection substrate has similar effects of drawing and poling of films that produce piezoelectricity of the proper materials (**Figure 1.6**). Electrospinning of PVDF precursor solutions intrinsically induces the formation of the electroactive phases and more or less aligns the domains in the resulting PVDF fibers, thus creating functional fibrous structures without the need for post-processing.[49] Moreover, electrospinning of P(VDF-TrFE) can enhance the piezoelectric properties of the material by inducing preferential orientations of the molecular chain.[50]

1.2 Piezoelectricity in biology

1.2.1. Piezoelectric biological materials

It has been known since 1957 that piezoelectricity exists in dry bone.[51] More specifically, it was discovered that the effect was not biological in origin but instead arose from the crystalline structure of the collagen fibers present within bone. Only a shear force applied to the bone to promote sliding of the collagen fibers past one another caused a measurable piezoelectric effect giving rise to the two equal in magnitude but opposite in sign piezoelectric coefficients, d_{14} and d_{25}. The values for ox bone measured one-tenth ($6x10^{-9}$ c.g.s.e.s.u or 0.2 pm V^{-1}, where $3x10^{-8}$ c.g.s.e.s.u.=1 pm V^{-1} [52]) the d_{11} value of quartz and much less for human bone (0.1 pm V^{-1}) . Similarly, collagen present in tendon is highly aligned and crystallized in the long axis of tendon hence larger piezoelectric coefficients have been extracted for this tissue (d_{14}= -2.7 and -1.9 pm V^{-1} for bovine and equine, respectively).[53] The directionality of hydrogen bonding between the three collagen chains, forming tropocollagen,[54] give rise to the piezoelectric like properties in dry tendon similar to the rise of piezoelectricity in electroactive PVDF and its derivatives.[55] Also similar to piezoelectric polymers, the degree of crystallinity and orientation (e.g., tendon versus bone) are essential for better piezoelectric biological materials. More recently, it was revealed that there exists a piezoelectric heterogeneity within collagen fibrils that coincide regionally to the D-periodicity of collagen (~ 67 nm)[56] that consists of gap (0.54D) and overlap areas (0.46D).[57] Through piezoresponse force microscopy it was shown that the overlap areas of tropocollagen molecular units within a collagen fibril exhibits a shear piezoelectric coefficient of approximately 2 pm V^{-1} while the gap areas show little to no piezoelectric response in the amplitude images (value not discernable from noise). The heterogeneity at this scale can be described by the crystal structure of quasi-hexagonally (C_6) packed molecules along the entire length of collagen microfibrils.[58, 59] Interestingly, the orientation of the symmetry is highly ordered in the overlap regions and disordered in the gap regions (in biological terms, those areas prone to proteolysis).[60] This effect was hierarchal in nature, since similar heterogeneity was observed at the macroscale of collagen still within the bone matrix, where the random orientation and stacking of collagen fibrils gave rise to varying piezoelectric coefficients from 0.1-0.3 pm V^{-1}, similar to the value reported by E. Fukada and I. Yusuda (1957). Interestingly, high-resolution piezoelectric response probing of isolated collagen fibrils is demonstrated similar in magnitude to that reported for macroscale, dry tendon by E. Fukuda and I. Yusuda (1964).[56, 61]

However, the discovery of piezoelectricity in dry tissue have raised the question regarding the effects of the electrical phenomenon taking place in the aqueous environment *in vivo*. Although a piezoelectric response from bone has been measured in liquid by the indirect piezoelectric effect (i.e., PFM),[61] the mechanoelectrical conversion occurring *in vivo* can also give rise to another electro-kinetic effect known as streaming potential. This phenomenon originates when the diffuse layer, associated with an electrical double layer in fluids, flows due to a pressure gradient.[62, 63] As a result, an associated streaming potential is created that acts to drive counter ions (conduction current) in the same layer in a direction opposite of the current. In this manner, the charged species in bone (collagen) act as the charged surface creating the electric double layer, which once stressed creates the streaming potential.[64, 65] Despite the differences in mechanisms, the fundamental effects of transducing mechanical to electrical cues to influence biological behaviors are significant enough to allow for both methods to be exploited for tissue regeneration.

1.1.1 Electrical stimulation healing and cellular function enhancement

Electrical stimulation to promote specific biological functions has garnered great interests in the utilization of piezoelectric materials. As a result of the direct piezoelectric effect, the creation of potentials due to charge generation has allowed many to mimic the effects of biopotentials arising *in vivo*. The most obvious of effects comes from the mobility of charged biological species at the cellular and organismal level in response to a potential, or galvanotaxis, which can, for example, promote cite targeted wound healing by allowing the migration of epithelial cells, fibroblasts, and macrophages.[66-69] It has been proposed that the voltage generated across the epithelia by epithelial cells is capable of driving current out of areas of low resistance such as areas where there are breaks in the epithelia (wounds).[70] It is this isotropic flow of ionic current around the wound that creates a lateral electric field, essentially indicating the site of injury. The influence of the electrical stimulation may arise from the interaction of the cellular surface charge and the interaction of passive ion flux across the cell membrane (i.e., Ca^{2+}) .[71, 72]

In regards to the skeletal system, it has been shown that bone remodeling is correlated to the endogenous electronegativity in biopotential surrounding the site. [73] Negative potentials have the effect of promoting bone formation, while resorption is seen in electropositive environments.[74] In this regard, the basis of Wolff's Law, which states that bone adaptation is directly influenced by the stress exposure via internal and external forces,[75]may be in part due to the piezoelectricity of bone. Compression of bone leads to the creation of negative potentials while the opposite is true where tension creates positive potentials. In addition, exogenous exposure to direct current (DC) negative voltages showed enhancement in the rate of non-union bone healing and stimulated ossification within the marrow cavity.[76-78] DC stimulation along with capacitive coupling and inductive coupling are three popular techniques for fracture healing, all based on the endogenous mechanisms for bone formation and healing.[74, 79]

Naturally, the nervous system also benefits from the effects of electrical stimulation for healing and enhancing function. There exists endogenous electric fields after nerve injury and neural development.[80] *In vivo* studies have provided proof of the efficacy of electrical stimulation in promoting nerve regeneration from damaged nerves in rat models. For example, an optimal electrical stimulation of 20 Hz for 1 hour to the site of repair, following transection and surgical repair of the femoral trunk nerve, lead to a significant increase in dorsal root ganglion (DRG) neurons regenerating back into skin and muscle tissue as compared to no or longer than 1 hour electrical stimulation.[81] Moreover, it led to an increase in neuron number that were able to regenerate axons beyond the repair site which was also correlated to the upregulation of growth-associated protein 43, GAP-43, in regenerating neurons. Specifically, the molecular basis for enhancing the regeneration and function of nerve cells begins with the induced elevation of cyclic adenosine monophosphate (cAMP) and increase in expression of neurotrophic factors and associated receptors.[82] The electrical stimulated induced release of neurotrophic factors, in particular nerve growth factor, by Schwann cells indicates that stimulation can promote accelerated outgrowth from the proximal stump to the distal stump compared to the innate regenerative rate. Finally, polarity of the applied stimulation has been demonstrated to influence the direction of the neurite growth cone where negative and positive polarity attracts and deflects the growth cone to the direction of the applied electric field, respectively.[83]

Another biological process that exhibits innate electrical properties is the action potential associated with the sinus rhythm contractions of cardiac cells in response to the electrical impulses imposed by the sinoatrial node.[84] A common technique utilizing electrical stimulation to restore normal function to the heart is electrical cardioversion.[85] An example of this is the delivery of external electrical stimulation to induce defibrillation of cardiac dysrhythmias (e.g., ventricular fibrillation) thus restoring sustainable normal sinus rhythm by the sinoatrial node. Internal electrical cardioversions include implantable cardioinverter defibrillators (ICD) that are surgically implanted to prevent arrhythmic, and in severe cases as a dual-functioning unit as a pacemaker to maintain rhythmic beating after defibrillation.[86-88] In terms of cardiac tissue engineering, studies have shown the ability to promote and maintain functionally differentiated cardiac cells, which would otherwise dedifferentiate *in vitro*,[89, 90] by mimicking the electric fields native to the heart.[91, 92] Furthermore, electrical stimulation promotes the maturation, alters the automaticity, and enhances expression of the gap junction protein, connexin, in human stem cell-derived cardiomyocytes in a three-dimensional culture.[93] Specialization of these cell types are crucial for *in vivo* delivery since non-synchronous contraction and poor cell-to-cell contact poses the threat of arrhythmia.[94, 95]

Various studies have induced the effects of electrical stimulation of healing and enhanced cellular functionality with the use of piezoelectric materials. In regards to wound healing, a piezoelectric dermal patch based on aligned zinc oxide nanorods induced electric fields at the wound site in response to animal movement.[96] The generated fields enhanced the effects of the endogenous wound healing process of cellular metabolism, the synthesis of wound healing-associated proteins such as vascular endothelial growth factor (VEGF) and connective tissue growth factor (CTGF/CCN-2), for which the latter promotes fibroblast migration and proliferation. Osteoblast cultured on hydroxy 10% hydroxyapatite/90%$BaTiO_3$ and exposed to a 3 Hz, 60 N cyclic compression showed greater biocompatibility and bone-induction compared to pure hydroxyapatite (non-piezoelectric) under the same cyclic regimen.[97] *In vitro* osteogenic studies utilizing mouse bone marrow-derived mesenchymal stem cells cultured in spatially controlled piezoelectric constructs made of potassium sodium niobite showed a greater differentiation efficiency than hydroxyapatite (non-piezoelectric) and non-spatially controlled constructs (fully piezoelectric) controls.[98] *In vivo*, the same constructs contributed to bone regeneration without the need for seeded stem cells due to the dynamic electrical response of the construct to bodily movements and vibration in the rabbit model. Mouse neuroblastoma cells cultured on piezoelectric PVDF substrates showed greater numbers of process outgrowth and neurite length compared to neurons cultured on otherwise identical non-piezoelectric PVDF substrates.[99] In the context of neuronal differentiation, human neural stem cells cultured on aligned, micro fibrous P(VDF-TrFE) scaffolds showed differentiation towards neurite-bearing β-III$^+$ cells when compared to laminin-coated culture plates.[100] The use of piezoelectric substrates composed of multilayered zinc oxide/PDMS composite layers allowed for cardiomyogenesis of mesenchymal stem cells.[101] The physical bending and bending-induced electrical pulses upregulated early stage cardiac phenotype markers such as NK2 homeobox 5, myocyte enhancer factor 2, and GATA binding protein 4, as well as late stage makers such as sarcomeric α-actinin and gap junction protein. These studies prove the efficacy of utilizing a piezoelectric platform to affect biological behavior through electromechanical effects similar to endogenous effects.

1.3 Conclusions

The presence of piezoelectricity *in vivo* and multi-facet utilization of electrical stimulation has allowed for the sophisticated use of piezoelectricity in biological applications. In this regard, the overall objective of my study was to investigate the fundamental characteristics of a known piezoelectric polymer, P(VDF-TrFE), and utilize the electrospinning technique as a means to manipulate these characteristics to engineer a high-performing piezoelectric platform for vastly different bio applications. In one aspect, use of the large surface area-to-volume ratio inherent to nanomaterials together with the transformative piezoelectric properties at this scale, allowed us to use the material as an ultrasensitive, stimulus-responsive, drug-release platform driven by the direct piezoelectric effect. Additionally, optimization of a balanced high-performing piezoelectric and topographical-suitable scaffold allowed for nerve stem cell specification through the direct piezoelectric effect. Finally, a proof-of-concept cell culture platform was devised, based on the indirect piezoelectric effect, for the on-demand change in the cellular microenvironment stiffness in hopes of promoting favorable cellular behaviors from physical cues.

1.4 Figures

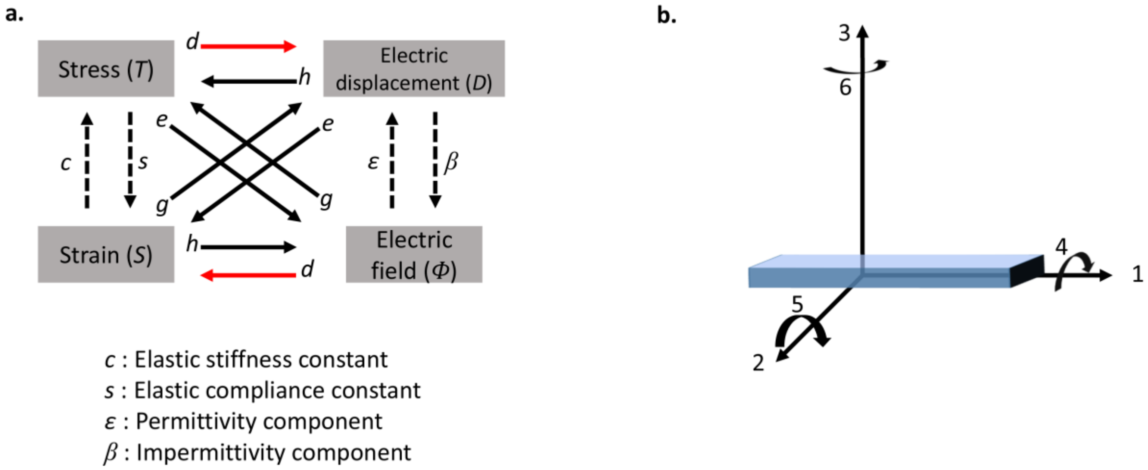

Figure 1.1 Conceptualization of piezoelectric equations and notations.

Illustrative mapping between the four dependent components of the constitutive piezoelectric equations and the piezoelectric coefficients (solid arrows) used to relate all components. (b) Numerical assignment to the direction of the compressed notation form used in the constitutive piezoelectric equations.

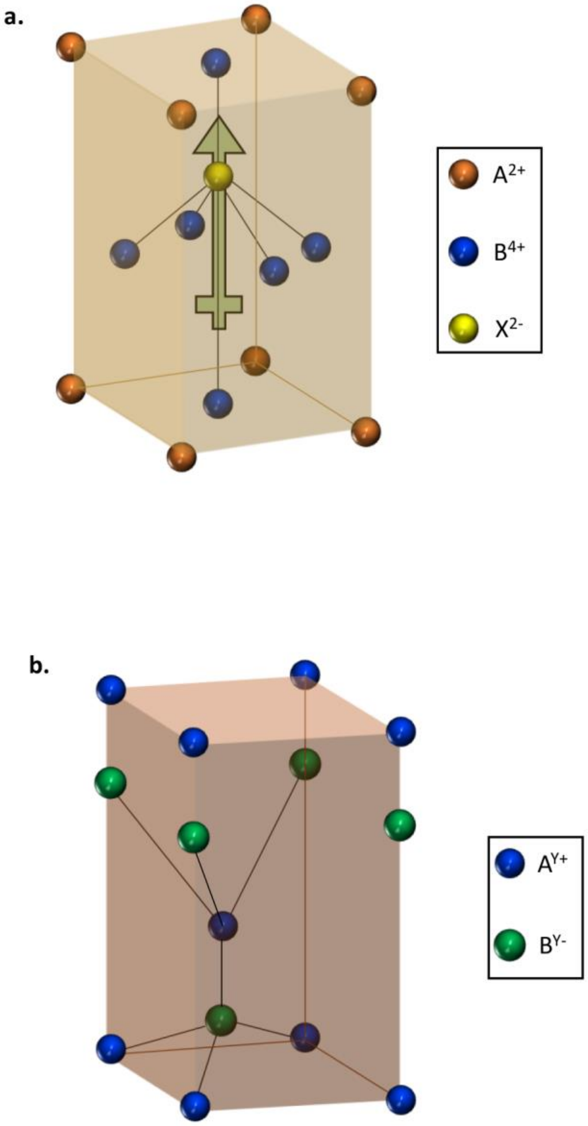

Figure 1.2 Common crystal structures of ceramic-based piezoelectric materials.

(a) A perovskite unit cell typical of piezoelectric materials such as lead zirconate titanate and barium titanate. (b) A wurtzite unit cell typical of piezoelectric zinc oxide.

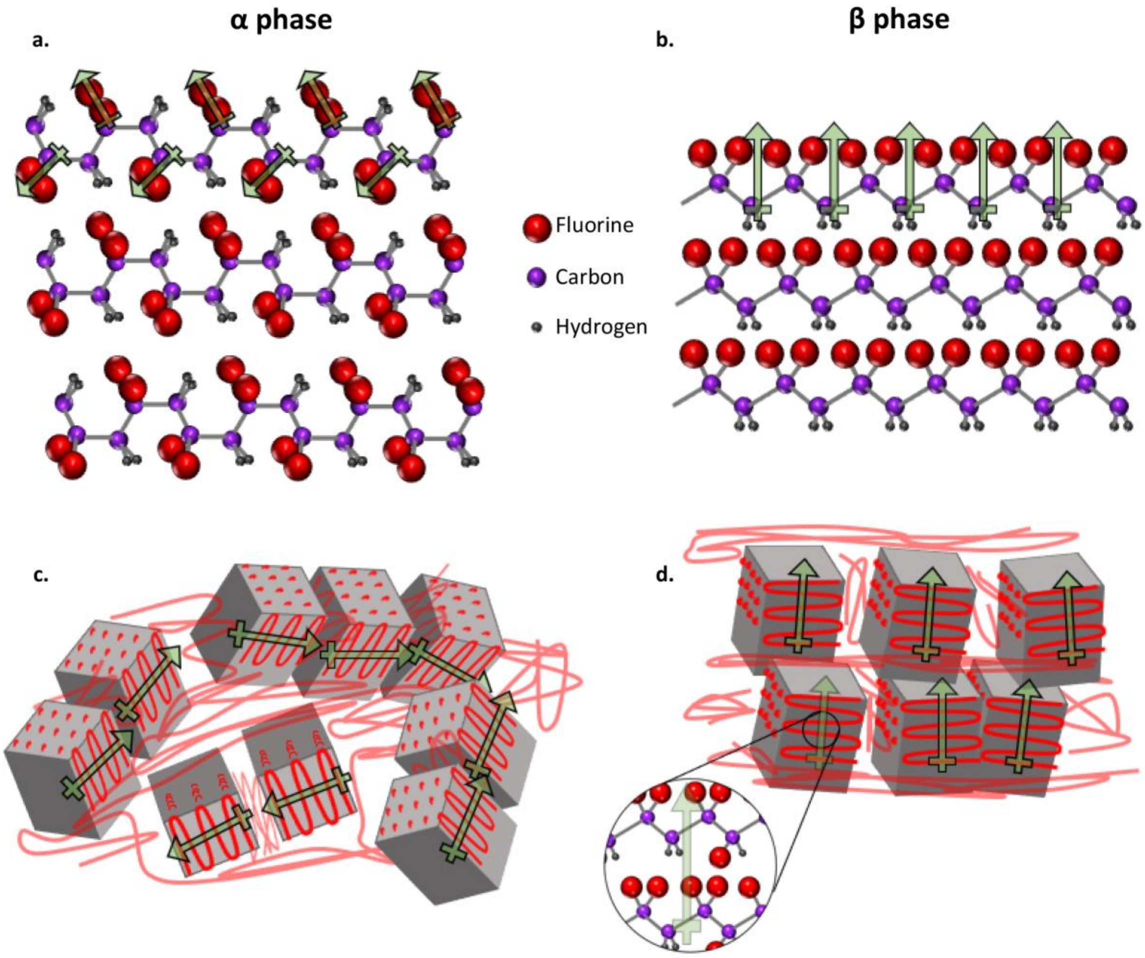

Figure 1.3 Atomic and molecular conformation of polyvinylidene fluoride (PVDF).

(a) The energetically favorable α-phase exhibits a zero-net dipole across the molecular chains due to the TGTG’ configuration as compared to (b) the β-phase in which there is a net dipole across the chain as a result of the TTTT configuration. The semi-crystalline nature of PVDF can exist in a (c) disordered state where the crystallites (domains) are randomly oriented within the amorphous state or (d) an ordered state where the domains have a preferential orientation, exemplified by the directionality of the overall dipole of each domain.

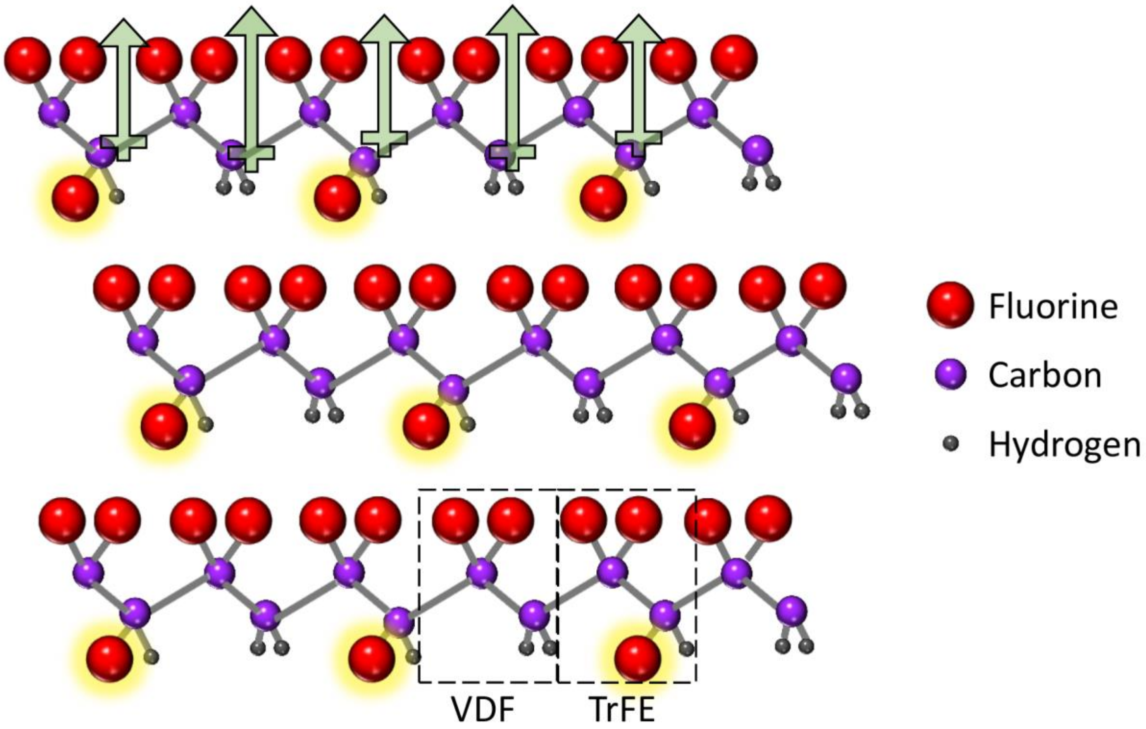

Figure 1.4 Atomic and molecular conformation of polyvinylidene fluoride (PVDF).

(a) The energetically favorable α-phase exhibits a zero net dipole across the molecular chains due to the TGTG' configuration as compared to (b) the β-phase in which there is a net dipole across the chain as a result of the TTTT configuration. The semi-crystalline nature of PVDF can exist in a (c) disordered state where the crystallites (domains) are randomly oriented within the amorphous state or (d) an ordered state where the domains have a preferential orientation, exemplified by the directionality of the overall dipole of each domain.

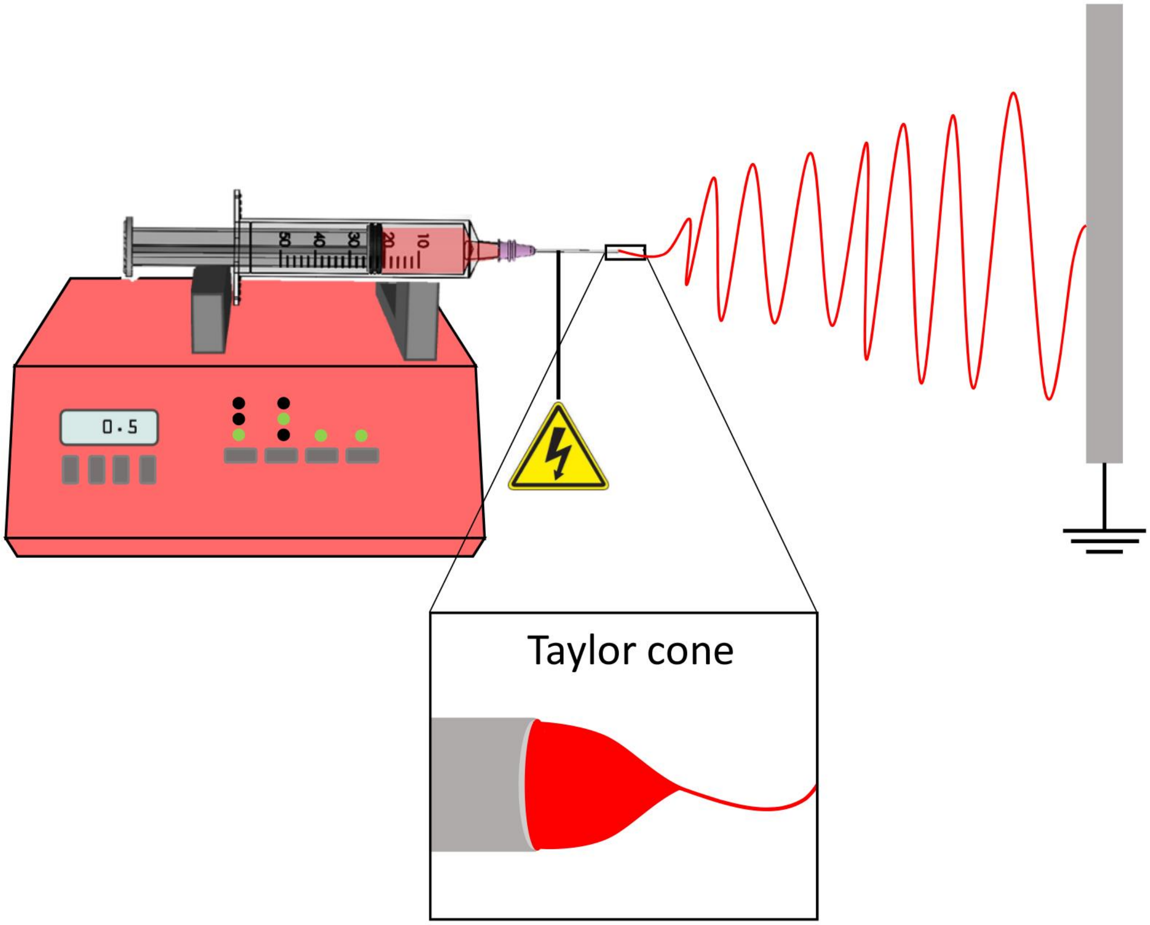

Figure 1.5 Schematic illustration of the electrospinning technique.

A solution-loaded syringe is driven by a syringe pump and charged with a high-voltage power supply with a resulting formation of a Taylor cone that is thinned into a dry fiber and attracted to a grounded collection substrate.

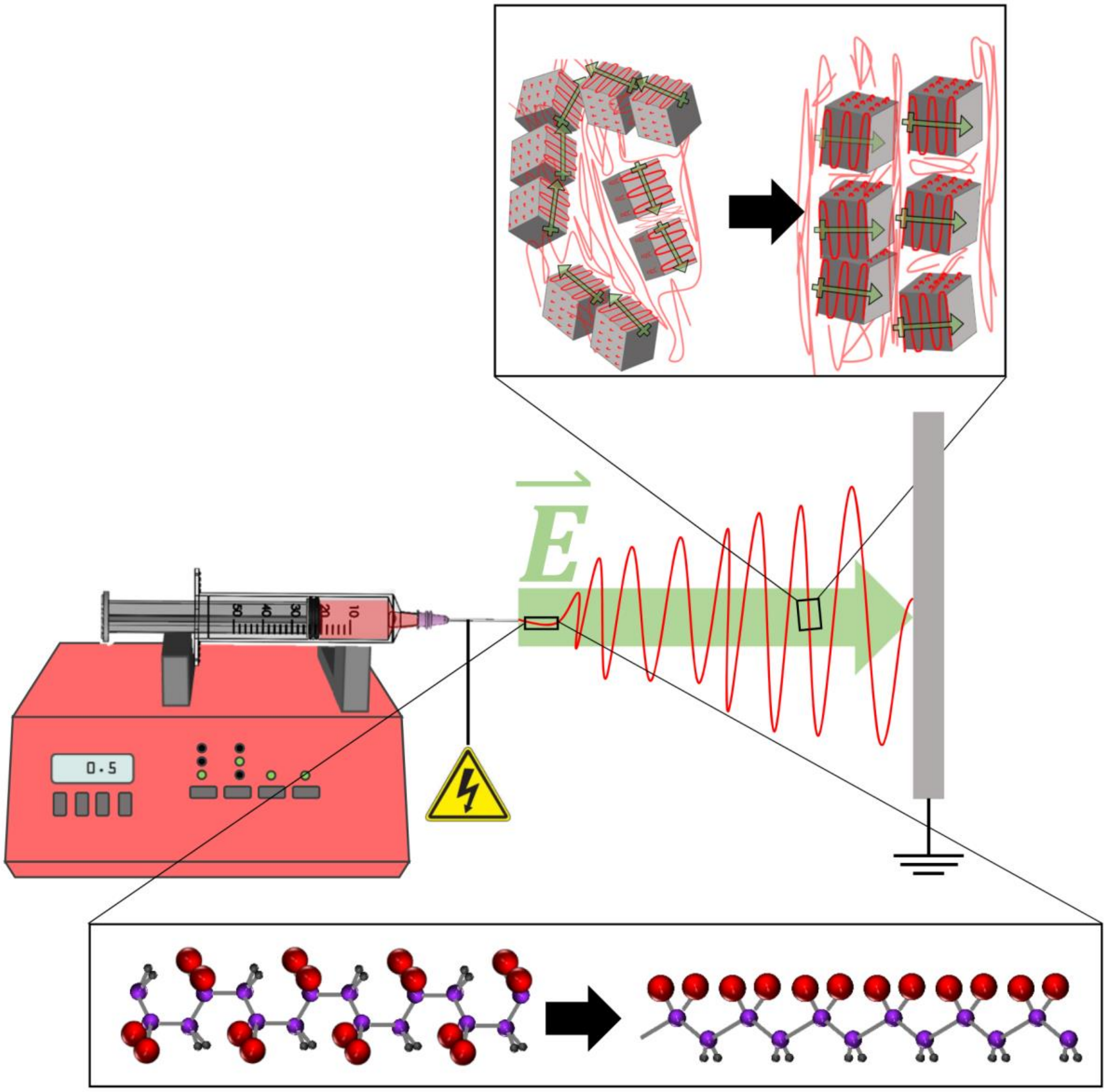

Figure 1.6 In situ processing of PVDF into its piezoelectric form by electrospinning.

The inherent stretching/thinning of the polymer solution and electric field present during electrospinning induces the molecular re-orientation from the α- to β-phase along with preferential domain orientation.

1.5 References

[1] J. Curie, P. Curie. *Développement, par pression, de l'électricité polaire dans les cristaux hémièdres à faces inclinées*. Comptes rendus 1880, 91, 294.

[2] M. G. Lippmann. *On the principle of the conservation of electricity*. 1881.

[3] J. Curie, P. Curie. *Contractions and expansions produced by voltages in hemihedral crystals with inclined faces*. Comptes rendus 1881, 93, 1137.

[4] W. J. Fleming. *Overview of automotive sensors*. IEEE sensors journal 2001, 1, 296.

[5] J. Eargle, *The Microphone Book: From mono to stereo to surround-a guide to microphone design and application*, CRC Press, 2012.

[6] E. J. Schlosser, Google Patents, 1981.

[7] W. Mohr, Google Patents, 1976.

[8] C. R. Bowen, H. A. Kim, P. M. Weaver, S. Dunn. *Piezoelectric and ferroelectric materials and structures for energy harvesting applications*. Energy & Environmental Science 2014, 7, 25.

[9] J. Briscoe, S. Dunn. *Piezoelectric nanogenerators–a review of nanostructured piezoelectric energy harvesters*. Nano Energy 2015, 14, 15.

[10] H. Nouraei, R. Ben-Mrad, A. N. Sinclair. *Development of a piezoelectric fuel injector*. IEEE Transactions on Vehicular Technology 2016, 65, 1162.

[11] M. Singh, H. M. Haverinen, P. Dhagat, G. E. Jabbour. *Inkjet printing—process and its applications*. Advanced materials 2010, 22, 673.

[12] H. Schafft. *Wide range audio transducer using piezoelectric ceramic*. Ferroelectrics 1976, 10, 121.

[13] H. J. Kim, K. Koo, S. Q. Lee, K. H. Park, J. Kim. *High performance piezoelectric microspeakers and thin speaker array system*. ETRI journal 2009, 31, 680.

[14] Y. Kurita, F. Sugihara, J. Ueda, T. Ogasawara. *Piezoelectric tweezer-type end effector with force-and displacement-sensing capability*. IEEE/ASME Transactions on Mechatronics 2012, 17, 1039.

[15] T. McPherson, J. Ueda. *A force and displacement self-sensing piezoelectric MRI-compatible tweezer end effector with an on-site calibration procedure*. IEEE/ASME Transactions on Mechatronics 2014, 19, 755.

[16] Y.-Y. Lin, H.-t. Wu, C.-A. Hsu, P.-C. Huang, Y.-H. Huang, Y.-L. Lo. *Sleep Apnea Detection Based on Thoracic and Abdominal Movement Signals of Wearable Piezoelectric Bands*. IEEE journal of biomedical and health informatics 2017, 21, 1533.

[17] U. Erdenebayar, J.-U. Park, P. Jeong, K.-J. Lee. *Obstructive Sleep Apnea Screening Using a Piezo-Electric Sensor*. Journal of Korean medical science 2017, 32, 893.

[18] T. R. Gururaja, W. A. Schulze, L. E. Cross, R. E. Newnham, B. A. Auld, Y. J. Wang. *Piezoelectric composite materials for ultrasonic transducer applications. Part I: Resonant modes of vibration of PZT rod-polymer composites*. IEEE Trans. Sonics Ultrason 1985, 32, 481.

[19] K. Nakamura, *Ultrasonic transducers: Materials and design for sensors, actuators and medical applications*, Elsevier, 2012.

[20] E. A. Geiser, L. H. Oliver. *Echocardiography: physics and instrumentation*. Cardiac Imaging and Image Processing, ed. by SM Collins and DJ Skorton, McGraw-Hill, New York 1986, 3.

[21] I. B. Rosen, P. G. Walfish, M. Miskin. *The ultrasound of thyroid masses*. The Surgical clinics of North America 1979, 59, 19.

[22] M. Miskin, A. M. Noyek, M. S. Kazdan. *Diagnostic ultrasound in otolaryngology*. Otolaryngologic Clinics of North America 1978, 11, 513.

[23] R. C. Gentile, C. J. Pavlin, J. M. Liebmann, M. Easterbrook, C. Tello, F. S. Foster, R. Ritch. *Diagnosis of traumatic cyclodialysis by ultrasound biomicroscopy*. Ophthalmic Surgery, Lasers and Imaging Retina 1996, 27, 97.

[24] D. J. Coleman, D. H. Abramson, R. L. Jack, L. A. Franzen. *Ultrasonic diagnosis of tumors of the choroid*. Archives of Ophthalmology 1974, 91, 344.

[25] M. A. Qureshi, K. Laghari. *Role of B-Scan Ultrasonography in pre-operative cataract patients*. International journal of health sciences 2010, 4, 31.

[26] P. Callen, *Ultrasonography in Obstetrics and*, Gynecology, 2000.

[27] T. Sauerbruch, M. Delius, G. Paumgartner, J. Holl, O. Wess, W. Weber, W. Hepp, W. Brendel. *Fragmentation of gallstones by extracorporeal shock waves*. New England Journal of Medicine 1986, 314, 818.

[28] M. J. Weir, N. Tariq, R. J. D'A. Honey. *Shockwave frequency affects fragmentation in a kidney stone model*. Journal of endourology 2000, 14, 547.

[29] M. M. Ciccone, A. Notarnicola, P. Scicchitano, M. Sassara, S. Carbonara, M. Maiorano, B. Moretti. *Shockwave therapy in patients with peripheral artery disease*. Advances in therapy 2012, 29, 698.

[30] R. Gregorio. *Determination of the α, β, and γ crystalline phases of poly (vinylidene fluoride) films prepared at different conditions*. Journal of Applied Polymer Science 2006, 100, 3272.

[31] N. Soin, D. Boyer, K. Prashanthi, S. Sharma, A. A. Narasimulu, J. Luo, T. H. Shah, E. Siores, T. Thundat. *Exclusive self-aligned β-phase PVDF films with abnormal piezoelectric coefficient prepared via phase inversion*. Chemical Communications 2015, 51, 8257.

[32] S. J. Kang, Y. J. Park, J. Sung, P. S. Jo, C. Park, K. J. Kim, B. O. Cho. *Spin cast ferroelectric beta poly (vinylidene fluoride) thin films via rapid thermal annealing*. Applied Physics Letters 2008, 92, 012921.

[33] F. Wang, P. Frübing, R. Gerhard, "Influence of uniaxial stretching rate and electric poling on crystalline phase transitions in poly (vinylidene fluoride) films", 2010.

[34] I. Y. Dmitriev, V. K. Lavrentyev, G. K. Elyashevich. *Polymorphic transformations in poly (vinylidene fluoride) films during orientation*. Polymer Science Series A 2006, 48, 272.

[35] V. Sencadas, R. Gregorio Jr, S. Lanceros-Méndez. *α to β phase transformation and microestructural changes of PVDF films induced by uniaxial stretch*. Journal of Macromolecular Science® 2009, 48, 514.

[36] R. I. Mahdi, W. C. Gan, W. H. Majid. *Hot plate annealing at a low temperature of a thin ferroelectric P (VDF-TrFE) film with an improved crystalline structure for sensors and actuators*. Sensors 2014, 14, 19115.

[37] J. F. Legrand. *Structure and ferroelectric properties of P (VDF-TrFE) copolymers*. Ferroelectrics 1989, 91, 303.

[38] S. B. Lang, H. L. W. Chan, *Frontiers of ferroelectricity: a special issue of the journal of materials science*, Springer Science & Business Media, 2007.

[39] S. Abdalla, A. Obaid, F. M. Al-Marzouki. *Preparation and characterization of poly (vinylidene fluoride): A high dielectric performance nano-composite for electrical storage*. Results in physics 2016, 6, 617.

[40] J. S. Harrison, Z. Ounaies, *Piezoelectric polymers*, Wiley Online Library, 2002.

[41] A. J. Lovinger, T. Furukawa, G. T. Davis, M. G. Broadhurst. *Crystallographic changes characterizing the Curie transition in three ferroelectric copolymers of vinylidene fluoride and trifluoroethylene: 1. As-crystallized samples*. Polymer 1983, 24, 1225.

[42] N. Tucker, J. Stanger, M. Staiger, H. Razzaq, K. Hofman. *The history of the science and technology of electrospinning from 1600 to 1995*. Journal of engineered fibers and fabrics 2012, 7, 63.

[43] W. E. Teo, S. Ramakrishna. *A review on electrospinning design and nanofibre assemblies*. Nanotechnology 2006, 17, R89.

[44] Q. P. Pham, U. Sharma, A. G. Mikos. *Electrospinning of polymeric nanofibers for tissue engineering applications: a review*. Tissue engineering 2006, 12, 1197.

[45] F. E. Ahmed, B. S. Lalia, R. Hashaikeh. *A review on electrospinning for membrane fabrication: challenges and applications*. Desalination 2015, 356, 15.

[46] B. Ding, M. Wang, X. Wang, J. Yu, G. Sun. *Electrospun nanomaterials for ultrasensitive sensors*. Materials Today 2010, 13, 16.

[47] P. Shirazi, G. Ico, C. S. Anderson, M. C. Ma, B. S. Kim, J. Nam, N. V. Myung. *Size-Dependent Piezoelectric Properties of Electrospun BaTiO3 for Enhanced Energy Harvesting*. Advanced Sustainable Systems 2017, 1.

[48] J. Yuh, L. Perez, W. M. Sigmund, J. C. Nino. *Electrospinning of complex oxide nanofibers*. Physica E: Low-dimensional Systems and Nanostructures 2007, 37, 254.

[49] H. Shao, J. Fang, H. Wang, T. Lin. *Effect of electrospinning parameters and polymer concentrations on mechanical-to-electrical energy conversion of randomly-oriented electrospun poly (vinylidene fluoride) nanofiber mats*. RSC advances 2015, 5, 14345.

[50] L. Persano, C. Dagdeviren, Y. Su, Y. Zhang, S. Girardo, D. Pisignano, Y. Huang, J. A. Rogers. *High performance piezoelectric devices based on aligned arrays of nanofibers of poly (vinylidenefluoride-co-trifluoroethylene)*. Nature communications 2013, 4, 1633.

[51] E. Fukada, I. Yasuda. *On the piezoelectric effect of bone*. Journal of the physical society of Japan 1957, 12, 1158.

[52] H. S. Nalwa, *Ferroelectric polymers: chemistry: physics, and applications*, CRC Press, 1995.

[53] E. Fukada, I. Yasuda. *Piezoelectric effects in collagen*. Japanese Journal of Applied Physics 1964, 3, 117.

[54] E. D. Hay, in *Cell biology of extracellular matrix*, Springer, 1991, 419.

[55] A. A. Marino, J. A. Spadaro, E. Fukada, L. D. Kahn, R. O. Becker. *Piezoelectricity in collagen films*. Calcified tissue international 1980, 31, 257.

[56] M. Minary-Jolandan, M.-F. Yu. *Uncovering nanoscale electromechanical heterogeneity in the subfibrillar structure of collagen fibrils responsible for the piezoelectricity of bone*. ACS nano 2009, 3, 1859.

[57] M. D. Shoulders, R. T. Raines. *Collagen structure and stability*. Annual review of biochemistry 2009, 78, 929.

[58] J. P. R. O. Orgel, T. C. Irving, A. Miller, T. J. Wess. *Microfibrillar structure of type I collagen in situ*. Proceedings of the National Academy of Sciences 2006, 103, 9001.

[59] D. J. S. Hulmes, A. Miller. *Quasi-hexagonal molecular packing in collagen fibrils*. Nature 1979, 282, 878.

[60] S. Perumal, O. Antipova, J. P. R. O. Orgel. *Collagen fibril architecture, domain organization, and triple-helical conformation govern its proteolysis*. Proceedings of the National Academy of Sciences 2008, 105, 2824.

[61] C. Halperin, S. Mutchnik, A. Agronin, M. Molotskii, P. Urenski, M. Salai, G. Rosenman. *Piezoelectric effect in human bones studied in nanometer scale*. Nano Letters 2004, 4, 1253.

[62] D. Li, *Electrokinetics in microfluidics*, Vol. 2, Academic Press, 2004.

[63] J. Lyklema, *Fundamentals of interface and colloid science: soft colloids*, Vol. 5, Academic press, 2005.

[64] N. Guzelsu, W. R. Walsh. *Streaming potential of intact wet bone*. Journal of biomechanics 1990, 23, 673.

[65] M. Otter, S. Goheen, W. S. Williams. *Streaming potentials in chemically modified bone*. Journal of orthopaedic research 1988, 6, 346.

[66] J. W. Vanable Jr. *Integumentary potentials and wound healing*. Electric Fields in Vertebrate Repair 1989, 171.

[67] C. A. Erickson, R. Nuccitelli. *Embryonic fibroblast motility and orientation can be influenced by physiological electric fields*. The Journal of cell biology 1984, 98, 296.

[68] N. Orida, J. D. Feldman. *Directional protrusive pseudopodial activity and motility in macrophages induced by extracellular electric fields*. Cytoskeleton 1982, 2, 243.

[69] L. C. Kloth, J. M. McCulloch. *Promotion of wound healing with electrical stimulation*. Advances in wound care 1996, 9, 42.

[70] R. Nuccitelli. *A role for endogenous electric fields in wound healing*. Current topics in developmental biology 2003, 58, 1.

[71] M. E. Mycielska, M. B. A. Djamgoz. *Cellular mechanisms of direct-current electric field effects: galvanotaxis and metastatic disease*. J Cell Sci 2004, 117, 1631.

[72] L. F. Jaffe, J. W. Vanable. *Electric fields and wound healing*. Clinics in dermatology 1984, 2, 34.

[73] A. Rubinacci, L. Tessari. *A correlation analysis between bone formation rate and bioelectric potentials in rabbit tibia*. Calcified tissue international 1983, 35, 728.

[74] J. C. Gan, P. A. Glazer. *Electrical stimulation therapies for spinal fusions: current concepts*. European Spine Journal 2006, 15, 1301.

[75] J. J. Forsyth, R. C. Davey, in *Exercise Physiology in Special Populations*, Churchill-Livingston, 2008, 225.

[76] C. T. Brighton, J. Black, Z. B. Friedenberg, J. L. Esterhai, L. J. Day, J. F. Connolly. *A multicenter study of the treatment of non-union with constant direct current*. JBJS 1981, 63, 2.

[77] J. L. Esterhai, Z. B. Friedenberg, C. T. Brighton, J. Black. *Temporal course of bone formation in response to constant direct current stimulation*. Journal of orthopaedic research 1985, 3, 137.

[78] Z. B. Friedenberg, L. M. Zemsky, R. P. Pollis. *The response of non-traumatized bone to direct current*. JBJS 1974, 56, 1023.

[79] P. R. T. Kuzyk, E. H. Schemitsch. *The science of electrical stimulation therapy for fracture healing*. Indian journal of orthopaedics 2009, 43, 127.

[80] R. B. Borgens, *Electric fields in vertebrate repair: natural and applied voltages in vertebrate regeneration and healing*, Wiley-Liss, 1989.

[81] N. M. Geremia, T. Gordon, T. M. Brushart, A. A. Al-Majed, V. M. K. Verge. *Electrical stimulation promotes sensory neuron regeneration and growth-associated gene expression*. Experimental neurology 2007, 205, 347.

[82] M. P. Willand, M.-A. Nguyen, G. H. Borschel, T. Gordon. *Electrical stimulation to promote peripheral nerve regeneration*. Neurorehabilitation and neural repair 2016, 30, 490.

[83] N. B. Patel, M.-M. Poo. *Perturbation of the direction of neurite growth by pulsed and focal electric fields*. Journal of Neuroscience 1984, 4, 2939.

[84] O. Monfredi, H. Dobrzynski, T. Mondal, M. R. Boyett, G. M. Morris. *The anatomy and physiology of the sinoatrial node—a contemporary review*. Pacing and clinical electrophysiology 2010, 33, 1392.

[85] M. Sucu, V. Davutoglu, O. Ozer. *Electrical cardioversion*. Annals of Saudi medicine 2009, 29, 201.

[86] M. Mirowski, P. R. Reid, M. M. Mower, L. Watkins, V. L. Gott, J. F. Schauble, A. Langer, M. S. Heilman, S. A. Kolenik, R. E. Fischell. *Termination of malignant ventricular arrhythmias with an implanted automatic defibrillator in human beings*. N Engl j Med 1980, 303, 322.

[87] G. H. Bardy, K. L. Lee, D. B. Mark, J. E. Poole, D. L. Packer, R. Boineau, M. Domanski, C. Troutman, J. Anderson, G. Johnson. *Amiodarone or an implantable cardioverter–defibrillator for congestive heart failure*. New England Journal of Medicine 2005, 352, 225.

[88] A. E. Epstein, G. N. Kay, V. J. Plumb, R. B. Shepard, J. K. Kirklin. *Combined automatic implantable cardioverter-defibrillator and pacemaker systems: implantation techniques and follow-up*. Journal of the American College of Cardiology 1989, 13, 121.

[89] M. Fitzgerald, C. B. Neylon, A. R. Marks, E. A. Woodcock. *Reduced ryanodine receptor content in isolated neonatal cardiomyocytes compared with the intact tissue*. Journal of molecular and cellular cardiology 1994, 26, 1261.

[90] M. Eppenberger-Eberhardt, I. Flamme, V. Kurer, H. M. Eppenberger. *Reexpression of α-smooth muscle actin isoform in cultured adult rat cardiomyocytes*. Developmental biology 1990, 139, 269.

[91] N. Tandon, C. Cannizzaro, P.-H. G. Chao, R. Maidhof, A. Marsano, H. T. H. Au, M. Radisic, G. Vunjak-Novakovic. *Electrical stimulation systems for cardiac tissue engineering*. Nature protocols 2009, 4, 155.

[92] Z. Feng, T. Matsumoto, Y. Nomura, T. Nakamura. *An electro-tensile bioreactor for 3-D culturing of cardiomyocytes*. IEEE engineering in medicine and biology magazine 2005, 24, 73.

[93] G. Eng, B. W. Lee, L. Protas, M. Gagliardi, K. Brown, R. S. Kass, G. Keller, R. B. Robinson, G. Vunjak-Novakovic. *Autonomous beating rate adaptation in human stem cell-derived cardiomyocytes*. Nature communications 2016, 7, 10312.

[94] S.-Y. Liao, Y. Liu, C.-W. Siu, Y. Zhang, W.-H. Lai, K.-W. Au, Y.-K. Lee, Y.-C. Chan, P. M.-C. Yip, E. X. Wu. *Proarrhythmic risk of embryonic stem cell–derived cardiomyocyte transplantation in infarcted myocardium*. Heart Rhythm 2010, 7, 1852.

[95] Y. Mandel, A. Weissman, R. Schick, L. Barad, A. Novak, G. Meiry, S. Goldberg, A. Lorber, M. R. Rosen, J. Itskovitz-Eldor. *Human Embryonic and Induced Pluripotent Stem Cell–Derived Cardiomyocytes Exhibit Beat Rate Variability and Power-Law BehaviorClinical Perspective*. Circulation 2012, 125, 883.

[96] S. H. Bhang, W. S. Jang, J. Han, J. K. Yoon, W. G. La, E. Lee, Y. S. Kim, J. Y. Shin, T. J. Lee, H. K. Baik. *Zinc Oxide Nanorod-Based Piezoelectric Dermal Patch for Wound Healing*. Advanced Functional Materials 2017, 27.

[97] Y. Tang, C. Wu, Z. Wu, L. Hu, W. Zhang, K. Zhao. *Fabrication and in vitro biological properties of piezoelectric bioceramics for bone regeneration*. Scientific reports 2017, 7, 43360.

[98] P. Yu, C. Ning, Y. Zhang, G. Tan, Z. Lin, S. Liu, X. Wang, H. Yang, K. Li, X. Yi. *Bone-Inspired Spatially Specific Piezoelectricity Induces Bone Regeneration*. Theranostics 2017, 7, 3387.

[99] R. F. Valentini, T. G. Vargo, J. A. Gardella Jr, P. Aebischer. *Electrically charged polymeric substrates enhance nerve fibre outgrowth in vitro*. Biomaterials 1992, 13, 183.

[100] Y.-S. Lee, T. L. Arinzeh. *The influence of piezoelectric scaffolds on neural differentiation of human neural stem/progenitor cells*. Tissue Engineering Part A 2012, 18, 2063.

[101] J.-K. Yoon, T. I. Lee, S. H. Bhang, J.-Y. Shin, J.-M. Myoung, B.-S. Kim. *Stretchable piezoelectric substrate providing pulsatile mechanoelectric cues for cardiomyogenic differentiation of mesenchymal stem cells*. ACS applied materials & interfaces 2017, 9, 22101.

2. Size-dependent piezoelectric and mechanical properties of electrospun P(VDF-TrFE) nanofibers

2.1 Introduction

Piezoelectric materials have generated a growing interest in the diverse field of electromechanical applications for their ability to reciprocally link mechanical and electrical energies. Under the direct piezoelectric effect, an external mechanical stress induces a charge separation on the material's surface, whereas the reverse effect allows the material to exhibit a mechanical strain in response to an applied external electric field.[1] The growing demand for clean and renewable energy sources has driven the interest in developing "green" materials and systems based on such novel material characteristics for ambient energy harvesting. For example, various configurations of devices comprised of piezoelectric materials have demonstrated their ability to harvest unutilized mechanical energies.[2-5]

Inorganic materials, such as barium titanate ($BaTiO_3$), zinc oxide (ZnO), and lead zirconate titanate (PZT), are known to exhibit the highest piezoelectric responses.[6, 7] Despite their superior electromechanical response, however, these inorganic materials are brittle, therefore imposing mechanical limitations for a wide range of energy harvesting applications. In contrast, organic piezoelectric materials are mechanically resilient, providing an alternative for addressing this issue. Both polyvinylidene fluoride (PVDF), and its derivatives (*e.g.,* poly(vinylidene fluoride-trifluoroethylene (P(VDF-TrFE)), are semi-crystalline polymers that possess piezoelectric characteristics due to the polar carbon fluorine domains.[8, 9] PVDF normally settles in its α-phase which is composed of chain conformation in the trans (T) and gauche (G) linkages (*i.e.*, TGTG’). In order to produce the piezoelectric effect, PVDF has to be poled into its electroactive phases, either its more pronounced β-phase containing all trans conformation (*i.e.,* TTTT) and/or γ-phase (T_3GT_3G') by physical stretching and/or exposing the linkages to a strong electric field.[10] The electroactive phases allow for permanent dipoles within macroscopic domains, for which unidirectional re-orientation under a physical stress or an electric field leads to the development of a net surface charge accumulation. Trifluoroethylene residues in the copolymer, P(VDF-TrFE), act as steric hindrance stabilizers to form the β-phase[11] which minimizes the necessity for extra processing (*i.e.,* physical stretching) to attain piezoelectric properties albeit such a post-process can further enhance piezoelectricity.[12]

In this context, electrospinning is advantageous to produce high performance piezoelectric polymers because the technique intrinsically subjects the polymers to a high electric field. A charged polymer jet under an electric field is attracted to a collection plate, resulting in the formation of a fibrous structure whose dimensions are controlled from a few microns down to several nanometers in diameter. During the process, the fibers are also subjected to a mechanical stretching/poling due to polymer jet elongation and whipping, further enhancing piezoelectricity. Indeed, it has been shown that electrospinning enhances piezoelectric properties of P(VDF-TrFE)[9], and even induces piezoelectricity in PVDF without the typically required post-poling process.[13]

The capacity of a piezoelectric material is commonly represented by electric charge separation and mathematically represented by the constitutive piezoelectric strain-charge equation,

$$D_i = d_{ij}\sigma_j = d_{ij}E_{kj}\varepsilon_k, \tag{2.1}$$

where D_i is the electric charge separation, d_{ij}, the piezoelectric coefficient, σ_j, the applied stress, E_{kj}, the Young's modulus, ε_k, the applied strain. Intuitively from the equation, changes in d_{ij} and/or E_{kj} would effectively modulate charge separation and affect the efficiency of energy harvesting. Thus far, most studies aimed to enhance piezoelectricity via modulation of the piezoelectric coefficient, d_{ij}, by novel material development. Examples include polymer-based piezocomposite materials with inorganic piezoelectric materials[14, 15] or multiwalled carbon nanotubes.[16] In spite of an equivalent contribution from E_{kj} to the overall piezoelectric response, the mechanical aspects of piezoelectric materials are often neglected.

It has been recently demonstrated that the energy conversion efficiency of electrospun PVDF is superior to that of thin films of the same thickness, and it is further enhanced by decreasing fiber diameter.[17] The enhancement was proposed to arise from a few possible factors, including fewer defects due to a higher degree of crystallinity, size-dependent flexoelectricity, or nonlinear extrinsic responses known as domain wall motion.[17] These phenomenological observations provide critical information regarding methodologies to further enhance the performance of electrospun organic piezoelectric materials, yet the fundamental mechanisms are still elusive. Herein, we take a systematic approach to precisely control the fiber diameter of electrospun P(VDF-TrFE) ranging from approximately 1000 nm down to 70 nm. We then investigated the electric output of fibrous mats composed of these nanofibers by subjecting them to precisely controlled mechanical strains. To determine the underlying mechanisms of dimensional dependency of piezoelectricity, we examined both electromechanical and mechanical behaviors of electrospun P(VDF-TrFE) at the single fiber level by experimentally measuring the piezoelectric constant (d_{33}) and elastic modulus (E). Finally, an analysis of the phase and crystallinity content provides further explanation as to the enhanced piezoelectric response we observe with nanofibers having fiber diameter below 100 nm. The results provide a guide to design efficient piezoelectric energy harvesting devices utilizing electrospun nanofibers.

2.2 Experimental

2.2.1. Synthesis of electrospun P(VDF-TrFE)

P(VDF-TrFE) (70/30 mole%) (Solvay Group, France) was dissolved in a 60/40 vol. ratio of *N-N* dimethylformamide to acetone (Fisher Scientific, Pittsburgh, PA) at various polymer concentrations. For select solutions, pyridinium formate buffer (PF) (Santa Cruz

Biotechnology, Dallas, TX) was added at the indicated concentrations. All solutions were magnetically stirred for 1 hr until the solution was visually transparent.

Each solution was separately loaded into a 10 ml syringe attached with a 250 µm inner diameter needle. The solution feed rate was controlled at 0.5 ml/hr by a syringe pump (New Era Pump Systems, Inc., Farmingdale, NY). The solution was negatively charged at 14 kV by a high voltage supply (Glassman High Voltage, Inc., High Bridge, NJ). A metal collection substrate was placed 20 cm from the needle, and positively charged at a fixed voltage of 0.5 kV for all conditions. Environmental conditions were kept constant at 24 °C and absolute humidity of 7.6 g/m^3.

2.2.2. Characterization of electrospinning solutions and resulting nanofibers

The viscosity, electrical conductivity, and surface tension of the electrospinning solutions were characterized by a viscometer (Brookfield Engineering Laboratories, Inc., Middleboro, MA), a 4-cell conductivity probe (Fisher scientific, Pittsburgh, PA) and a tensiometer (Scientific Gear LLC, Fairfax, VA), respectively. The morphology of resulting electrospun nanofibers from the solutions were characterized using a VEGA3 scanning electron microscope (SEM) (Tescan Brno, Czech Republic). Fiber diameter (n=30) and bead density were assessed using ImageJ software.

2.2.3. Electric output measurements of electrospun nanofiber mats

Electrospun P(VDF-TrFE) having four different average fiber diameters (approximately 90, 166, 242, and 859 nm) were separately collected at a thickness of approximately 20 µm. A cantilever set up was adopted to induce a controlled strain on the fiber samples (**Figure 2.1a**).[18, 19] The cantilever was composed of a 7.2x 1.6 x 0.01 cm^3 brass shim covered on both sides with polyimide tape to electrically isolate it from the electrical system. A 1 x 1 cm^2 sample was cut from the 20 µm thick electrospun nanofiber mat and fixed to the center of the cantilever with double sided copper tape which served as the bottom-contact electrode while a similar size aluminum foil was used as the top electrode. Two separate 24 gauge wires were fixed to the contacts, sealed with a strip of polyimide tape, and led to a breadboard with inputs to an oscilloscope (Lecroy, Chestnut Ridge, NY) to measure the output voltage from the nanofiber mat.

Cantilever bending was enhanced by attaching a 2.3 g proof mass at the end of the cantilever and driven by a custom-made vibrational system (**Figure 2.1b**). The system utilizes a cantilever holder mounted on the top of the diaphragm of a subwoofer speaker. An ACC103 accelerometer (OMEGA Engineering, Inc., Stamford, CT) and a GoPro Hero3+ (GoPro, Inc., San Mateo, CA) were also fixed on the surface, to correlate the vibrational acceleration to cantilever surface strain which was calculated by,

$$Strain\,\% = \frac{t/_2}{R} \times 100, \tag{2.2}$$

where t is the thickness of the assembled cantilever, and R is the radius of curvature of a circle overlaid on the curved cantilever surface, measured by the video camera (**Figure 2.1c**).[20] A sinusoidal sound wave with controlled frequency and amplitude was delivered to the speaker via a custom LabVIEW VI. 10 Hz was the resonance frequency of the cantilever set-up determined through a frequency sweep test at a fixed acceleration of 30 m/s^2 (**Figure 2.1d**). This frequency was kept constant for all subsequent experiments.

Total current (I_{total}) measurements were conducted by measuring the voltage drop (V) across the total resistance ($R_T = \frac{R_I R_L}{R_I + R_L}$) of the circuit and utilizing the current equation, $I_{total} = \frac{V}{R_T}$, where R_I is the internal resistance of the oscilloscope (10 MΩ) and R_L is a varying load resistor resulting in R_T to be 0.5, 0.9, 1.7, 3.3, 6.88, or 10 MΩ. Similarly, power (P) was calculated by $P = \frac{V^2}{R_T}$.

To demonstrate the feasibility of real-world applications of the device from a common source of wasted energy, the assembled cantilever was mounted on a side-mirror of a moving vehicle and exploited the resulting air-flow around the vehicle for energy generation. Measurement of the output voltage was recorded using an oscilloscope powered by a power inverter connected to an amplifier in the vehicle.

2.2.4. Determination of piezoelectric constant using piezoresponse force microscopy (PFM)

To measure the piezoelectric constant of individual fibers, P(VDF-TrFE) nanofibers were sparsely collected on a gold coated silicon (Si) substrate during electrospinning. A MFP-3D AFM (Asylum Research, Santa Barbara, CA) in tapping mode was used to first visualize and locate individual fibers, followed by precise placement of the AFM tip on a fiber. The AFM was then switched to PFM mode where single point measurements were conducted by applying an alternating step voltage to the AFM cantilever (AC240TM, Olympus). Contact resonance was used to amplify the responding signal. At least, five independent fibers were tested at five different locations along the fiber length for each condition. Thick P(VDF-TrFE) film (80 μm) was synthesized by drop-casting a 15 wt.% P(VDF-TrFE) in acetone solution onto a gold coated Si substrate and utilized as a reference.

2.2.5. Mechanical characterization of individual electrospun nanofibers

A nanoscale three-point flexural test was used to determine the Young's modulus of individual nanofibers having different fiber diameters. To serve as a support for the suspended fiber, trench grated Si substrates were microfabricated as described elsewhere.[21] Briefly, the grated patterns, placed on the Si surface by photolithography, were transferred into the Si substrate using a fluorine-based dry etching process. Each Si chip contained 0.5, 0.75, 1, 2.5, 5, 10, 25, and 50 μm trenches that are specifically designed for the proper gap distance for measuring the mechanical properties of a fiber with a particular fiber diameter.

Electrospinning on the patterned Si substrate was conducted similar to the fiber collection for PFM. After fiber deposition, the AFM was first used in tapping mode to map the location of a suspended fiber across a trench having a desired separation, followed by precise placement of the AFM tip at the center of the suspended fiber. The AFM was then switched to force mode to collect force-displacement curves. The extension and retraction speed of the AFM cantilever (AC160TS, Olympus) was fixed at 5 µm/s and the trigger force for each measurement was set at 1 µN.

In order to calculate the Young's modulus (E) from AFM force-displacement curves, Euler's beam theory was used by relating the force (F), indentation (δ), fiber suspension length (L), and fiber polar moment of inertia (I) in the equation,

$$E = \frac{L^3\left({}^{F}/_{\delta}\right)}{48I} \ . \tag{2.3}$$

Fiber radius (r) is taken into account in the inertia terms such that,

$$I = \frac{\pi r^4}{4} \ . \tag{2.4}$$

Equation 2.3 accounts for non-fixed ends at the ends of the fiber suspension length.[22] The trench size was selected for each fiber such that the ratio between suspension length and fiber diameter (D) was greater than 16 (*i.e.,* L/D > 16) in order to minimize the effects of shear forces in the force measurements.[23]

2.2.6. Phase and crystallinity content determination of electrospun fibers

Fourier transform infrared spectroscopy (FTIR) of electrospun nanofibers was conducted to quantify phase changes depending on nanofiber diameter with an Equinox 55 FTIR spectrometer (Bruker Corp., Billerica, MA) in absorbance mode from 600 to 1600 cm^{-1}. Five spectrums per condition were collected and averaged. The electroactive phases (β- and γ-phase) percentage was calculated by the following equation utilizing the measured absorbance spectrum,

$$EA\% = \frac{A_{EA}}{1.3A_{\alpha} + A_{EA}} \times 100 \tag{2.5}$$

where A_{EA} is the absorbance value at 841 cm^{-1} , A_{α} is the absorbance at 764 cm^{-1}, and the factor 1.3 is the ratio of absorption coefficients at 841 cm^{-1} (K_{841}= 7.7x10^4 cm^2 mol^{-1}) to 764 cm^{-1} (K_{764} = 6.1x10^4 cm^2 mol^{-1}) at the respective wavenumber.[24]

The degree of crystallinity of electrospun P(VDF-TrFE) nanofibers having various fiber diameters was calculated from X-ray diffraction (XRD) spectra collected with an

Empyrean X-ray diffractometer (PANalytical, Almelo, the Netherlands) at 2θ from 10 - 27°, through the summation of integrated area under each crystallinity phase (α, β, and γ) over the total summation of integrated area under both crystallinity and amorphous. [25, 26]

2.3 Results and discussion

2.3.1. Solution properties and fiber morphology

In order to correlate the electromechanical and mechanical properties of P(VDF-TrFE) nanofibers as a function of fiber dimension, we first set out to precisely control the electrospun fiber dimensions and eliminate defects (*i.e.,* beads) through a systematic approach using statistics-oriented design of experiments (DOEs). A two-level full factorial design with two factors (*i.e.,* P(VDF-TrFE) and PF solution concentrations) was designed. This requires four experimental runs, with factor analysis focusing on fiber diameter and bead density (**Table 2.1**). A fifth run was added to the design to serve as a center point to potentially reveal any second order quadratic effects, deviating from the general linear model on fiber diameter and bead density.

The initial low (-) and high (+) values of each design factor were empirically determined. The high P(VDF-TrFE) concentration was set based on a solution that exhibited a stable Taylor cone during electrospinning (*i.e.,* 15 wt.%), while the low concentration was determined from a solution that exhibited an unstable Taylor cone with bead formation (*i.e.,* 7 wt.%). A high PF concentration of 1 wt.% was determined from a solubility limit test when PF was mixed with the P(VDF-TrFE) solution while the low limit was set to 0 wt.%. The center point solution was synthesized at 11 wt.% P(VDF-TrFE) and 0.5 wt.% PF. The five solutions showed the expected trends in solutions properties, including concentration-dependent solution viscosity and electrical conductivity with a relatively stable surface tension (**Table 2.1**). Electrospinning the five solutions at the fixed electrospinning parameters resulted in various fiber morphologies (**Figure 2.2**). Without or with the presence of PF, the high concentration of P(VDF-TrFE) resulted in uniform fibers with smooth surfaces with average fiber diameters of approximately 375 and 457 nm, respectively (**Figure 2.2a** and **Figure App.A1a; Figure 2.2b** and **Figure App.A1b**). When the P(VDF-TrFE) concentration was reduced to 7 wt.% in the absence of PF, thus effectively reducing the solution viscosity, electrospinning produced smaller fiber diameters of approximately 177 nm (**Figure 2.2c** and **Figure App.A1c**). However, these fibers exhibited bead formation possibly caused by the unbalance between the viscoelastic and electrical properties of the solution leading to Taylor cone instability.[27] The addition of 1 wt.% PF to the same 7 wt. % P(VDF-TrFE) solution composition effectively increased solution conductivity from 3.2 to 30.4 µS/cm and eliminated the formation of beaded fibers, but it increased the fiber diameter from 177 nm to approximately 208 nm (**Figure 2.2d** and **Figure App.A1d**). Electrospinning of the center point solution produced fibers with an average diameter of approximately 255 nm, yielding a curvature (quadratic term) of 49 nm or about 16% below the expected (linear) value (304 nm) given by averaging the 4-corners (**Figure 2.2e** and **Figure App.A1e**).

The factor analysis showed that P(VDF-TrFE) concentration exerts the greatest effect on fiber diameter, as demonstrated by the stiffest slope in the main effect plot (**Figure 2.2f** and **Figure App.A1f**). Additionally, the direction of the slope indicates that a decrease in fiber diameter is achieved by decreasing P(VDF-TrFE) concentration. PF concentration also had an effect on fiber diameter, albeit to a significantly lesser extent than P(VDF-TrFE) concentration. The combination of the two factors has a less of an effect on fiber diameter as compared to P(VDF-TrFE) concentration . In addition, factor analysis revealed that both P(VDF-TrFE) concentration and PF concentration are highly influential to bead density (**Figure 2.2g** and **Figure App.A1g**). The increased concentration of the factors have a similar effect in magnitude and manner, exhibiting a decrease in bead formation. Unlike fiber diameter, the interactions between the two factors significantly affected the bead density. For example, it is necessary to increase the PF concentration in order to prevent bead formation when the P(VDF-TrFE) concentration is lowered to promote the reduction of fiber dimensions. These results collectively indicate that both P(VDF-TrFE) and PF concentrations should be addressed accordingly to yield the desired fiber diameter and morphology.

Based on these observations, a second DOE was designed to further reduce fiber size while limiting the bead formation (**Table 2.2**). The low and high values for each P(VDF-TrFE) and PF concentrations were set at 7 and 2 wt.% and 1 and 1.5 wt.%, respectively. Similar to the first DOE, the lower bound concentration of P(VDF-TrFE) was determined by the Taylor cone instability and formation of beads at the set low value of 1 wt.% PF.

The upper-bound limit of PF concentration was tested for solubility in the P(VDF-TrFE) solution. A center point solution consisting of 4.5 wt.% P(VDF-TrFE) and 1.25 wt.% PF was also included. Similar to the previous sets of solutions in the first DOE, only the solution viscosity and electrical conductivity were affected by the changes in the factors. The difference in the viscosity of sample 4 from DOE 1 and that of sample 1 from DOE 2 is noted. This is due to the additional adjustment of water content depending on the amount of added PF concentration.

SEM imaging of the DOE 2 fibers showed a decrease in the average fiber diameter by decreasing the P(VDF-TrFE) concentration from 7 wt.% (approximately 405 nm at 1 wt.% PF, 481 nm at 1.5 wt.% PF) (**Figure 2.3a** and **Figure App.A2a; Figure 2.3b** and **Figure App.A2b**) to 2 wt.%-1 wt.%PF (approximately 71 nm), but with bead formation (**Figure 2.3c** and **Figure App.A2c**). Increasing the PF concentration to 1.5 wt. % at the low concentration of P(VDF-TrFE) led to the elimination of beads with an average fiber diameter of approximately 67 nm (**Figure 2.3d** and **Figure App.A2d**). The center point solution produced fibers with an average diameter of approximately 197 nm, yielding a curvature (quadratic term) of 59 nm or about 23% below the expected (linear) value (256 nm) given by averaging the 4-corners. (**Figure 2.3e** and **Figure App.A2e**). Similar to the first factor analysis, decreasing P(VDF-TrFE) concentration leads to a decrease in fiber diameter (**Figure 2.3f** and **Figure App.A2f**) while increasing PF concentration prevents bead formation (**Figure 2.3g** and **Figure App.A2g**). The effect of PF concentration on fiber diameter was significantly reduced as compared to that in the first DOE, in this fiber size range. The effects of both individual factors and interactions between the factors on bead density were similar to the results in the first DOE. Considering that the used PF concentration is the maximum allowed for complete solubility, the resulting fiber size from 2 wt.% P(VDF-TrFE) concentration is likely in the range of the smallest fiber sizes that can be produced without the bead formation in this polymer-solvent system.

2.3.2. Electric performance of different average fiber diameter nanofiber mats

After establishing a means to precisely control fiber diameter, the electrospun P(VDF-TrFE) nanofiber mats of various fiber diameters were investigated to determine size-dependent piezoelectric properties under controlled strains. Five separate cantilevers each with either 90, 166, 242, and 859 nm average fiber diameter mats were tested in the custom vibrational system. At a fixed frequency of 10 Hz and surface strain of 0.18%, the results showed that the voltage generation was exponentially increased by decreasing the fiber diameter fibers especially below approximately 200 nm (**Figure 2.4a** and **Figure App.A3**). At a maximum peak-to-peak voltage of approximately 700 mV, this value exceeds the reports from other studies.[7, 28] It should be noted that the electric output of piezoelectric materials strongly depends on many factors such as test-measurement set up and strain rate, making a direct comparison difficult.[29, 30]

Determination of the maximum peak-to-peak total current (**Figure 2.4b**) and maximum peak-to-peak power (**Figure 2.4c**) outputs for each nanofiber mat required measuring the voltage drop across a total resistance which was adjusted by varying the load resistor (**Figure App.A4**). The potential drop across each total resistance increased as the load was increased from 0.5 MΩ to an open circuit potential (i.e., ∞ MΩ). This behavior is expected since the induced charge separation from the piezoelectric nanofiber mat is greater for larger resistance values. Further analysis showed that the current and power outputs are also fiber size dependent where each measured fiber diameter has an optimum output at a particular total resistance. The maximum peak-to-peak total current and peak-to-peak power, extracted from **Figure App.A5,** for each nanofiber mat having different fiber size is plotted in **Figure 2.4b** and **Figure 2.4c**. This indicates that, in addition to the fiber diameter, total resistance in the system can be adjusted to meet power requirements.

Additionally, translation of the cantilever assembly to a real world application demonstrates the potential of utilizing the nanofibers for harvesting wasted energy (**Figure 2.5**). By mounting the piezoelectric cantilever on the surface of a moving vehicle, the mechanical strain produced by the wind turbulence generated approximately 2.5 V_{p-p} from the cantilever containing the 90 nm average diameter nanofiber mat (**Figure 2.5c**).

2.3.3. Piezoelectric coefficient dependency on nanofiber size

To elucidate the underlying mechanisms governing the dimension dependent piezoelectricity of electrospun P(VDF-TrFE) nanofibers, electromechanical and mechanical properties were investigated at the single fiber level. As shown in the constitutive strain-charge piezoelectric equation (**Equation 2.1**), the electrical response of a piezoelectric material depends on the intrinsic piezoelectric coefficient (d_{33}), Young's modulus of the material (E), and an applied strain (ε). **Equation 2.1** can be further derived to describe the output voltage (V) of varying fiber sizes through the voltage equation[31]

$$V = \frac{D_3 d}{k} = \frac{[d_{33}\sigma_3\ ]d}{k} = \frac{[d_{33}(E_{33}\varepsilon_3)\ ]d}{k}, \tag{2.6}$$

where k is the permittivity of the material and d is the charge separation distance (*i.e.,* fiber diameter). **Equation 2.6** indicates that the piezoelectric coefficient, Young's modulus of the material and nanofiber diameter collectively determine electric output of the electrospun P(VDF-TrFE) at a particular dimension.

The fiber size dependent d_{33} values were determined by PFM (**Figure 2.6**). The PFM phase response image showed a relatively uniform color distribution across the fiber surface, indicating a uniaxial oriented dipole moment as expected from other studies that demonstrated polarization of PVDF by electrospinning[32] (**Figure 2.6a**). PFM imaging in amplitude mode also showed a relatively uniform amplitude response across the same fiber (**Figure 2.6b**). It should be noted that due to the triangular nature of the AFM tip, in-plane scanning leads to a common artifact which makes a fiber appear to be larger in width than the measured fiber diameter through other methods such as SEM, as described by Schneider et al.[28] Therefore, only the out-of-plane height value was used to properly determine the actual fiber diameter during the PFM measurements. To determine the piezoresponse of the fibers in more detail, individual fibers were subjected to single point piezoresponse spectroscopy in contact mode. Under an applied step voltage (top), representative raw signals of a PFM measurement shows the phase (middle) and amplitude (bottom) responses of a P(VDF-TrFE) fiber (**Figure 2.6c**). Due to the direction of the electric field of our electrospinning set up (*i.e.,* from the positive collection plate to a negative spinneret) we expected the dipole orientation of electrospun P(VDF-TrFE) domains to be perpendicular to, and pointing away from, the collection surface. As expected, the phase response shows a 180 degree orientation switch in dipole moment when a positive bias is applied while a 0 degree response was observed when a negative bias is applied. Amplitude response, however, remains the same in magnitude regardless of the polarity of the applied voltage.

Similarly, the fiber dimension-dependent d_{33} of electrospun P(VDF-TrFE) fibers was determined from the amplitude response of individual fibers having different diameters. For the calculation of d_{33}, the quality factor (Q) of the AFM cantilever was taken into account since the amplitude responses were amplified by utilizing a resonance tracking technique, such that

$$d_{33} = \frac{A}{VQ}, \qquad (2.7)$$

where A is the amplitude and V is the applied voltage.[33] The results show that any sized electrospun P(VDF-TrFE) fibers exhibit a greater d_{33} as compared to bulk, and the fibers between 500 - 1000 nm in diameter exhibit slightly greater or equal d_{33} value as compared to thick film P(VDF-TrFE) (**Figure 2.6d**). More importantly, there is a substantial increase in d_{33} when the fiber diameter decreases below 500 nm. Curve-fitting shows a linear log-log relationship between d_{33} and the inverse of fiber diameter as

$$\log d_{33} = 1.96 + 0.19 \log \frac{1}{d}, \qquad (2.8)$$

where d is the fiber diameter (R^2=0.89, **Figure 2.6e**). To the best of our knowledge, the empirically determined maximum d_{33} perpendicular to the fiber length in this study (-56 pm/V) exceeds the reported values of PVDF (fiber:45pm/V[14]; film: 33 pm/V[34]) and P(VDF-TrFE) (film: -40 pm/V[35, 36]). This is likely due to the effects of substantial dimensional reduction that may lead to structural changes such as an increase in the electroactive phase, or lowered domain wall barriers.[7] The only comparable d_{33} (-56.7 pm/V) value was reported from a single PVDF fiber deposited by near-field electrospinning.[37] However, it should be noted that the dipole orientation of the near-field electrospun fiber runs parallel with the fiber axis, different from the perpendicular dipole orientation in the fibers produced by the far-field electrospinning process, utilized in this study. Therefore, a direct comparison between the two values is inappropriate.

2.3.4. Young's Modulus dependency on nanofiber size

Dimensional reduction of a material typically results in the substantial increase in the material stiffness, represented by Young's modulus.[38, 39] As shown in **Equation 2.6**, such an increase in Young's modulus can significantly affect the overall charge separation, thus the piezoelectric performance. To investigate the effects of dimensional reduction on the mechanical properties of individual nanofibers, a three-point flexural test at the nanoscale was utilized (**Figure 2.7**). In order to subject an individual nanofiber to the three-point bending, a Si substrate having micro-patterned trenches with well-defined gap distances was utilized (**Figure 2.7a**). Individual fibers were visualized by AFM in imaging mode prior to being subjected to loading by the AFM in force mode (**Figure 2.7b**). A representative force-displacement curve from these measurements is shown in **Figure 2.7c**. A linear region of the extension curve from the force-displacement data and **Equation 2.3** were used to calculate the Young's moduli of P(VDF-TrFE) fibers of different diameters (**Figure 2.7d**). The Young's moduli of the individual fibers having diameters between the range of 800 nm to 1000 nm were relatively close in value to that of bulk P(VDF-TrFE) at 1 GPa. However, fibers showed significant increase in Young's modulus as the diameter was further decreased. As shown in **Figure 2.7e**, a linear log-log relationship was revealed between *E* and the inverse of fiber diameter (R^2=0.89) as

$$\log E = 4.89 + 1.62 \log \frac{1}{d} \ . \qquad (2.9)$$

These results are comparable to the study in which the dimensional reduction in poly(2-acrylamido-2-methyl-1-propanesulfonic acid) (PAMPS) nanofibers exponentially increased Young's modulus from ~ 0.3 GPa to 2.0 GPa as the diameter was reduced.[39]

2.3.5. Phase and crystal structure content dependency on nanofiber size

To understand the mechanisms underlying the fiber size-dependent increase in piezoresponse and Young's modulus of electrospun P(VDF-TrFE), electroactive phase content and the degree of crystallinity were characterized by FTIR and XRD, respectively for the selected fiber diameters (**Figure 2.8** and **Figure App.A6**). An increase in electroactive phase formation in electrospun PVDF as compared to thick film was observed similar to the reports by others[40, 41]. Interestingly, Fig. 8a shows that the electroactive phases ratio increased as the fiber dimension decreased, which is expected to contribute to the observed increase in d_{33}. The electroactive content of the electrospun P(VDF-TrFE) fibers in this study (up to approximately 89%) exhibited a similar, or higher values than the reported values in literature.[9, 16, 40, 42]

Simultaneously, the decrease in fiber diameter resulted in an increase in the degree of crystallinity (**Figure 2.8b** and **Figure App.A6d**). The increase in ordered microstructure of polymer chains likely contributed to the enhanced mechanical properties of the electrospun P(VDF-TrFE) fibers as has been observed for other polymer types.[43, 44] Furthermore, the predicted Young's modulus by **Equation 2.9** can be curve-fitted to the degree of crystallinity with an R^2=0.96 as shown in **Figure 2.8b**, further demonstrating the strong correlation between the crystallinity and the fiber mechanical properties. Similarly, the calculated amount of the electroactive phases (*i.e.,* the product of electroactive phases content and crystallinity) was curve-fitted by the predicted d_{33} using **Equation 2.8** ($R^2 = 0.98$) since the electroactive phases of P(VDF-TrFE) is responsible for the piezoelectric properties of the polymer[32] (**Figure 2.8c**). The results demonstrate a possibility of further enhancing piezoelectric properties of electrospun P(VDF-TrFE) by increasing not only the electroactive phases content but also material crystallinity.

Since both the electromechanical and mechanical properties of electrospun P(VDF-TrFE) fibers contribute to energy generation, the interaction of the two on electric output at the single fiber level as a function of fiber diameter was numerically determined and compared to the measured values (**Figure 2.8d**). **Equations 2.8** and **2.9**, which correlate piezoelectric constant and Young's modulus to fiber diameter, were combined with **Equation 2.6** to predict voltage generated by a single fiber with different fiber diameters. A significant correlation was found between the predicted values of single fibers and the measure voltage values of nanofiber mats from Fig. 4a (R^2=0.84). This correlation strongly indicates that while the piezoelectric coefficient is significant in determining the electrical performance of a piezoelectric material, mechanical properties of the material equally contribute to piezoelectric efficiency.

2.4 Conclusion

In summary, a systematic approach using DOE was used to precisely control fiber size (from sub-100 nm to 1000 nm) and morphology of electrospun P(VDF-TrFE) fibers. The dependency of the electromechanical and mechanical properties of electrospun P(VDF-TrFE) on fiber size was demonstrated. Specifically, the electric output of electrospun P(VDF-TrFE) nanofiber mats strongly depended on fiber diameter with an exponential behavior, where smaller fibers exhibited greater electric output. This is likely due to the substantial increases in both piezoelectric constant (approximately 2-fold change) and Young's modulus (80-fold change) at the smaller dimensions. These findings are attributed to the combination of increases in the electroactive phase content and crystallinity by the dimensional reduction. Both the electromechanical and mechanical properties of electrospun P(VDF-TrFE) have demonstrated to be important fundamental factors in determining piezoelectric properties of the nanofibers, suggesting a new strategy to improve/optimize the piezoelectric performance of electrospun P(VDF-TrFE).

2.5 Tables and figures

Table 2.1 . First design of experiment matrix.

Experimental design variables (P(VDF-TrFE) concentration, PF concentration) each with their respective low (-) and high (+) values and their effect on solution properties. Viscosity taken at a shear rate 90.5 s^{-1}.

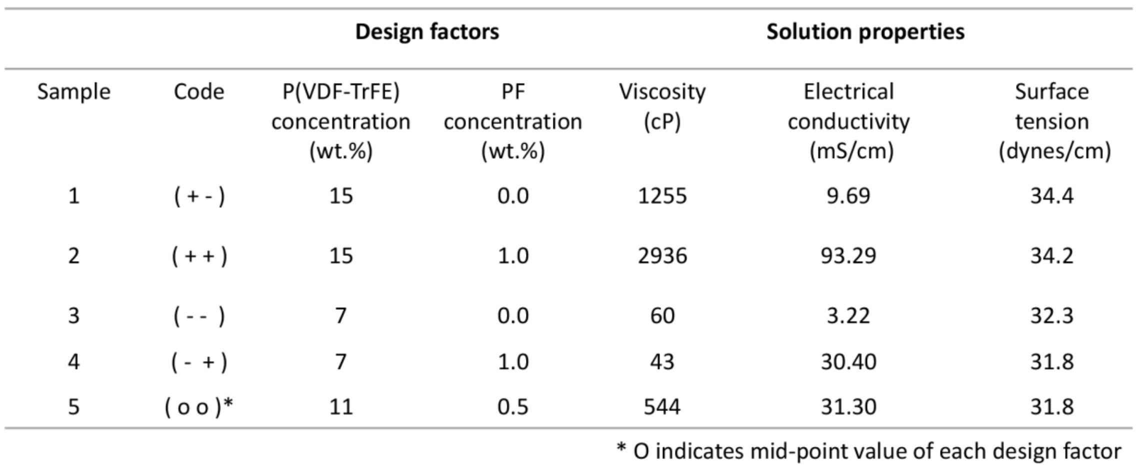

		Design factors		**Solution properties**		
Sample	Code	P(VDF-TrFE) concentration (wt.%)	PF concentration (wt.%)	Viscosity (cP)	Electrical conductivity (mS/cm)	Surface tension (dynes/cm)
1	(+ -)	15	0.0	1255	9.69	34.4
2	(+ +)	15	1.0	2936	93.29	34.2
3	(- -)	7	0.0	60	3.22	32.3
4	(- +)	7	1.0	43	30.40	31.8
5	(o o)*	11	0.5	544	31.30	31.8

* O indicates mid-point value of each design factor

Table 2.2. Second design of experiment matrix.

Modified experimental design variables (P(VDF-TrFE) concentration, PF concentration) each with their respective low (-) and high (+) values and their effect on solution properties. Viscosity taken at a shear rate 90.5 s^{-1}.

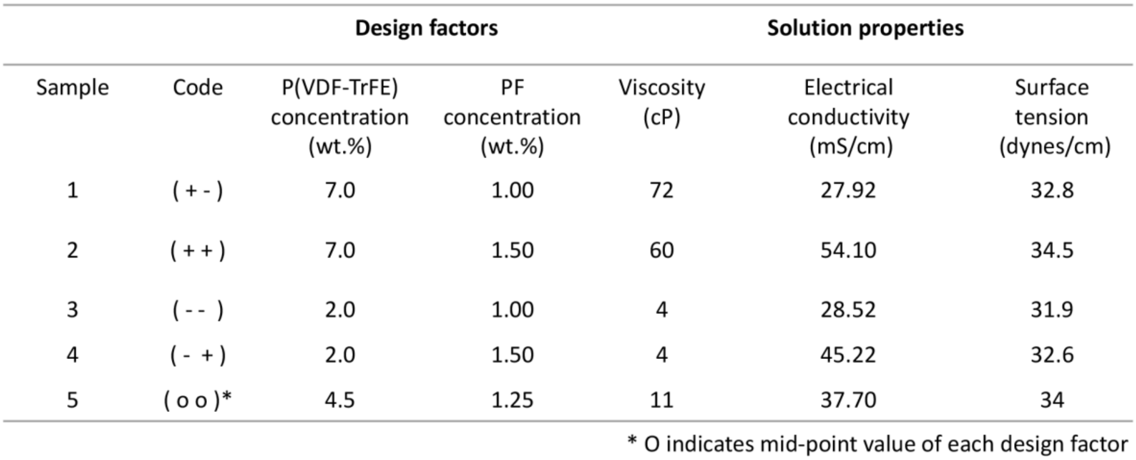

		Design factors		Solution properties		
Sample	Code	P(VDF-TrFE) concentration (wt.%)	PF concentration (wt.%)	Viscosity (cP)	Electrical conductivity (mS/cm)	Surface tension (dynes/cm)
1	(+ -)	7.0	1.00	72	27.92	32.8
2	(+ +)	7.0	1.50	60	54.10	34.5
3	(- -)	2.0	1.00	4	28.52	31.9
4	(- +)	2.0	1.50	4	45.22	32.6
5	(o o)*	4.5	1.25	11	37.70	34

* O indicates mid-point value of each design factor

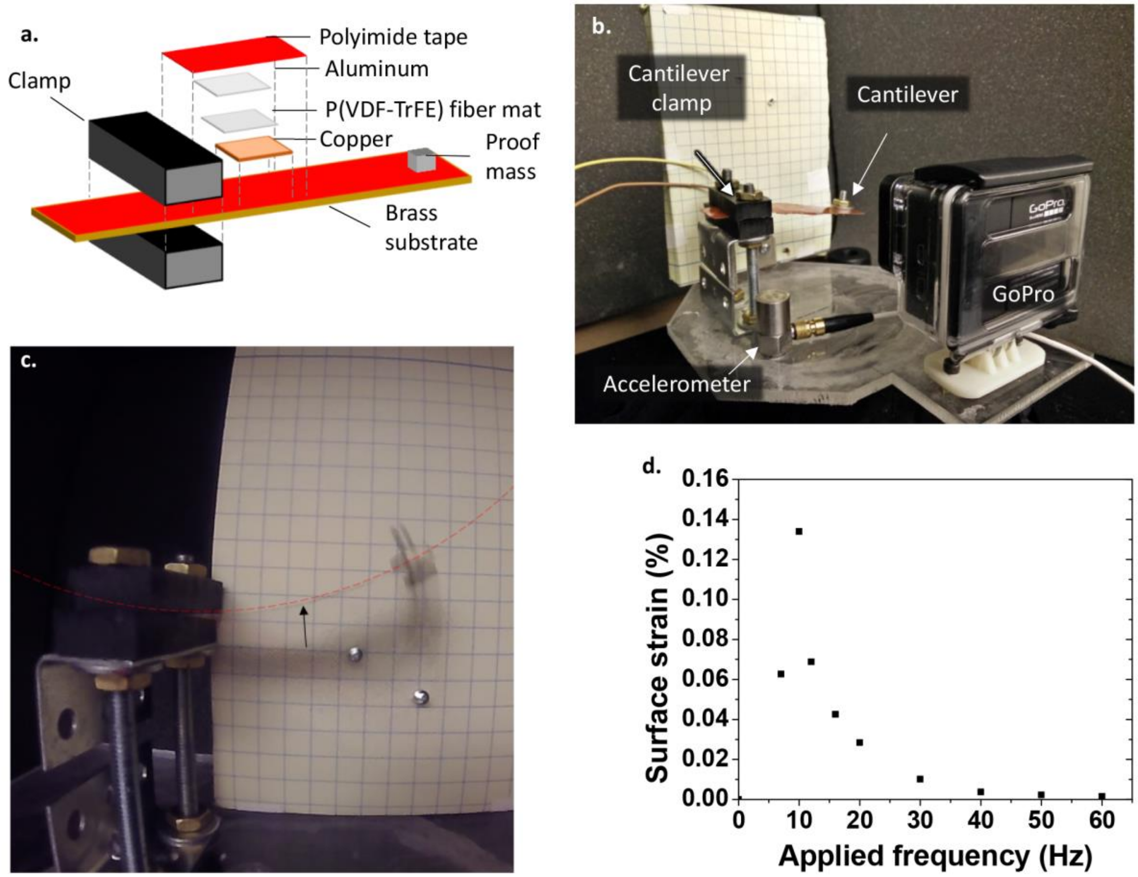

Figure 2.1 Custom piezoelectric actuation system.

(a) A schematic showing a cantilever where electrospun P(VDF-TrFE) nanofiber mat is sandwiched between two electrodes and sealed in the middle of the beam with polyimide tape. The proof mass aids in bending the cantilever while it is clamped on the vibrating surface on (b) which an accelerometer and a video camera are also mounted. The surface strain imposed on the sample is calculated using *Equation 2*, where the radius of the curvature is captured in the video and tracing an overlaid circle on the bend of the cantilever (red dashed curve). (d) Frequency sweep from 0 to 60 Hz correlation to surface strain calculated from Equation 2 shows the optimum frequency at 10 Hz.

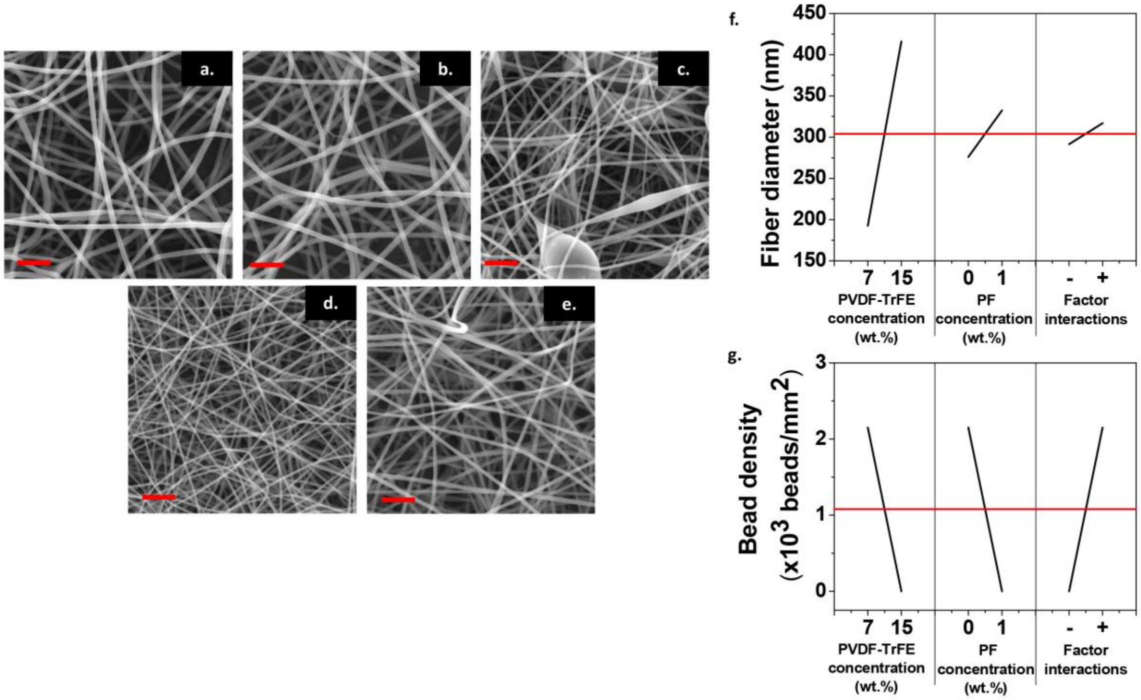

Figure 2.2 Morphological characterization of electrospun P(VDF-TrFE) fibers and factor effects from the first DOE conditions.

Resulting fiber morphology of 15 wt.% P(VDF-TrFE) solution with 0 wt.% (a) and 1 wt.% (b) PF, 7 wt.% P(VDF-TrFE) solution with 0 wt.% (c) and 1 wt.% (d) PF, and midpoint 11 wt.% P(VDF-TrFE) solution with 0.5 wt.% PF(e). (Scale bar = 2 µm). Effect of each design parameters, P(VDF-TrFE) concentration and PF concentration, low and high on fiber diameter (f) (n=30) and bead density (g). The red line indicates the mean value of the respective morphology.

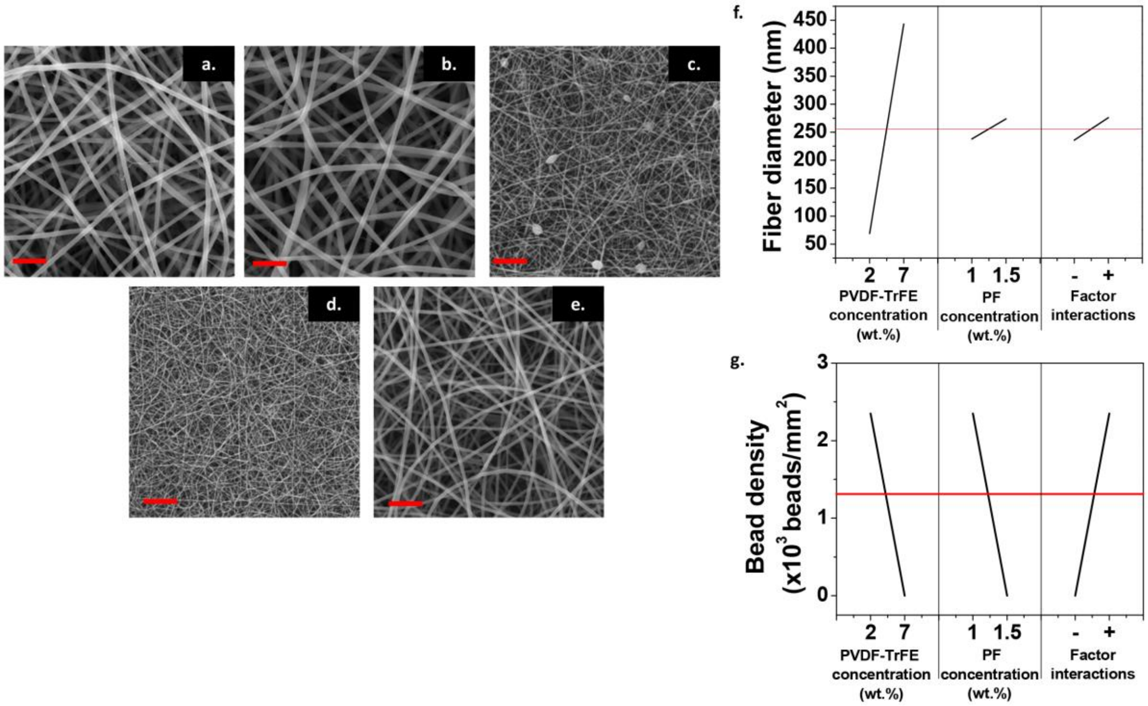

Figure 2.3 Morphological characterization of electrospun P(VDF-TrFE) fibers and factor effects from second DOE conditions.

Resulting fiber morphology of 7 wt.% P(VDF-TrFE) solution with 1 wt.% (a) and 1.5 wt.% (b) PF, 2 wt.% P(VDF-TrFE) solution with 1 wt.% (c) and 1.5 wt.% (d) PF, and midpoint 4.5 wt.% P(VDF-TrFE) solution with 1.25 wt.% PF (e). (Scale bar = 2 μm). Effect of each design parameters, P(VDF-TrFE) concentration and PF concentration, low and high on fiber diameter (f) (n=30) and bead density (g). The red line indicates the mean value of the respective morphology.

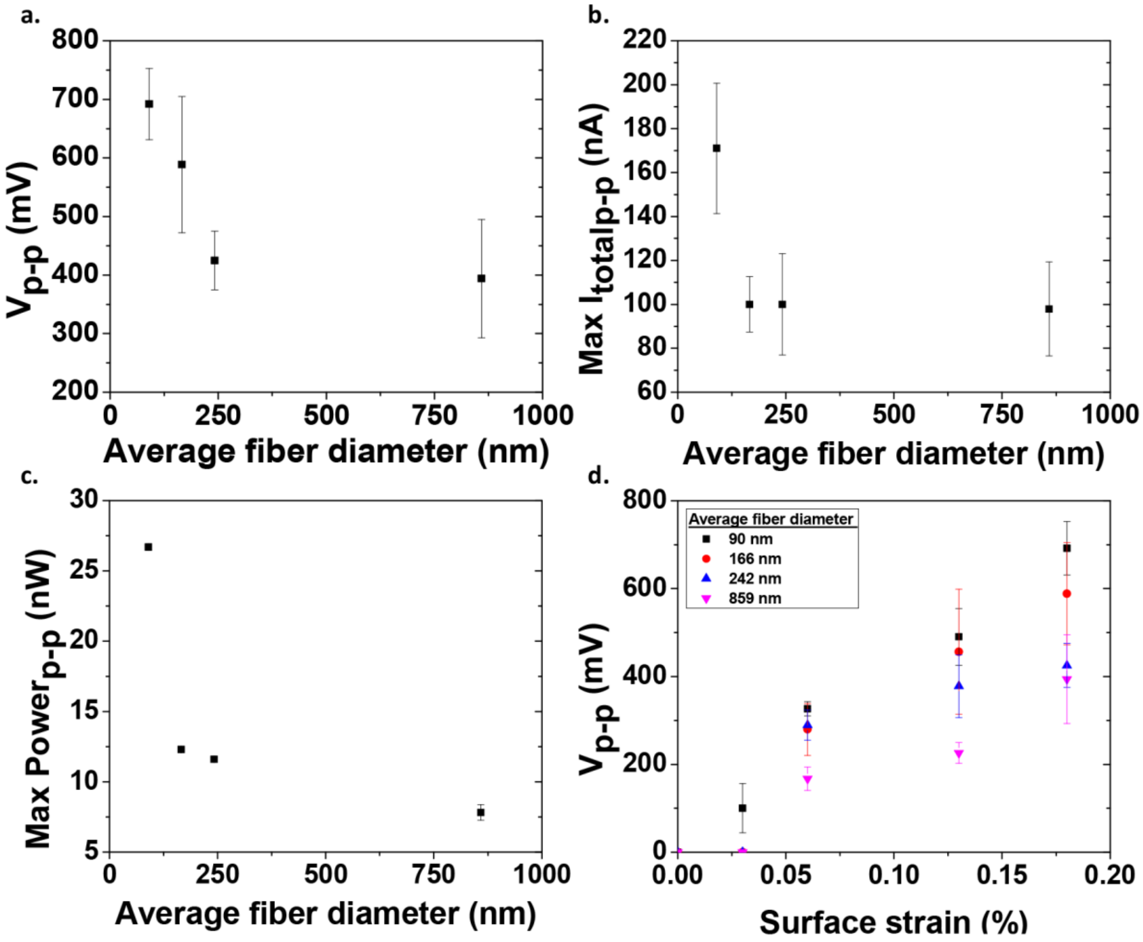

Figure 2.4 The effects of (a-c) fiber diameter and (d) applied strain on the electric output of electrospun P(VDF-TrFE) nanofiber mats.

(a) Peak-to-peak voltage, (b) maximum peak-to-peak current, and (c) maximum peak-to-peak power of electrospun P(VDF-TrFE) nanofiber mats having various average fiber diameter under 0.18% strain. (b) Peak-to-peak voltage generation of electrospun P(VDF-TrFE) nanofiber mats having various average fiber diameter under various applied strains.

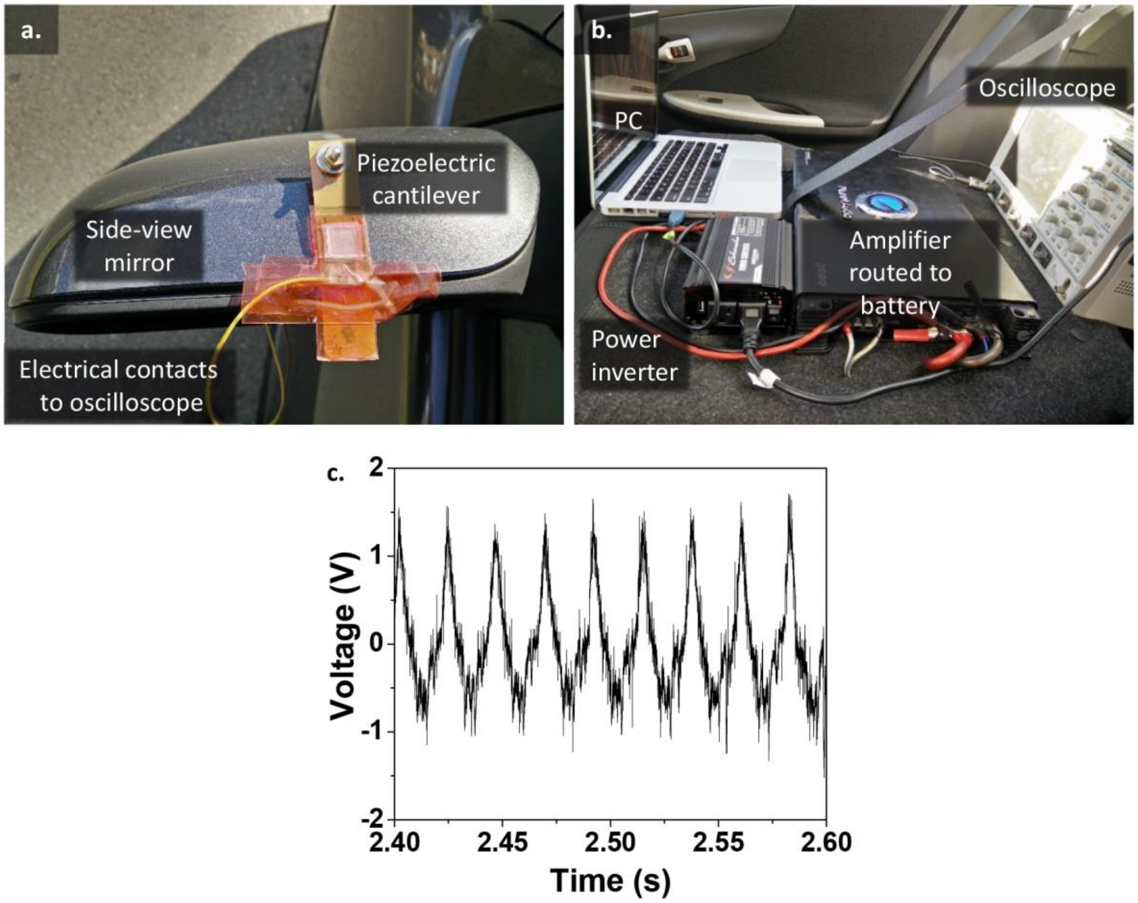

Figure 2.5 Wasted energy harvesting using electrospun P(VDF-TrFE) nanofibers.

(a) The P(VDF-TrFE) nanofibers having an average fiber diameter of 90 nm were assembled to the cantilever system and mounted on the side-view mirror of a vehicle. (b) Wires from the mounted cantilever were routed to an oscilloscope powered by a power inverter connected to an amplifier. (c) An example of the voltage generation in the electrospun P(VDF-TrFE) nanofibers mounted on a moving vehicle over a period of 200 ms.

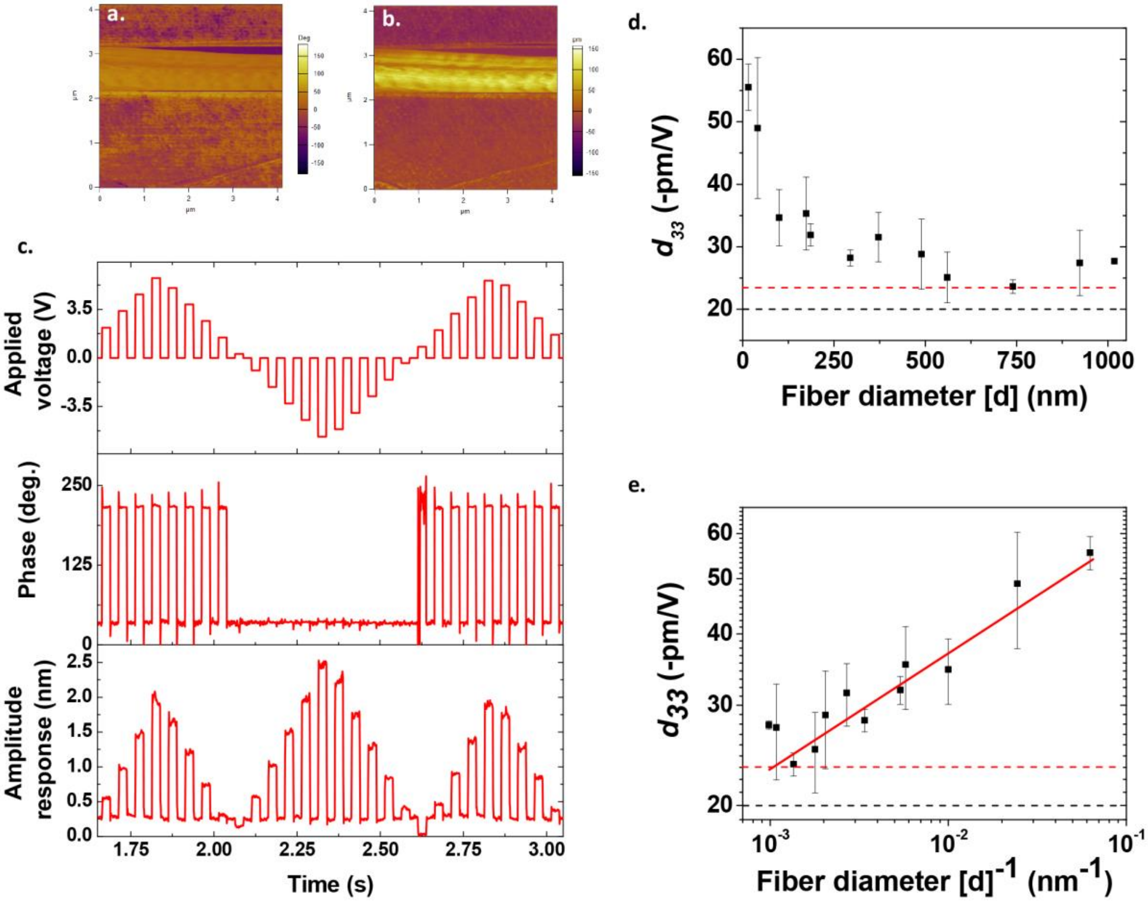

Figure 2.6 Piezoresponse force microscopy (PFM) on individual P(VDF-TrFE) nanofibers.

PFM contrast mapping with consistent phase response along the fiber (a), and amplitude response of the same fiber (b). Amplitude and phase change in response to an applied bias over time (c). Measured d_{33} as a function of fiber diameter from point specific PFM (d) and in log-log form (e) showing an increase in d_{33} with a decrease in fiber diameter. The red dashed line indicates the measured d_{33} of a 80 µm thick film and the black dashed line indicates the d_{33} of bulk P(VDF-TrFE). The solid red line is a linear best-fit (Equation 2.7).

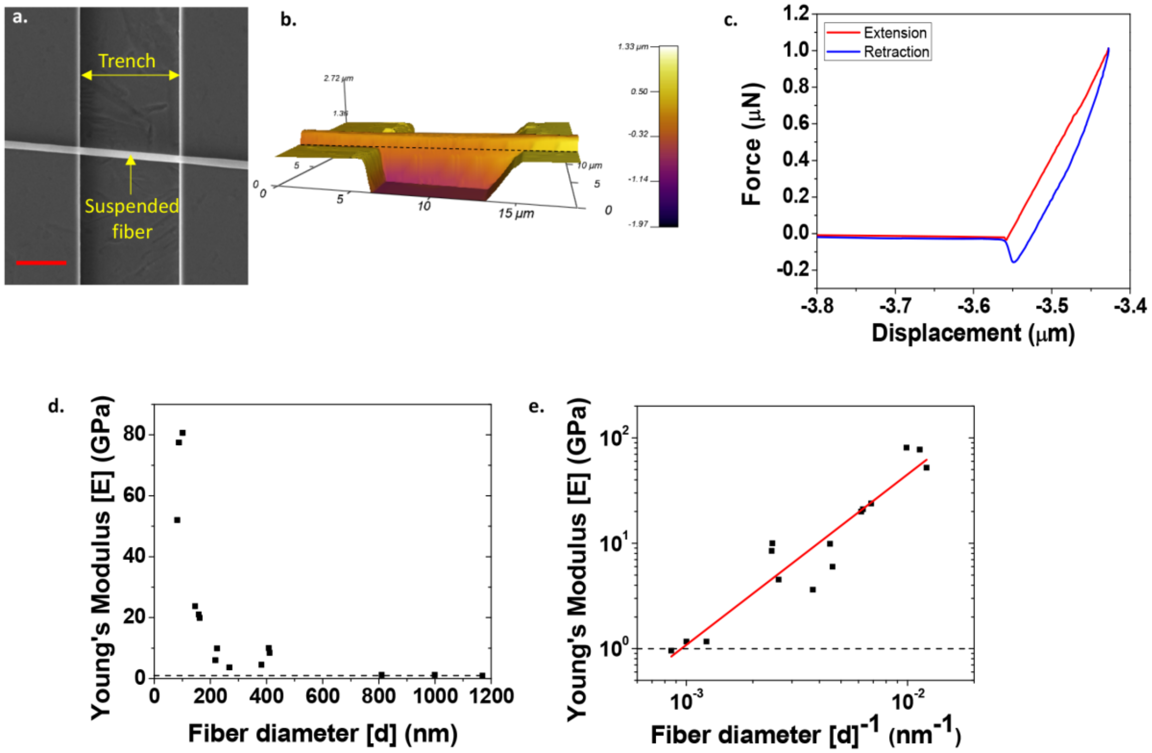

Figure 2.7 Young's modulus of individual fiber.

SEM (a) and AFM topographical image (b) of a representative set up of the three-point bending test consisting of an individual suspended fiber across a 10 µm grating (scale bar = 5 µm). Force and displacement values are extracted from AFM force curves (c). Calculated Young's modulus, using Equation 3, as a function of fiber diameter (d) and in log-log form (e) showing an increase in Young's modulus with a decrease in fiber diameter. The black dashed line represents the bulk Young's modulus of P(VDF-TrFE). The red solid line is a linear best-fit describing the relationship between fiber diameter and Young's modulus (Equation. 2.8).

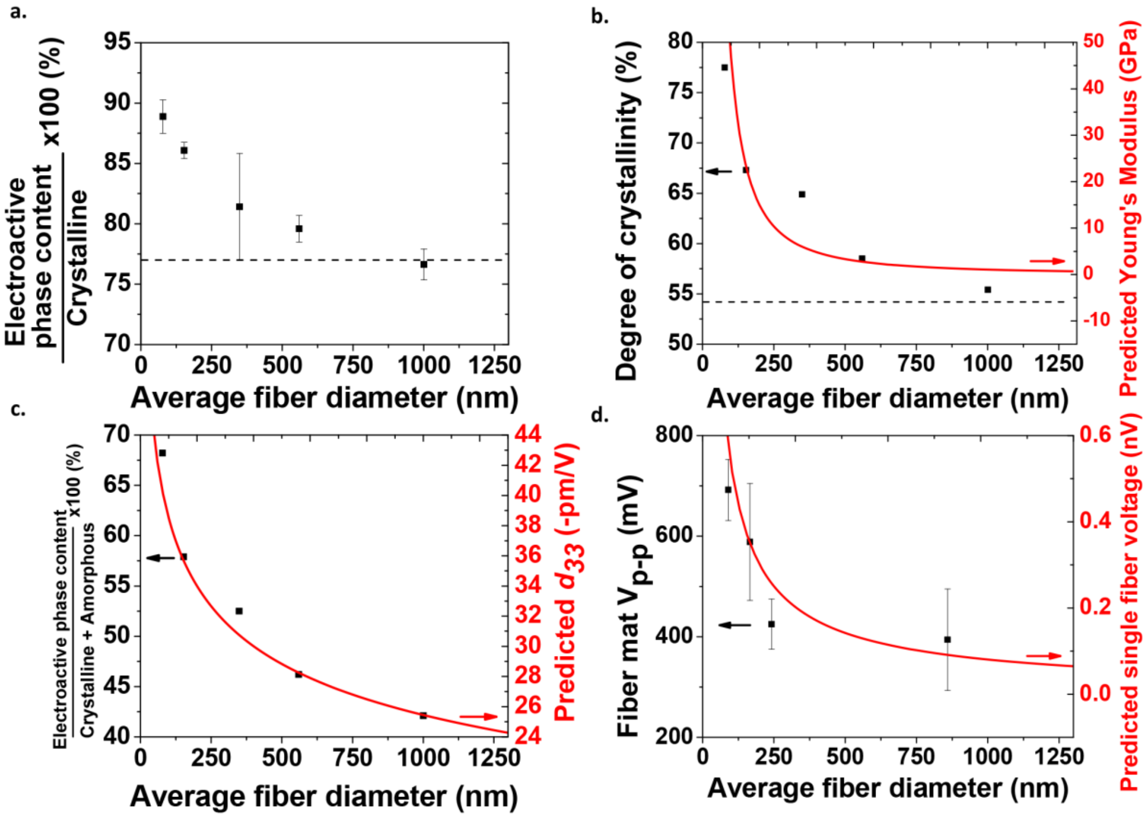

Figure 2.8 EA-Phase and crystallinity quantification, and EA-phase content correlation to d_{33}.

EA-phase (a) and Young's modulus dependence, as calculated from equation 2.8, on the degree of crystallinity (b) as a function of fiber diameter. The black dotted line indicates the measured EA-percentage and degree of crystallinity, respectively, of the measured drop casted thick film. Comparison between the dependence of predicted d_{33} (Equation 2.7) and EA-phase content on fiber diameter (c). Comparison between empirically determined output voltage of fiber mats and numerically determined output voltage of a single fiber (d).

2.6 References

[1] J. Sirohi, I. Chopra. *Fundamental understanding of piezoelectric strain sensors*. Journal of Intelligent Material Systems and Structures 2000, 11, 246.

[2] W. Zeng, X.-M. Tao, S. Chen, S. Shang, H. L. W. Chan, S. H. Choy. *Highly durable all-fiber nanogenerator for mechanical energy harvesting*. Energy & Environmental Science 2013, 6, 2631.

[3] M. Lee, C.-Y. Chen, S. Wang, S. N. Cha, Y. J. Park, J. M. Kim, L.-J. Chou, Z. L. Wang. *A Hybrid Piezoelectric Structure for Wearable Nanogenerators*. Advanced Materials 2012, 24, 1759.

[4] Y. Yang, H. Zhang, G. Zhu, S. Lee, Z.-H. Lin, Z. L. Wang. *Flexible Hybrid Energy Cell for Simultaneously Harvesting Thermal, Mechanical, and Solar Energies*. ACS Nano 2012, 7, 785.

[5] V. Corral-Flores, D. Bueno-Baqués, R. F. Ziolo. *Hybrid BaTiO3-PVDF Piezoelectric Composites for Vibration Energy Harvesting Applications*. MRS Online Proceedings Library 2011, 1325, null.

[6] C.-N. Xu, M. Akiyama, K. Nonaka, T. Watanabe. *Electrical power generation characteristics of PZT piezoelectric ceramics*. Ultrasonics, Ferroelectrics and Frequency Control, IEEE Transactions on 1998, 45, 1065.

[7] K. Tomoaki, Y. Kang, M. Toshiyuki, A. Masatoshi. *Lead-Free Piezoelectric Ceramics with Large Dielectric and Piezoelectric Constants Manufactured from BaTiO 3 Nano-Powder*. Japanese Journal of Applied Physics 2007, 46, L97.

[8] Y. R. Wang, J. M. Zheng, G. Y. Ren, P. H. Zhang, C. Xu. *A flexible piezoelectric force sensor based on PVDF fabrics*. Smart Materials and Structures 2011, 20, 045009.

[9] L. Persano, C. Dagdeviren, Y. Su, Y. Zhang, S. Girardo, D. Pisignano, Y. Huang, J. A. Rogers. *High performance piezoelectric devices based on aligned arrays of nanofibers of poly(vinylidenefluoride-co-trifluoroethylene)*. Nat Commun 2013, 4, 1633.

[10] A. Salimi, A. A. Yousefi. *Analysis Method: FTIR studies of β-phase crystal formation in stretched PVDF films*. Polymer Testing 2003, 22, 699.

[11] D.-W. Kim, Lee, Gwang-Geun, Park, Byung-Eun. *The Ferroelectricity and Electrical Properties of P(VDF-TrFE) Copolymer Film*. Journal of the Korean Physical Society 2007, 51, 719

[12] H. L. W. Chan, Z. Zhao, K. W. Kwok, C. L. Choy, C. Alquié, C. Boué, J. Lewiner. *Polarization of thick polyvinylidene fluoride/trifluoroethylene copolymer films*. Journal of applied physics 1996, 80, 3982.

[13] H. Shao, J. Fang, H. Wang, T. Lin. *Effect of electrospinning parameters and polymer concentrations on mechanical-to-electrical energy conversion of randomly-oriented electrospun poly(vinylidene fluoride) nanofiber mats*. RSC Advances 2015, 5, 14345.

[14] A. Baji, Y.-W. Mai, Q. Li, Y. Liu. *Nanoscale investigation of ferroelectric properties in electrospun barium titanate/polyvinylidene fluoride composite fibers using piezoresponse force microscopy*. Composites Science and Technology 2011, 71, 1435.

[15] J. S. Dodds, F. N. Meyers, K. J. Loh, "Enhancing the piezoelectric performance of PVDF-TrFE thin films using zinc oxide nanoparticles", 2012.

[16] Y. Ahn, J. Y. Lim, S. M. Hong, J. Lee, J. Ha, H. J. Choi, Y. Seo. *Enhanced piezoelectric properties of electrospun poly (vinylidene fluoride)/multiwalled carbon nanotube composites due to high β-phase formation in poly (vinylidene fluoride)*. The Journal of Physical Chemistry C 2013, 117, 11791.

[17] C. Chang, V. H. Tran, J. Wang, Y.-K. Fuh, L. Lin. *Direct-write piezoelectric polymeric nanogenerator with high energy conversion efficiency*. Nano letters 2010, 10, 726.

[18] L. Gu. *Low-frequency piezoelectric energy harvesting prototype suitable for the MEMS implementation*. Microelectronics Journal 2011, 42, 277.

[19] K.-Q. Fan, F.-B. Chao, J.-G. Zhang, W.-D. Wang, X.-H. Che. *Design and experimental verification of a bi-directional nonlinear piezoelectric energy harvester*. Energy Conversion and Management 2014, 86, 561.

[20] G. Alici, N. N. Huynh. *Predicting force output of trilayer polymer actuators*. Sensors and Actuators A: Physical 2006, 132, 616.

[21] P. Vandrangi, S. C. Gott, R. Kozaka, V. G. J. Rodgers, M. P. Rao. *Comparative Endothelial Cell Response on Topographically Patterned Titanium and Silicon Substrates with Micrometer to Sub-Micrometer Feature Sizes*. 2014.

[22] P. Zhou, C. Wu, X. Li. *Three-point bending Young's modulus of nanowires*. Measurement Science and Technology 2008, 19, 115703.

[23] W. Wang, P. Ciselli, E. Kuznetsov, T. Peijs, A. H. Barber. *Effective reinforcement in carbon nanotube–polymer composites*. Philosophical Transactions of the Royal Society of London A: Mathematical, Physical and Engineering Sciences 2008, 366, 1613.

[24] S. K. Ghosh, M. M. Alam, D. Mandal. *The in situ formation of platinum nanoparticles and their catalytic role in electroactive phase formation in poly (vinylidene fluoride): a simple preparation of multifunctional poly (vinylidene fluoride) films doped with platinum nanoparticles*. RSC Adv. 2014, 4, 41886.

[25] M.-C. García-Gutiérrez, A. Linares, I. Martín-Fabiani, J. J. Hernández, M. Soccio, D. R. Rueda, T. A. Ezquerra, M. Reynolds. *Understanding crystallization features of P (VDF-TrFE) copolymers under confinement to optimize ferroelectricity in nanostructures*. Nanoscale 2013, 5, 6006.

[26] P. Martins, A. C. Lopes, S. Lanceros-Mendez. *Electroactive phases of poly (vinylidene fluoride): Determination, processing and applications*. Progress in polymer science 2014, 39, 683.

[27] H. Fong, I. Chun, D. H. Reneker. *Beaded nanofibers formed during electrospinning*. Polymer 1999, 40, 4585.

[28] J. J. Schneider, J. Engstler, S. Franzka, K. Hofmann, B. Albert, J. Ensling, P. Gütlich, P. Hildebrandt, S. Döpner, W. Pfleging. *Carbon Nanotube Bags: Catalytic Formation, Physical Properties, Two-Dimensional Alignment and Geometric Structuring of Densely Filled Carbon Tubes*. Chemistry-A European Journal 2001, 7, 2888.

[29] J. Fang, X. Wang, T. Lin. *Electrical power generator from randomly oriented electrospun poly (vinylidene fluoride) nanofibre membranes*. Journal of Materials Chemistry 2011, 21, 11088.

[30] B. J. Hansen, Y. Liu, R. Yang, Z. L. Wang. *Hybrid nanogenerator for concurrently harvesting biomechanical and biochemical energy*. ACS Nano 2010, 4, 3647.

[31] A. Meitzler, H. F. Tiersten, A. W. Warner, D. Berlincourt, G. A. Couqin, F. S. Welsh Iii, Society, 1988.

[32] D. Mandal, S. Yoon, K. J. Kim. *Origin of Piezoelectricity in an Electrospun Poly (vinylidene fluoride-trifluoroethylene) Nanofiber Web-Based Nanogenerator and Nano-Pressure Sensor*. Macromolecular rapid communications 2011, 32, 831.

[33] S. Xie, A. Gannepalli, Q. N. Chen, Y. Liu, Y. Zhou, R. Proksch, J. Li. *High resolution quantitative piezoresponse force microscopy of BiFeO 3 nanofibers with dramatically enhanced sensitivity*. Nanoscale 2012, 4, 408.

[34] J. Gomes, J. S. Nunes, V. Sencadas, S. Lanceros-Méndez. *Influence of the β-phase content and degree of crystallinity on the piezo-and ferroelectric properties of poly (vinylidene fluoride)*. Smart Materials and Structures 2010, 19, 065010.

[35] A. V. Bune, C. Zhu, S. Ducharme, L. M. Blinov, V. M. Fridkin, S. P. Palto, N. G. Petukhova, S. G. Yudin. *Piezoelectric and pyroelectric properties of ferroelectric Langmuir–Blodgett polymer films*. Journal of applied physics 1999, 85, 7869.

[36] Y.-Y. Choi, T. G. Yun, N. Qaiser, H. Paik, H. S. Roh, J. Hong, S. Hong, S. M. Han, K. No. *Vertically aligned P (VDF-TrFE) core-shell structures on flexible pillar arrays*. Scientific reports 2015, 5.

[37] J. Pu, X. Yan, Y. Jiang, C. Chang, L. Lin. *Piezoelectric actuation of direct-write electrospun fibers*. Sensors and Actuators A: Physical 2010, 164, 131.

[38] S. Cuenot, S. Demoustier-Champagne, B. Nysten. *Elastic modulus of polypyrrole nanotubes*. Physical Review Letters 2000, 85, 1690.

[39] M. K. Shin, S. I. Kim, S. J. Kim, S.-K. Kim, H. Lee, G. M. Spinks. *Size-dependent elastic modulus of single electroactive polymer nanofibers*. Applied physics letters 2006, 89, 231929.

[40] J. S. Andrew, D. R. Clarke. *Effect of Electrospinning on the Ferroelectric Phase Content of Polyvinylidene Difluoride Fibers*. Langmuir 2008, 24, 670.

[41] A. Baji, Y.-W. Mai, Q. Li, Y. Liu. *Electrospinning induced ferroelectricity in poly (vinylidene fluoride) fibers*. Nanoscale 2011, 3, 3068.

[42] A. Baji, Y.-W. Mai, S.-C. Wong. *Effect of fiber size on structural and tensile properties of electrospun polyvinylidene fluoride fibers*. Polymer Engineering & Science 2015, 55, 1812.

[43] S. Y. Gu, Q. L. Wu, J. Ren, G. J. Vancso. *Mechanical properties of a single electrospun fiber and its structures*. Macromolecular rapid communications 2005, 26, 716.

[44] R. Jaeger, H. Schönherr, G. J. Vancso. *Chain packing in electro-spun poly (ethylene oxide) visualized by atomic force microscopy*. Macromolecules 1996, 29, 7634.

3. Transformative piezoelectric enhancement of P(VDF-TrFE) synergistically driven by nanoscale dimensional reduction and thermal treatment

3.1 Introduction

Applications of piezoelectric materials have grown in the broad fields of actuators, sensors, and more recently for miniaturized energy harvesting electronics (e.g., wearable devices).[1-3] The piezoelectric conversion of salvageable mechanical energy (e.g., bodily movements and ambient vibrations) provides a sustainable electric source. Although inorganic piezoelectric materials such as lead zirconate titanate (PZT) and barium titanate ($BaTiO_3$) exhibit excellent piezoelectric properties, their brittle nature limits the applicability and long-term stability in flexible devices and mechanically challenging applications.

In this regard, organic polyvinylidene fluoride (PVDF) and its derivatives including a conjugated form with trifluoroethylene, P(VDF-TrFE), have demonstrated promising properties for flexible piezo- and ferroelectric applications.[4-7] PVDF is semi-crystalline, a critical characteristic for its mechanical compliance, and consists of three main phases depending on the conformation of the fluorine atoms to one another.[8] The α-phase is energetically favorable and is composed of chains conformed in trans (T) and gauche (G) linkages (i.e., TGTG’), which does not exhibit a molecular net dipole charge. The electroactive phases of PVDF include the β-phase (TTTT) and γ-phase (T_3GT_3G') for which the chain exhibits a net dipole charge perpendicular to the chain *c-axis*. Local crystalline domains, composed of either of the electroactive phases, respond to an external mechanical or electrical stimulus to produce the piezoelectric response. Therefore, the main approaches to enhance the piezoelectric properties of PVDF have been by increasing the electroactive phase content via mechanical/electrical poling [9] and thermal treatment.[10] Alternative approaches include stabilization of the electroactive phases at room temperature by incorporation of phase stabilizers (e.g., TrFE), which modulates polymer chain organization via steric hindrance.[8, 11] With approximately an order of magnitude lower piezoelectric coefficient, however, the piezoelectric performance of organic-based materials even with such efforts do not compare to their inorganic counterparts.

Recent studies of inorganic piezoelectric materials have shown significant piezoelectric enhancement via dimensional reduction below 100 nm.[12] In regards to organic-based materials, we have previously shown that a decrease in the fiber diameter of P(VDF-TrFE) via electrospinning induced enhancement of the piezoelectric properties, primarily due to an increase in the electroactive phase content and Young's modulus of the nanofibers.[13] Nevertheless, the piezoelectric coefficient of P(VDF-TrFE) has not reached comparable levels of those found in commonly used inorganic piezoelectric materials.

In this work, the electrospinning process of P(VDF-TrFE) was optimized via solution tuning to produce the smallest possible nanofibers with an average fiber diameter of approximately 30 nm. Combined with a thermal treatment, the dimensional reduction in the nanofibers unexpectedly resulted in the highest piezoelectric coefficient (d_{33}) from any pure organic piezoelectric material, to the best of our knowledge, at approximately -108 pm V^{-1}. This value approaches the magnitude of the piezoelectric coefficient in inorganic piezoelectric materials. We demonstrate that this transformative improvement in the piezoelectric properties of P(VDF-TrFE) is largely due to the combination of an enhancement of the polarized domain alignment and the materialization of flexoelectricity, only realized by synergistic interactions between dimensional reduction and thermal treatment.

3.2 Experimental

3.2.1. Electrospinning of P(VDF-TrFE) nanofibers

A systematic approach was utilized to optimize solution properties including viscosity, conductivity and surface tension, in order to synthesize P(VDF-TrFE) nanofibers with an average fiber diameter of approximately 30 nm (**Figure App. B1-B4, Table App.B1**). A solution containing 1.3 wt.% P(VDF-TrFE) (70/30 mol%) (Solvay Group, France) dissolved in a 50/50 volume ratio of N,N-dimethylformamide (DMF) (Fisher Scientific, Pittsburgh, PA) and tetrahydrofuran (THF) (Sigma-Aldrich, St. Louis, MO), supplemented with 1.5 wt.% pyridinium formate (PF) buffer (Sigma-Aldrich, St. Louis, MO) and 0.05 wt.% BYK-377 (BYK Additives and Instruments, Wesel Germany) to increase and decrease the solution conductivity and surface tension, respectively, was utilized. Alternatively, P(VDF-TrFE) nanofibers with an average diameter of 90 nm were synthesized from a 4.0 wt.% P(VDF-TrFE) solution dissolved in 60/40 volume ratio of DMF and acetone (Fisher Scientific, Pittsburgh, PA) supplemented with 1.5 wt.% PF buffer.[13] Each solution was separately electrospun under optimized conditions of electrospinning distance (20 cm), applied voltage (approx. -15 kV) and solution feed rate (0.5 ml hr^{-1}) at 23 °C and an absolute humidity of 7.6 g m^{-3}.

3.2.2. Morphological characterization and phase analysis of P(VDF-TrFE) nanofibers

The morphology of electrospun nanofibers was characterized by scanning electron microscopy (FEI NNS450, FEI Corp., Hillsboro, OR). Fourier transform infrared (FTIR) of the electrospun fibers was conducted in absorbance mode from 600 to 1600 cm^{-1} with an Equinox 55 FTIR spectrometer (Bruker Corp., Billercia, MA). Five independent samples per condition were utilized to determine an average value of electroactive phase content. X-ray diffraction (XRD) peaks from each condition were collected from 2θ of 10-50° using an Empyrean X-ray diffractometer (PANalytical, Almelo, the Netherlands), and their patterns were analyzed to determine degree of crystallinity. Lattice constants were also determined from the XRD patterns. The combination of FTIR and XRD data was utilized to calculate the overall electroactive phase content.[13]

3.2.3. Piezoelectric coefficient measurement

To properly measure the piezoelectric coefficient, a standard periodically poled lithium niobate (PPLN) with a known piezoelectric coefficient was used to determine a correction factor for all subsequent measurements. Nanofibers were sparsely collected on a gold coated, thermal-oxide silicon substrate and subjected to single-point piezoresponse force microscopy on individual fibers. A MFP-3D AFM (Asylum Research, Santa Barbara, CA) was first used in tapping imaging mode to locate an individual fiber. Five points were chosen on the scanned fiber and the AFM was switched to PFM where single point spectroscopy measurements were conducted. Step voltages from -3 to +3 V was applied across the fiber via the AFM cantilever (AC240TM, Olympus) to the grounded substrate. Alternatively, the thin film structure was achieved by collecting a thin fiber mat of 30 nm average diameter fibers on the same substrate and thermo-treated at 135 °C, and subjected to PFM measurements. A value of d_{33} was calculated by,

$$d_{33} = \frac{A}{VQ} f \ ,$$

where A is the amplitude response of the nanofiber in response to an applied voltage (V), Q is the quality factor of the AFM cantilever, and f is the correctional factor taken from the PPLN standard.

3.2.4. Electric output measurements

Nanofibrous mats of approximately 15 µm thickness were utilized for electric output measurements using a vibrational system modified from our previous report (**Figure App. B5**).[13] Briefly, the samples were cut to a rectangle with a size of 47x12 mm^2 and assembled into a cantilever using brass substrates (51x16 mm^2) (**Figure App.B5**). A proof mass of 2.3 g was placed at the end of the clamped cantilever to induce a bending strain under vibration. Voltage was measured utilizing an oscilloscope (Pico Technology, St Neots, United Kingdom) and power was calculated by utilizing the internal resistance of the oscilloscope (10 MΩ).

The same cantilever design was utilized in a custom-made strain cycler to demonstrate the durability of the flexible P(VDF-TrFE) after long-term strain exposure. Briefly, a 120 rpm gear motor was used as the driving force for an eccentric sheave that converts rotary to a linear reciprocating motion on a beam affixed to a ball bearing rail. The sample was driven for approximately 85 minutes to cycle the sample at 2 Hz for 10,000 cycles.

Alternatively, utilizing the same cantilever setup, the sample was fixed to a fitness armband to demonstrate the practical application of turning on low power wearable devices. The electrical leads from the cantilever was connected to a full-bridge rectifier to convert the AC voltage signal generated from the P(VDF-TrFE) to a DC output to power on and off multiple blue LEDs when the arm is repeatedly bent and extended.

3.2.5. Strain-gradient computational simulation

To determine the strain profile induced within an individual nanofiber under the compressive strain exerted by the AFM probe during piezoresponse measurements, a finite element analysis of structural mechanics by COMSOL Multiphysics was utilized. An arbitrary aspect ratio of 5:1 (length: diameter) was used to model the nanofiber. The length was large enough to contain the AFM probe, which was modeled as a circular punch with a diameter of a 120 nm in order to encompass the 90 nm diameter nanofiber but small enough to reduce computational time. The cross section of the fiber was modeled as a core-sheath structure which has been shown to arise during electrospinning process due to non-uniform solvent evaporation, where the sheath thickness is independent and constant over a range fiber diameters.[14, 15] To assign the proper mechanical properties of the core and sheath for modelling, measured Young's Modulus data from individual P(VDF-TrFE) fibers having various fiber diameters were fitted with a non-linear regression of a rules of mixture model,[15]

$$E_f D_f^4 = E_c D_c^4 + E_s (D_f^4 - D_c^4),$$

where E_f is the measured elastic modulus of the fiber, E_c is the elastic modulus of the core, E_s is the elastic modulus of the sheath, D_f is the fiber diameter, and D_c is the diameter of the core. The core and sheath moduli were calculated to be approximately 1 and 6400 GPa, respectively, with a sheath thickness of approximately 8 nm. The AFM probe and underlying supporting substrate for the fiber were assigned with values of silicon within the built-in library. Fixed boundary constraints were applied to the AFM probe and substrate, and a fixed displacement of the AFM probe of -15% of the fiber diameter was used to impose compression on the fiber. The strain value was selected based on the average applied strain between the individual 30 and 90 nm diameter fibers during the actual PFM measurements at a fixed force. The third principle strain was observed for the analysis of the strain profile with respect to the diameter of the nanofiber and the differential of this strain with respect to the z-coordinate through the length of the cross-section was plotted for strain gradient analysis.

3.3 Results and Discussion

3.3.1 Synthesis of P(VDF-TrFE) nanofibers and their piezoelectric characterization

The piezoelectric properties of P(VDF-TrFE) nanofibers with an average fiber diameter of 90 nm (**Figure 3.1a**) or 30 nm (**Figure 3.1b**) were examined as-spun without thermal treatment (23 °C) or subsequently thermo-treated at 90 °C for 24 h. **Figures 3.1c** and **Figure 3.1d** show that the thermal treatment did not alter the nanostructure of electrospun P(VDF-TrFE) for either size of 90 or 30 nm average fiber diameter, respectively. To investigate the effects of dimensional reduction and thermal treatment on the piezoelectric coefficient, single-point piezoresponse force microscopy (PFM) measurements were conducted on individual fibers with approximately 30 or 90 nm fiber diameter. **Figure 3.1e** shows that the amplitude response of an individual 25 nm fiber is approximately 2-fold greater than that of an 85 nm nanofiber. Interestingly, the difference in the piezoelectric response between the two fiber sizes was further increased by the thermal treatment (**Figure 3.1f**). The exponential increase of d_{33} in response to reduction of the fiber diameter to a 30 nm range is shown in **Figure 3.1g**. More substantially, the thermal treatment combined with the dimensional reduction, induced a synergistic effect on the enhancement of d_{33}, especially below the fiber diameter of approximately 45 nm, reaching up to an average of -108 pm V^{-1} for a 28 nm nanofiber, the highest value reported for purely organic piezoelectric materials.

3.3.2. Piezoelectric performance of P(VDF-TrFE) nanofiber mats

To compare piezoelectric performance, 15 μm-thick mats composed of various electrospun P(VDF-TrFE) nanofibers with an average diameter of 30 nm, thermo-treated at 23 °C and 90 °C, or 90 nm at 23 °C were subjected to a controlled mechanical strain for energy generation (**Figure App.B5**). **Figure 3.2a** and **Figure 3.2b** show the peak-to-peak voltage and electric power generation as a function of applied strain, respectively, determined from the raw output voltage of the nanofiber mats under different applied strains (**Figure App.B6**). All measurements were conducted at open circuit, where the greatest electric output is observed (**Figure App.B7**). As expected, an increase in electric output is observed by simply reducing the fiber dimension from 90 to 30 nm due to the enhanced d_{33}. The thermal treatment of 30 nm nanofibers at 90 °C further increased the electric output, producing approximately 38.5 V and 74.1 μW at the maximum applied strain of 0.26%, an impressive enhancement of approximately 120% and 350% over those of untreated 90 nm nanofibers. Although a direct comparison to values in literature is not fully practical due to diverse testing platforms, the electric output reported here is at least an order of magnitude greater as compared to other PVDF piezoelectric based devices.[4, 16-18] Even with the limitation of applied strains, the observed 2.6 V_{p-p} μm^{-1}, normalized to the thickness of the sample, at a strain of 0.26% outperforms the electric output values ranging from approximately 0.19 – 0.26 V_{p-p} μm^{-1} in those studies.

Typical inorganic piezoelectric materials such as PZT and $BaTiO_3$ possess relatively low flexural yield strains of well below 0.2%.[19] This limits the application of inorganic piezoelectric materials typically to low displacements at high frequency ranges (hundreds of hertz).[20, 21] In contrast, we have demonstrated that P(VDF-TrFE) flexible nanofiber mats were able to operate at larger strains and at low frequencies (a few to tens of hertz). Additionally, the durability of electrospun P(VDF-TrFE) nanofibers was tested by subjecting the material to an actuation regimen repeated over 10,000 cycles at 2 Hz. Open-circuit voltage measured before and after the 10,000 cycles show that the sample maintained its piezoelectricity after the rigorous dynamic straining (**Figure 3.2c**). Considering the fact that the synthesized P(VDF-TrFE) nanofibers at 30 nm in this study exhibits a piezoelectric coefficient value similar to that of thin film $BaTiO_3$, we expect the organic piezoelectric material to be more efficient in its performance where inorganic-based materials would otherwise fail.[22-24] The exceptional flexibility with the potent piezoelectricity of electrospun P(VDF-TrFE) is demonstrated in an application for a wearable device in **Figure 3.2d (i).** A 15 µm-thick mat of 90 nm diameter fibers without the thermal treatment or 30 nm diameter fibers with the thermal treatment is attached to a fitness armband and connected to a full-bridge rectifier with a series of Super Bright blue LEDs. When the arm is in the extended static state the LEDs remains off (90 nm: **Figure 3.2d (ii)**, 30 nm: **Figure 3.2d (iii)**). A cycle between arm flexion and extension results in the LEDs turning on and off without the need for a capacitor. The mat composed of 90 nm diameter fibers was only able to turn on a maximum number of 3 LEDs (**Figure 3.2d (iv)**) while the mat composed of the thermo-treated 30 nm diameter fibers was able to light 10 LEDs (**Figure 3.2d (v)**). Therefore, our findings of the synergistic effects arising from dimensional reduction and thermal treatment on the piezoelectric performance of P(VDF-TrFE) nanofibers present promising potential applications for flexible thin-film-like devices.

3.3.3. Electroactive phase content quantification and its correlation to d_{33}

To understand the mechanism of such transformative enhancement on the piezoelectric performance of P(VDF-TrFE) nanofibers, synergistically by dimensional reduction and thermal treatment, the overall content of electroactive phases, the major determinant of d_{33}, was quantitatively determined by Fourier transform infrared spectroscopy (FTIR) and X-ray diffraction (XRD). The FTIR spectra of P(VDF-TrFE) nanofibers having an average diameter of 30 or 90 nm, both with and without the thermal treatment, are shown in **Figure 3.3a**, and were utilized to calculate the electroactive phase content in the crystalline domains (**Figure 3.3b**). The electroactive phase content of the as-spun P(VDF-TrFE) nanofibers (23 °C) increased as a function of fiber diameter. As expected from the PFM results (**Figure 3.1**), the thermal treatment further increased the electroactive phase content up to a maximum average of approximately 94% at the 30 nm average fiber diameter.

The XRD spectra of these fibers (**Figure 3.3c**) were subjected to peak deconvolution to quantify the degree of crystallinity as a function of fiber diameter and thermal treatment (**Figure 3.3d**). As expected, an increase in the degree of crystallinity was observed in the thermo-treated samples. The overall piezoelectric response of P(VDF-TrFE) nanofibers are likely derived from and proportional to the overall electroactive phase content, which was calculated from the product of electroactive phase in the crystalline and the degree of crystallinity (**Figure 3.3e**). Surprisingly, the increase in electroactive phase content was not proportional to that in the piezoelectric coefficient as 5% increase in electroactive phase content at the smallest fiber diameter by the thermal treatment resulted in approximately 35% increase in d_{33}. **Figure 3.3f** shows an extrapolation of d_{33} with respect to electroactive phase content of as-spun (23 °C) nanofibers, which predicts a d_{33} value of approximately -60 pm V^{-1} at 100% electroactive phase content. However, the 25 nm nanofiber shows a deviation from this prediction, reaching almost -60 pm V^{-1} at the electroactive phase content of only 71%. Such deviation was further escalated by the thermal treatment, exhibiting a d_{33} of –108 pm V^{-1} for a 28 nm P(VDF-TrFE) nanofiber at an overall electroactive phase content of 76%. The unexpected aberration of d_{33}, as much as approximately 35% increase from the prediction by electroactive phase content quantification, led us to investigate alternative mechanisms responsible for such a substantial increase.

3.3.4. Piezoelectric dipole alignment

Electrospinning has been shown to induce polymer chain alignment by restricting the degree of freedom in chain organization due to fiber elongation during the process, resulting in the high aspect ratio.[25, 26] It has been also shown that the annealing of electrospun fibers further enhances chain alignment via thermo-induced chain re-arrangement.[27, 28] To determine the effects of dimensional reduction and/or the thermal treatment on polymer chain/dipole alignment, hence piezoelectric performance, PFM phase imaging was conducted on P(VDF-TrFE) nanofibers with 30 or 90 nm average fiber diameter both as-spun (23 °C) and after the thermal treatment at 90 °C (**Figure 3.4**). Precise fiber location was determined from tapping imaging mode (3D images as shown), and the PFM phase imaging was conducted along the length of the fiber (inset) from which phase angle distribution profiles were determined. It should be noted that the pyramidal geometry of the AFM tip causes an imaging artifact in which the fiber appears wider than the actual fiber diameter (height) in the 3D image. Statistical analysis of the phase angle histograms from 3 independent nanofibers per condition shows that both dimensional reduction and the thermal treatment enhanced the alignment of piezoelectric domains in electrospun P(VDF-TrFE). The thermal treatment of 90 nm decreased the average phase angle from 15.3 ± 9.9° (**Figure 3.4a**) to 2.9 ± 2.3° (**Figure**

3.4b) while the dimensional reduction to 30 nm decreased it to 4.0 ± 3.0° (**Figure 3.4c**). More significantly, the thermal treatment of 30 nm fibers further enhanced the piezoelectric phase alignment, resulting in an average phase angle of 2.7 ± 2.2° (**Figure 3.4d**), partly explaining the observed substantial increase in d_{33} synergistically by dimensional reduction and thermal treatment.

3.3.5. Nanoscaling effects

To examine if nanostructuring of P(VDF-TrFE) via electrospinning also contributed to the substantially enhanced d_{33}, the nanofibers having an average fiber diameter of 30 nm were alternatively thermo-treated at 135 °C to destroy the nanostructure and subsequently subjected to piezoelectric characterization. **Figure 3.5a** depicts that this post-spinning thermal treatment abolished the nanofibrous structure, resulting in a rough film morphology. Albeit the loss of the nanofibrous structure, phase and crystallinity characterization by FTIR (**Figure App.B8a**) and XRD (**Figure App.B8b**) shows an increase in the total electroactive phase content (**Figure 3.5b** and **Figures App.B9a, App.B9b**). In spite of the high electroactive phase content, however, piezoelectric response dramatically decreased by the absence of the nanofibrous structure (**Figure 3.5c**). The d_{33} of the melted fiber mat after the thermal treatment at 135 °C exhibited a significantly reduced coefficient of -54 pm V^{-1} when compared to that of the 90 °C treated nanofibers at -108 pm V^{-1}. Interestingly, the d_{33} of an individual 30 nm nanofiber after the thermal treatment at 135 °C, which retained its nanofiber structure, exhibited a similar value (-110 pm V^{-1})

to that of the individual nanofibers thermo-treated at 90 °C. Furthermore, when compared to the results presented in **Figure 3.2a**, destruction of the nanofibrous morphology by the thermal treatment at 135 °C resulted in a significant decrease in the open-circuit voltage production (**Figure App.B10**) of 38.5 V and 74.1 µW from the 90 °C sample down to 30.4 V and 46.2 µW at the highest strain (**Figure 3.5d**) comparable to the 23 °C sample whose d_{33} is also comparable to the melted mat. These results demonstrate that the nanostructuring of P(VDF-TrFE) is critical for the enhanced piezoelectric performance.

Possible mechanisms to account for the substantial increase in d_{33} from nanostructuring could be stemmed from piezoelectric crystal lattice change and/or flexoelectricity. Computational analysis of hexagonal GaN nanowires of varying diameter has shown that the absolute polarization and localized dipole moment are significantly affected by the dimension due to interatomic rearrangement with respect to wire diameter.[29] To examine if such lattice restructuring caused the transformative enhancement in the piezoelectric properties of electrospun P(VDF-TrFE), the unit cell lattice constants were calculated from the XRD data (**Figure 3.3C** and **Figure App.B8b**). We note no significant change in the crystal lattice size for the 30 nm average fiber diameter samples thermo-treated at 23, 90 and 135 °C as well as nanofibrous mats of 90 nm average fiber diameter thermo-treated at 23 and 90 °C (**Table App.B1**). This may indicate insignificant atomic restructuring that affects piezoelectricity in P(VDF-TrFE) nanofibers, different from what was shown for the computationally determined GaN nanowire by dimensional reduction.

Another possible nanoscaling effect is the materialization of flexoelectricity by the dimensional reduction due to the close confinement of the surface and interior molecules/atoms.[30, 31] More specifically, the same surface stresses imparted on nanoscale materials composed of a few to tens of molecular layers induce greater strain gradients as compared to those of bulk materials.[32-34] These large strain gradients have been shown to impose a reconfiguration of the lattice structure and induce polarity in otherwise centrosymmetric materials which results in piezoelectric-like properties.[35] Such phenomenon, known as flexoelectricity, is also expected to further enhance piezoelectric responses in already piezoelectric materials by a similar mechanism,[32, 36] where the large strain gradient may further polarize the material likely in the non-electroactive phase under mechanical loading.[37] In this regard, electrospinning creates a structure that may intensify flexoelectricity as it produces a thin sheath on the surface of the fibers due to non-uniform evaporation of solvent during the process.[14, 38] The thickness of the sheath, which exhibits a greater molecular density, hence higher mechanical modulus compared to the core,[15, 39] has been shown to remain constant independent of fiber diameter.[15] To determine the sheath thickness as well as the elastic moduli of the core and the sheath from P(VDF-TrFE) nanofibers, the modulus of P(VDF-TrFE) nanofibers with various fiber diameters was measured and fitted into a rule of mixture model (**Figure 3.6a**).[15] By utilizing the calculated parameters (sheath thickness:

8 nm, core modulus: 1 GPa, and sheath modulus: 6400 GPa), computational simulation results show that a compressive strain of 15% induces a greater radial strain gradient, perpendicular to the fiber length, in the smaller 30 nm fiber as compared to that of the 90 nm fiber (**Figure 3.6b**). Specifically, a significantly greater strain gradient in the 30 nm fiber near the fiber surface is observed likely due to the increasing contribution of the sheath as the overall fiber diameter decreases and the dramatically different moduli of the core and the sheath (**Figure 3.6c**). This indicates that dimensional reduction in combination with the native core-sheath structure of electrospun fibers, is critical to induce large strain gradients in the smaller nanofibers under mechanical loading, resulting in the realization of the flexoelectric phenomenon to augment piezoelectricity.

3.4 Conclusions

In summary, we investigated the effects of dimensional reduction and thermal treatment on the piezoelectric properties of electrospun P(VDF-TrFE). In particular, we report the highest piezoelectric coefficient observed for a purely organic-based piezoelectric material. With dimensional reduction to approximately 30 nm in diameter of electrospun P(VDF-TrFE) nanofibers and post-spinning thermal treatment, we unexpectedly achieved a d_{33} value of -108 pm V^{-1}; an almost 60% increase as compared to as-spun nanofibers having a 3 times larger fiber diameter. Such transformative enhancement in piezoelectric performance was partly due to increased electroactive phase content, quantified by FT-IR and XRD. More significantly, we showed that the combination of dimensional reduction and thermal treatment synergistically induces the tightly distributed alignment of the electroactive domains and manifests the flexoelectric effect through greater strain gradients. Overall, we demonstrate that proper synthesis of organic-based piezoelectric nanofibers at the nanoscale via optimized electrospinning and thermal treatment promotes a transformative enhancement of piezoelectric properties that are comparable to currently available inorganic materials while providing significantly superior mechanical resiliency.

3.5 Figures

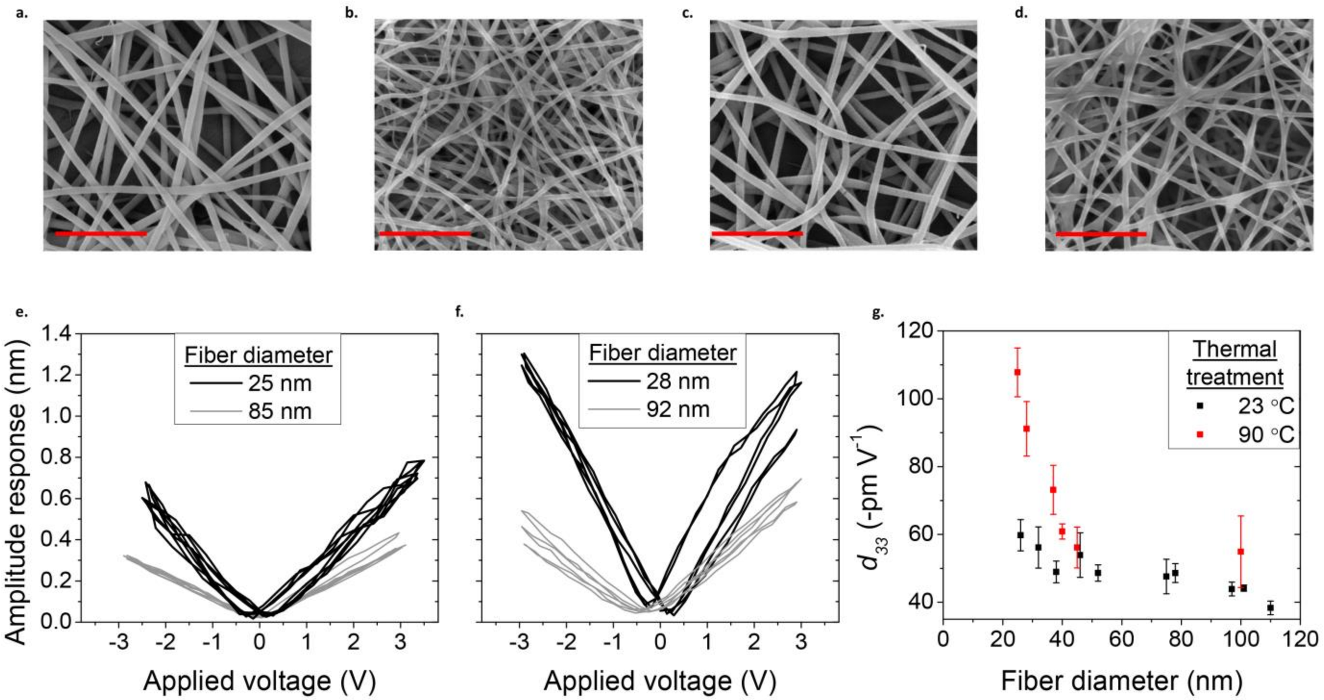

Figure 3.1 Morphology and piezoelectric properties of P(VDF-TrFE) nanofibers with various fiber diameters.

(a – d) Scanning electron microscopy (SEM) images of electrospun P(VDF-TrFE) nanofibers with an average fiber diameter of 90 nm (a and c) and 30 nm (b and d) before (a and b) or after (c and d) the thermal treatment at 90 °C (scale bar = 1 µm). (e, f) Piezoelectric responses from individual P(VDF-TrFE) nanofibers before (e) and after (f) the thermal treatment, determined by piezoresponse force microscopy (PFM). (g) Piezoelectric coefficient (d_{33}) as a function of fiber diameter for as-spun or thermal-treated P(VDF-TrFE) nanofibers.

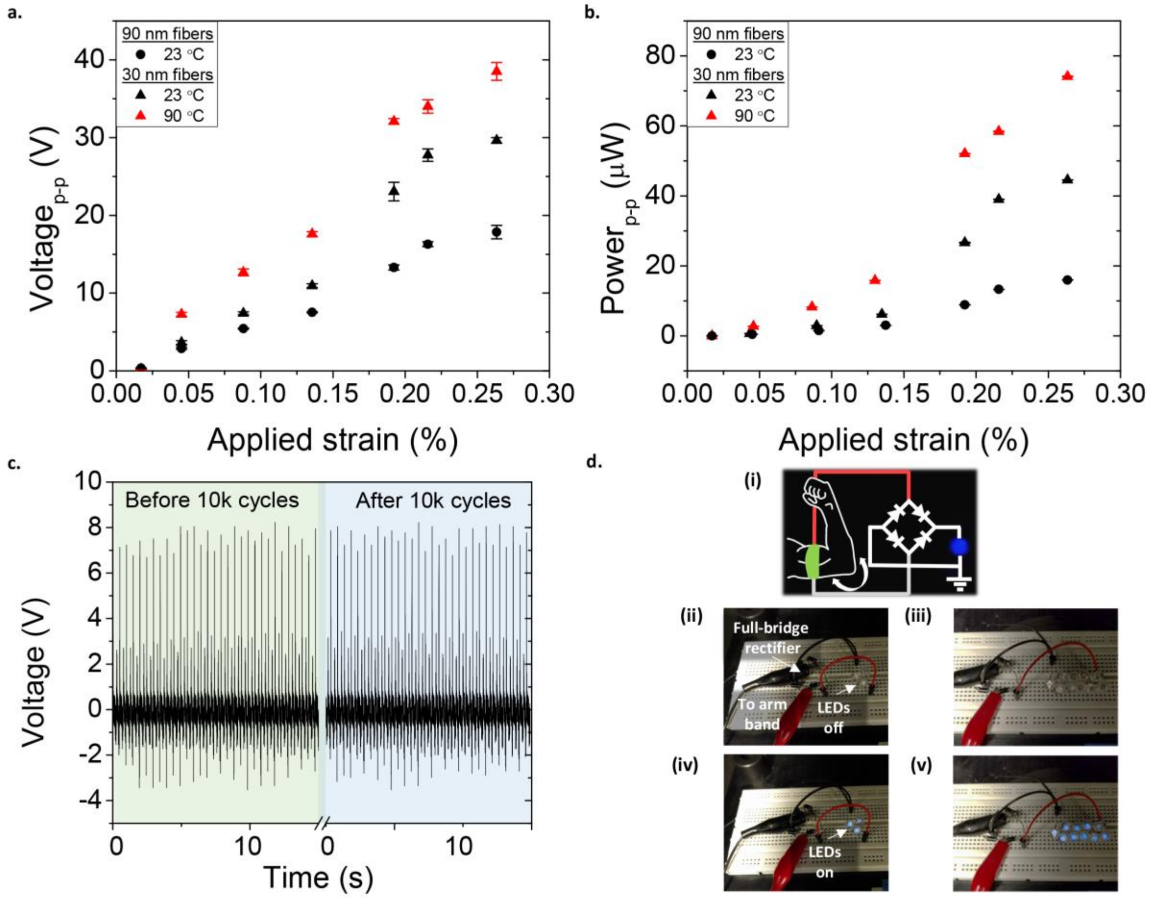

Figure 3.2 Applied strain-dependent electric outputs of P(VDF-TrFE) nanofibrous mats composed of fibers with an average diameter of 30 or 90 nm after various thermal treatments.

(a) Peak-to-peak voltage and (b) peak-to-peak power. (c) Open circuit voltage before and after 10,000 cycles of 2 Hz strain. (d) Wearable piezoelectric (i) powering a blinking LED off (ii) and on (iii).

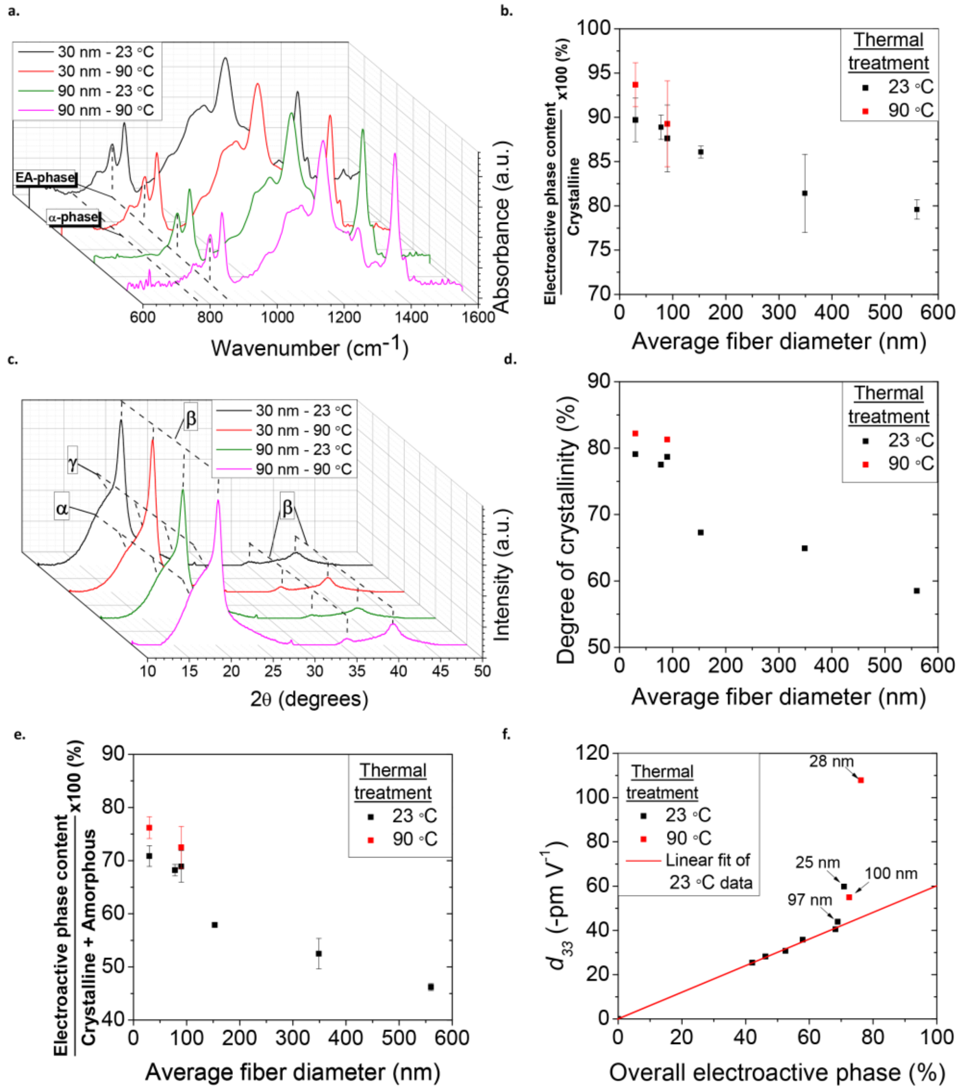

Figure 3.3 Fiber size- and thermal treatment-dependent changes in electroactive phase content and their correlation to the piezoelectric coefficient, d_{33}.

(a) FTIR spectra of electrospun P(VDF-TrFE) mats composed of nanofibers with an average diameter of 30 or 90 nm with or without the thermal treatment at 90 °C were used to quantify electroactive phase content in (b). (c) XRD spectra of electrospun P(VDF-TrFE) mats composed of nanofibers with an average diameter of 30 or 90 nm with or without the thermal treatment at 90 °C were used to calculate degree of crystallinity in (d). (e) The overall electroactive phase content calculated from (b) and (d). (f) Correlation between d_{33} and overall electroactive phase of as-spun nanofibers. Data of 23 °C in Figure (b), (d), (e) and (f) include data from Chapter 2.

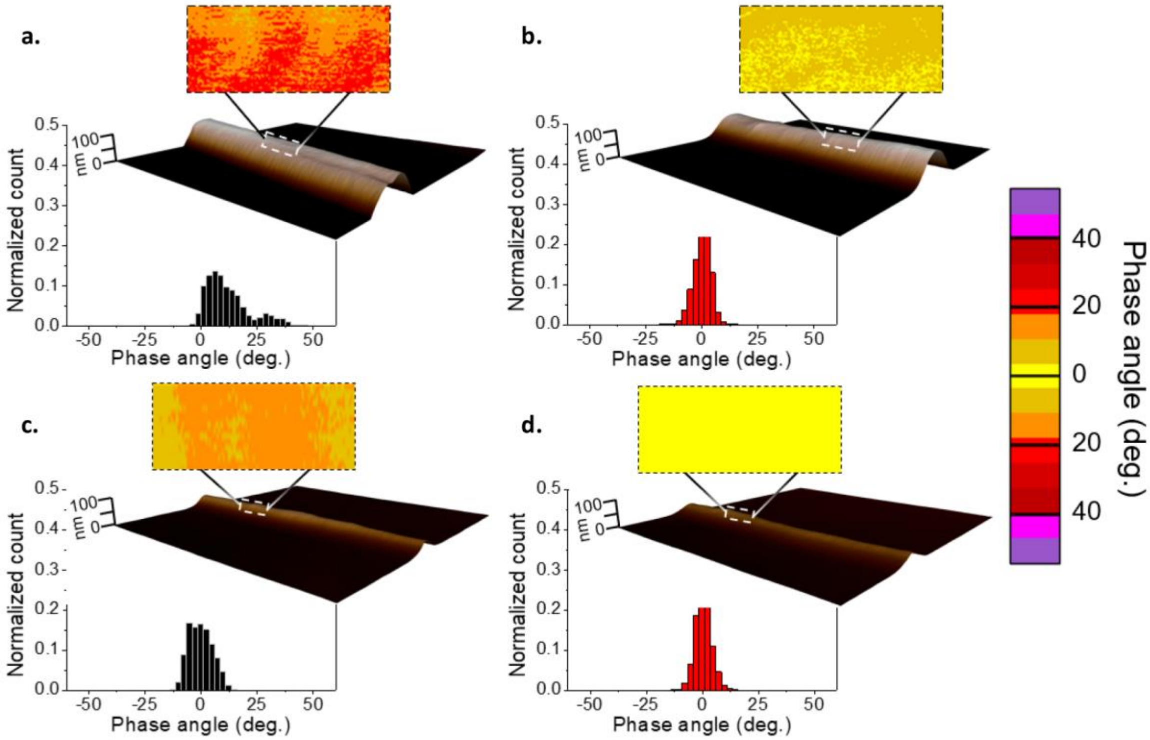

Figure 3.4 Phase angle distribution of P(VDF-TrFE) nanofibers with an average diameter of 90 or 30 nm with or without the thermal treatment at 90 °C..

(a) As-spun 90 nm diameter fibers showing a wider phase angle distribution centered approximately around 15.3° compared to (b) the thermo-treated 90 nm nanofibers, determined from the corresponding representative PFM phase image shown above the histogram. (c) The decrease in the fiber diameter from 90 nm to 30 nm narrowed the phase angle distribution and (d) was further narrowed by the thermal treatment, yielding a tighter distribution around 2.7°. n = 3000 (1000 measurement points, 3 independent fibers).

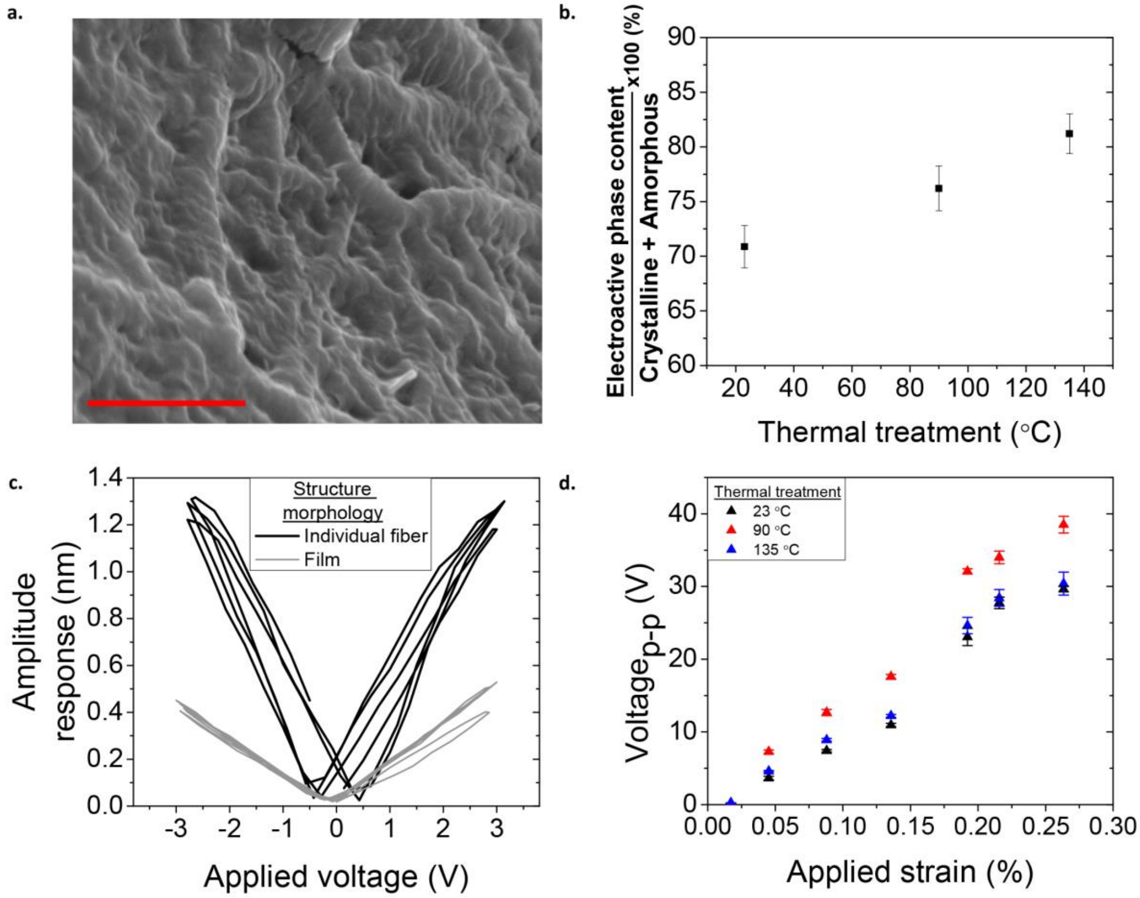

Figure 3.5 The effects of nanofibrous structure on the piezoelectric properties of P(VDF-TrFE).

(a) Destruction of nanofibrous morphology, from P(VDF-TrFE) nanofibers with an average diameter of 30 nm, after the thermal treatment at 135 °C, examined by SEM (scale bar = 1μm). (b) Thermal treatment-dependent electroactive phase content of P(VDF-TrFE) nanofiber mats with an average fiber diameter of 30 nm. (c) PFM comparison of an individual 30 nm fiber and a melted film after the thermal treatment of a mat composed of multiple 30 nm fibers both at 135 °C. (d) Peak-to-peak voltage comparison of 30 nm nanofiber mats at 23, 90, and 135 °C.

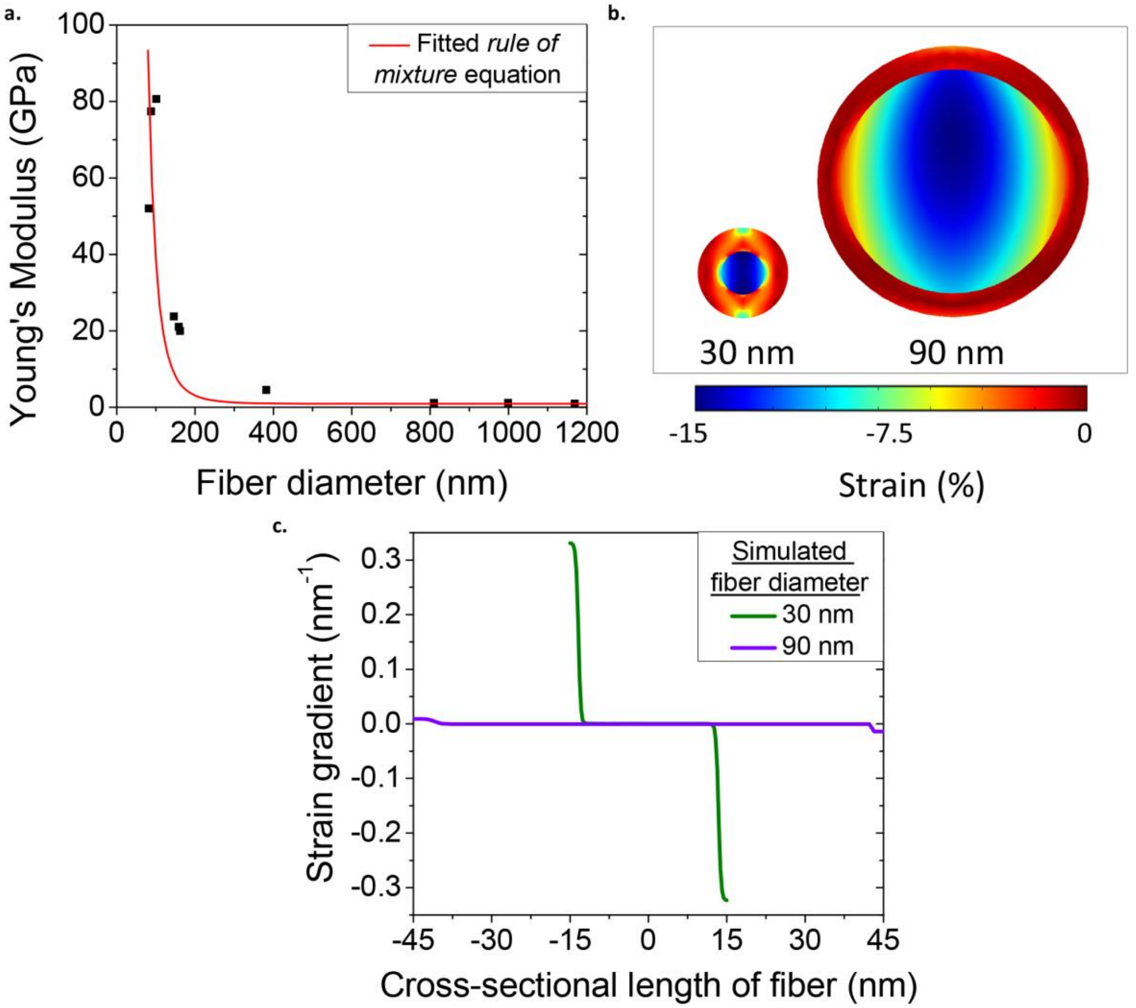

Figure 3.6 Fiber diameter dependent strain gradient.

(a) Measured Young's modulus of P(VDF-TrFE) nanofibers as a function of fiber diameter and fitted with a rule of mixture equation to calculate the sheath thickness, and the core/sheath modulus of the nanofibers. (b) The cross-sectional strain distribution within the fiber of 30 nm or 90 nm diameter under a fixed −15% mechanical strain, simulated by COMSOL. (c) Strain gradient within the fiber of 30 nm or 90 nm diameter as a function of cross-sectional length (perpendicular to the length of the nanofiber).

3.6 References

[1] W.-S. Jung, M.-J. Lee, M.-G. Kang, H. G. Moon, S.-J. Yoon, S.-H. Baek, C.-Y. Kang. *Powerful curved piezoelectric generator for wearable applications*. Nano Energy 2015, 13, 174.

[2] M. Lee, C. Y. Chen, S. Wang, S. N. Cha, Y. J. Park, J. M. Kim, L. J. Chou, Z. L. Wang. *A hybrid piezoelectric structure for wearable nanogenerators*. Advanced Materials 2012, 24, 1759.

[3] K. H. Mak, S. McWilliam, A. A. Popov. *Piezoelectric energy harvesting for tyre pressure measurement applications*. Proceedings of the Institution of Mechanical Engineers, Part D: Journal of Automobile Engineering 2013, 227, 842.

[4] V. Bhavanasi, V. Kumar, K. Parida, J. Wang, P. S. Lee. *Enhanced Piezoelectric Energy Harvesting Performance of Flexible PVDF-TrFE Bilayer Films with Graphene Oxide*. ACS applied materials & interfaces 2015, 8, 521.

[5] J. H. Lee, K. Y. Lee, M. K. Gupta, T. Y. Kim, D. Y. Lee, J. Oh, C. Ryu, W. J. Yoo, C. Y. Kang, S. J. Yoon. *Highly stretchable piezoelectric-pyroelectric hybrid nanogenerator*. Advanced Materials 2014, 26, 765.

[6] R. I. Haque, R. Vié, M. Germainy, L. Valbin, P. Benaben, X. Boddaert. *Inkjet printing of high molecular weight PVDF-TrFE for flexible electronics*. Flexible and Printed Electronics 2015, 1, 015001.

[7] Y. R. Wang, J. M. Zheng, G. Y. Ren, P. H. Zhang, C. Xu. *A flexible piezoelectric force sensor based on PVDF fabrics*. Smart Materials and Structures 2011, 20, 045009.

[8] P. Martins, A. C. Lopes, S. Lanceros-Mendez. *Electroactive phases of poly (vinylidene fluoride): determination, processing and applications*. Progress in polymer science 2014, 39, 683.

[9] A. Salimi, A. A. Yousefi. *Analysis method: FTIR studies of β-phase crystal formation in stretched PVDF films*. Polymer Testing 2003, 22, 699.

[10] I. N. Bhatti, M. Banerjee, I. N. Bhatti. *Effect of annealing and time of crystallization on structural and optical properties of PVDF thin film using acetone as solvent*. IOSR-JAP 2013, 4, 42.

[11] D.-W. Kim, G.-G. Lee, B.-E. Park. *The ferroelectricity and electrical properties of P (VDF-TrFE) copolymer film*. Journal of the Korean Physical Society 2007, 51, 719.

[12] H. D. Espinosa, R. A. Bernal, M. Minary-Jolandan. *A review of mechanical and electromechanical properties of piezoelectric nanowires*. Advanced Materials 2012, 24, 4656.

[13] G. Ico, A. Showalter, W. Bosze, S. C. Gott, B. S. Kim, M. P. Rao, N. V. Myung, J. Nam. *Size-dependent piezoelectric and mechanical properties of electrospun P (VDF-TrFE) nanofibers for enhanced energy harvesting*. Journal of Materials Chemistry A 2016, 4, 2293.

[14] M. Richard-Lacroix, C. Pellerin. *Orientation and partial disentanglement in individual electrospun fibers: diameter dependence and correlation with mechanical properties*. Macromolecules 2015, 48, 4511.

[15] U. Stachewicz, R. J. Bailey, W. Wang, A. H. Barber. *Size dependent mechanical properties of electrospun polymer fibers from a composite structure*. Polymer 2012, 53, 5132.

[16] J.-Y. Ke, H.-J. Chu, Y.-H. Hsu, C.-K. Lee, "A highly flexible piezoelectret-fiber pressure sensor based on highly aligned P (VDF-TrFE) electrospun fibers", 2017.

[17] U. Yaqoob, A. S. M. I. Uddin, G.-S. Chung. *A novel tri-layer flexible piezoelectric nanogenerator based on surface-modified graphene and PVDF-BaTiO 3 nanocomposites*. Applied Surface Science 2017, 405, 420.

[18] L. Persano, C. Dagdeviren, Y. Su, Y. Zhang, S. Girardo, D. Pisignano, Y. Huang, J. A. Rogers. *High performance piezoelectric devices based on aligned arrays of nanofibers of poly (vinylidenefluoride-co-trifluoroethylene)*. Nature communications 2013, 4, 1633.

[19] S. R. Anton, A. Erturk, D. J. Inman. *Bending strength of piezoelectric ceramics and single crystals for multifunctional load-bearing applications*. IEEE transactions on ultrasonics, ferroelectrics, and frequency control 2012, 59, 1085.

[20] B. Yang, C. Lee, W. L. Kee, S. P. Lim. *Hybrid energy harvester based on piezoelectric and electromagnetic mechanisms*. Journal of Micro/Nanolithography, MEMS, and MOEMS 2010, 9, 023002.

[21] A. Koka, H. A. Sodano. *A Low-Frequency Energy Harvester from Ultralong, Vertically Aligned BaTiO3 Nanowire Arrays*. Advanced Energy Materials 2014, 4.

[22] K.-I. Park, S. Xu, Y. Liu, G.-T. Hwang, S.-J. L. Kang, Z. L. Wang, K. J. Lee. *Piezoelectric BaTiO3 thin film nanogenerator on plastic substrates*. Nano letters 2010, 10, 4939.

[23] Y.-B. Park, J. L. Ruglovsky, H. A. Atwater. *Microstructure and properties of single crystal BaTiO3 thin films synthesized by ion implantation-induced layer transfer*. Applied Physics Letters 2004, 85, 455.

[24] Y. F. Hou, W. L. Li, T. D. Zhang, W. Wang, W. P. Cao, X. L. Liu, W. D. Fei. *Large piezoelectric response of BiFeO 3/BaTiO 3 polycrystalline films induced by the low-symmetry phase*. Physical Chemistry Chemical Physics 2015, 17, 11593.

[25] M. V. Kakade, S. Givens, K. Gardner, K. H. Lee, D. B. Chase, J. F. Rabolt. *Electric field induced orientation of polymer chains in macroscopically aligned electrospun polymer nanofibers*. Journal of the American Chemical Society 2007, 129, 2777.

[26] J. Ma, Q. Zhang, A. Mayo, Z. Ni, H. Yi, Y. Chen, R. Mu, L. M. Bellan, D. Li. *Thermal conductivity of electrospun polyethylene nanofibers*. Nanoscale 2015, 7, 16899.

[27] G. S. Y. Yeh, R. Hosemann, J. Loboda-Čačković, H. Čačković. *Annealing effects of polymers and their underlying molecular mechanisms*. Polymer 1976, 17, 309.

[28] S.-Y. Min, Y.-H. Kim, C. Wolf, T.-W. Lee. *Synergistic effects of doping and thermal treatment on organic semiconducting nanowires*. ACS applied materials & interfaces 2015, 7, 18909.

[29] R. Agrawal, H. D. Espinosa. *Giant piezoelectric size effects in zinc oxide and gallium nitride nanowires. A first principles investigation*. Nano letters 2011, 11, 786.

[30] J. Wang, Z. Huang, H. Duan, S. Yu, X. Feng, G. Wang, W. Zhang, T. Wang. *Surface stress effect in mechanics of nanostructured materials*. Acta Mechanica Solida Sinica 2011, 24, 52.

[31] P. Zubko, G. Catalan, A. K. Tagantsev. *Flexoelectric effect in solids*. Annual Review of Materials Research 2013, 43, 387.

[32] M. S. Majdoub, P. Sharma, T. Cagin. *Enhanced size-dependent piezoelectricity and elasticity in nanostructures due to the flexoelectric effect*. Physical Review B 2008, 77, 125424.

[33] F. Wang, J. B. Wang, X. L. Zhong, B. Li, Y. Zhang, C. J. Lu, W. N. Ye, Y. C. Zhou. *Enhanced piezoelectric response in single-crystalline Bi4Ti3O12 nanoplates*. EPL (Europhysics Letters) 2013, 103, 37002.

[34] S. S. Nonnenmann, O. D. Leaffer, E. M. Gallo, M. T. Coster, J. E. Spanier. *Finite curvature-mediated ferroelectricity*. Nano letters 2010, 10, 542.

[35] S. Dai, M. Gharbi, P. Sharma, H. S. Park. *Surface piezoelectricity: size effects in nanostructures and the emergence of piezoelectricity in non-piezoelectric materials*. Journal of Applied Physics 2011, 110, 104305.

[36] J. Zhang, C. Wang, S. Adhikari. *Surface effect on the buckling of piezoelectric nanofilms*. Journal of Physics D: Applied Physics 2012, 45, 285301.

[37] S. Baskaran, X. He, Q. Chen, J. Y. Fu. *Experimental studies on the direct flexoelectric effect in alpha-phase polyvinylidene fluoride films*. Applied Physics Letters 2011, 98, 2901.

[38] M. Richard-Lacroix, C. Pellerin. *Partial disentanglement in continuous polystyrene electrospun fibers*. Macromolecules 2014, 48, 37.

[39] N. E. Zander, K. E. Strawhecker, J. A. Orlicki, A. M. Rawlett, T. P. Beebe Jr. *Coaxial Electrospun Poly (methyl methacrylate)–Polyacrylonitrile Nanofibers: Atomic Force Microscopy and Compositional Characterization*. The Journal of Physical Chemistry B 2011, 115, 12441.

4. Acoustic-responsive piezoelectric membrane as a controlled drug delivery system

4.1. Introduction

The field of drug delivery has been revolutionized in part to the functional advancement of biodegradable polymers, allowing sophisticated drug delivery schemes. More recently, the use of diverse nanoparticles as drug carriers has enabled the precisely timed release of therapeutics to the intended site. However, their otherwise favorable surface to volume ratio often leads to substantially high degradation rates, and their small sizes promote removal from the system by phagocytosis, resulting in rapid drop-off in drug release as compared to more macroscale carriers. More significantly, typical nanoparticle-based drug delivery systems only account for the pharmacokinetics and pharmacodynamics of a drug delivery/release system. Therefore, the total passive release of drugs can only be adjusted by the initial prescribed dose at a pre-determined rate. The pharmacogenetics of these drugs in terms of the effective dosage at a particular instance is often overlooked and thus do not take into account the specific needs of each patient.[1]

In this regard, stimuli-responsive drug delivery systems are promising methods in overcoming the pharmacogenetics associated vulnerabilities in response to systemic drug administration, by controlling when, where, and how much drug is released to accommodate a more personalized therapy.[2] Understanding the changes in homeostasis associated to a particular disease has shifted the focus from utilizing nanoparticles with passive degradation type release to utilizing nanoparticles responsive to a particular environment as a method to activate drug release. For example, diseases that shift the physiological conditions such as pH, presence of reactive oxygen species, or inflammation may be used as triggers to release surface decorated drugs.[3-5] In a similar manner, externally controlled triggers such as thermo-responsive release, light-responsive release, ultrasound-responsive release, and magnetic-responsive release are other avenues to circumvent the limitations associated with nanoparticle degradation-type release.[6-11] Among these stimuli-responsive drug delivery systems, triggering the release of adsorbed molecules on the surface of electrically active components is yet another method for controlled drug release. For example, graphene oxide nanocomposite films can successfully adsorb anionic drug molecules and release them on demand with an externally applied negative potential.[12] One of the major advantages of such release scheme is its capability for fine-tuning the release kinetics by the magnitude of applied potential.

Piezoelectric materials may provide a superior platform for the electric potential-based drug delivery system, due to their ability in generating intrinsic electric potentials necessary to release surface adsorbed drugs, therefore bypassing the need for external electrical connections. However, significant biotoxicity of typical high-performing ceramic piezoelectric materials, e.g., PZT,[13] prevent their use in *in vivo* drug delivery applications. Polyvinylidene fluoride (PVDF), an organic material capable of exhibiting piezoelectricity, has excellent biocompatibility that is currently being used as a vascular suture.[14] Its negative surface charge readily induces the adsorption of cationic molecules. However, its relatively low piezoelectricity requires a very high magnitude of mechanical force to activate the material, diminishing its value for an *in vivo* drug delivery platform. In this regard, we have recently shown a transformative enhancement of piezoelectric polyvinylidene-trifluoroethylene (P(VDF-TrFE) polymer via dimensional reduction to approximately 30 nm in fiber diameter and thermal treatment of the synthesized fibers.[15] The increase in piezoelectric coefficient (108 pm V^{-1}), comparable to typical ceramic piezoelectric materials, allows for developing a wide range of electromechanically sensitive flexible devices.

In this work, we demonstrate the feasibility of utilizing stimulus-responsive piezoelectric nanofibers for controlled drug release. We show that the drug release characteristics of P(VDF-TrFE) nanofibers can be fine-tuned by modulating their piezoelectric properties via fiber size control, thus the sensitivity of the material to the magnitude and frequency of the applied pressures. We demonstrate that the release of model drug, crystal violet, is fully governed by the piezoelectric-mechanoelectrical conversion from the applied mechanical perturbation to change in surface potential, regulating the adsorption of electrostatically adhered drug molecules.

4.2 Experimental

4.2.1. Electrospinning of P(VDF-TrFE) nanofiber-based membranes

Fiber membranes composed of approximately 30 nm in diameter P(VDF-TrFE) nanofibers were synthesized as described previously.[15] Briefly, a solution containing 4.0 wt.% P(VDF-TrFE) (70/30 mol%) (Solvay Group, France) dissolved in a 50/50 weight ratio of N,N-dimethylformamide (DMF) (Fisher Scientific, Pittsburgh, PA) and tetrahydrofuran (THF) (Sigma-Aldrich, St. Louis, MO) was prepared. The solution was supplemented with 1.5 wt.% pyridinium formate (PF) buffer (Sigma-Aldrich, St. Louis, MO) and 0.05 wt.% BYK-377 (BYK Additives and Instruments, Wesel Germany) to increase and decrease the solution conductivity and surface tension, respectively. Nanofibers with the average fiber diameter of approximately 100, 200, and 500 nm fibers were synthesized from a solution of 7.0, 11.5, and 17.5 wt.% P(VDF-TrFE), respectively, dissolved in a 60/40 ratio of DMF/acetone(Fisher Scientific, Pittsburgh, PA), and 1.5 wt.% PF buffer. As a control, a solution of 13.5 wt.% of PVDF dissolved in the same DMF/acetone/PF solvent system was created to synthesize fibers of approximately 500 nm. Each solution was electrospun under optimized conditions of electrospinning distance (20 cm), applied voltage (approximately -15 kV) and solution feed rate (0.2 ml hr^{-1} for the 4.0 and 7.0 wt.% solutions; 0.5 ml hr^{-1} for the 11.5 and 17.5 wt.% solutions) at 23 °C and an absolute humidity of approximately 7.6 g m^{-3}. Electrospinning duration was adjusted to yield roughly 20 µm thick mats on a 76 x 76 mm^2 aluminum foil collector. The fibers were subsequently annealed at 90 °C for 24 hours. The control PVDF fibers, herein called heat-inactivated PVDF, were thermal treated in a rapid thermal annealing oven (Allwin21 Corp) for precise temperature control at 157 °C for 1 hour, followed by quenching in in -20 °C ethanol, to induce the β- to α-phase transition for the suppression of piezoelectricity without any morphological changes.

4.2.2. Piezoelectric characterization of P(VDF-TrFE) and PVDF nanofibers by piezoresponse force microscopy (PFM)

Piezoelectric coefficient, d_{33}, were measured as described in Chapter 3. Briefly, to properly measure the piezoelectric coefficient, a standard periodically poled lithium niobate (PPLN) with a known piezoelectric coefficient was used to determine a correction factor for all subsequent measurements. Various P(VDF-TrFE) or PVDF nanofibers were sparsely collected on a gold coated, thermal-oxide silicon substrate and subjected to single-point piezoresponse force microscopy on individual fibers. A MFP-3D AFM (Asylum Research, Santa Barbara, CA) was first used in tapping imaging mode to locate an individual fiber. Five points were chosen on the scanned fiber and the AFM was switched to PFM where single point spectroscopy measurements were conducted. Step voltages from -3 to +3 V was applied across the fiber via the AFM cantilever (AC240TM, Olympus) to the grounded substrate. A value of d_{33} was calculated by,

$$d_{33} = \frac{A}{VQ} f \ ,$$

where A is the amplitude response of the nanofiber in response to an applied voltage (V), Q is the quality factor of the AFM cantilever, and f is the correctional factor taken from the PPLN standard.

4.2.3. Zeta potential of membranes

The zeta potential of each nanofiber membrane was calculated by measuring the streaming current formed tangentially to the fibrous surface with an electrokinetic analyzer (SurPASS Electrokinetic Analyzer, Anton Paar, Graz Austria). By utilizing the streaming current, the zeta potential (ζ) can be calculated by,

$$\zeta = \frac{dI}{dP}\frac{\eta}{\varepsilon\varepsilon_0}\frac{L}{A},$$

where I is the measured streaming current, P the pressure difference across the length of the sample, η and ε the viscosity and dielectric constant of electrolyte solution, ε_0 the dielectric constant of free space, L the channel length of the measured sample, and A the cross sectional area along the sample. Two- 1 cm x 2 cm cuts of each sample were fixed inside an adjustable gap cell of the electrokinetic analyzer and the gap between the two opposing faces of the sample was adjusted to approximately 100 µm. An electrolyte solution of 1 mM KCl was used to generate a titration curve of the zeta potential for each sample. The streaming current was logged after 20 seconds of flow through of a given titration at a pressure of 400 mbar.

4.2.2. Drug loading into nanofiber membranes

To promote full wettability of the hydrophobic P(VDF-TrFE) and PVDF nanofiber membranes, a 30 second pre-wash in ethanol was conducted on each sample followed by a series of three washes in 1x PBS, prior to the subsequent drug loading. To determine the saturation capacity of crystal violet, a model drug used in this study, various concentrations of crystal violet (Sigma-Aldrich, St. Louis, MO) dissolved in PBS at 15.6, 31.2, 62.5, and 125.0 µg mL^{-1} were utilized for its adsorption onto a 1x1 cm^2 sample. After exposing the sample to the crystal violet solution overnight on a shaker plate, any loosely bound dye was removed by a two-step process. The first is a diffusion-based desorption in fresh PBS for 24 hours on a shaker plate. The second is a PBS wash of the sample through a vacuumed filter.

4.2.3. Drug release calibration and quantification

From a series of concentrated dye solutions (8, 16, 32, 125, and 250 µg/ml), 1 µl of each solution was blotted onto a nitrocellulose paper (5 different blots per solution) to determine a standard curve between optical density and drug amount. Optical images of the stained nitrocellulose membrane were scanned by a desktop image scanner at a resolution of 3200 dpi and processed in ImageJ for total gray value quantification. Briefly, the images were converted to 32-bit, gray values inverted, and LUT values inverted so true whites and blacks would pertain to a value of 0 and 256, respectively. The stain regions were manually selected and analyzed for total gray value by multiplying the average gray value with the total pixel density of the selected area. The produced standard curve of total gray value versus dye amount was used to quantify the amount of drug released from the piezoelectric nanofibers.

4.2.3. In vitro drug release quantification

A 1x1 cm^2 samples of the different P(VDF-TrFE) and non-piezo PVDF, loaded with the same amount of crystal violet (62.5 μg), were placed between two layers of nitrocellulose membrane (Bio-Rad, Hercules, CA) pre-wetted with PBS acting as a drug-capturing film. This configuration was placed in between two layers of 0.5 cm thick PDMS membranes acting as buffer pads between the applied shockwave and the drug-loaded membrane. A shockwave system (MP-100 Vet, Storz Medical, Tägerwilen, Switzerland) was used to deliver the mechanical stimulation to the samples to induce the piezoelectric effect. The number of delivered shockwaves, as well as the applied pressure, was varied while maintaining the frequency fixed at 12 Hz. After each regimen, the crystal violet-stained nitrocellulose papers were collected to be optically scanned for drug release quantification.

4.2.4. In vivo drug release

To demonstrate the feasibility of the piezoelectric nanofiber-based drug delivery system in an *in vivo* condition, a rat carcass was used. Specifically, a membrane of crystal violet-loaded 30 nm P(VDF-TrFE) nanofibers was either subcutaneously implanted in the back or used to wrap around a femur, and connective tissues/muscles, which were initially moved away from the implantation sites and carefully put back to cover the implants. The membranes were activated by the application of shockwave for either 1000 or 2000 doses, respectively, at 5 bar/12 Hz. After the shockwave application, the implant sites were opened to observe the release of the drug, evident from stains around the implants.

4.3. Results and discussion

4.3.1. Drug release calibration

The working principle of the mechanical stimulus-responsive piezoelectric drug delivery platform is based on the control over electrostatic binding strength between a charged molecule and the surface of the P(VDF-TrFE) having a particular zeta potential

(**Figure 4.1a**). Due to the piezoelectricity of P(VDF-TrFE), a mechanical perturbation can effectively change the value of zeta potential from the static state value (**Figure 4.1b**) to a value closer to the opposite of the intrinsic polarity (**Figure 4.1c**). This change in the effective zeta potential of the P(VDF-TrFE) surface would induce the release of the electrostatically adhered drug molecules; the mechanical perturbation alters the microscopic domains of the crystalline electroactive phase causing a shift in polarity which results in a net charge change at the surface of the P(VDF-TrFE). Thus, we hypothesize that this stimulus-responsive piezoelectric membrane can serve as an on-demand drug delivery system, where precise drug release *in vivo* can be tuned with a particular magnitude of mechanical stimulation.

To quantify the release of adsorbed molecules via the piezoelectric effect, crystal violet was used as a model drug due to its simplistic nature of confirming adsorption by its color and quantifying release by colorimetry. In this regard, nitrocellulose membrane was used to act as a molecule catcher upon the release of drug in solution for the accurate detection at low concentration. To generate a standard curve, various concentrations of the standard solution (8, 16, 32, 125, and 250 μg mL^{-1}) were prepared and 1 μL of each was blotted on a nitrocellulose paper (**Figure 4.2a**). Once the drop of crystal violet solution was dried, the stain of crystal violet on the nitrocellulose with the known amount at 8, 16, 32, 125, or 250 ng was optically scanned (**Figure 4.2b**). Conversion of the scanned images of the stains to gray scale allowed for quantification of the intensity values between 0 and 255 via the ImageJ software. The varying sizes of stain area were accounted for during the calculation of the total gray value by multiplying the pixel density of this area by the average gray value of the selected region. The final standard curve is shown in **Figure 4.2c**, as a log-log plot of the total gray value versus stain amount and utilized in the subsequent quantification of the drug molecule release from the piezoelectric membranes.

4.3.2. Zeta potential and piezoelectric coefficient comparisons of P(VDF-TrFE) and PVDF membranes

To demonstrate the proof-of-concept of utilizing electrospun piezoelectric nanofibers as an on-demand drug delivery platform, several different variations of P(VDF-TrFE) nanofibers were synthesized and characterized. As demonstrated in our previous study,[15, 16] P(VDF-TrFE) nanofibers with different fiber diameters were synthesized by controlling electrospinning parameters such as solution concentration, conductivity, and surface tension (the nanofibers with the average fiber diameters of 34 ± 18 nm (herein referred to 30 nm) and 476 ± 122 nm (herein referred to 500 nm) are shown in **Figure 4.3a and 4.3b** as examples). In addition, PVDF control sample of 469 ± 144 nm (herein referred to 500 nm) in average fiber diameter was synthesized and thermally treated between the Curie and melting temperature to eliminate the piezoelectric phase but keep the fibrous morphology (**Figure 4.3c**). This heat-inactivated PVDF sample was used to determine whether the release of the model drug was mechanical dependent, piezoelectrically driven, or the combination of both. As a comparison of three significantly different performing nanofibers, the piezoelectric coefficients for the 30 and 500 nm P(VDF-TrFE) nanofibers and the 500 nm PVDF nanofibers were determined from PFM measurements as 103 ± 22, 37 ± 4, and 6 ± 2 pm V^{-1} (**Figure 4.3d**). However, the changes in piezoelectric properties did not significantly alter the zeta potential, showing a similar value of approximately -50 mV at the physiological pH of 7.4 (30 or 500 nm P(VDF-TrFE) or 500 nm PVDF was -48, -54, and -51 mV, respectively) (**Figure 4.3e**). The zeta potential analysis revealed that the surface charge remains negative above pH 3 for all samples. These isoelectric points were beyond the titrated concentrations of HCl during the measurement and irrelevant to the use of drug release in practical *in vivo* applications. These values agree closely with those reported in literature for PVDF films and membranes,[17-20] although the explanation for the persistent negative surface of PVDF remains ambiguous throughout literature.[17] One explanation is the hydroxide ion accumulation at the interface between the solution (water) and hydrophobic PVDF surface, thus the apparent negative zeta potential arises not necessarily from the PVDF but the hydroxide ions.[21] It is also suggested that the electronegativity of the C-F moiety relative to the hydrogen atom gives the bulk material its negative zeta potential.[22] Regardless of the origin of the negative zeta potential, however, the proposed working principle for the release of adsorbed drug at the surface of the membranes still stands to be affected directly by the piezoelectric response of the nanofibers. Since the zeta potentials across all samples are similar, therefore, the energy barrier that must be overcome to release the drug can be considered similar for all samples tested herein.

4.3.3. Tunable drug release from various P(VDF-TrFE) membranes

The model drug was loaded to various samples including P(VDF-TrFE) with different fiber diameters and heat-inactivated PVDF nanofibers, by incubating them in 1 mL aqueous solution of crystal violet at 62.5 µg mL^{-1} concentration, determined by a preliminary adsorption saturation assessment. To test the release of adsorbed drug molecules in response to the mechanical stimulation, an extracorporeal shockwave system was utilized (**Figure 4.4a**), which has been implemented therapeutically in reducing pain caused by chronic pelvic pain syndrome,[23] calcifying tendonitis,[24] fragmenting kidney stones,[25] or triggering anti-inflammatory actions associated with many inflammatory diseases.[26] A 1x1 cm^2 membrane of each sample was loaded with the drug, pre-washed, and placed in between two nitrocellulose membranes, which was then sandwiched between two pieces of PDMS to simulate soft tissues/muscles.

To show the size-dependent effects on the drug release tunability, a study was conducted comparing the previously mentioned P(VDF-TrFE) nanofiber membranes of diameters 30 and 500 nm in addition to membranes with intermediate fiber sizes of 72 ± 14, 96 ± 15, and 210 ± 75 nm (herein referred to 70, 100, and 200 nm, respectively) (**Figure 4.4b-f, above dotted line**). All samples showed complete adsorption of the same concentration of drug in solution (62.5 μg mL^{-1}) with no apparent change in the fiber morphology or fibrous structure (**Figure 4.4b-f, bellow dotted line**). Additionally, the heat-inactivated PVDF was also compared (**Figure 4.4g**). Furthermore, the apparent colors of the membranes of different fiber diameter were indistinguishable (**Figure 4.4h**).

A dosage of 1000 shockwaves was delivered at a pressure of 5 bar and frequency of 12 Hz, to five replicates of each sample. Due to the piezoelectric performance dependency on fiber size, the smaller fibers released the greater amount of drugs under the shockwave application (**Figure 4.4i**). This increase in drug release can be attributed to the transformative enhancement of piezoelectric properties when the nanofibers are synthesized well below the nanoscale (<100 nm) and favorably thermal treated to induce both greater alignment in piezoelectric domains and materialization of flexoelectricity.[15] The effects of difference in surface area due to different nanofiber diameters can be disregarded since all samples were loaded with the same amount of the drug. Moreover, the heat-inactivated PVDF showed a negligible amount of drug release compared to all other samples such that the amount released from the 500 nm P(VDF-TrFE) sample was approximately 200-fold more than that of the 500 nm heat-inactivated PVDF sample (red dashed line in **Figure 4.4i**). These results show that very little, to none, of the released drug is due to the mechanical stimulation. This is further affirmed with the similar zeta potentials of the sample, together with similarity in the material chemistry, enabling the development a mechanical stimulus-responsive platform based purely on piezoelectricity. Similar to how other drug delivery platforms based on pore size or material degradation rate have allowed the tunability in the amount of drug released over time,[27, 28] these results collectively demonstrate that the sensitivity of the piezoelectric fibers to a given mechanical stimulation can be tuned for specific therapeutic applications. For example, less sensitive piezoelectric fibers can be used for subcutaneously implanted drug delivery system to avoid false activation by accidental impact while highly sensitive piezoelectric nanofibers are desired for the use in deep tissues to be activated with a physiologically safe magnitude of mechanical stimulation.

To further demonstrate the utility of piezoelectric nanofibers as a stimulus-responsive drug delivery system capable of releasing a controlled amount of molecules, the high-performing 30 nm fibers were tested as a function of the applied pressure as shown in **Figure 4.5a**. A linear increase in the curve is observed as the pressure of the shockwave system is increased from 1 to 5 bar. From 1 to 2.5 bar a linear trend is observed which we attribute to the initial linear compression of the PDMS-sample-PDMS *in vitro* construct which may be producing a generated voltage close to, but not, overcoming the zero-zeta potential point. Thus, a small amount of dye is released at this range. After the full compression of the construct, the applied pressure from 3-5 bar begins to affect the compressive elastic region of PDMS. More specifically, as the shockwave is set to a fixed pressure acting on a compressible material (i.e., PDMS) the stress transfer to the PDMS, and subsequently to the P(VDF-TrFE) membrane, rises exponentially as a function of strain applied to the PDMS layer. As a result, the piezoelectric membrane responds proportionally to the applied stress (**Equation 1.4**), thus overcoming the zero-negative potential barrier, and an exponential drug release is observed for pressures above 3 bar. Moreover, as the electrostatic attraction between the negatively charged fiber surface and cationic drug is switched (zeta potential approaching and going towards positive values) the ability for the drug to release and repel from the fiber surface and diffuse towards the capturing film is favored. This is similar to materials undergoing ferroelectric switching which have been shown to induce switchable forces of attraction and repulsion on charged probes within the double layer formed depending on the state of polarization of the material.[29] Although the model drug used here is cationic, we propose that the use of anionic based molecules is possible with the proper pre-functionalization of the P(VDF-TrFE) membrane surface with a cationic linker, still working under the same principle.

The effects of shockwave dosage on drug release (at 500, 1000, 2000, and 4000 applications at 5 bar/12 Hz) were also examined (**Figure 4.5b**). The amount of drug released with respect to the number of shockwaves shows a linear increase in the drug released, indicative of a controllable release of adsorbed molecules. Compared to more traditional drug delivery systems based on degradation or diffusion release that typically shows multiphasic profiles with an initial burst release,[28, 30, 31] the linear profile of drug release from the piezoelectric-based system allows for the precise administration of drug molecules regardless of implantation duration. Moreover, since the same sample was used to survey the release response from 1 to 5 bar, the ability for the membrane to maintain a consistent release rate independent of the previous release history is also attractive. All together, these observations suggest four different ways of controllable drug release from this stimulus-responsive piezoelectric system: 1. number of shockwaves, 2. applied shockwave pressure, 3. the combination of number and applied pressure of shockwaves, and 4. the aforementioned methods with a different level of piezoelectric sensitivity.

4.3.4. In vivo drug delivery

An *in vivo* drug delivery test was conducted by implanting drug loaded 30 nm membranes either subcutaneously in the back of a rat (**Figure 4.6a**) or within deep tissue wrapped around the femur of the rat (**Figure 4.7a**). After application of shockwaves at 1000 or 2000 impulses, respectively, at 5 bar/12 Hz, the staining of the subcutaneous tissue (**Figure 4.6b**) and femur (**Figure 4.7b**) was optically evident. Moreover, the original coloring of the femur (i.e., femur portion outside of the region indicated by arrows of the zoomed image in **Figure 4.7b**) is clearly different in color than the femur portion that was wrapped with the drug delivery membrane (region within the indicated arrows).

Accordingly, in comparison to other electrospun drug delivery systems, [32, 33] the piezoelectric membranes present a fully versatile platform that is not limited to placement *in vivo* or environmental conditions. For example, membranes based on ibuprofen-loaded, sodium bicarbonate-doped, poly(L-lactide) microfibers were shown to take advantage of the acidic spike in inflammatory microenvironments to react with sodium bicarbonate to produce CO_2, thus causing the release of ibuprofen from the bulk of the microfibers.[34] In this case, this drug delivery system is only applicable where the proper acidic environment is present, whereas our platform can perform in various *in vivo* environmental pH, only limited to probably the inside lining of the stomach (pH <3). Another example of a stimulus-responsive platform is are temperature responsive, *N*-isopropylacrylamide (PNIPAM) and *N*-hydroxymethylacrylamide copolymer nanofibers blended with model drug dextran-FITC . This platform showed controlled cyclic release of the drug when the temperature was increased from 10 °C to 45 °C.[35] However, depending on the location of the system *in vivo*, for example reaching deep tissue, may necessitate the use of high intensities of heat at the surface of the body to promote release. A similar example are blended nanofibers of PNIPAM, silica-coated doxorubicin loaded gold nanorods, and polyhedral oligomeric silsesquinoxanes which utilize the photothermal effect of the gold nanoparticles to simultaneously activate the temperature responsive properties of PNIPAM and release the doxorubicin upon excitation with near-infrared (NIR) light.[36] Again, application of this system may be limited by the penetration depth of NIR light of a few centimeters.[37] In comparison, since shockwave has been used to stimulate anti-inflammatory response of deep tissue, the mode of stimulating our piezoelectric fibers is not limited to extreme discomfort needed to achieve release or attenuation of stimulus.

4.4 Conclusion

In summary, we have developed a stimulus-responsive drug delivery system based piezoelectric nanofibrous membrane. The working principle of this system was tested by comparing the release among various piezoelectric membranes having different piezoelectric properties as well as to a heat-inactivated PVDF membrane. Although the zeta potential for the different membranes are similar, we demonstrate a tunable release profile by changing the diameter of the fibers composing the membranes, and a negligible release from heat-inactivated PVDF membranes. Overall, we show that the amount of drug release can be controlled by either the piezoelectric properties via the size dependent properties of P(VDF-TrFE), the applied pressure of stimulus driving the piezoelectric effect, as well as the number of stimulus delivered to the membrane.

4.5 Figures

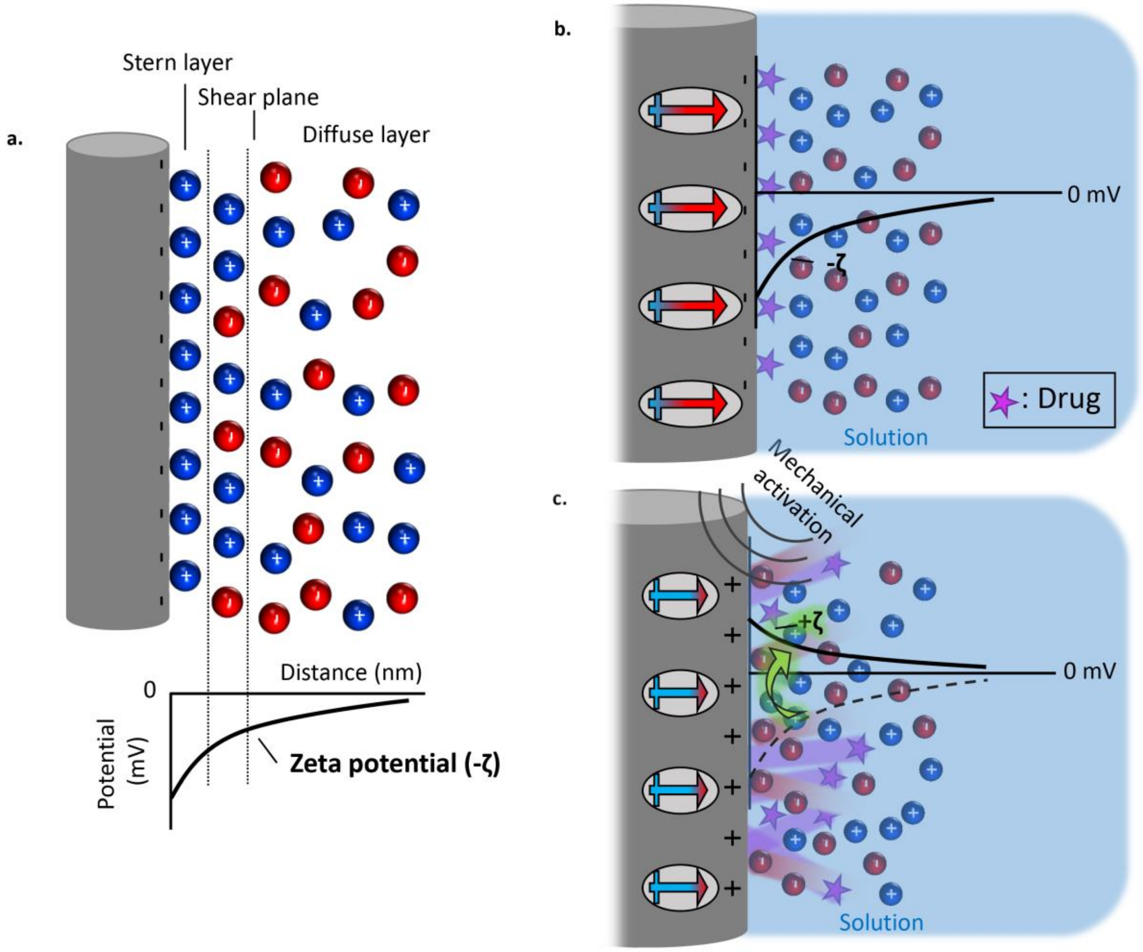

Figure 4.1 Schematic of acoustic responsive drug delivery.

(a) Negative zeta potential (potential at the shear plane) of a P(VDF-TrFE) fiber formed by the positively charged Stern layer and gradient of charge towards the diffuse layer. (b) Piezoelectric dipole domains of P(VDF-TrFE) (red to blue arrows) at the steady state with the associated zeta potential profile in a solution containing cationic drug molecules. (c) Piezoelectric response of domain polarity towards positive values (blue) under a mechanical perturbation, effectively changing the apparent zeta potential of the fiber from negative to positive values, which repels the drug molecules away from the surface.

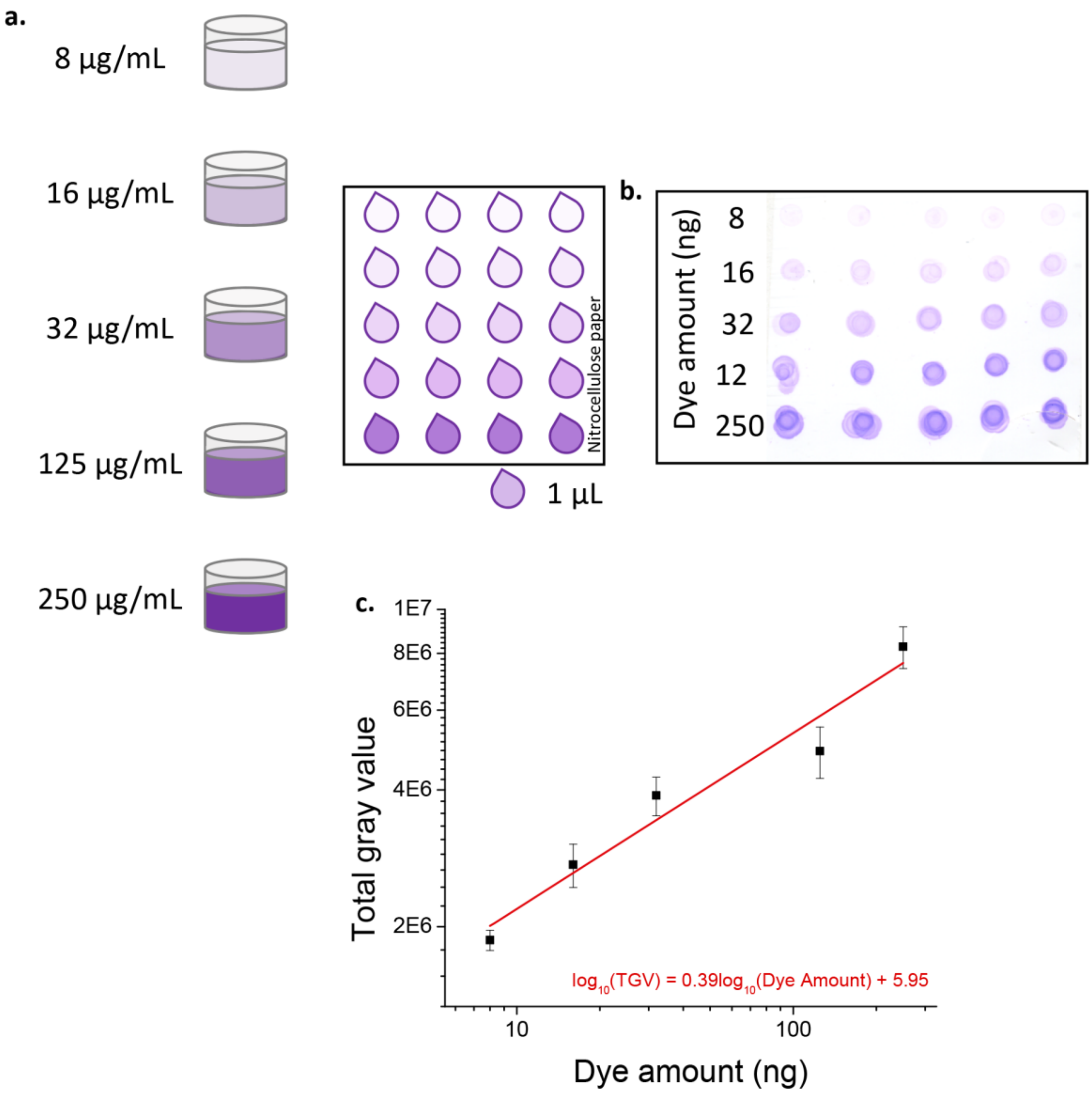

Figure 4.2 Drug calibration curve for acoustic responsive drug release from piezoelectric nanofibers.

(a) Schematic of a titration study for aqueous solutions with different concentrations of crystal violet, a cationic model drug, blotted onto nitrocellulose paper. (b) Scanned optical image of the blot with different crystal violet amount ranging 8-250 ng. (c) Total gray value calculated from the converted image in (b) used as the standard curve for all subsequent drug release quantification.

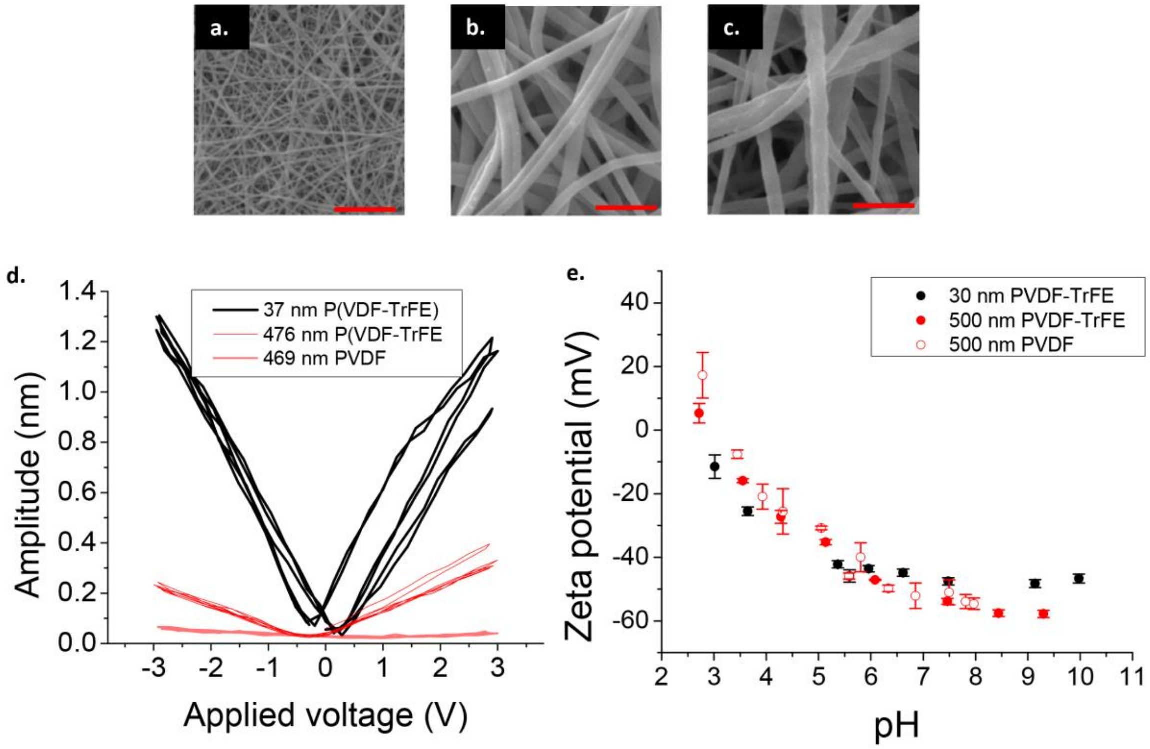

Figure 4.3 Morphological, piezoelectric and electrochemical characterization of various electrospun fibers.

SEM of (a) 37 ± 18 and (b) 476 ± 122 nm piezoelectric P(VDF-TrFE) nanofibers, and (c) 469 ± 144 nm heat inactivated PVDF nanofibers (scale bar = 2 µm). (d) Piezoresponse force microscopy of individual fibers from the three different samples (a-c) showing the decreasing piezoelectric performance of the P(VDF-TrFE) fibers by increasing fiber size, and virtually no piezoelectric response from the heat inactivated PVDF fibers. (e) Zeta potential of the three samples showing similar values as a function of solution pH.

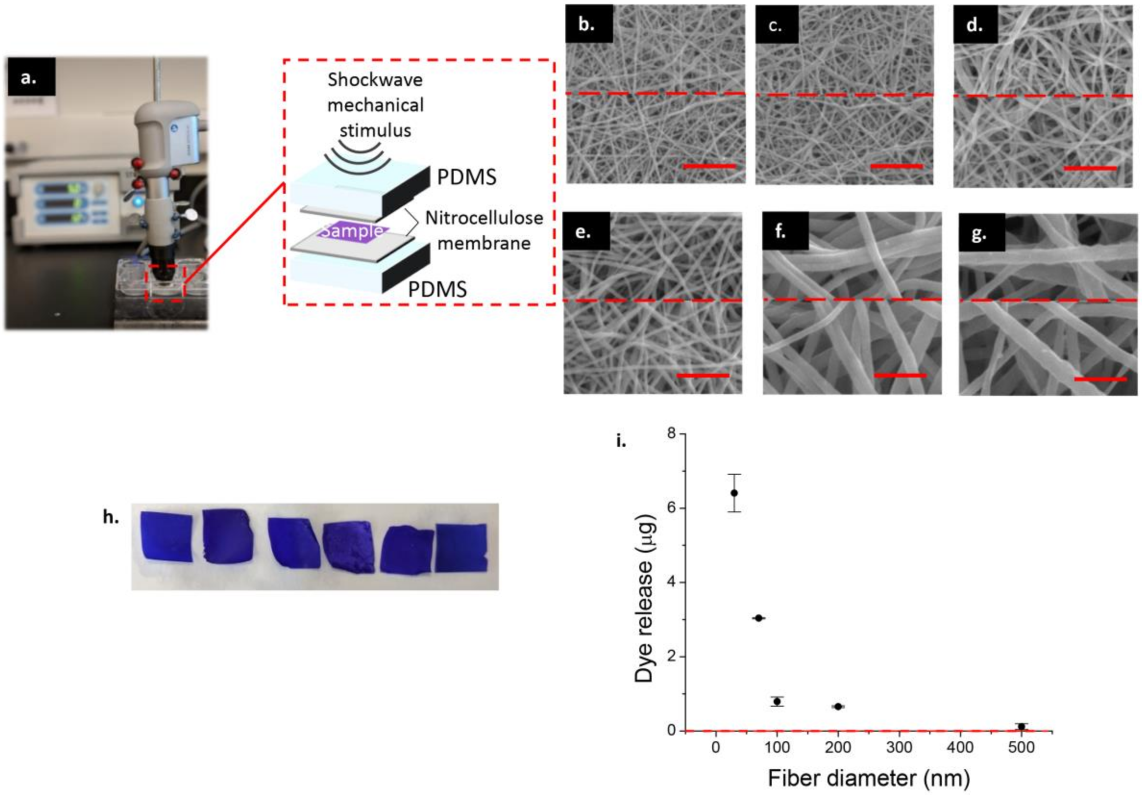

Figure 4.4 Piezoelectric performance-dependent drug release.

(a) An image and a schematic of the *in vitro* set up to simulate and quantify drug release under mechanical perturbation via shockwave applications. SEM of P(VDF-TrFE) (b-f) and PVDF (g) nanofibers before (above red dashed line) and after (below red dashed line) drug adsorption having diameters of 37 ± 18 (b), 72 ± 14 (c), 96 ± 15 (d), 210 ± 75 (e), 472 ± 22 (f), and 496 ± 144 nm (g) (scale bar = 2 µm). (h) Optical image of drug loaded membranes of (left to right) 37, 72, 96, 210, and 472 nm P(VDF-TrFE), and 496 nm PVDF. (i) Dye release of each sample after 1000 shockwave doses at 5 bar/12 Hz as a function of fiber diameter (n=4). A red dotted line indicates the drug release from heat inactivated PVDF samples.

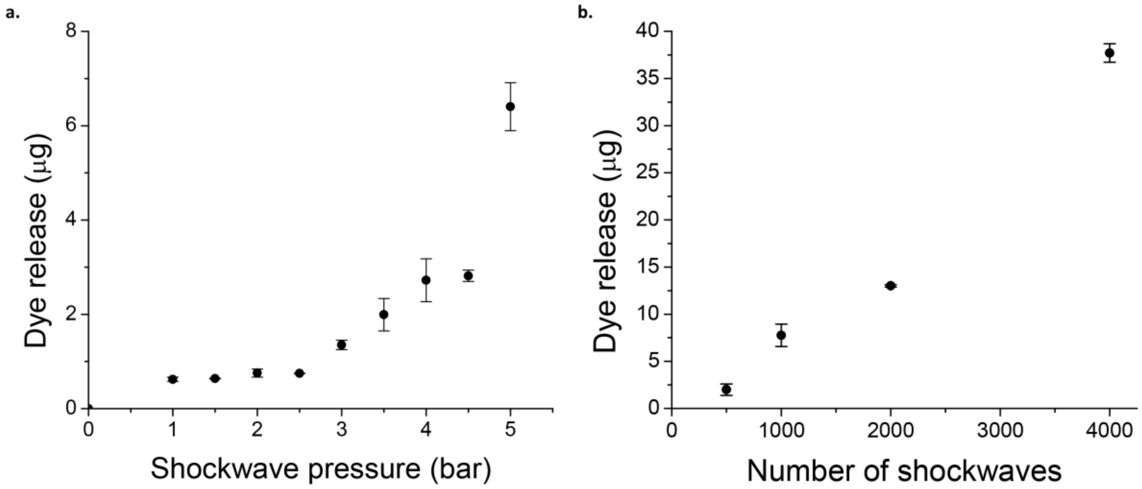

Figure 4.5 Stimuli-dependent drug release.

Dye release of the membrane composed of 30 nm average fiber diameter as a function of shockwave pressure (a) and number of shockwaves (b).

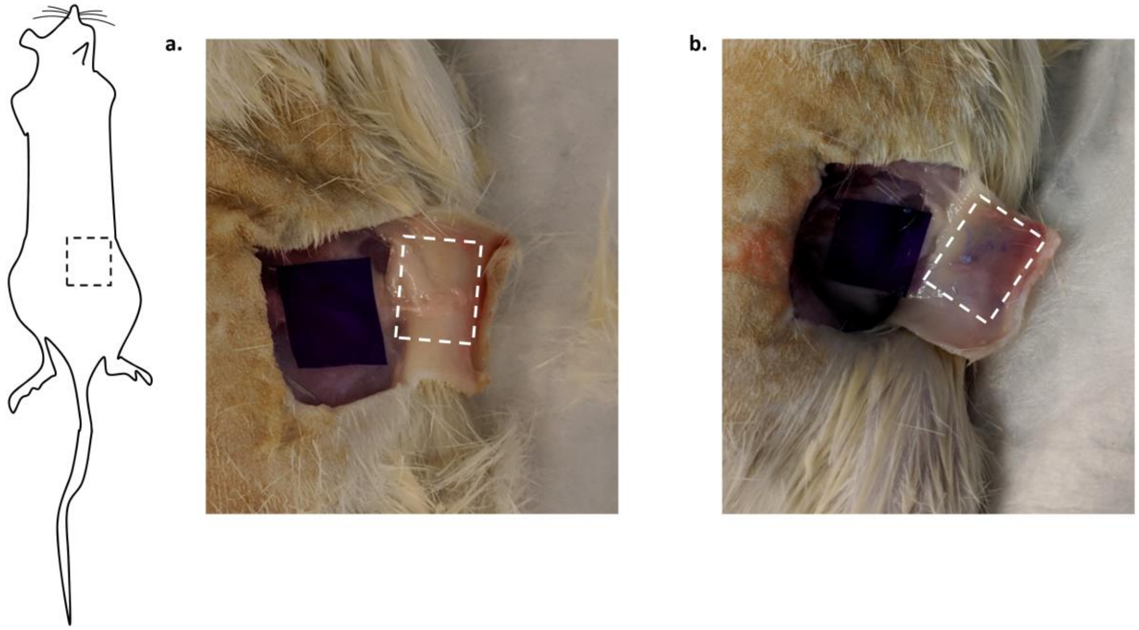

Figure 4.6 ***In vivo*** **drug release - Subcutaneous.**

Optical image of a subcutaneously implanted drug loaded membrane before (a) and after (b) mechanical stimulation. Dotted box shows the area stained with dye.

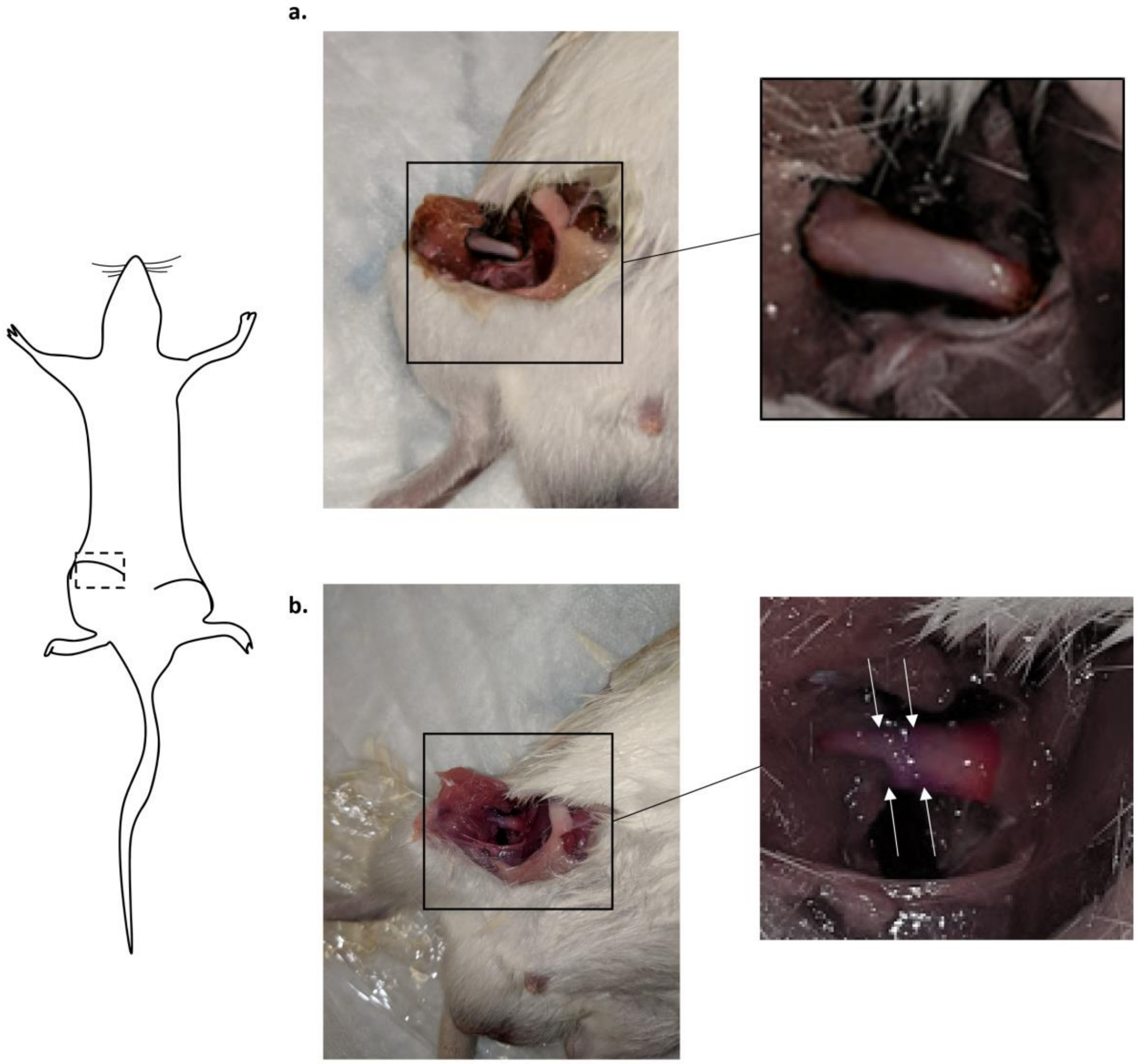

Figure 4.7 ***In vivo*** **drug delivery – Deep tissue.**

(a) Optical image of a deep-tissue site of implantation of drug loaded membrane before (a) and after (b) mechanical stimulation. Region within arrows shows are where membrane was wrapped.

4.6 References

[1] W. Sadée, Z. Dai. *Pharmacogenetics/genomics and personalized medicine*. Human molecular genetics 2005, 14, R207.

[2] C. S. Linsley, B. M. Wu. *Recent advances in light-responsive on-demand drug-delivery systems*. Therapeutic delivery 2017, 8, 89.

[3] C. Zheng, Y. Wang, S. Z. F. Phua, W. Q. Lim, Y. Zhao. *ZnO–DOX@ ZIF-8 Core–Shell Nanoparticles for pH-Responsive Drug Delivery*. ACS Biomaterials Science & Engineering 2017, 3, 2223.

[4] W. Gao, J. M. Chan, O. C. Farokhzad. *pH-responsive nanoparticles for drug delivery*. Molecular pharmaceutics 2010, 7, 1913.

[5] Y. Zheng, L. Wang, L. Lu, Q. Wang, B. C. Benicewicz. *pH and Thermal Dual-Responsive Nanoparticles for Controlled Drug Delivery with High Loading Content*. ACS Omega 2017, 2, 3399.

[6] J. Zhou, M. V. Pishko, J. L. Lutkenhaus. *Thermoresponsive layer-by-layer assemblies for nanoparticle-based drug delivery*. Langmuir 2014, 30, 5903.

[7] S. Imanifard, A. Zarrabi, A. Zarepour, M. Jafari, A. Khosravi, A. Razmjou. *Nanoengineered Thermoresponsive Magnetic Nanoparticles for Drug Controlled Release*. Macromolecular Chemistry and Physics 2017, 218.

[8] A.-L. Papa, N. Korin, M. Kanapathipillai, A. Mammoto, T. Mammoto, A. Jiang, R. Mannix, O. Uzun, C. Johnson, D. Bhatta. *Ultrasound-sensitive nanoparticle aggregates for targeted drug delivery*. Biomaterials 2017, 139, 187.

[9] S. D. Kong, M. Sartor, C.-M. J. Hu, W. Zhang, L. Zhang, S. Jin. *Magnetic field activated lipid–polymer hybrid nanoparticles for stimuli-responsive drug release*. Acta biomaterialia 2013, 9, 5447.

[10] Y. Wang, Y. Deng, H. Luo, A. Zhu, H. Ke, H. Yang, H. Chen. *Light-Responsive Nanoparticles for Highly Efficient Cytoplasmic Delivery of Anticancer Agents*. ACS nano 2017, 11, 12134.

[11] V. A. N. Huu, J. Luo, J. Zhu, J. Zhu, S. Patel, A. Boone, E. Mahmoud, C. McFearin, J. Olejniczak, C. de Gracia Lux. *Light-responsive nanoparticle depot to control release of a small molecule angiogenesis inhibitor in the posterior segment of the eye*. Journal of Controlled Release 2015, 200, 71.

[12] C. L. Weaver, J. M. LaRosa, X. Luo, X. T. Cui. *Electrically controlled drug delivery from graphene oxide nanocomposite films*. ACS nano 2014, 8, 1834.

[13] C. K. Jeong, J. H. Han, H. Palneedi, H. Park, G.-T. Hwang, B. Joung, S.-G. Kim, H. J. Shin, I.-S. Kang, J. Ryu. *Comprehensive biocompatibility of nontoxic and high-output flexible energy harvester using lead-free piezoceramic thin film*. APL Materials 2017, 5, 074102.

[14] G. Laroche, Y. Marois, R. Guidoin, M. W. King, L. Martin, T. How, Y. Douville. *Polyvinylidene fluoride (PVDF) as a biomaterial: from polymeric raw material to monofilament vascular suture*. Journal of biomedical materials research 1995, 29, 1525.

[15] G. Ico, A. Myung, B. S. Kim, N. V. Myung, J. Nam. *Transformative piezoelectric enhancement of P (VDF-TrFE) synergistically driven by nanoscale dimensional reduction and thermal treatment*. Nanoscale 2018, 10, 2894.

[16] G. Ico, A. Showalter, W. Bosze, S. C. Gott, B. S. Kim, M. P. Rao, N. V. Myung, J. Nam. *Size-dependent piezoelectric and mechanical properties of electrospun P (VDF-TrFE) nanofibers for enhanced energy harvesting*. Journal of Materials Chemistry A 2016, 4, 2293.

[17] J. Guo, M. U. Farid, E.-J. Lee, D. Y.-S. Yan, S. Jeong, A. K. An. *Fouling behavior of negatively charged PVDF membrane in membrane distillation for removal of antibiotics from wastewater*. Journal of Membrane Science 2018, 551, 12.

[18] A. Schulze, M. Went, A. Prager. *Membrane functionalization with hyperbranched polymers*. Materials 2016, 9, 706.

[19] D. Breite, M. Went, A. Prager, A. Schulze. *Tailoring membrane surface charges: A novel study on electrostatic interactions during membrane fouling*. Polymers 2015, 7, 2017.

[20] Y. Chen, M. Tian, X. Li, Y. Wang, A. K. An, J. Fang, T. He. *Anti-wetting behavior of negatively charged superhydrophobic PVDF membranes in direct contact membrane distillation of emulsified wastewaters*. Journal of Membrane Science 2017, 535, 230.

[21] R. Zangi, J. B. F. N. Engberts. *Physisorption of hydroxide ions from aqueous solution to a hydrophobic surface*. Journal of the American Chemical Society 2005, 127, 2272.

[22] S. Y. Park, S. H. Choi, J. W. Chung, S.-Y. Kwak. *Anti-scaling ultrafiltration/microfiltration (UF/MF) polyvinylidene fluoride (PVDF) membranes with positive surface charges for Ca2+/silica-rich wastewater treatment*. Journal of Membrane Science 2015, 480, 122.

[23] R. Zimmermann, A. Cumpanas, F. Miclea, G. Janetschek. *Extracorporeal shock wave therapy for the treatment of chronic pelvic pain syndrome in males: a randomised, double-blind, placebo-controlled study*. European urology 2009, 56, 418.

[24] S. Farr, F. Sevelda, P. Mader, A. Graf, G. Petje, M. Sabeti-Aschraf. *Extracorporeal shockwave therapy in calcifying tendinitis of the shoulder*. Knee Surgery, Sports Traumatology, Arthroscopy 2011, 19, 2085.

[25] M. M. Osman, Y. Alfano, S. Kamp, A. Haecker, P. Alken, M. S. Michel, T. Knoll. *5-year-follow-up of patients with clinically insignificant residual fragments after extracorporeal shockwave lithotripsy*. European urology 2005, 47, 860.

[26] S. Mariotto, A. C. de Prati, E. Cavalieri, E. Amelio, E. Marlinghaus, H. Suzuki. *Extracorporeal shock wave therapy in inflammatory diseases: molecular mechanism that triggers anti-inflammatory action*. Current medicinal chemistry 2009, 16, 2366.

[27] Y. Wang, Q. Zhao, N. Han, L. Bai, J. Li, J. Liu, E. Che, L. Hu, Q. Zhang, T. Jiang. *Mesoporous silica nanoparticles in drug delivery and biomedical applications*. Nanomedicine: Nanotechnology, Biology and Medicine 2015, 11, 313.

[28] A. Kumari, S. K. Yadav, S. C. Yadav. *Biodegradable polymeric nanoparticles based drug delivery systems*. Colloids and Surfaces B: Biointerfaces 2010, 75, 1.

[29] R. J. Ferris, S. Lin, M. Therezien, B. B. Yellen, S. Zauscher. *Electric double layer formed by polarized ferroelectric thin films*. ACS applied materials & interfaces 2013, 5, 2610.

[30] N. Kamaly, B. Yameen, J. Wu, O. C. Farokhzad. *Degradable controlled-release polymers and polymeric nanoparticles: mechanisms of controlling drug release*. Chemical reviews 2016, 116, 2602.

[31] J. Huang, Q. Shu, L. Wang, H. Wu, A. Y. Wang, H. Mao. *Layer-by-layer assembled milk protein coated magnetic nanoparticle enabled oral drug delivery with high stability in stomach and enzyme-responsive release in small intestine*. Biomaterials 2015, 39, 105.

[32] L. Weng, J. Xie. *Smart electrospun nanofibers for controlled drug release: recent advances and new perspectives*. Current pharmaceutical design 2015, 21, 1944.

[33] L. R. Pires, in *Electrofluidodynamic Technologies (EFDTs) for Biomaterials and Medical Devices*, Elsevier, 2018, 157.

[34] Z. Yuan, J. Zhao, W. Zhu, Z. Yang, B. Li, H. Yang, Q. Zheng, W. Cui. *Ibuprofen-loaded electrospun fibrous scaffold doped with sodium bicarbonate for responsively inhibiting inflammation and promoting muscle wound healing in vivo*. Biomaterials Science 2014, 2, 502.

[35] Y.-J. Kim, M. Ebara, T. Aoyagi. *Temperature-responsive electrospun nanofibers for 'on–off'switchable release of dextran*. Science and technology of advanced materials 2012, 13, 064203.

[36] Y. F. Li, P. Slemming-Adamsen, J. Wang, J. Song, X. Wang, Y. Yu, M. Dong, C. Chen, F. Besenbacher, M. Chen. *Light responsive hybrid nanofibres for on-demand therapeutic drug and cell delivery*. Journal of tissue engineering and regenerative medicine 2017, 11, 2411.

[37] T. A. Henderson, L. D. Morries. *Near-infrared photonic energy penetration: can infrared phototherapy effectively reach the human brain?* Neuropsychiatric disease and treatment 2015, 11, 2191.

5. Piezoelectric scaffold for multi-phenotypic differentiation of neural stem cells towards neurons and glial cells

5.1 Introduction

Many neurological diseases/disorders including, multiple sclerosis (MS), leukodystrophies, Guillain-Barre syndrome and progressive inflammatory neuropathy, as well as spinal cord and peripheral nerve injuries involve damage to- or abnormalities of neural structures.[1] Such pathologies result in the demyelination of nerve in which the myelin sheath of neurons is damaged, causing a noticeable decrease in sensation, movement, cognition and other functional impairments. In addition to myelin damages caused by genetics, infectious agents, and autoimmune reactions, normal aging has also been shown to affect the health of myelination. Despite the prevalence of myelin-related diseases/syndromes (over 100 out of 100,000 cases in North America),[2] there is currently no cure available other than relieving symptoms or slowing the rate of demyelination.

Due to the limitations of human studies, including restricted access to human tissues and unmodifiable experimental conditions for mechanistic studies, various animal models have been developed to depict demyelinating diseases in an attempt to understand the fundamental pathogenesis and develop effective treatments.[3-5] However, a single animal *in vivo*/*ex vivo* model cannot accurately represent all aspects of pathological and clinical features of human diseases due to dissimilarities in genetics and metabolism.[4]

Alternatively, *in vitro* models have been established to begin to dissect the underlying molecular mechanisms of neurologic diseases and/or to discover potential pharmacological targets by overcoming limitations of *in vivo* and *ex vivo* models.[6] Despite their simplicity, *in vitro* models allow researchers to study the role of isolated cells of one particular type in a controlled environment that simulates the disease, which allows for facilitated screening of potential drugs. *In vitro* models using patient-derived cells further demonstrate their significant utility in studying neurological diseases as recent studies discovered a strong contribution of genetics to several of these diseases that were traditionally considered as non-genetic diseases such as MS.[7] Still, many of these *in vitro* models are limited to a single cell type, failing to accurately account for significant cell-cell interactions, for example, myelination of neurons by glial cells, which are crucial for nerve physiology. To this effect, several studies have attempted to develop *in vitro* models that address such cell-cell interactions by co-culturing different cell phenotypes.[8, 9] Although they showed cell-cell interactions, the cellular structure was limited to two-dimension, failing to resemble the sophisticated structures of the native tissues, i.e., the 3D network of nerves in the brain or the native aligned bundles of nerve tracts in the spinal cord.

With regard to the morphological characteristics of the cell culture substrate, studies have shown that unidirectional grooves promote cellular alignment of neurons and subsequent neurite elongation, a physical marker for neurogenesis.[10] Due to the innate electrical properties of the nervous system, another controllable *in vitro* factor is that of electrical stimulation as an exogenous stimulating factor which has also been shown to enhance neurogenesis from neural stem cells. However, many of these techniques require the use of conducting substrates which can interfere with innate nerve signal transduction during experimentation.

In this regard, piezoelectric materials provide a means to electrically stimulate the cells without interfering with innate signal transduction. Piezoelectric materials generate surface potentials under dynamic mechanical strain while simultaneously remaining electric insulators under static conditions. By the direct piezoelectric effect, the materials induce an electric charge separation at their surface in response to mechanical deformation (tension or compression), providing a means to produce electric potentials without the need of an external electric source. As we have recently shown, electrospinning is advantageous in producing high performance piezoelectric polymers because the technique intrinsically subjects the polymers to a high electric field, enhancing their piezoelectric properties.[11, 12] Furthermore, electrospinning has the capability of producing an aligned fibrous structure that resembles native ECM and which can guide unidirectional cellular orientation as found in spinal nerves.

In this study, electrospun P(VDF-TrFE) nanofibers were employed as a cell culture scaffold for mouse neural stem cells (NSCs). An acoustic mechanical stimulation was used to remotely activate the piezoelectric effect of these scaffolds to induce an electrical stimulation on the NSCs to enhance their differentiation capacity. The multi-phenotypic differentiation towards the neuron and glial cells (oligodendrocytes and astroctyes) was assessed by changes in gene expression and difference in protein expression. By utilizing a heat-inactivated control scaffold composed of PVDF nanofibers, we demonstrate that the electrical stimulation resulting from the piezoelectric effect of the scaffold is the main factor affecting the differentiation of NSCs towards all three phenotypes.

5.2 Experimental

5.2.1. Synthesis and morphological characterization of P(VDF-TrFE) scaffolds

Nanofibrous scaffolds of P(VDF-TrFE) were electrospun from a 11.5 wt.% P(VDF-TrFE) (Solvay Group, France) dissolved in a 60/40 volume ratio of dimethylformamide (DMF, Sigma Aldrich, St. Louis, MO) to acetone (Fisher Scientific, Pittsburgh, PA) solvent system, with the addition of 1.5 wt.% pyridinium formate (PF) buffer (Sigma Aldrich). The solution was magnetically stirred at 1200 rpm for 3 hr at room temperature until the solution turned clear. As a non-piezoelectric control, a solution of 13.5 wt.% of PVDF dissolved in the same DMF/acetone/PF solvent system was created. Each solution was electrospun under optimized conditions of electrospinning distance (10 cm), applied voltage (approximately -15 to -20 kV) and solution feed rate (6 ml hr^{-1}) at 23 °C and an absolute humidity of approximately 7.6 g m^{-3}. The formed fibers were collected onto a high-speed, grounded mandrel rotating at an angular velocity of 47.9 m s^{-1} for four hours to yield scaffolds of aligned fibers having a thickness of approximately 200 μm. The P(VDF-TrFE) scaffolds were subsequently annealed at 90 °C for 24 hours which we have previously shown to enhance the piezoelectric properties. The PVDF fibers were thermal treated in a rapid thermal annealing oven (Allwin21 Corp) for precise temperature control at 157 °C for 1 hour, to induce the β- to α-phase transition without causing the melting of the fibrous structure, and immediately quenched in -20 °C ethanol to preserve the non-piezoelectric α-phase.

5.2.2. Piezoelectric characterization of electrospun nanofibers

A piezoelectric cell culture system, based on 3-D printed acrylonitrile butadiene styrene (ABS) chambers (**Figure 5.1a**), was engineered to contain and apply an non-contact mechanical stimulation to induce the piezoelectric effect of the nanofibrous P(VDF-TrFE) scaffold by the vertical translation of a stage fixed on a subwoofer (**Figure 5.1b**). The chambers were designed to be accommodated within a typical 6-well tissue culture plate. The subcomponents of the chamber consist of top and bottom mating surfaces each with o-rings which serve to both create fixed points for the scaffold and create a mechanical seal when both surfaces are mated with stainless steel screws. The cylindrical nature of the chambers allows the suspension of the scaffold thus promoting an unrestricted region for the scaffold to deflect in response to the indirect mechanical stimulation in an aqueous solution.

To quantify the voltage generated across the P(VDF-TrFE) scaffolds and absence of voltage generated across the control PVDF scaffolds, acellular scaffolds were subjected to the acoustic stimulation inside the cell culture system. Scaffolds were cut to the dimensions of 45 x 5 mm^2. Gold electrodes with the dimension 40 x 4 mm^2 were sputtered on both sides of the scaffolds (**Figure 5.1c,left**). A hydrophobic poly(styrene-block-isobutylene-block-styrene) (SIBS, Sibstar, Kaneka, Pasadena, TX) coating was applied, via brush from a 30 wt.% SIBS in toluene (Fisher Scientific, Pittsburgh, PA) solution, on top of gold sputtered surfaces to prevent an electrical short circuit. The processed scaffold was assembled into the cell culture chamber and 2 mL of DI water was added into the center region of the chamber submerging the scaffold. The chamber was placed on the vertical translating stage and various magnitudes of strains were applied indirectly to the scaffold by driving a 3 Hz step signal via a LabVIEW-controlled function generator bridged to the subwoofer by an amplifier (**Figure 5.1b**). The generated voltage across the scaffold was simultaneously measured by an oscilloscope (Pico Technologies, St. Neots, UK). The magnitude of applied strain was correlated to the matched output voltage generated by our previously designed cantilever system (Chapters 2 and 3).

5.2.3. Cell culture for mechanical/electrical stimulation

Following thermal treatment of the P(VDF-TrFE) and PVDF scaffolds, 40 x 5 mm^2 strips of each were prepared and a layer of SIBS coasting was applied to the periphery of a 7 mm x 5 mm cell culture area isolated at the center of the pristine scaffold (**Figure 5.1c,right**). The scaffolds were centered and bridged across the culture chambers, as described for the voltage measurement, and assembled to yield the final piezoelectric cell culture system which was gamma irradiated at a dose of 10kGy.[13] After sterilization, the cell culture area of each scaffold was pre-wetted with 70% ethanol, washed in three changes of PBS, and coated overnight with 20% FBS in DMEM.

C17.2 neural stem cells (NSCs), derived from the cerebellum of neonatal mouse, were cultured in high glucose DMEM, supplemented with 10% FBS (VWR, Radnor, PA), 5% horse serum (Gibco, Gaithersburg, MD), 1% sodium pyruvate (Gibco), and 1% penicillin/streptomycin in a standard 37 °C incubator with 5% CO_2. The cells were cultured up to 70-80% confluency and media replaced every 3-4 days. Once the cells reached confluency, the cells were incubated in 0.05% trypsin EDTA/PBS for 2 min at 37 °C. The NSCs were seeded onto the sterile scaffolds assembled in the cell culture chamber at a seeding density of 1,000 cells cm^{-2} and the cells were allowed to attach for 2 hours before filling up the chamber with additional media. During the experiment, the cells were maintained in the maintenance media with no additional growth factors.

The cells seeded on the P(VDF-TrFE) scaffolds were cultured for 48 hours before subjecting them to either mechanical stimulation or maintained statically (i.e., no stimulation). The cell-seeded scaffold was actuated on the vertical translating stage at 3 Hz to apply a surface strain of approximately 0.031%, which was determined to generate approximately 200 mV_{p-p} for a 200 µm thick P(VDF-TrFE) scaffold. The scaffold-cell constructs were either stimulated daily for 2 hr for six days or maintained statically with no mechanical/electrical stimulation. After 24 hrs from the last mechanical stimulation on the sixth day post pre-culture, cells were subjected to RNA extraction for gene expression analysis or fixation by 4% paraformaldehyde (PFA) for protein expression analysis.

5.2.4. Gene expression analysis

The effects of piezoelectric stimulation on NSCs were analyzed by gene expression by real-time polymerase chain reaction (RT-PCR). Total RNA was extracted using an RNeasy Micro Kit (Qiagen, Valencia, CA), and cDNA synthesis was performed using iScript cDNA Synthesis Kit (Bio-Rad, Hercules, CA) according to manufacturers' protocols. Real-time PCR was performed to determine the gene expression of phenotypic markers for mouse NSCs **(Table 5.1**). Data were analyzed by the comparative threshold cycle (CT) method using GAPDH as an endogenous control.

5.2.5. Protein expression analysis

To characterize the differentiation associated protein expression of NSCs towards neuronal or glial cells promoted by piezoelectric stimulation, fixed cells were immuno-stained with primary antibody markers specific for either neurons (βIII tubulin, Thermo Fisher Scientific, Waltham, MA), oligodendrocytes (MBP, Santa Cruz Biotechnology, Dallas, TX), or astrocytes (EAAT2, Santa Cruz Biotechnology) with the appropriate secondary mouse binding protein marker (m-IgGκ BP-CFL 488, Santa Cruz Biotechnology). The samples were counter-stained with DAPI and phalloidin conjugated with Alexa Fluor-594 for visualization of the cell nucleus and actin filament, respectively, followed by analysis using immunofluorescence microscopy (Eclipse Ti, Nikon, Melville, NY).

5.2.6. Statistical analysis

Statistical analysis was performed with at least three biologically independent samples and represented as an average ± standard deviation (SD) or standard error of mean (SEM) as indicated. The data were subjected to ANOVA with Tukey’s post-hoc test using the SPSS software (IBM) to determine statistical significance ($p < 0.05$).

5.3 Results and discussion

5.3.1. Morphological characterization of Aligned P(VDF-TrFE) and PVDF scaffolds

The microstructure of aligned P(VDF-TrFE) and PVDF nanofibers is shown in **Figure 5.2a** and **Figure 5.2b**, respectively. The thermal enhancement of P(VDF-TrFE) at 90 °C and the thermal inactivation of PVDF at 157 °C shows no apparent effect on the structure of the scaffolds with the resulting fiber diameter of 476 ± 58 and 502 ± 72 nm, respectively. The alignment of the neuronal culture substrate has been shown to enhance the extension of neuron axis in *in vitro* experiments,[14, 15] with the combination of aligned microstructure with exogenous electrical stimulation having a synergistic effect.[16] Thus, the expected enhancement differentiation enhancement due to the preferentially aligned piezoelectric-scaffold with the culture topography can be determined by comparing the piezoelectric P(VDF-TrFE) scaffold with the heat-inactivated PVDF scaffold.

5.3.2. Electrical characterization of P(VDF-TrFE) and PVDF scaffolds

The electrical characteristics of the scaffolds were measured using the piezoelectric cell-culture system equipped with scaffolds having deposited thin gold film acting as electrical contact and SIBS coating as insulation (**Figure 5.1a** and **Figure**

5.1b,top). Activation of the piezoelectric effect of the scaffolds was achieved by applying acoustic waves via the vertical translation of the speaker-mounted stage. Under these controlled acoustic perturbations, the piezoelectric scaffold produces an electric potential across its surface (**Figure 5.3a**). As a function of applied strain, the peak-to-peak voltage generated at the surface of the scaffolds shows a linear trend for P(VDF-TrFE) as the strain is increased (**Figure 5.3b**). Due to the heat-inactivation, a negligible voltage generated is observed for the PVDF scaffold up until 0.031% strain. From preliminary testing of NSCs to a similar profile of an externally applied AC voltage source (**Figure 5.4**), a minimum voltage of 150 mV_{p-p} was determined as the necessary stimulation to induce a phenotypic change in from NSCs to specialized neuronal and glial cells (**Figure 5.5-5.7**). Thus, a strain of 0.030% to produce approximately 150 mV_{p-p} from the P(VDF-TRFE) scaffold and an insignificant voltage of approximately the PVDF scaffold was chosen for all subsequent studies herein.

5.3.3. Effect of mechano-electrical stimulation on NSC differentiation via piezoelectric scaffolds

The effects of electrical stimulation by the piezoelectric effect on the differentiation capability of NSCs towards neuronal, oligodendrocyte, or astrocyte cells were quantitatively determined by rt-PCR (**Figure 5.8**). Mature neuron markers, *Map2* and *Eno2* (**Figure 5.8a** and **5.8b**, respectively), were downregulated from the PVDF scaffolds but significantly upregulated from the P(VDF-TrFE) scaffolds. The upregulation of *Eno2* was improved by actuating the piezoelectric scaffold to induce an electrical stimulation on the NSCs. These results corroborate with the protein expression of β-III tubulin in which the piezoelectric scaffolds showed greater expression and formation of longer extended axons indicative of maturing neurons, whereas the inactive PVDF scaffold showed less mature neurons (i.e., shorter extended axons) (**Figure 5.8c**).

Oligodendrocyte genes, *Olig1* and *Mog*, were both upregulated in all conditions as compared to untreated controls (**Figure 5.9a** and **5.9b**, respectively). The former is part of the neural stem cell differentiation pathway and thus expressed in oligodendrocyte precursors whereas the latter is expressed on the outermost surface of myelin sheaths indicative of more mature oligodendrocytes. Though all conditions showed some upregulation of both genes, the fold change within each gene for the inactive PVDF scaffolds and static (non-actuated) condition of P(VDF-TrFE) scaffold showed no statistical significance, in comparison to the statistically significant higher expression of the actuated P(VDF-TrFE), especially for *Olig1*, indicating that the electrically stimulated cells have a better differentiation efficiency for both precursor and more mature oligodendrocytes. The protein expression of MBP (myelin basic protein) (**Figure 5.9c**) supports the notion that the higher fold change for the electrically stimulated cells, by inducing the piezoelectric effect on the P(VDF-TrFE) scaffolds, promotes higher efficiency towards myelinating oligodendrocytes in comparison to the other conditions where the fold change is similar in level to the control gene.

In regards to the differentiation of NSCs towards the astrocyte phenotype, *Gfap* and *Cspg4* (**Figure 5.10a** and **5.10b**, respectively), also show similar level of slight upregulation for both conditions of inactive PVDF scaffolds as well as static P(VDF-TrFE) scaffold, though not statistically significant from one another. Again, only the actuated P(VDF-TrFE) scaffold producing the electrical stimulation to the cells shows a significant upregulation for both genes. *Gfap* encodes a major filament protein in mature astrocytes, allowing the ability to distinguish these cells types from the other glial cell types (i.e., oligodendrocytes). In regards to the specific astrocyte cell-type, *Cspg4* is known to be expressed in reactive astrocytes;[17] i.e., astrocytes involved in the phagocytosis of synapses, secretion of specific neurotrophins, and clearance of debris and dead cells, following injury to the central nervous system (CNS).[18] It has been thought that some of these reactive astrocytes prevent full axon regeneration in the CNS following injury. However, recently it has been shown that the same scar-forming astrocytes also express multiple axon-growth-supporting molecules as well as the CSPG4 gene necessary for axons regeneration.[19] As expected, the expression of EAAT2, an astrocyte marker, at the protein level was observed only in the actuated piezoelectric P(VDF-TrFE) condition (**Figure 5.10c**). Thus a higher level of expression of these genes, together with the neuron and oligodendrocyte gene expression, shows that the activated piezoelectric scaffold allows for the co-differentiation of NSCs towards all neuronal cell types. More specifically the remote activated piezoelectric scaffold promotes the production of mature, elongated neurons in the presence of myelinating oligodendrocytes and axon-regeneration promoting astrocytes.

5.4 Conclusion

In summary, a piezoelectric scaffold system capable of electrically stimulating cells without any physical connections has been developed to enable multi-phenotypic differentiation of NSCs in culture. To decouple the effects of the electrical stimulation and the mechanical stimulation needed to induce such an electrical stimulation through the piezoelectric effect, a heat-inactivated PVDF scaffold was also produced which produced negligible amount of electrical stimulation. Using our piezoelectric cell culture system, we show that the electrical stimulation promotes the differentiation of NSCs towards neuron, oligodendrocyte, and astrocyte cell types. Moreover, the maturity level of each cell type is enhanced with this scaffold in comparison to a static P(VDF-TrFE) scaffold or heat-inactivated PVDF scaffolds. We show that the resulting glial cells are phenotypes supportive of axon growth and elongation. Thus, this platform offers the capability of producing functioning neuronal cells for *in vitro* disease models encompassing all neural cell types.

5.5 Tables and figures

Table 5.1 Primer sets for mouse NSCs used in rt-PCR analysis.

Marker	Primer	Forward	Reverse
Housekeeping	*Gapdh*	5’-GGCAAATTCAACGGCACAGT-3’	5’-TCGCTCCTGGAAGATGGTGAT-3’
Neuron	*Map2*	5’-AAGCCATTGTGTCCGAACCA-3’	5’-GAGCGGAAGAGCAGTTTGTCA-3’
	Eno2	5’-ATCGCCACATTGCTCAGCTAG-3’	5’-TGAGAGCCACCATTGATCACA-3’
Oligodendrocyte	*Olig1*	5’-ACGCCAAAGAGGAACAGCA-3’	5’-TCCATGGCCAAGTTCAGGT-3’
	Mog	5’-TGCCCTGCTGGAAGATAACAC-3’	5’-TGCAGCCAGTTGTAGCAGATG-3’
Astrocyte	*Cspg4*	5’-CTGAGCAATCTGTCTTTCCCAGT-3’	5’-TGTGTATGCAGAGGTTCAAGCCT-3’
	Gfap	5’-TGGAGCTCAATGACCGCTTT-3’	5’-GCTCGAAGCTGGTTCAGTTCA-3’

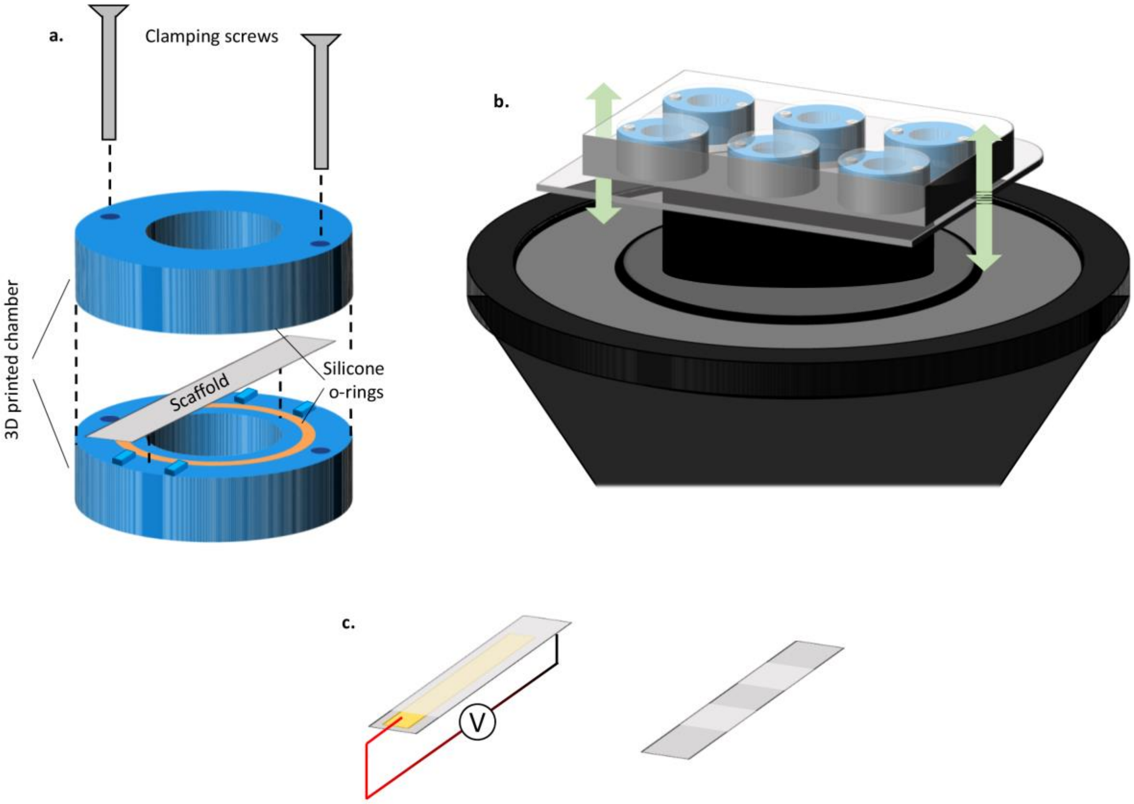

Figure 5.1 Piezoelectric cell-culture system.

(a) Exploded schematic showing the components of the cell culture system. (b) Schematic of the system used to actuate the scaffolds by translating a stage vertically with a subwoofer. (c) Scaffold preparation method for the electrical characterization of the scaffold (left) and use as a cell culture scaffold (right).

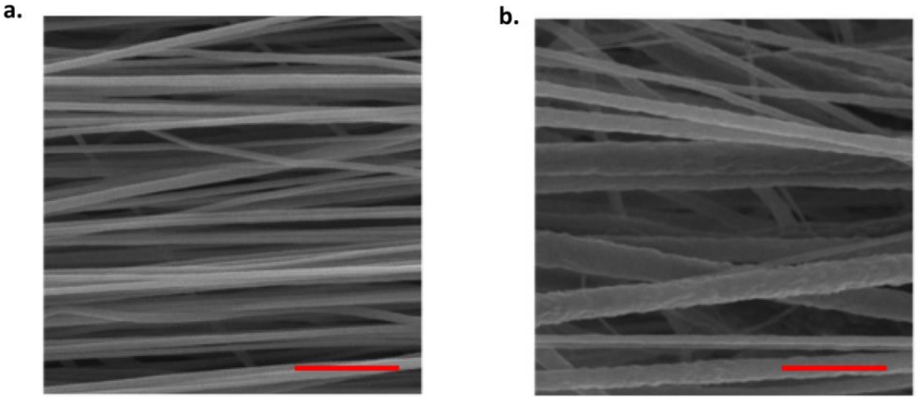

Figure 5.2 Morphology of aligned scaffolds.

Scanning electron micrographs of electrospun fibers of P(VDF-TrFE) (a) and heat-inactivated PVDF (b). (Scale bar = 5µm).

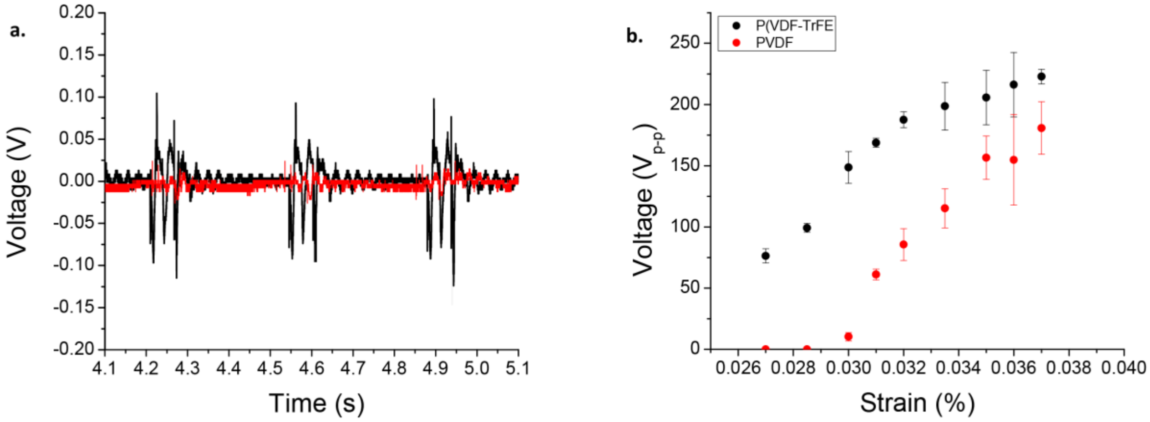

Figure 5.3 Electrical characterization of electrospun scaffolds.

(a) Representative raw voltage output of P(VDF-TrFE) and heat-inactivated PVDF scaffolds at 0.030% strain. (b) Voltage versus strain graph of P(VDF-TrFE) and inactive PVDF scaffolds.

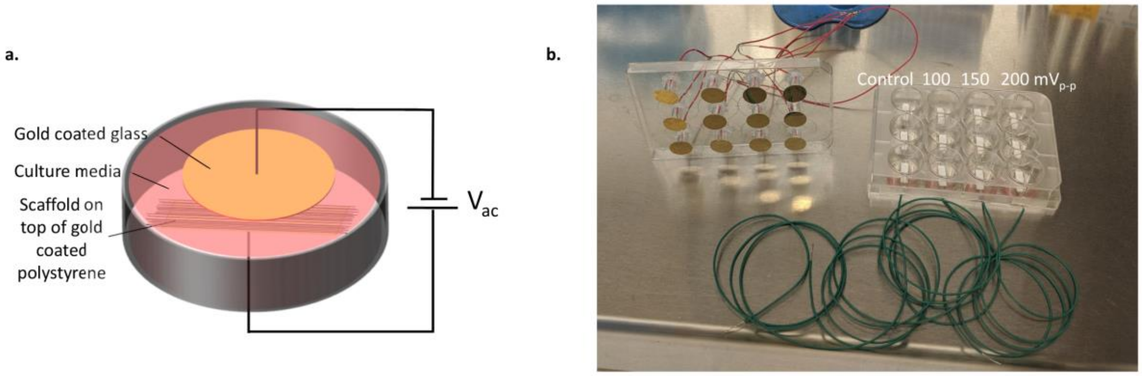

Figure 5.4 Direct electrical stimulation cell culture device.

(a) Schematic of cell culture device used to deliver a direct electrical stimulation using an AC voltage of either 0, 100, 150, or 200 $mV_{p\text{-}p}$. (b) Optical image of cell culture device in a 12-well plate format.

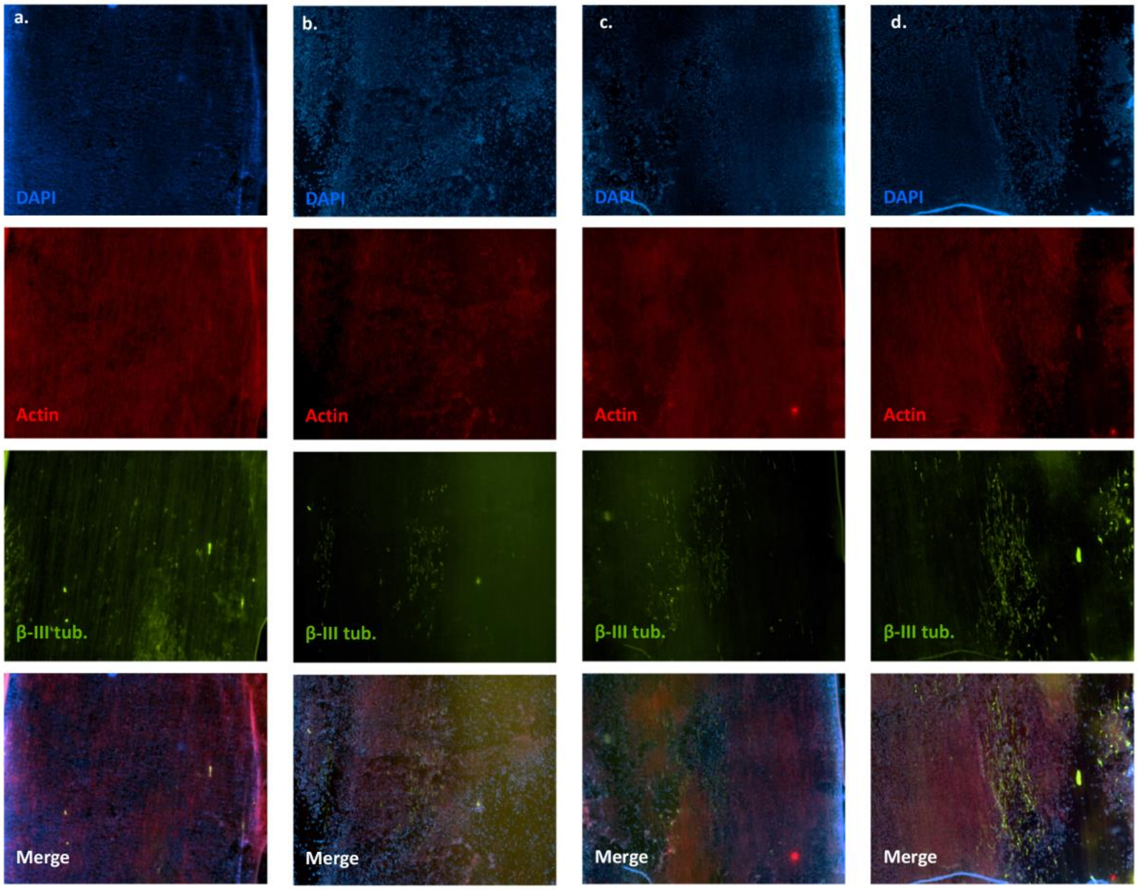

Figure 5.5 β-III tubulin protein expression of NSCs cultured on scaffolds with direct electrical stimulation.

Immunofluorescence images of cells exposed to 0 (a), 100 (b), 150 (c), or 200 mV_{p-p} (d). Magnification 4x.

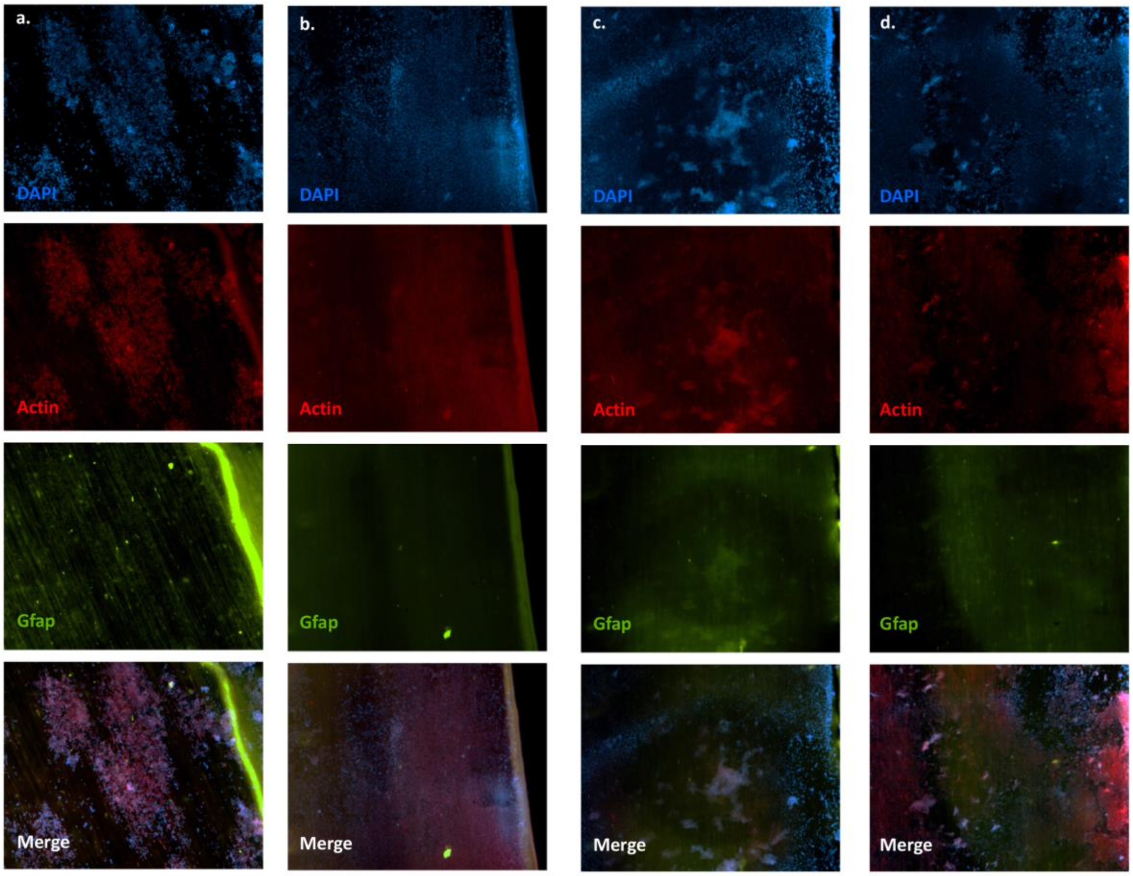

Figure 5.6 Gfap protein expression of NSCs cultured on scaffolds with direct electrical stimulation.

Immunofluorescence images of cells exposed to 0 (a),100 (b), 150 (c), or 200 $mV_{p\text{-}p}$ (d). Magnification 4x.

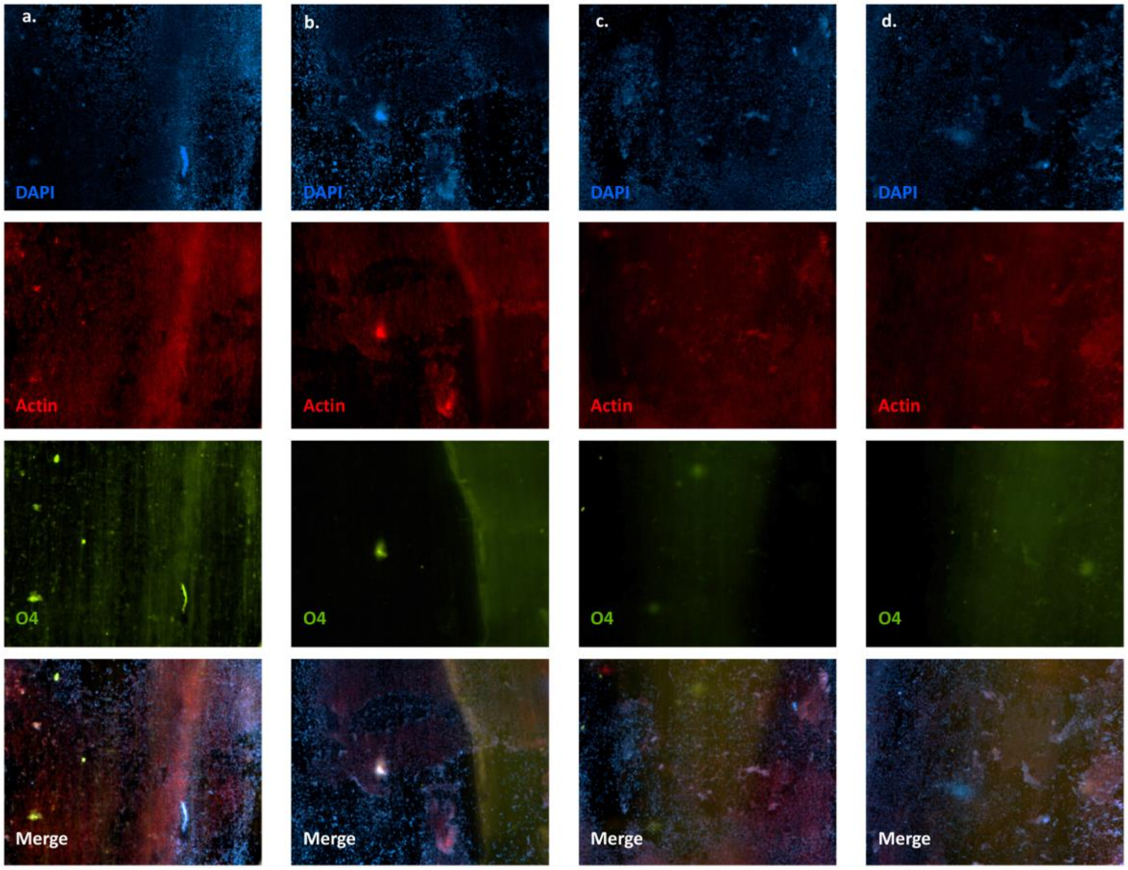

Figure 5.7 O4 protein expression of NSCs cultured on scaffolds with direct electrical stimulation.

Immunofluorescence images of cells exposed to 0 (a), 100 (b), 150 (c), or 200 mV_{p-p} (d). Magnification 4x.

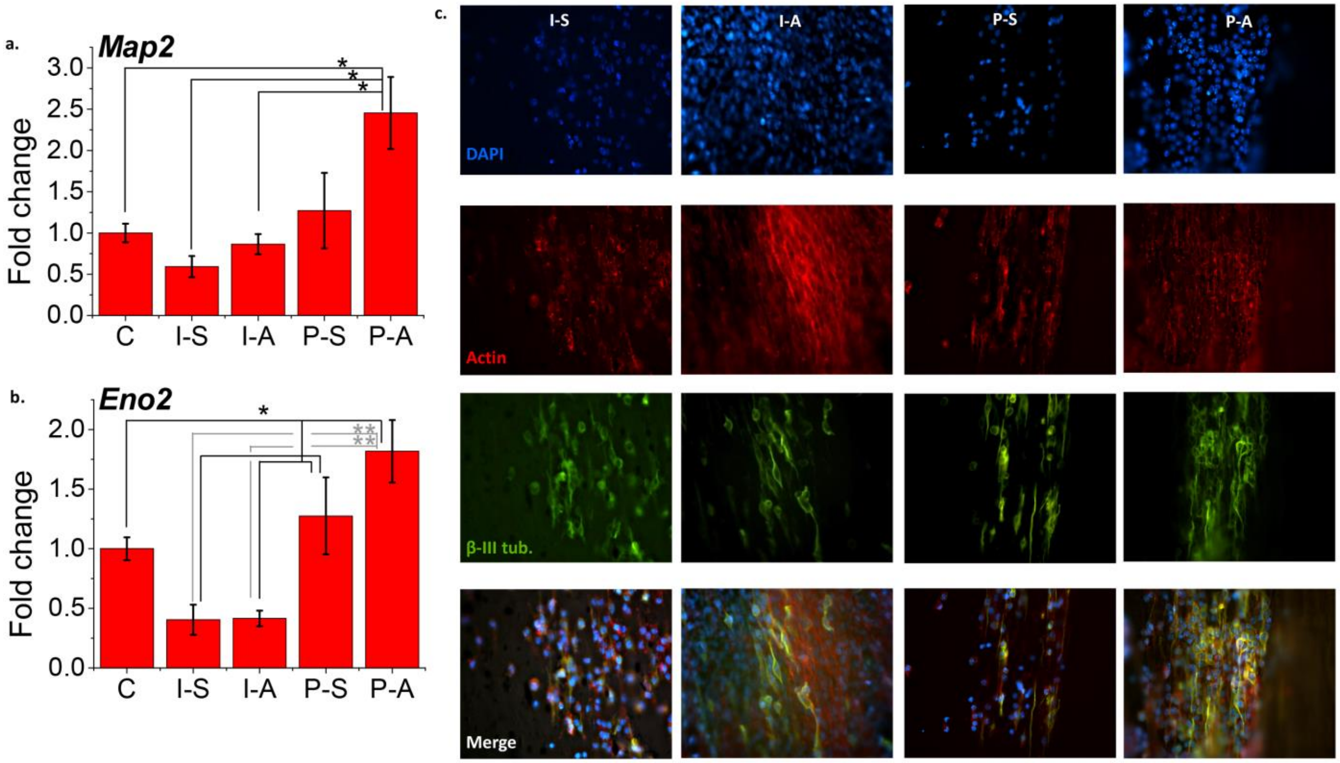

Figure 5.8 Neuron gene and protein expression of NSCs cultured on various scaffolds.
Gene expression of neuron markers, *Map2* and *Eno2* (a and b), and expression of β-III tubulin (c) from NSCs after 6 day culture on either inactivated PVDF static or actuated [I-S or I-A, respectively], or piezoelectric P(VDF-TrFE) static or actuated scaffolds [P-S or P-A, respectively]. Fluorescence images taken at 20x magnification. * denotes statistical significance of $p < 0.05$; ** denotes statistical significance of $p < 0.01$.

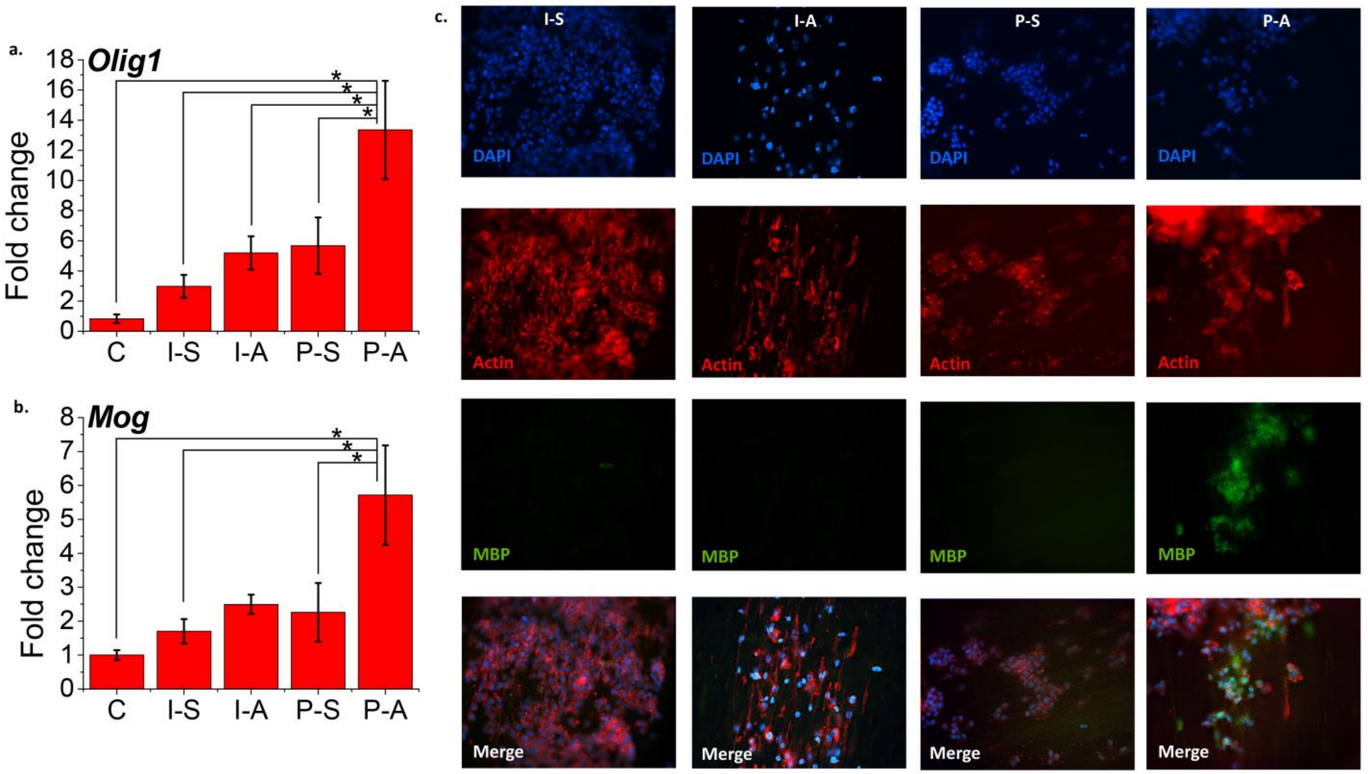

Figure 5.9 Oligodendrocyte gene and protein expression of NSCs cultured on various scaffolds. Gene expression of oligodendrocyte markers, *Olig1* and *Mog* (a and b), and expression of MBP (c) from NSCs after 6 day culture on either inactivated PVDF static or actuated [I-S or I-A, respectively], or piezoelectric P(VDF-TrFE) static or actuated scaffolds [P-S or P-A, respectively]. Fluorescence images taken at 20x magnification. * denotes statistical significance of $p < 0.05$; ** denotes statistical significance of $p < 0.01$.

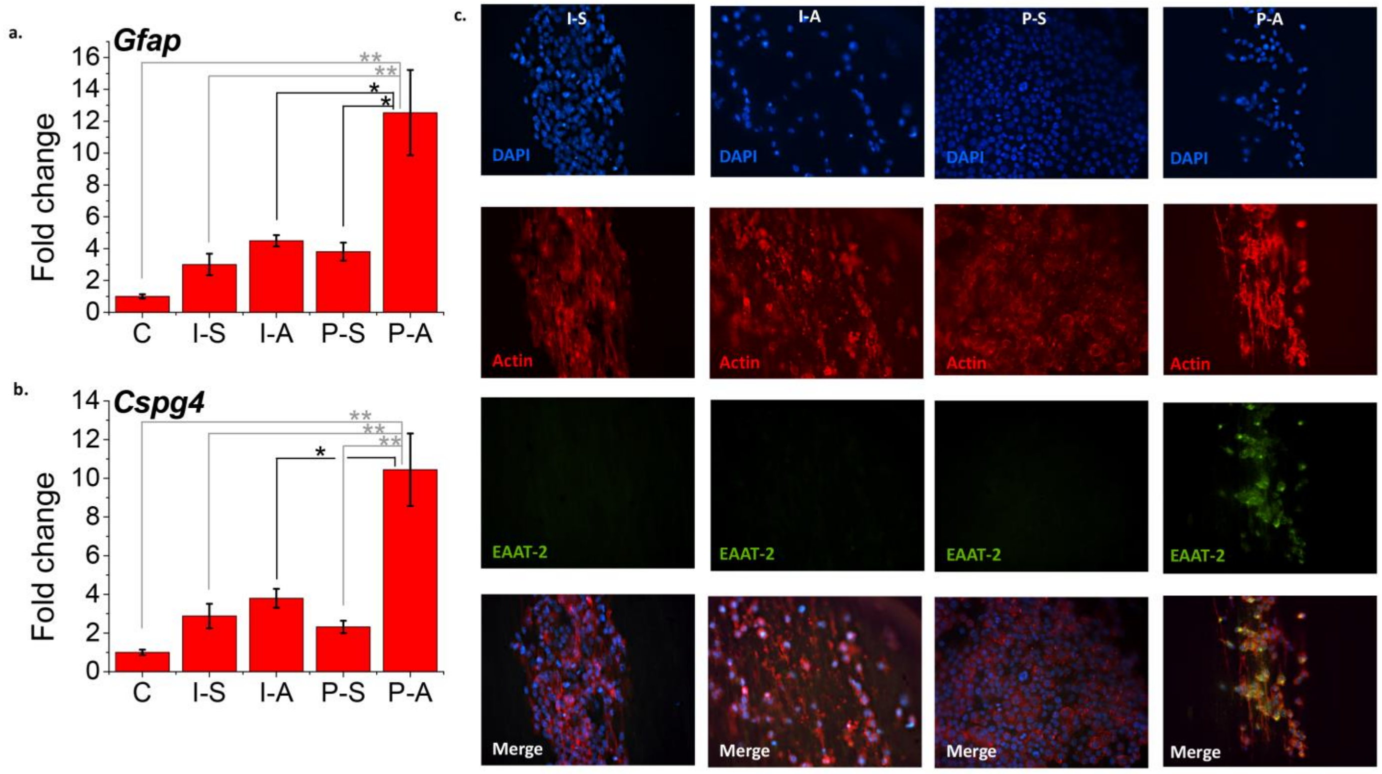

Figure 5.10 Astrocyte gene and protein expression of NSCs cultured on various scaffolds.
Gene expression of oligodendrocyte markers, *Gfap* and *Cspg4* (a and b), and expression of EAAT2 (c) from NSCs after 6 day culture on either inactivated PVDF static or actuated [I-S or I-A, respectively], or piezoelectric P(VDF-TrFE) static or actuated scaffolds [P-S or P-A, respectively]. Fluorescence images taken at 20x magnification. * denotes statistical significance of $p < 0.05$; ** denotes statistical significance of $p < 0.01$.

5.6 References

[1] S. Love. *Demyelinating diseases*. Journal of clinical pathology 2006, 59, 1151.

[2] M. M. Mehndiratta, N. S. Gulati. *Central and peripheral demyelination*. Journal of neurosciences in rural practice 2014, 5, 84.

[3] M. Bradl, C. Linington. *Animal models of demyelination*. Brain pathology 1996, 6, 303.

[4] A. Denic, A. J. Johnson, A. J. Bieber, A. E. Warrington, M. Rodriguez, I. Pirko. *The relevance of animal models in multiple sclerosis research*. Pathophysiology 2011, 18, 21.

[5] H. Zhang, J. L. Bennett, A. S. Verkman. *Ex vivo spinal cord slice model of neuromyelitis optica reveals novel immunopathogenic mechanisms*. Annals of neurology 2011, 70, 943.

[6] B. J van der Star, D. Ys Vogel, M. Kipp, F. Puentes, D. Baker, S. Amor. *In vitro and in vivo models of multiple sclerosis*. CNS & Neurological Disorders-Drug Targets (Formerly Current Drug Targets-CNS & Neurological Disorders) 2012, 11, 570.

[7] P. Khankhanian, T. Matsushita, L. Madireddy, A. Lizée, L. Din, J. M. Moré, P.-A. Gourraud, S. L. Hauser, S. E. Baranzini, J. R. Oksenberg. *Genetic contribution to multiple sclerosis risk among Ashkenazi Jews*. BMC medical genetics 2015, 16, 55.

[8] Y. Pang, B. Zheng, S. L. Kimberly, Z. Cai, P. G. Rhodes, R. C. S. Lin. *Neuron-oligodendrocyte myelination co-culture derived from embryonic rat spinal cord and cerebral cortex*. Brain and behavior 2012, 2, 53.

[9] E. V. Jones, D. Cook, K. K. Murai, in *Astrocytes*, Springer, 2012, 341.

[10] M. Y. Laura, N. D. Leipzig, M. S. Shoichet. *Promoting neuron adhesion and growth*. Materials today 2008, 11, 36.

[11] G. Ico, A. Showalter, W. Bosze, S. C. Gott, B. S. Kim, M. P. Rao, N. V. Myung, J. Nam. *Size-dependent piezoelectric and mechanical properties of electrospun P (VDF-*

TrFE) nanofibers for enhanced energy harvesting. Journal of Materials Chemistry A 2016, 4, 2293.

[12] G. Ico, A. Myung, B. S. Kim, N. V. Myung, J. Nam. *Transformative piezoelectric enhancement of P (VDF-TrFE) synergistically driven by nanoscale dimensional reduction and thermal treatment*. Nanoscale 2018, 10, 2894.

[13] E. Eljarrat-Binstock, A. Bentolila, N. Kumar, H. Harel, A. J. Domb. *Preparation, characterization, and sterilization of hydrogel sponges for iontophoretic drug-delivery use*. Polymers for advanced technologies 2007, 18, 720.

[14] Y.-t. Kim, V. K. Haftel, S. Kumar, R. V. Bellamkonda. *The role of aligned polymer fiber-based constructs in the bridging of long peripheral nerve gaps*. Biomaterials 2008, 29, 3117.

[15] Y.-S. Lee, G. Collins, T. L. Arinzeh. *Neurite extension of primary neurons on electrospun piezoelectric scaffolds*. Acta biomaterialia 2011, 7, 3877.

[16] A. N. Koppes, N. W. Zaccor, C. J. Rivet, L. A. Williams, J. M. Piselli, R. J. Gilbert, D. M. Thompson. *Neurite outgrowth on electrospun PLLA fibers is enhanced by exogenous electrical stimulation*. Journal of neural engineering 2014, 11, 046002.

[17] V. Rusnakova, P. Honsa, D. Dzamba, A. Ståhlberg, M. Kubista, M. Anderova. *Heterogeneity of astrocytes: from development to injury–single cell gene expression*. PLoS One 2013, 8, e69734.

[18] S. A. Liddelow, B. A. Barres. *Reactive astrocytes: production, function, and therapeutic potential*. Immunity 2017, 46, 957.

[19] M. A. Anderson, J. E. Burda, Y. Ren, Y. Ao, T. M. O'Shea, R. Kawaguchi, G. Coppola, B. S. Khakh, T. J. Deming, M. V. Sofroniew. *Astrocyte scar formation aids central nervous system axon regeneration*. Nature 2016, 532, 195.

6. A piezoelectric scaffold-based device for modulating the dynamic mechanical microenvironment of the cells

6.1 Introduction

The derivation of human iPSCs from adult somatic cells has significantly increased the possibility of using pluripotent stem cells in personalized clinical applications.[1] However, the high risks of oncogenicity and teratoma formation in vivo still limits their therapeutic usage.[2, 3] Among various strategies to reduce the risks, differentiation of iPSCs into a required cell type prior to their implantation may limit the adverse effects. For example, the feasibility of using iPSCs in cartilage repair in a cartilage explant model has been shown by differentiating the cells to chondrocytes by BMP-4 and dexamethasone, followed by cell sorting.[4] However, the differentiation efficiency was low at approximately 10%. In this regard, development of efficient methods for phenotype-specific differentiation is critical for facile clinical applications of pluripotent stem cells in regenerative medicine.

Recent advances of our understanding in developmental molecular biology have inspired directed stem cell differentiation schemes by sequential supplementation of biomolecules, mimicking the transient changes of endogenous growth factors/cytokines during embryo development. Several studies have successfully directed pluripotent stem cells into various types of cells, but often resulted in low differentiation efficiencies which may limit translational applications.[5-7] Among many environmental factors, the mechanical microenvironment of pluri- and multi-potent cells has shown to be a significant contributor in cell function and cell feedback interaction with their environment.[8-10] Examples of current techniques of manipulating the mechanical microenvironment of cells include variably compliant polyacrylamide gels, [8] cell-encapsulating three-dimensional hydrogel matrices,[10] or geometrically distinct substrates.[11] Interestingly, the aforementioned studies may also indicate that a specific stiffness of substrate is necessary for efficient differentiation. More importantly, a recent study showed that there’s a specific substrate stiffness for enhanced differentiation in a lineage- and phenotype-specific manner. The efficiency of differentiation partly depends on the colony morphology that governs cell-cell interactions and cellular adhesion to substrates.[12, 13] Although there is mounting evidence that the mechanical microenvironment of stem cells significantly influences differentiation through the regulation of cell morphology and adhesion, understanding in how the changes of the mechanical niche over the course of stage-wise differentiation process is still elusive.

One of the obstacles to investigate the effect of the mechanical environment on the stage-dependent differentiation/development of stem cells is the lack of appropriate substrates that can alter their mechanical properties in real time. Unfortunately, multiple studies have focused on the effects of varying mechanical properties on cell behavior and fate by utilizing multiple separate substrates which involves the use of proteolytic enzymes to detach cells from the substrate. This constant perturbation on cells in culture has been shown to have a negative effect on cells, leading to apoptosis and cell loss. Therefore, a biocompatible scaffold enabling real-time manipulation of its mechanical microenvironment is critical in order eliminate the need for multiple scaffolds to enhance differentiation.

In this regard, piezoelectric poly(vinylidene fluoride) (P(VDF)) or its derivatives including poly(vinylidene fluoride)-trifluoroethylene (P(VDF-TrFE)) has the ability to respond mechanically to an external electric field (the indirect piezoelectric effect) making it an ideal candidate to serve as the basis of such a mechano-modulating scaffold. Several studies have demonstrated that the electrospinning process promotes the formation of functionally enhanced form of P(VDF-TrFE), including our previous studies where tunability of its piezoelectric properties via optimizing electrospinning parameters has been shown.[14, 15] Furthermore, electrospinning produces unwoven nanofibrous morphology, resembling that of native extracellular matrix.[16, 17] Typically these fibrous networks of P(VDF-TrFE) are used in energy applications utilizing the direct piezoelectric effect with only select studies showing single nanofibers responding to an external electric field through the inverse piezoelectric effect.[18-20] The capability of using P(VDF-TrFE) nanofibers as a culture substrate has been shown, however only in studies using the material for its intrinsically charged surface.[21, 22]

Thus, the current lack of a controllable dynamic cell culture substrate for guiding stem cell differentiation has motivated the work presented herein. Governed by the goal of controlling the cellular mechanical microenvironment through the indirect piezoelectric effect, we utilize electrospun synthesized P(VDF-TrFE) nanofibers as the primary culture substrate while developing a system to control their stiffness *on-demand*. Driving the indirect piezoelectric effect is the focus of the design, fabrication, and validation of a microfabricated electrode array which controls the mechanical properties of overlaying P(VDF-TrFE) scaffold.

6.2 Experimental

6.2.1. Piezoelectric scaffold synthesis and device integration

A 15 wt.% P(VDF-TrFE) (70/30 mol%) (Solvay Group, France) dissolved in a 60/40 volume ratio of N,N-dimethylformamide (DMF) (Fisher Scientific, Pittsburgh, PA) and acetone (THF) (Fisher Scientific, Pittsburgh, PA), supplemented with 1.5 wt.% pyridinium formate (PF) buffer (Sigma-Aldrich, St. Louis, MO) was used as the electrospinning solution. The solution was electrospun under optimized conditions of a needle-to-collector distance of 20 cm, an applied voltage of approximately -15 kV, and a solution feed rate at 0.5 ml hr^{-1} for 3 hours at 23 °C and an absolute humidity of approximately 7.6 g m^{-3}.

6.2.2 Indirect piezoelectric response measurement by atomic force microscopy (AFM)

All assembled samples and devices tested for the indirect piezoelectric response were measured by AFM in a similar manner. Briefly, an AFM (MFP-3D, Asylum Research, Santa Barbara, CA) in contact force mode was utilized to probe the intrinsic mechanical properties and dynamic changes in fiber deflection in response to an applied electric field. Due to the porosity of the fibrous mesh, a modified cantilever equipped with a 20 µm-diameter borosilicate bead was used to survey the network of fibers. In this mode, a total of five force curves were collected for which the Hertz Model,

$$E^{*} = \left[\frac{3}{4\sqrt{R}}\right]\frac{F}{\sqrt[3]{\delta}} \tag{6.1}$$

was fitted to extract the Reduced Young's Modulus (E^*) of the sample, where R is radius of the bead probe, F is the applied force, and δ is the indentation. Subsequently, a modified version of a force measurement was executed by conducting a dwelling period of the AFM probe on the fiber mat at a fixed force for a fixed amount of time. During the dwelling period, an external electric field was applied and the indentation of the fibers was detected by a force feedback loop of the AFM probe. Each sequence of indentation was recorded, and added to the original indentation value which was used to find the intrinsic Reduced Young's Modulus, for a change in Reduced Young's Modulus as a function of applied electric field over time such that,

$$E(V)^{*} = \left[\frac{3}{4\sqrt{R}}\right]\frac{F}{\sqrt[3]{\delta + \delta(V)}} \tag{6.2}$$

6.2.3. Microfabrication of passivated electrode substrate and final device assembly

A glass wafer (Corning EAGLE XG wafer 100 mm diameter x 0.5mm thick, Corning, NY) was used as the base substrate for all the subsequent microfabrication processes (**Figure 6.1**). All patterns described herein were transferred to the glass via photolithography. After developing and checking for a defect free pattern transfer, a 10 nm adhesion layer of titanium was deposited by electron beam evaporation, followed by a 90 nm thick gold layer as the final electrode. Lift-off of the metallized photoresist was conducted and checked to ensure a clean substrate, free of electrical contact between interdigitated electrodes.

For the preliminary testing of the piezoelectric response, the 15 wt.% P(VDF-TrFE) solution described in section *6.2.1.* was electrospun directly onto diced glass having a parallel electrode pattern with a separation distance between electrodes of 150 µm (Top pattern in *Masks* box of **Figure 6.1**). The fibers were anchored in the area immediately outside of the electrode pattern by UV-curable resin.

The process described from this point applies only to the optimized electrode pattern (Bottom pattern in *Masks* box of **Figure 6.1** and described in section *6.2.4*). Before depositing the biocompatible passivation layer, Parylene-C, a silanization process of 3-(Trimethoxysilyl)propyl methacrylate (A-174) was carried out on the glass/electrodes as an adhesion promoter for parylene.[23, 24] Briefly, a bath of 100:100:1 parts water:isopropanol alcohol(IPA):A-174 was prepared the day prior. After submerging the patterned wafer in the bath for 30 minutes the wafer was removed and allowed to air dry for 30 minutes. Following the initial coating, the wafer was washed of excess A-174 by submerging in pure IPA for 30 seconds with agitation. The wafer was then dried with N_2 and immediately coated with a 3 µm thick layer of Parylene C by chemical vapor deposition at room temperature to ensure a pinhole-free conformal coating. Contact pads covered by the parylene coating were exposed first by depositing a sacrificial layer of photoresist, by pattern transfer (area of contact pads did not have photoresist). The exposed parylene was etched by dry reactive etching with CH_4 gas while the rest of the device was protected from etching by the photoresist layer. After confirming the successful exposure of the contact pads, the sacrificial photoresist was washed with acetone leaving a fully passivated circular interdigitated electrode array with exposed contact pads.

To allow more space for fiber deflection, a fiber layer riser was transferred to the final electrode device. Briefly, a sacrificial layer of photoresist was spin coated on a glass wafer. A two-part polydimethylsiloxane (PDMS) was mixed at a 10:1 ratio then spin coated on top of the photoresist at 6000 rpm for 120 seconds to achieve a thickness of approximately 10 µm. Using a 6 mm biopsy punch and scalpel, the raiser was cut to accommodate the underlying electrode pattern and lifted-off by wetting the photoresist with isopropanol to achieve a riser as shown in **Figure 6.1l**.

P(VDF-TrFE) nanofibers were assembled to the microfabricated electrode device via two methods . The first was the direct collection onto the device with the PDMS riser. The second was conducted by having a wire frame collector that allowed for a collection of fibers suspended across the frame. These fibers were then transferred to the device with riser and adhered around the perimeter of the device with UV-curable resin. The two separate methods will be described in the discussion section *6.3.3*.

6.2.4. Model simulation of optimum electrode dimensions driven by design of experiment

All modeling and simulation was conducted in COMSOL Multiphysics in the AC/DC module. A schematic representation of the model is shown in **Figure 6.2**. A glass substrate of an arbitrary thickness of 1µm was used as the electrode substrate. The electrodes were modeled as empty boundaries with a thickness of 100 nm. This thickness was chosen as the minimum thickness at the beginning of saturation on a resistance versus thickness curve where a thicker electrode would lead to a minimal decrease in resistance and an increase in Joule heating due to the relationship of $P \propto I^2R$, where P is the power of heating generated by the current (I) running through a conductor of resistance (R), inversely proportionally to the cross-sectional area of the electrode. Since the analysis for optimization considers a normalization with respect to the simulated length, an arbitrary number of 8 pairs of electrodes was chosen to reduce computational time while still providing a meaningful set of data. A passivation layer of parylene was modeled as a 3 µm thick conformal film following the contours of the electrode array. A solid boundary, 10 µm thick, representing the porous piezoelectric fibrous structure with pore filled media was placed above the parylene and a separate solid boundary of an arbitrary thickness representing the pure media on top of the piezoelectric material. The interface between the porous piezoelectric material and pure media spanning 8 pairs of electrodes was used as the boundary analyzed for the generated electric field. The electrical properties of each boundary is presented in **Table 6.1**. An arbitrary 5 V was applied to the charged electrode with the other electrodes grounded; the electric field is expected to change proportionally to the applied voltage thus the chosen 5 V will not affect the optimization analysis.

The three design factors towards the optimum electrode geometry include the electrode width (EW), electrode pair separation (EPS), and electrode pair-pair separation (EPPS) (*, †, ‡, respectively in **Figure 6.2**). Three dependent, full-factorial design of experiments (DOEs) were designed around these factors with each subsequent DOE designed based on the previous' results. **Table 6.2-6.4** show the lower and upper bounds of DOE1, 2, and 3, respectively. The measured responses of all three DOEs was the absolute sum of electric field normalized to the spanning length of the assessed electrodes.

6.3 Results and discussion

6.3.1. Preliminary test of piezoelectric response based on parallel electrodes

To determine the feasibility of synthesizing mechanically active scaffolds, P(VDF-TrFE) nanofibers were electrospun on a glass substrate (**Figure 6.3a**) patterned with microfabricated parallel gold electrodes (**Figure 6.1a-f**). Voltage was applied with a step or triangle function from 0 to 70V and fiber network deflection was measured by AFM under a constant applied force of 50 nN (**Figure 6.3b**). The deflection of the nanofiber network (or AFM indentation depth change) was positively related to the applied voltage (**Figure 6.3c**), resulting in the inverse relationship (stiffness decreases as applied electric field increases) between reduced Young's modulus and applied electric field (**Figure 6.3d**) calculated from **Equation 6.2**.

Though the controllable stiffness range from approximately 85 kPa to 190 kPa is a narrower range than what we have previously reported (19 to 313 kPa) as a significant influence on enhancing iPSC differentiation efficiency,[25] these results show the potential of using piezoelectric based nanofibers as a controllable dynamic cell culture scaffold. Yet this current set up, while promising, is limited in two aspects. The first is the small effective culture area in between the electrodes (0.015 cm^2) which will prove cumbersome in obtaining quantifiable data such as gene expression. Secondly, the applied voltage used in this study fails to consider the presence of an aqueous cell culture environment. Where the electrolysis of water occurs at 1.23 V, the presence of exposed electrodes will pose both a source of direct current and an environment rich in hydrogen gas evolution to the cells in culture. Furthermore, it is expected that the dielectric difference between air and water (1 and 80, respectively) will lead to a substantial decrease in the electric field presented to the nanofibers and thus the resulting range in Young's Modulus. To address these concerns, an interdigitated radial electrode array based on the culture area of a typical 96-well culture plate well was designed and optimized through computational simulations to allow for the maximum electric field strength at a given applied voltage. Next through a more sophisticated microfabrication process, the direct exposure of electrical components of the system was passivated from an electrolytic solution to maintain a compatible cell culture environment.

6.3.2. Optimum electrode dimensions for final device

Taking guidance by the criteria set by other similar designs for piezoelectric-based macro-fiber composite actuators (MFCs),[26, 27] the basis of the first DOE design factors were of relatively large electrode widths and separations compared to the piezoelectric element thickness. In this regard, our piezoelectric sample with a thickness of approximately 10 µm sets the criteria for a EW of at most 15 µm and EPS of at least 40 µm. Due to the nature of a DOE, the appropriate trend towards an optimized geometry will be revealed as to which criteria is most vital. As the preliminary DOE, we set all design factors at the same values to accommodate the criteria of EPS since it meets the minimum value (40 µm). The normalized electric field values across the fractionated simulated region show distinct profiles for each combination of the three factors (**Figure 6.4**). As the overall electromechanical response of the piezoelectric element is proportional to the summation of active, ineffective, and transition zone, the absolute electric field summation normalized to the simulated region was used as the response for the DOE analysis. The Pareto Chart of Effects indicates that all geometrical factors are similarly responsible for the absolute electric field with the EW having a slightly smaller effect (**Figure 6.5a**). Analysis of the Main effects plot (**Figure 6.5b**), reveals that decreasing the EPS, EPPS, and EW values lead towards the greater absolute electric field.

Based on these results, the values for all factors were minimized to similar ranges based on the limiting resolution of photolithography at the research level of a 2 µm feature with the resulting normalized electric field values across the fractionated simulated region summarized in **Figure 6.6**. The Pareto Chart of Effects (**Figure 6.7a**) and the Main effects plot (**Figure 6.7b**) both reveal that EW has a significant effect on the absolute electric field at this range of geometrical parameters. However, the trend lines of EPS, EPPS, and EW in the Main effects plot show that the optimized electrode geometry now points to larger geometrical parameters.

The final DOE design parameters were chosen on two basis. First, DOE 2 showed that the EW has the greatest effect on the absolute electric field. Secondly, due to the slight vagueness between the design criteria on EW between Beckert & Kreher and Bowen et al., (i.e., EW < 1.5x Piezo thickness and EW = 0.5x Piezo thickness) we set our final DOE range from 6 to 10 µm. The EPS and EPPS were set to the same design factor range and the normalized electric field values across the fractionated simulated region determined (**Figure 6.8**). Again, the EW at this range has the greatest effect on the absolute electric field with a trend pointing towards larger values greater than 10 µm (**Figure 6.9**). The EPS and EPPS have similar yet lower significance towards the absolute electric field. However, at this range, the factor values for these two factors point towards lower values, that is, less than 6 µm.

Thus, a final parametric sweep (**Table 6.5**) based on the results accumulated from the three DOEs was conducted utilizing the Parametric Sweep function in COMSOL. From this a final electrode geometry of an EPS and EPS of 5 µm and EW of 12 µm was found to produce the largest absolute electric field normalized to the simulated length (**Figure 6.10**). Interestingly, our results do not align with those found by Bowen et al., but do however closely fall in line found by Beckert & Kreher. In the former, the finite element was modeled especially for MFCs that have two sets (top and bottom) of interdigitated electrodes for the maximum piezoelectric strain. In the latter, the modeling was reduced to half the geometry used for MFC based actuators where only one set of interdigitated electrodes is used. Moreover, the design criteria in that study was based on the three main regions that are of concern to our design, i.e., active, ineffective, and transition zones. More specifically, the optimum EW found in our analysis satisfied their criteria of EW < 1.5 Piezo thickness. No specific criteria were set for EP in their study, however, our results correlate with their discussion of minimizing the separation so that the working voltage can be reduced to produce the same electric field values.

6.3.3. Device testing and integration

The final electrode chip fabrication achieved through the microfabrication process of **Figure 6.1a-l** is shown in **Figure 6.11a** with the exposed contact pad and preservation of a complete insulation of the remaining working area shown in greater detail in **Figure 6.11b**. AFM imaging (**Figure 6.11c**) shows the conformal nature of the parylene coating by maintaining the height profile of the deposited electrodes and glass underneath (i.e., ΔHeight = 100 nm).

The passivation performance of the parylene coating was tested using a modified IV-test in which a bias was applied to the interdigitated electrodes from 0-20 V while measuring the current leakage levels in a drop of electrolyte solution deposited on top of the parylene coating the electrodes. Due to the limitation of the characterization unit, only 20 V was applied with a negligible amount of current leakage detected (< 10 nA) (**Figure 6.12a**). Utilizing a high voltage source, a breakdown voltage of approximately 300 V was detected by the direct observation of film failure (**Figure 6.12b**). As a result, a safe working voltage up to 250 V can be applied for further testing.

The working chip with the thin-film PDMS riser is shown in **Figure 6.13a;left** where the white arrows show the outline of the circular opening of the riser. With the electrospun nanofibers on the wireframe collector transferred to the assembled device (**Figure 6.13a;right**) observation under SEM of a thin scaffold (**Figure 6.13b**) shows the successful suspension of the fibers due the PDMS riser. The same observation is not possible with a thicker scaffold (**Figure 6.13c**) but due to the technique of assembling the scaffold to the final device assembly, we have no reason to believe that the fibers do not remain suspended across the entire span of the electrodes. As confirmation, height probing of the surface of the fiber mat along the length of the riser (with the fibers in contact with the PDMS as our reference point) we noticed a height difference between fibers that were electrospun directly onto the device chip with the riser, method 1, versus the fiber transfer, method 2 (**Figure 6.13d**). Since the height profiling was conducted by AFM cantilever approach and detect at each point, the slightly erratic positive values for method 2 may be due to the attractive forces between the fibers and approaching cantilever. Another explanation is that the arbitrary height differences are in line with that of the opposite side of the PDMS riser (last point) which may be due to probing of the cantilever of regions with more or less fiber density. However, the patterned dip of height values for method 1 show that the fibers collected in this manner were in intimate contact (center point) with the parylene surface, thus indicating a non-suspended scaffold.

The final device assembly was tested under AFM to detect the piezoelectric response of the P(VDF-TrFE) nanofibers in aqueous conditions at 37 °C. The raw data of measured indentation over time in response to an applied voltage shows a magnitude dependent response (**Figure 6.14a**) similar to that observed of the preliminary testing. The processed indentation versus applied voltage (**Figure 6.14b**) was applied to **Equation 6.2** to yield the resulting change in Reduced Young's Modulus as a function of applied voltage (**Figure 6.14c**). The electrode device was able to generate a range of Reduced Young's Modulus of 60-170 kPa, a slightly larger range than the preliminary data which tested parallel electrodes in air. As mentioned before, a target Modulus range of 19-313 kPa allows for significant differences in the differentiation efficiency with regard to gene and protein expression analysis. The starting Young's Modulus of 170 kPa presented in this work may still have the same implications for gene expression as from our previous study since there was a significant difference in fold change for both mesendodermal and ectodermal genes between the 20 and 190 kPa scaffolds and within error in fold change between 190 and 313 kPa. Protein expression at the 19-190 kPa range was also qualitatively different for both lineages, though the expression or absence of the mesendo- and ecto-dermal markers, respectively, for the 313 kPa scaffold was more apparent. Although the applied voltage difference between the preliminary study and optimized study presented here is significant (250 V compared to 70 V), the effective passivation of electrical charge from the aqueous environment should protect the cell culture from ionic flow and hydrogen gas evolution. To at least achieve the required 90% decrease in Modulus (190 to 19 kPa) a remaining 25% decrease (60 to 17 kPa) must still be realized by the piezoelectric scaffold. Future directions can implement a couple of solutions to achieve this goal. First, though we limited our applied voltage to 250 V, a thicker parylene coating may allow the working voltage to be increased above the current limitation of 300 V. Furthermore, the PDMS riser can be reduced to lower the fibers closer to a stronger electric field which is present closer to the electrodes. Since the indentation values are in the range of hundreds of nanometers, a PDMS thin-film less than the 10 μm film used in this work can still achieve the effect we proposed.

6.4 Conclusion

In summary, motivated by our previous work which showed the influence of distinct mechanical properties of the mechanical microenvironment on iPSC differentiation efficiency, we designed a mechanically dynamic scaffold based on piezoelectric P(VDF-TrFE). We first showed the feasibility of using P(VDF-TrFE) as the dynamic scaffold material. Due to the extreme limitations on the preliminary testing, we designed an optimal electrode pattern by way of DOE analysis using computer simulation. The pattern was microfabricated and successfully passivated with biocompatible parylene coating. The change in the mechanical properties due to the indirect piezoelectric response of the P(VDF-TrFE) scaffolds in physiological conditions showed a working range of 60-170 kPa. This range may provide insight to the feasibility of using such dynamic scaffold for enhancing applications of stem cells, yet further optimization is required for truly significant results.

6.5 Tables and figures

Table 6.1 Dielectric constant of boundaries used in the design of optimal electrode geometry by computer simulation.

Material layer	Dielectric constant
Glass	3.80
Parylene	3.15
Porous piezoelectric	62.00
Media	81.00

Table 6.2 Design of experiment #1.

Design factors and values used to guide towards the optimum electrode parameters for the highest electric field at a fixed voltage.

Run number	Code	Pair-to-pair separation (μm)	Pair separation (μm)	Electrode width (μm)
1	(- - -)	20	20	20
2	(- - +)	20	20	50
3	(- + -)	20	50	20
4	(- + +)	20	50	50
5	(+ - -)	50	20	20
6	(+ - +)	50	20	50
7	(+ + -)	50	50	20
8	(+ + +)	50	50	50

Table 6.3 Design of experiment #2.

Adjusted design factors and values, based on results from DOE #1, used to guide towards the optimum electrode parameters for the highest electric field at a fixed voltage.

Run number	Code	Pair-to-pair separation (µm)	Pair separation (µm)	Electrode width (µm)
1	(- - -)	2	2	2
2	(- - +)	2	2	5
3	(- + -)	2	5	2
4	(- + +)	2	5	5
5	(+ - -)	5	2	2
6	(+ - +)	5	2	5
7	(+ + -)	5	5	2
8	(+ + +)	5	5	5

Table 6.4 Design of experiment #3.

Adjusted design factors and values, based on results from DOE #2, used to guide towards the optimum electrode parameters for the highest electric field at a fixed voltage.

Run number	Code	Pair-to-pair separation (µm)	Pair separation (µm)	Electrode width (µm)
1	(- - -)	6	6	6
2	(- - +)	6	6	10
3	(- + -)	6	10	6
4	(- + +)	6	10	10
5	(+ - -)	10	6	6
6	(+ - +)	10	6	10
7	(+ + -)	10	10	6
8	(+ + +)	10	10	10

Table 6.5 Fine parametric sweep.

Values of design factors used for the COMSOL parametric sweep. The boundaries of the parameters are set as starting value: increment value: ending value.

	Pair-to-pair separation (µm)	**Pair separation (µm)**	**Electrode width (µm)**
Fine parametric sweep	2:1:6	2:1:6	6:1.6:20

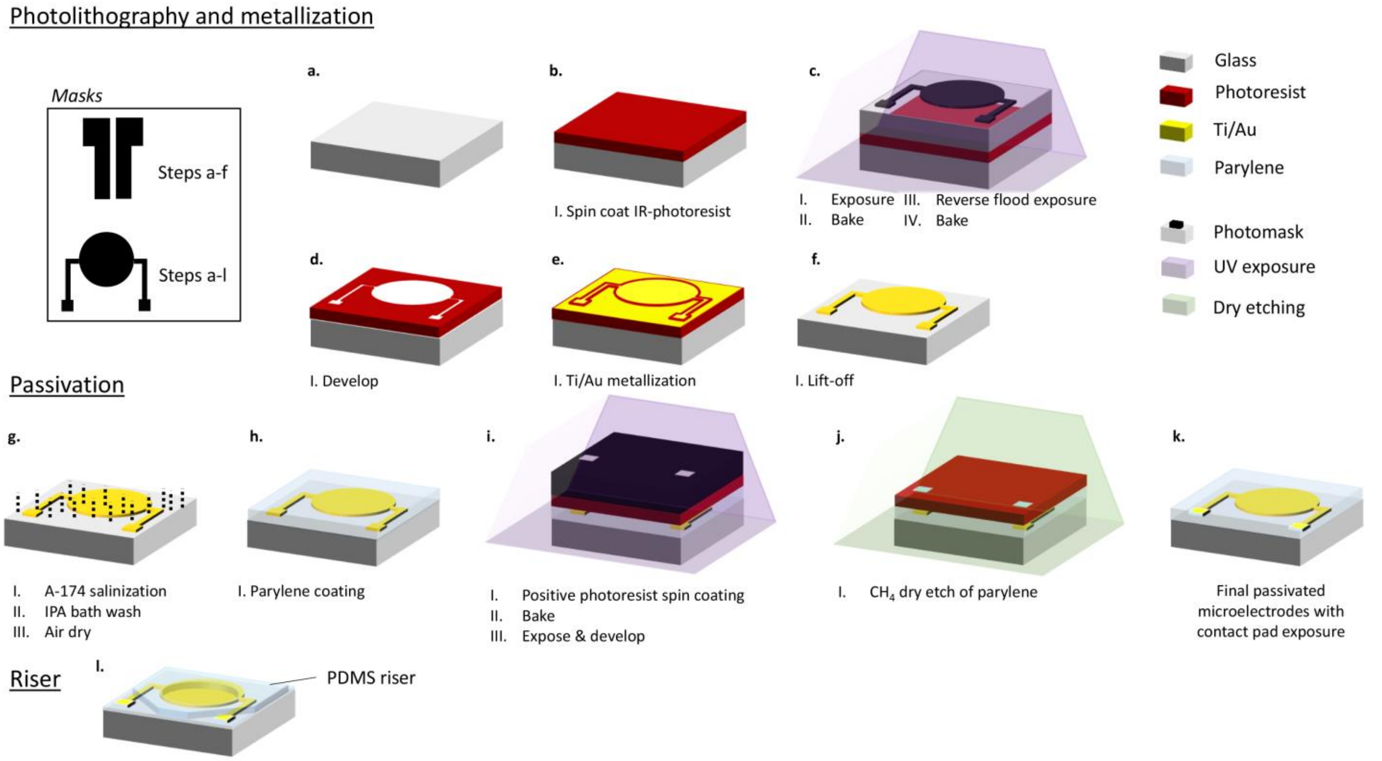

Figure 6.1 Microfabrication schematic of fully passivated microelectrodes.
Photolithography was conducted on (a) a glass substrate by (b) spin coating an image reversal resist and conducting the proper (c) exposure and (d) development. (e) Metallization of the exposed glass substrate was conducted by e-beam evaporation and the final electrode was presented after (f) lift-off. Passivation was achieved by (g) A-174 salinization as an adhesion promoter for the conformal coating of parylene (h). Contact pad exposure consisted of (i) photoresist protection and subsequent (j) dry etch of the exposed parylene above the contact pads. (k) The final passivated microelectrodes with exposed contact pads. (l) Thin-film PDMS riser used to suspend P(VDF-TrFE) nanofibers across

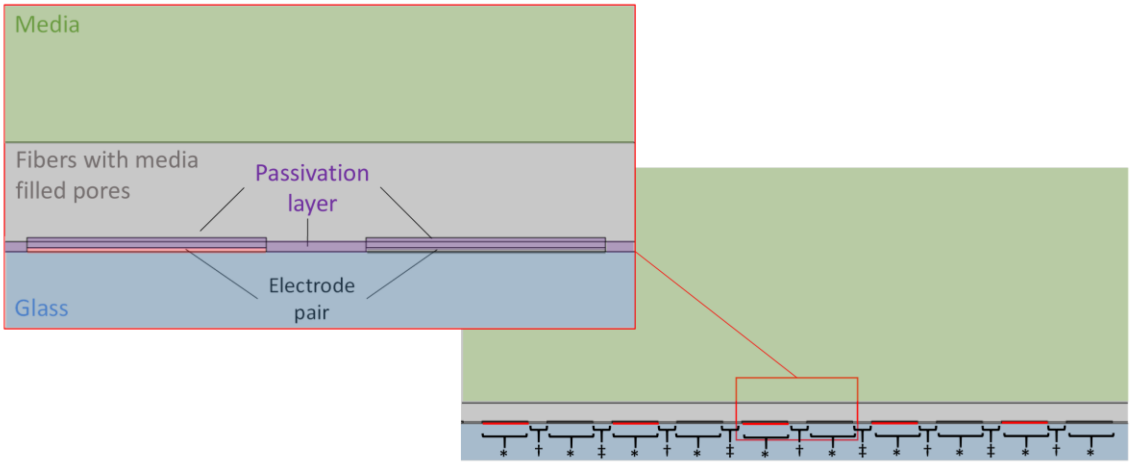

Figure 6.2 Schematic of geometrical domains for maximal electric field generation.

COMSOL domain modeling consists of a glass substrate, electrodes, passivation layer, media filled porous piezoelectric fibers, and media. The design factors towards optimizing the electric field include electrode width (*), electrode pair separation (†), and electrode pair-pair separation (‡).

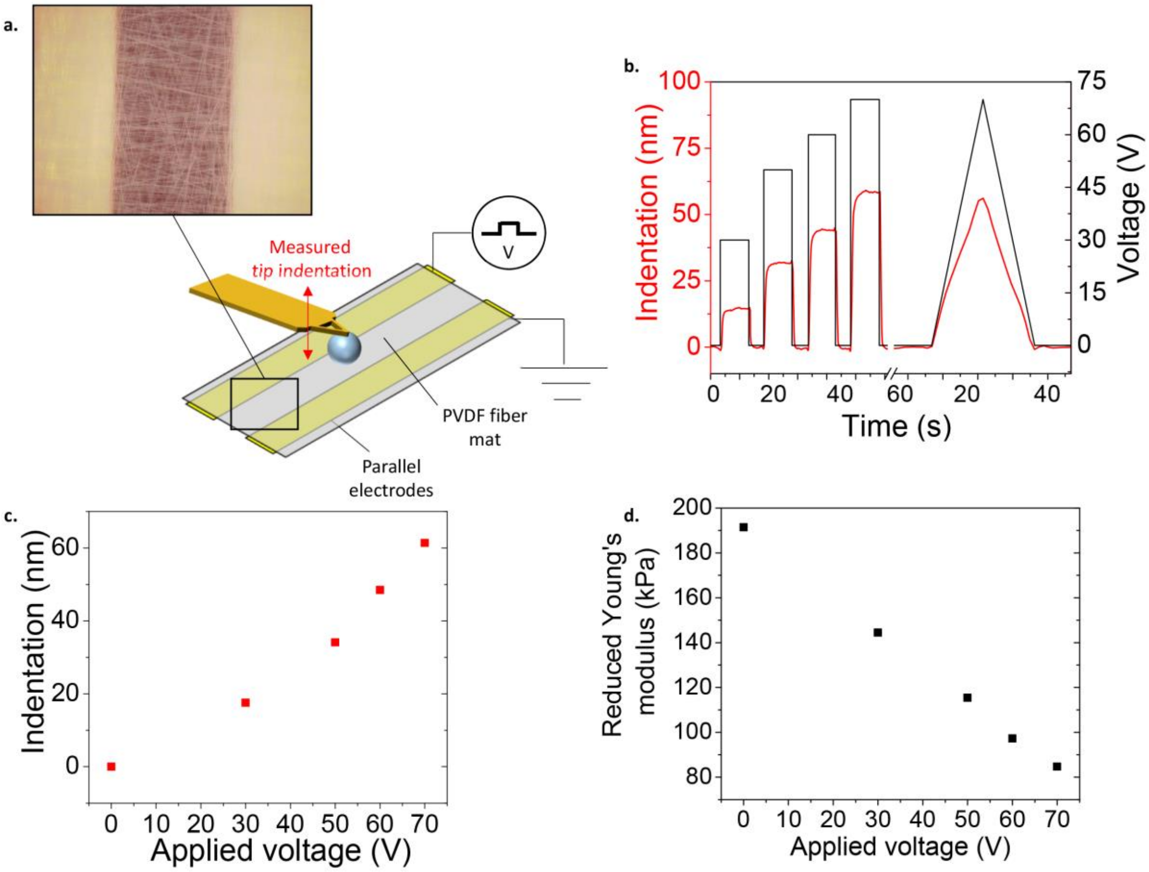

Figure 6.3 Piezoelectric responses of electrospun P(VDF-TrFE) nanofibers to applied voltages.

(a) An optical image of the P(VDF-TrFE) nanofibers on top of parallel gold electrodes and schematic of AFM testing of piezoelectric response. (b) Fiber deflection measured by AFM, under different amplitudes of voltage applied across the electrodes. (c & d) Indentation and stiffness of the fibers versus applied voltage plots derived from (b) showing a linear relationship between scaffold stiffness and applied electric field

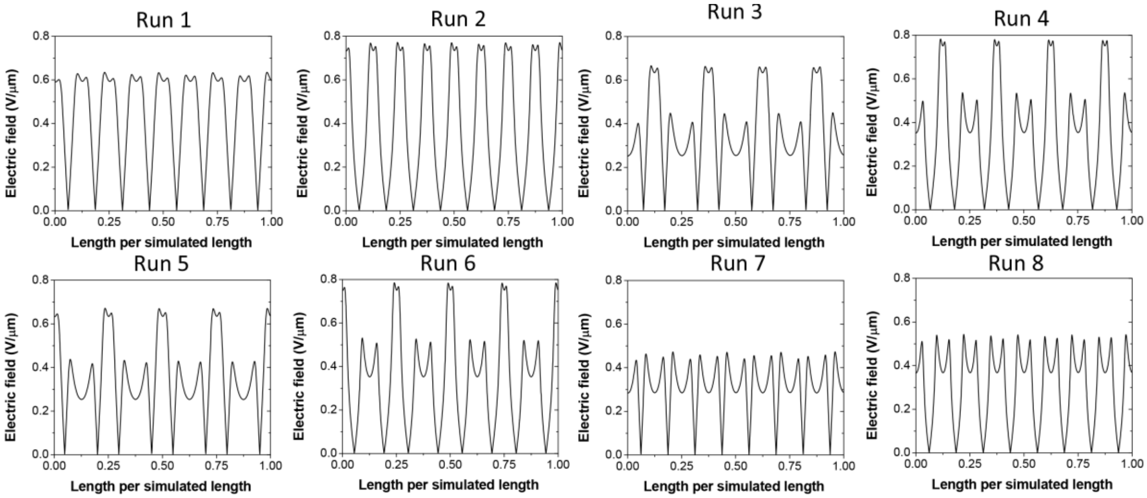

Figure 6.4 Absolute electric field strength for design runs in Table 6.1.

The electric field strength values are taken from the top surface of the fiber domain along the region of simulated length spanning across four pairs of electrodes.

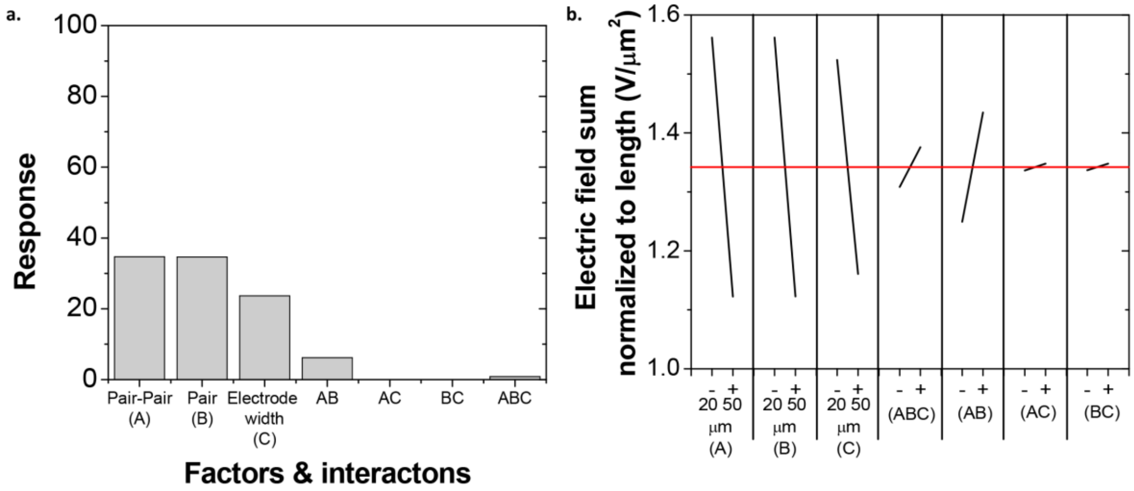

Figure 6.5 Design of experiment #1 factor analysis on electric field strength.

(a) Factor influence on electric field strength shows that pair-pair (A) and pair separation (B) have equal influence on the electric field generated, with electrode width the least influence of the three factors. The interaction between (A) and (B) (i.e., (AB)) has a slight influence on electric field while all other interactions are negligible. (b) Trend effect of the design factors on electric field strength indicates that a smaller (20 µm) electrode pair-pair and pair separation has the largest effect (magnitude of trend line) towards maximizing the strength of the electric field. A narrower electrode also has the same trend but to a lesser magnitude effect.

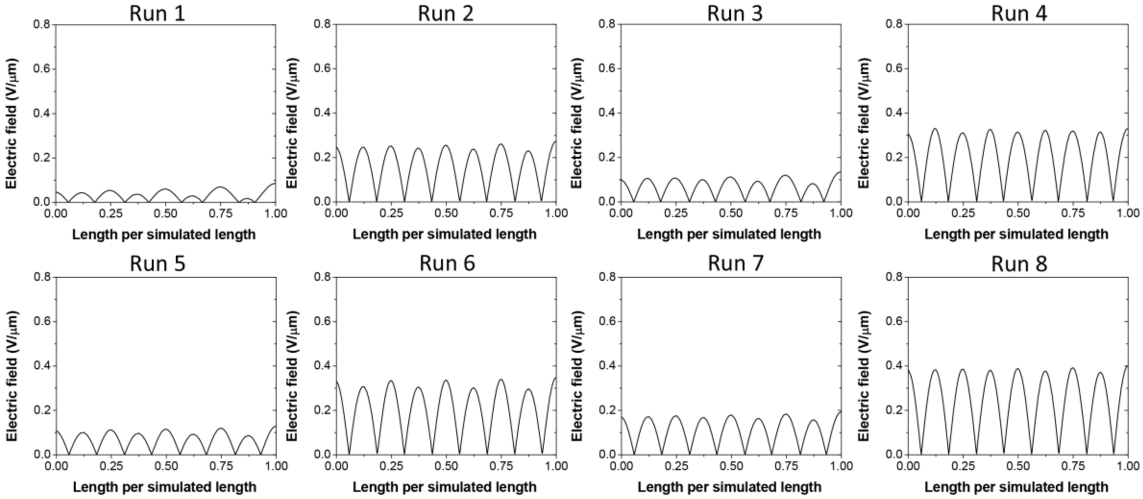

Figure 6.6 Absolute electric field strength for design runs in Table 6.2.

The electric field strength values at the top surface of the fiber domain along the region of simulated length spanning across four pairs of electrodes.

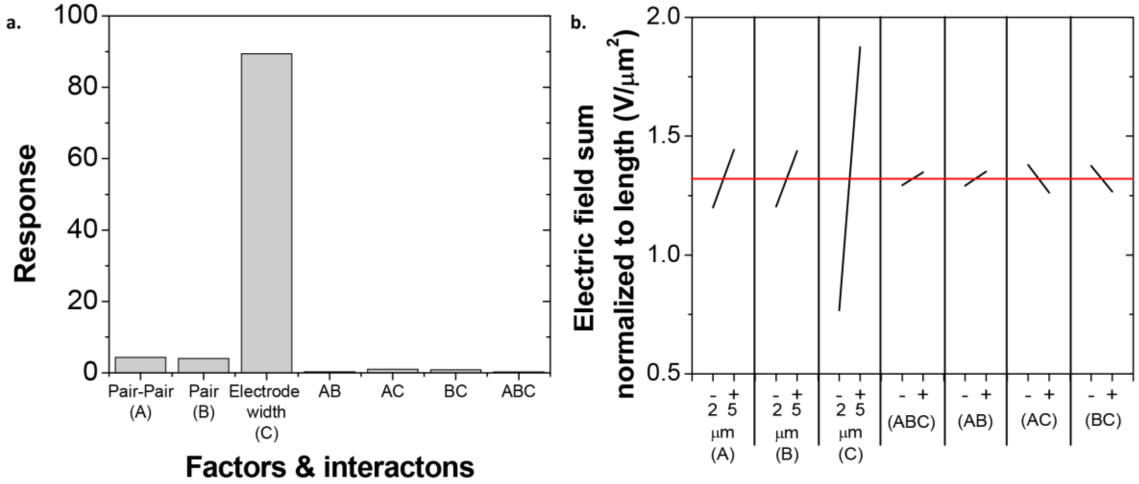

Figure 6.7 Design of experiment #2 factor analysis on electric field strength.

(a) Factor influence on electric field strength shows that electrode width at this design range has the largest influence of the three factors at ~90 %. (b) Trend effect of the design factors on electric field strength indicates that a wider (5 μm) electrode width has the largest effect (magnitude of trend line) towards maximizing the strength of the electric field. Larger electrode separations as this design range also has the same trend but to a significantly lesser magnitude.

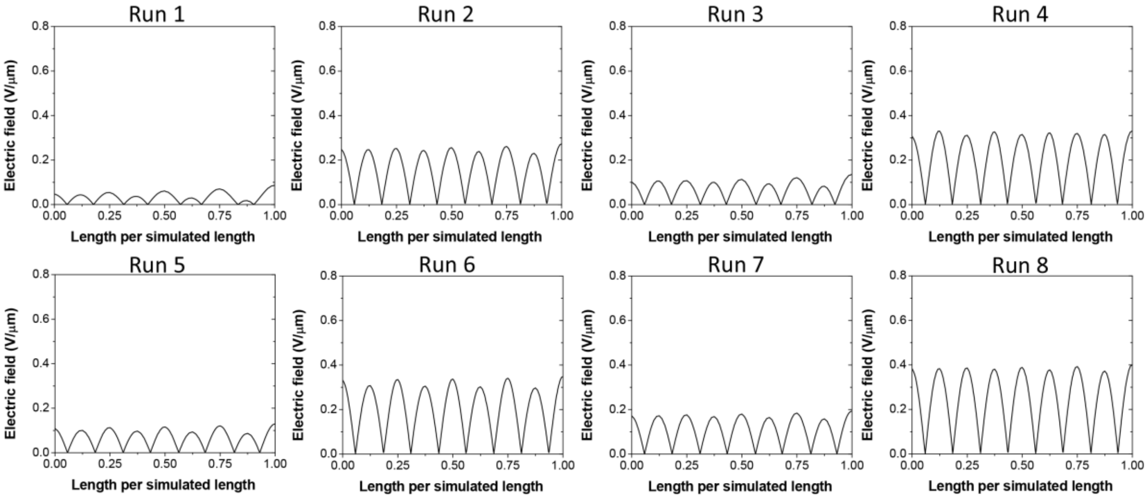

Figure 6.8 Absolute electric field strength for design runs in Table 6.3.

The electric field strength values at the top surface of the fiber domain along the region of simulated length spanning across four pairs of electrodes.

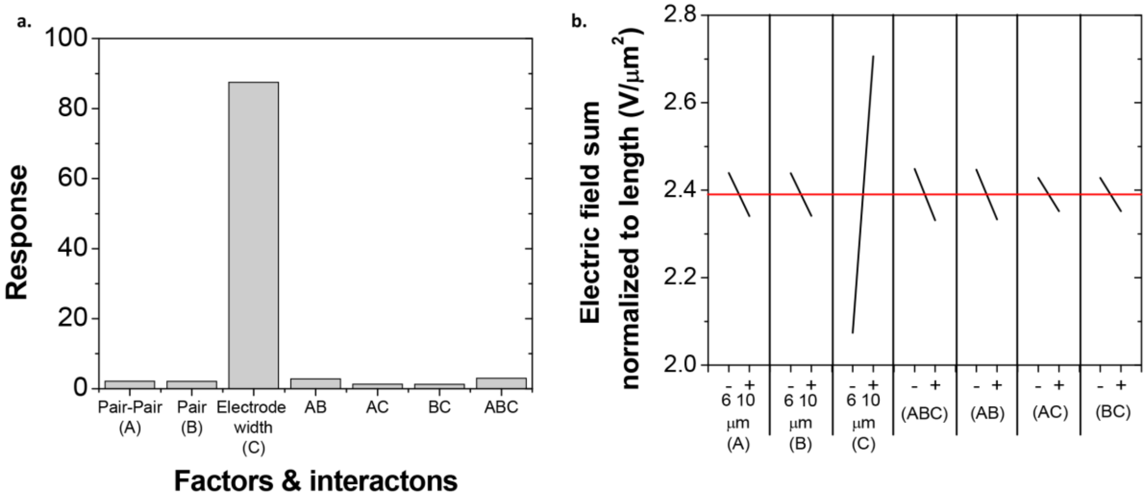

Figure 6.9 Design of experiment #3 factor analysis on electric field strength.

(a) Factor influence on electric field strength shows that electrode width at this final design range has the largest influence of the three factors at ~87 %. (b) Trend effect of the design factors on electric field strength indicates that a wider (10 μm) electrode width has the largest effect (magnitude of trend line) towards maximizing the strength of the electric field. Smaller electrode separations, towards 6 μm reveal the opposite trend from electrode width to a lesser magnitude.

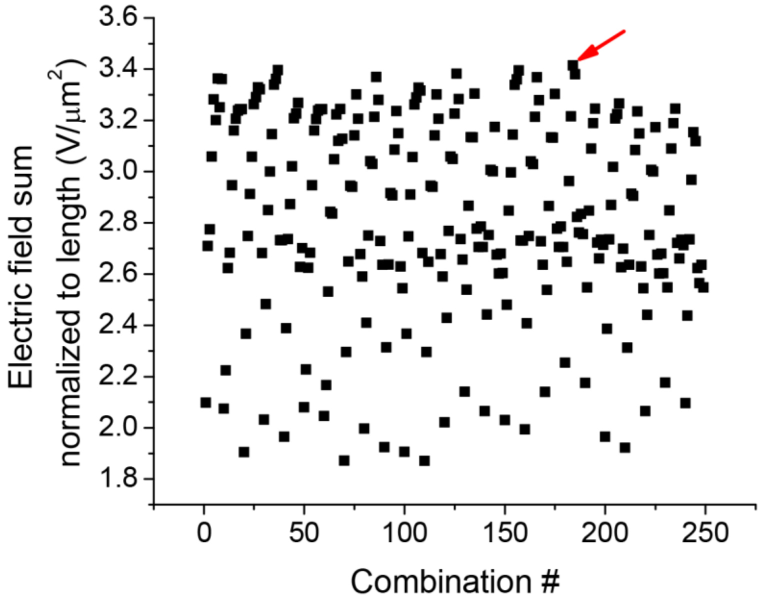

Figure 6.10 Fine parametric sweep of electrode design factors for maximum electric field strength.

All possible combinations of design factors of electrode pair-pair and pair separation both between 2-6 µm (increments of 1µm) and an electrode width between 6-20 µm (increments of 1.6 µm) were simulated to reveal the optimized electrode geometrical design of an electrode pair-pair and pair separation of 5 µm and an electrode width of ~12.2 µm (data point indicated by red arrow).

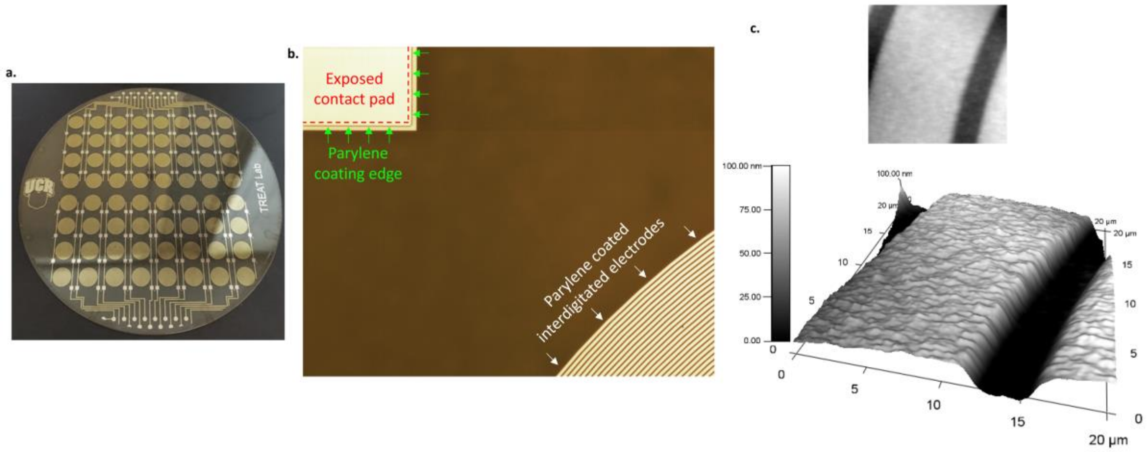

Figure 6.11 Passivated electrode device.

(a) An optical image of glass wafer having the patterned circular interdigitated electrodes that are able to be diced into individual chips or used as a whole for a 96-well culture plate. (b). High magnification optical image showing the exposed contact pad and full passivation of electrodes with parylene. (c) AFM topographical image showing the conformal coating of the parylene on the interdigitated electrodes.

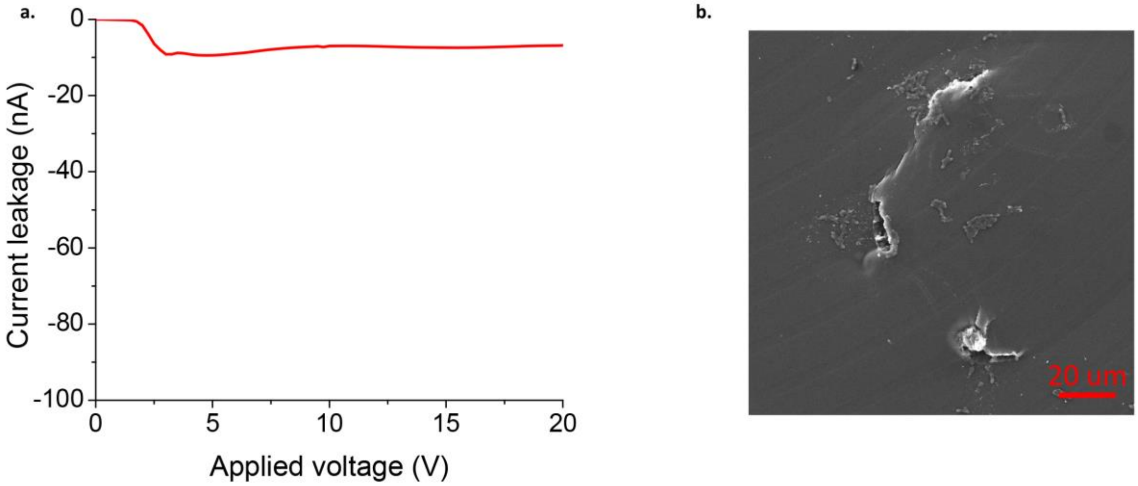

Figure 6.12 Passivation testing of parylene coating.

(a) Leakage current testing of parylene coating from 0-20 V with negligible current (<10 nA). (b) SEM of film failure after exposure to 300 V applied across the interdigitated electrodes.

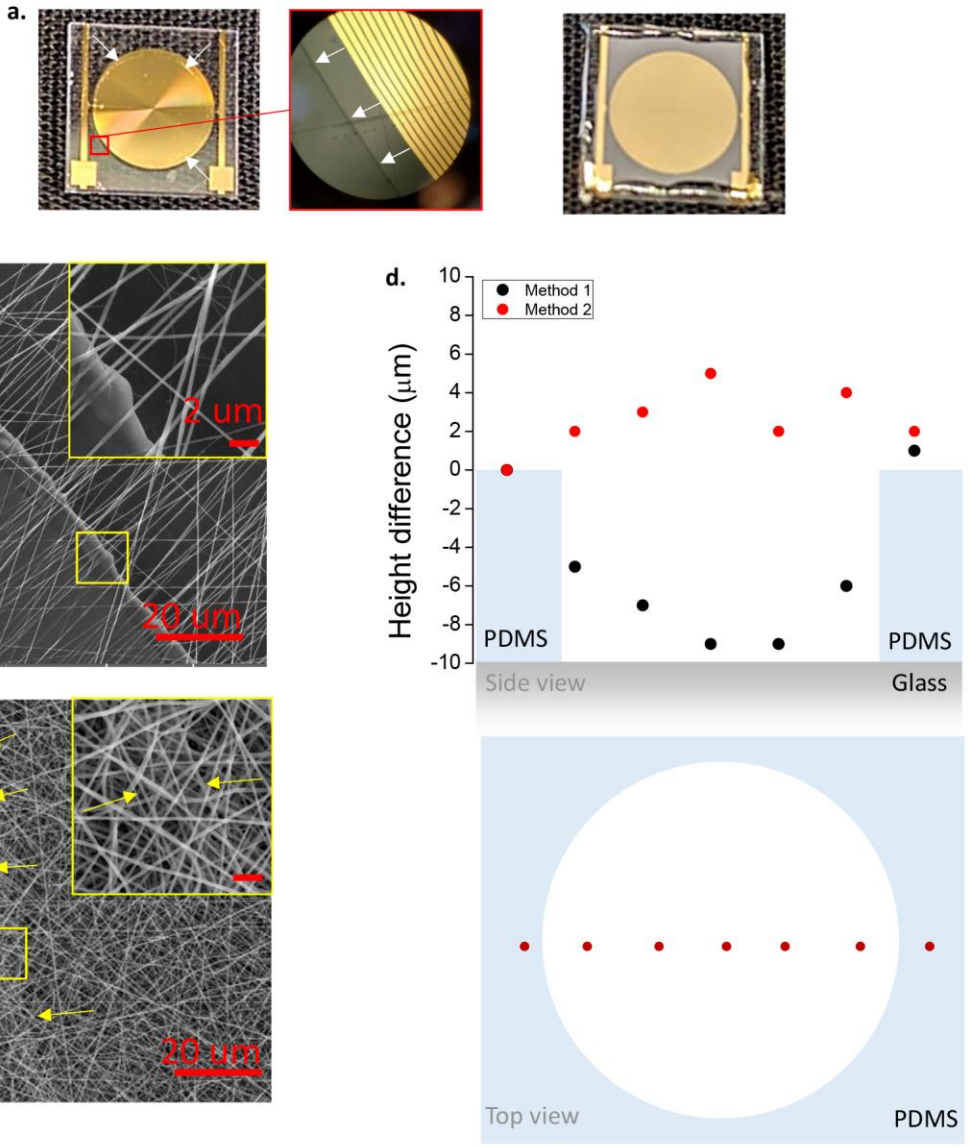

Figure 6.13 Assembly of electrospun piezoelectric scaffold on electrode device.

Optical images of PDMS riser on microelectrode pattern (a;left) without and (a;right) with nanofibers. White arrows in (a;left) show the PDMS riser border around the circumference of the microelectrode working area. SEM showing a thin (b) and thick (c) scaffold adhered to the device and suspended on PDMS riser; yellow arrows show trace of the PDMS riser is located. (d) Height difference comparison of the top layer of the P(VDF-TrFE) scaffold across the PDMS riser between method 1 of direct electrospinning onto the electrode device and method 2 of fiber transfer to the electrode device.

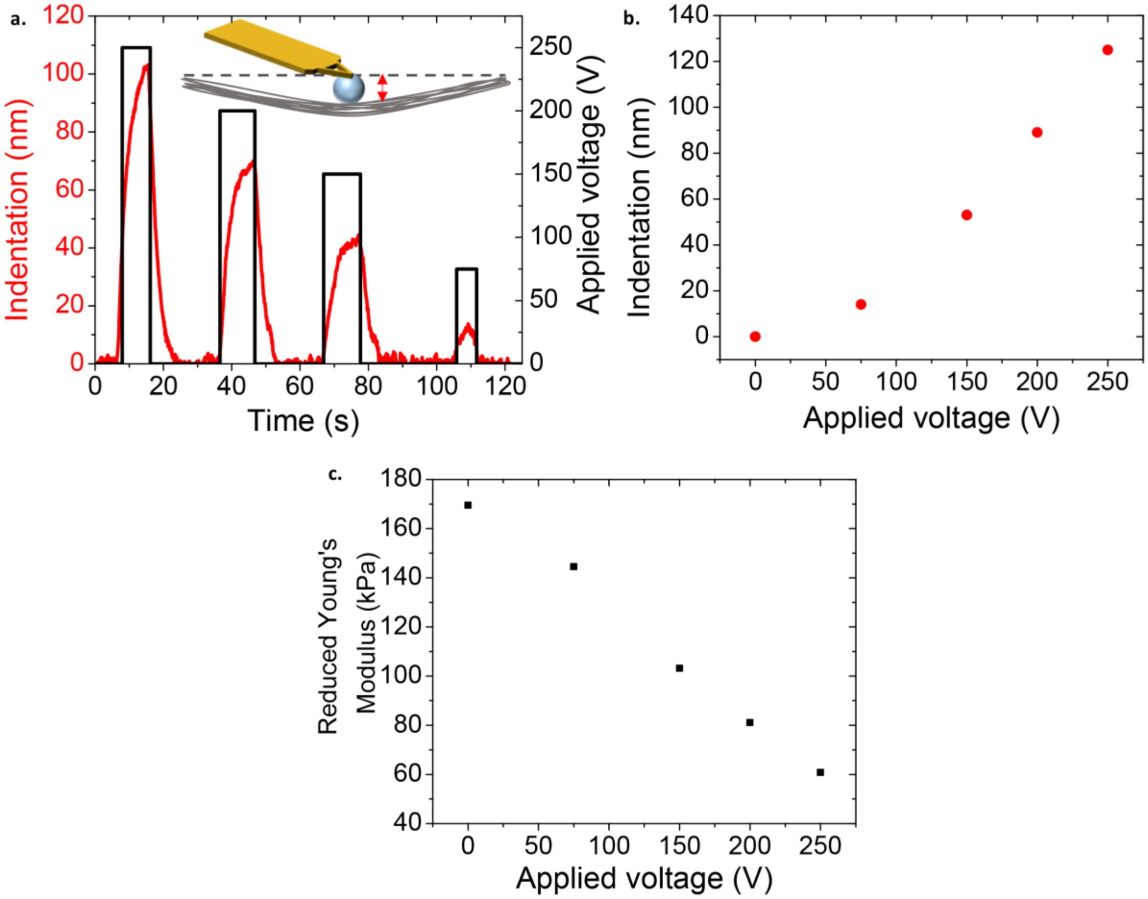

Figure 6.14 Electromechanical response with applied voltage of P(VDF-TrFE) measured by AFM and correlated to Reduced Young's Modulus.

(a) AFM tip indentation over time driven by an applied voltage from 250-0 V, correlated to the electromechanical response of P(VDF-TrFE) nanofibers; inset shows a schematic of the indentation response (red arrow) with an applied voltage. (b) Indentation vs voltage trend showing a direct correlation. (c) Reduced Young's Modulus versus voltage calculated by **Equation 6.2**.

6.6 References

[1] K. Takahashi, S. Yamanaka. *Induction of pluripotent stem cells from mouse embryonic and adult fibroblast cultures by defined factors*. cell 2006, 126, 663.

[2] K. Okita, T. Ichisaka, S. Yamanaka. *Generation of germline-competent induced pluripotent stem cells*. nature 2007, 448, 313.

[3] H. Hentze, P. L. Soong, S. T. Wang, B. W. Phillips, T. C. Putti, N. R. Dunn. *Teratoma formation by human embryonic stem cells: evaluation of essential parameters for future safety studies*. Stem cell research 2009, 2, 198.

[4] B. O. Diekman, N. Christoforou, V. P. Willard, H. Sun, J. Sanchez-Adams, K. W. Leong, F. Guilak. *Cartilage tissue engineering using differentiated and purified induced pluripotent stem cells*. Proceedings of the National Academy of Sciences 2012, 201210422.

[5] A. Suzuki, A. Iwama, H. Miyashita, H. Nakauchi, H. Taniguchi. *Role for growth factors and extracellular matrix in controlling differentiation of prospectively isolated hepatic stem cells*. Development 2003, 130, 2513.

[6] R. A. Oldershaw, M. A. Baxter, E. T. Lowe, N. Bates, L. M. Grady, F. Soncin, D. R. Brison, T. E. Hardingham, S. J. Kimber. *Directed differentiation of human embryonic stem cells toward chondrocytes*. Nature biotechnology 2010, 28, 1187.

[7] M. Schuldiner, O. Yanuka, J. Itskovitz-Eldor, D. A. Melton, N. Benvenisty. *Effects of eight growth factors on the differentiation of cells derived from human embryonic stem cells*. Proceedings of the National Academy of Sciences 2000, 97, 11307.

[8] A. J. Engler, S. Sen, H. L. Sweeney, D. E. Discher. *Matrix elasticity directs stem cell lineage specification*. cell 2006, 126, 677.

[9] J. Nam, J. Johnson, J. J. Lannutti, S. Agarwal. *Modulation of embryonic mesenchymal progenitor cell differentiation via control over pure mechanical modulus in electrospun nanofibers*. Acta biomaterialia 2011, 7, 1516.

[10] N. Huebsch, P. R. Arany, A. S. Mao, D. Shvartsman, O. A. Ali, S. A. Bencherif, J. Rivera-Feliciano, D. J. Mooney. *Harnessing traction-mediated manipulation of the cell/matrix interface to control stem-cell fate*. Nature materials 2010, 9, 518.

[11] K. A. Kilian, B. Bugarija, B. T. Lahn, M. Mrksich. *Geometric cues for directing the differentiation of mesenchymal stem cells*. Proceedings of the National Academy of Sciences 2010.

[12] M. Maldonado, L. Y. Wong, C. Echeverria, G. Ico, K. Low, T. Fujimoto, J. K. Johnson, J. Nam. *The effects of electrospun substrate-mediated cell colony morphology on the self-renewal of human induced pluripotent stem cells*. Biomaterials 2015, 50, 10.

[13] L. Ji, V. L. LaPointe, N. D. Evans, M. M. Stevens. *Changes in embryonic stem cell colony morphology and early differentiation markers driven by colloidal crystal topographical cues*. Eur Cell Mater 2012, 23, 135.

[14] G. Ico, A. Showalter, W. Bosze, S. C. Gott, B. S. Kim, M. P. Rao, N. V. Myung, J. Nam. *Size-dependent piezoelectric and mechanical properties of electrospun P (VDF-TrFE) nanofibers for enhanced energy harvesting*. Journal of Materials Chemistry A 2016, 4, 2293.

[15] G. Ico, A. Myung, B. S. Kim, N. V. Myung, J. Nam. *Transformative piezoelectric enhancement of P (VDF-TrFE) synergistically driven by nanoscale dimensional reduction and thermal treatment*. Nanoscale 2018, 10, 2894.

[16] R. Vasita, D. S. Katti. *Nanofibers and their applications in tissue engineering*. International Journal of nanomedicine 2006, 1, 15.

[17] X. Wang, B. Ding, B. Li. *Biomimetic electrospun nanofibrous structures for tissue engineering*. Materials today 2013, 16, 229.

[18] J. Chang, M. Dommer, C. Chang, L. Lin. *Piezoelectric nanofibers for energy scavenging applications*. Nano Energy 2012, 1, 356.

[19] J. Pu, X. Yan, Y. Jiang, C. Chang, L. Lin. *Piezoelectric actuation of direct-write electrospun fibers*. Sensors and Actuators A: Physical 2010, 164, 131.

[20] A. Baji, Y.-W. Mai, Q. Li, Y. Liu. *Electrospinning induced ferroelectricity in poly (vinylidene fluoride) fibers*. Nanoscale 2011, 3, 3068.

[21] N. Weber, Y. S. Lee, S. Shanmugasundaram, M. Jaffe, T. L. Arinzeh. *Characterization and in vitro cytocompatibility of piezoelectric electrospun scaffolds*. Acta biomaterialia 2010, 6, 3550.

[22] R. Costa, C. Ribeiro, A. C. Lopes, P. Martins, V. Sencadas, R. Soares, S. Lanceros-Méndez. *Osteoblast, fibroblast and in vivo biological response to poly (vinylidene fluoride) based composite materials*. Journal of Materials Science: Materials in Medicine 2013, 24, 395.

[23] J. Gao, T. Chen, C. Dong, Y. Jia, P.-I. Mak, M.-I. Vai, R. P. Martins. *Adhesion promoter for a multi-dielectric-layer on a digital microfluidic chip*. RSC Advances 2015, 5, 48626.

[24] J.-M. Hsu, S. Kammer, E. Jung, L. Rieth, R. A. Normann, F. Solzbacher, "Characterization of Parylene-C film as an encapsulation material for neural interface devices", 2007.

[25] M. Maldonado, G. Ico, K. Low, R. J. Luu, J. Nam. *Enhanced Lineage-Specific Differentiation Efficiency of Human Induced Pluripotent Stem Cells by Engineering Colony Dimensionality Using Electrospun Scaffolds*. Advanced healthcare materials 2016, 5, 1408.

[26] W. Beckert, W. S. Kreher. *Modelling piezoelectric modules with interdigitated electrode structures*. Computational Materials Science 2003, 26, 36.

[27] C. R. Bowen, L. J. Nelson, R. Stevens, M. G. Cain, M. Stewart. *Optimisation of interdigitated electrodes for piezoelectric actuators and active fibre composites*. Journal of Electroceramics 2006, 16, 263.

[28] M. J. Nalbandian, M. Zhang, J. Sanchez, Y.-H. Choa, D. M. Cwiertny, N. V. Myung. *Synthesis and optimization of BiVO 4 and co-catalyzed BiVO 4 nanofibers for visible light-activated photocatalytic degradation of aquatic micropollutants*. Journal of Molecular Catalysis A: Chemical 2015, 404, 18.

[29] C. J. Luo, E. Stride, M. Edirisinghe. *Mapping the influence of solubility and dielectric constant on electrospinning polycaprolactone solutions*. Macromolecules 2012, 45, 4669.

[30] C. M. Hansen, *Hansen solubility parameters: a user's handbook*, CRC press, 2007.

7. Conclusion

The aim of this work was to develop and utilize piezoelectric scaffold systems to modulate the physical and/or chemical microenvironment of cells to enhance cellular and regenerative behaviors. The appearance of piezoelectricity or phenomena associated with it (e.g., electrical stimulation) was the motivating factor for the work presented in this dissertation which utilized engineered piezoelectric P(VDF-TrFE) scaffolds for various applications. More specifically, the fundamental properties influencing the piezoelectric performance of electrospun P(VDF-TrFE) fibers were varied by electrospinning fibers at various diameters. We found that above 100 nm in fiber diameter, the electroactive phase content and degree of crystallinity were correlated to the piezoelectric coefficient, d_{33}. At a smaller scale (30 nm) the observed transformative enhancement of d_{33} was governed by the synergistic effects of flexoelectricity and preferential domain alignment due to the synthesis of the material at this scale and a proper thermal treatment, respectively. With these methods of tuning the piezoelectric properties, scaffolds or membranes were tailored for specific applications. One application shown was the acoustic-stimulus responsive piezoelectric membrane for a controlled delivery system. In this system, the amount of drug released was shown to be controllable by utilizing different fiber diameters, adjusting the strength of the applied acoustic stimulation, or changing the dosage number of applied stimulation. The feasibility of this system was exemplified in an *in vivo* model of a rat carcass for superficial- and deep-tissue applications. The second application consisted of utilizing aligned scaffolds, composed of approximately 500 nm in diameter P(VDF-TrFE), in conjunction with a custom-made piezoelectric culture chamber to serve as a culture system for mouse neural stem cells (NSCs). Specifically, the differentiation capacity of NSCs towards neuron, oligodendrocyte, or astrocyte cell types was enhanced on actuated piezoelectric scaffolds delivering an electrical stimulation to the cells. The implication for this study is the ability to differentiate NSCs towards the three main neuronal cell types as a co-culture by utilizing actuated piezoelectric scaffolds for disease *in vitro* models. The final application shown was the development of a culture system consisting of P(VDF-TrFE) nanofibers with the ability to change the stiffness of the cellular microenvironment on-demand. For this, interdigitated microelectrodes were designed and microfabricated to serve as the source of external electric field driving the indirect piezoelectric effect on the P(VDF-TrFE) scaffold. The achievable range of stiffness change was in a range previously shown to have some effect on the differentiation efficiency of induced pluripotent stem cells, however, further optimization for this system is needed for truly significant results.

Through the exemplified applications presented in this dissertation the technologies expandability has been demonstrated. In regard to these examples, the future direction for the drug delivery system would be to first devise a cell-culture experiment utilizing the membranes as molecule loaded scaffolds. Similar to the way the scaffold were stimulated for the NSC differentiation application, the use of these membranes to both release and stimulate cells in culture is an attractive combination for either neuronal cells or bone forming cells since bone has been shown to be piezoelectric in nature. Moreover, surface functionalization of the negative zeta potential membrane to transform it into a positive surface will allow for the use of anionic drug molecules. Exploring the release kinetics and their dependence on stimulation frequency and profile will also prove useful for further developing a fully tunable drug delivery system. For the NSC differentiation application, a longer culture period of applied stimulation is necessary to study the development of the cells to a nerve tissue-like model. Moreover, the use of this scaffold has been proposed to be used as a nerve guiding conduit for nerve regeneration. Finally, as mentioned, the dynamic-stiffness scaffold application needs further optimization to find the appropriate processing conditions to increase the range of achievable change in stiffness. Moreover, the studies driving the basis of this application may not be of the optimum range as well. Thus, exploring different ranges of stiffness may prove this application to be worthy as it has been presented in this dissertation. Thus, the future directions are manifold regarding the way this system may be used for other bioengineering applications.

APPENDIX A. SUPPLEMENTARY INFORMATION: Size-dependent piezoelectric and mechanical properties of electrospun P(VDF-TrFE) nanofibers

A.1 Figures

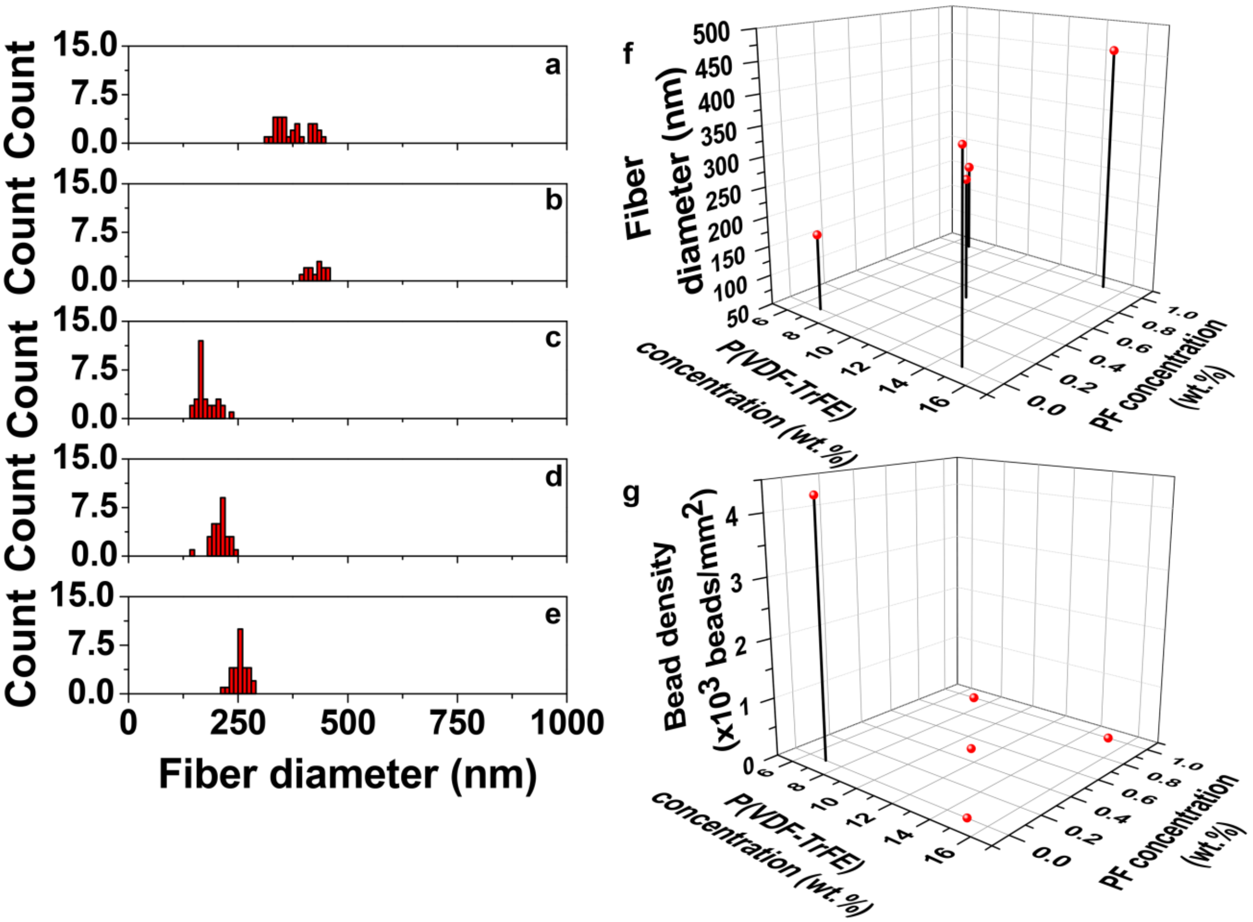

Figure App.A1. Fiber diameter and bead density with respect to design parameters. Resulting fiber diameter distribution of DOE1: 15 wt.% P(VDF-TrFE) solution with 0 wt.% (a) and 1 wt.% (b) PF, 7 wt.% P(VDF-TrFE) solution with 0 wt.% (c) and 1 wt.% (d) PF, and midpoint 11 wt.% P(VDF-TrFE) solution with 0.5 wt.% PF(e). Fiber diameter (f) and bead density (g) vs design parameters, P(VDF-TrFE(concentration (15,11, and 7 wt.%) and PF concentration (0, 0.5, and 1 wt.%) (n=30).

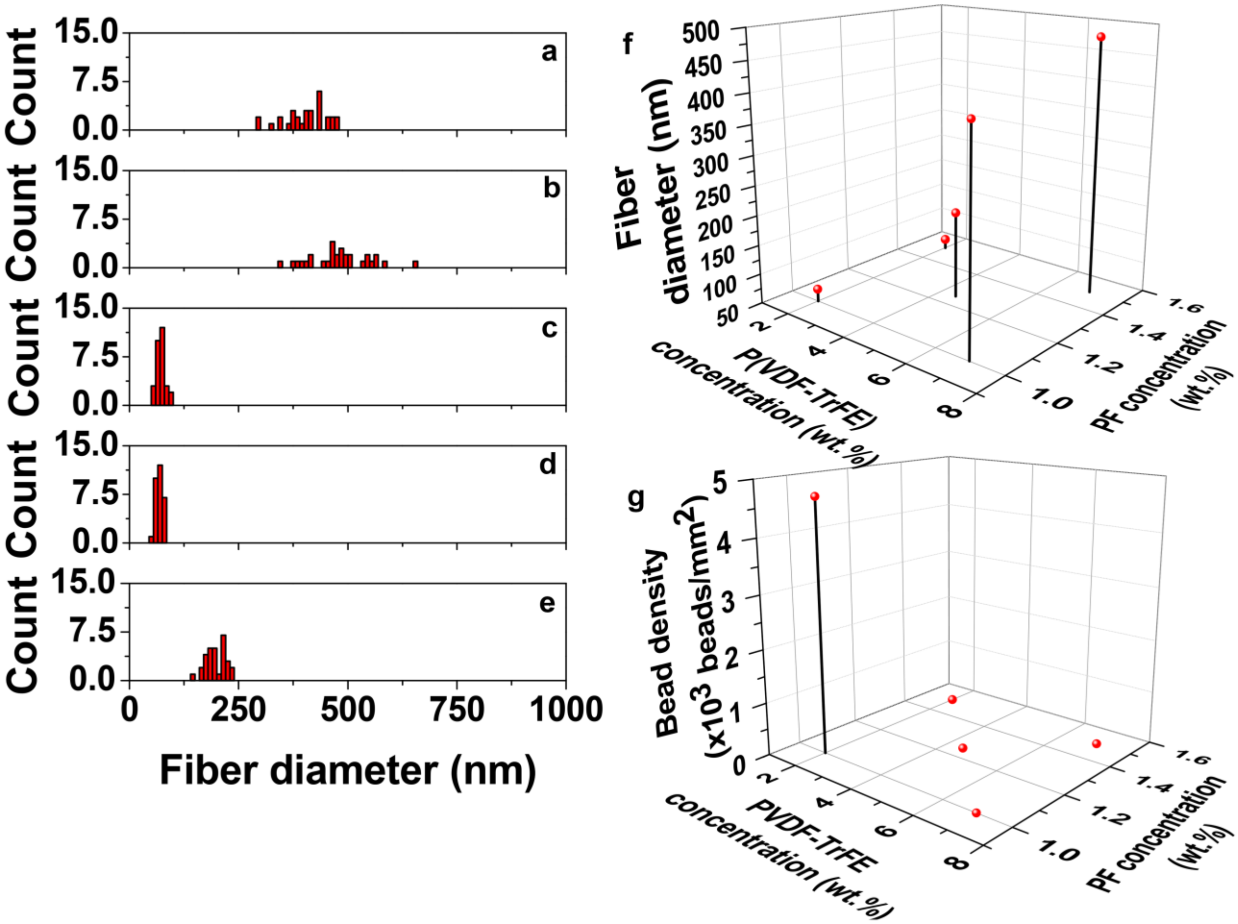

Figure App.A2. Fiber diameter and bead density with respect to design parameters. Resulting fiber diameter distribution of DOE2: 7 wt.% P(VDF-TrFE) solution with 1 wt.% (a) and 1.5 wt.% (b) PF, 2 wt.% P(VDF-TrFE) solution with 1 wt.% (c) and 1.5 wt.% (d) PF, and midpoint 4.5 wt.% P(VDF-TrFE) solution with 1.25 wt.% PF (e). Fiber diameter (a) and bead density (b) vs design parameters, P(VDF-TrFE) concentration (7, 4.5, and 2 wt.%) and PF concentration (1, 1.25, and 1.5 wt.%) (n=30).

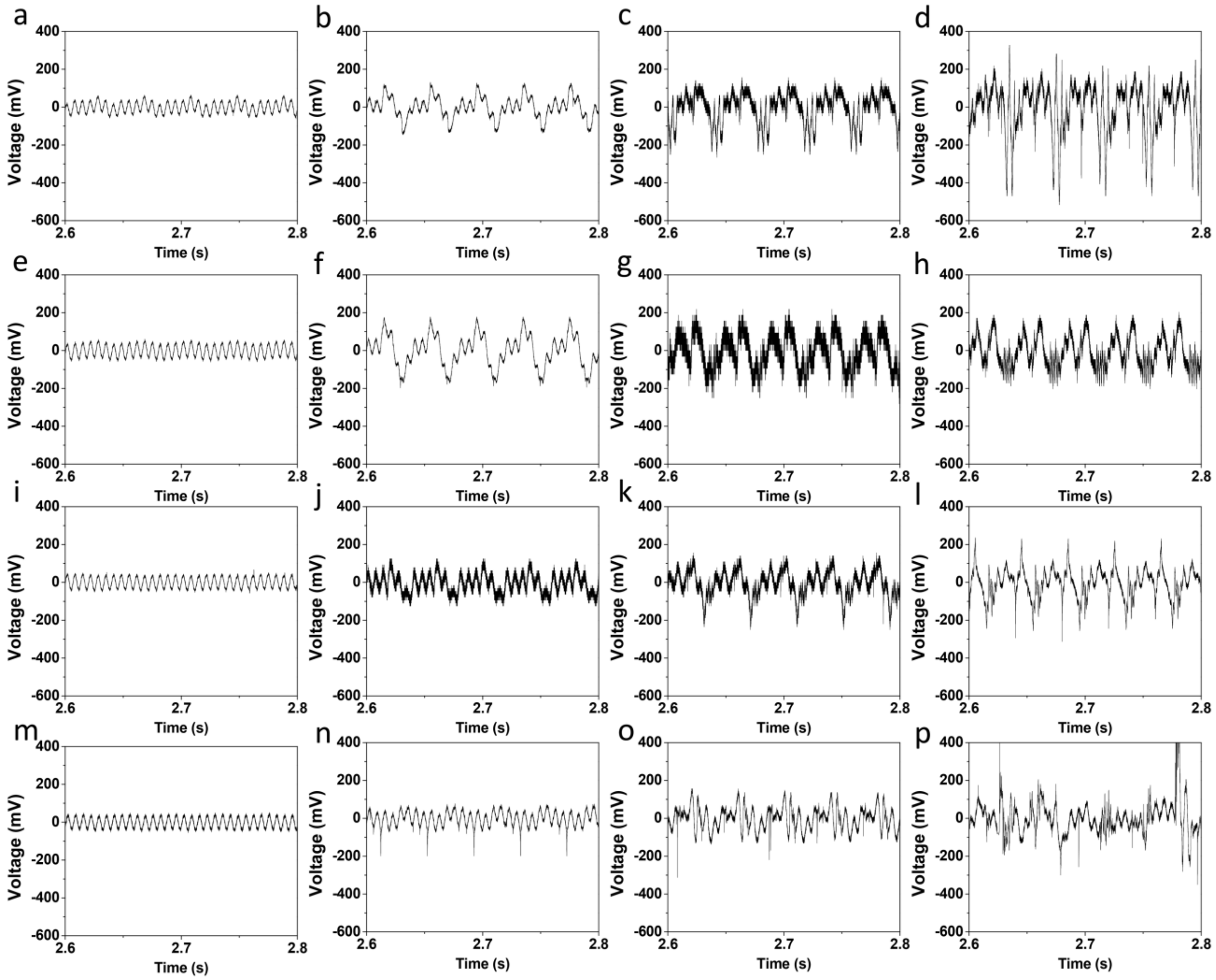

Figure App.A3. Representative voltage generation from electrospun P(VDF-TrFE) nanofiber mats composed of various average fiber diameters. Voltage output of the mats composed of average fiber diameters of 90 (a-d), 166 (e-h), 242 (i-l), and 859 nm (m-p) by surface strain of 0.03% (a,e,i,m), to 0.06% (b,f,j,n), to 0.13% (c,g,k,o), to 0.18% (d,h,l,p) at 10 Hz.

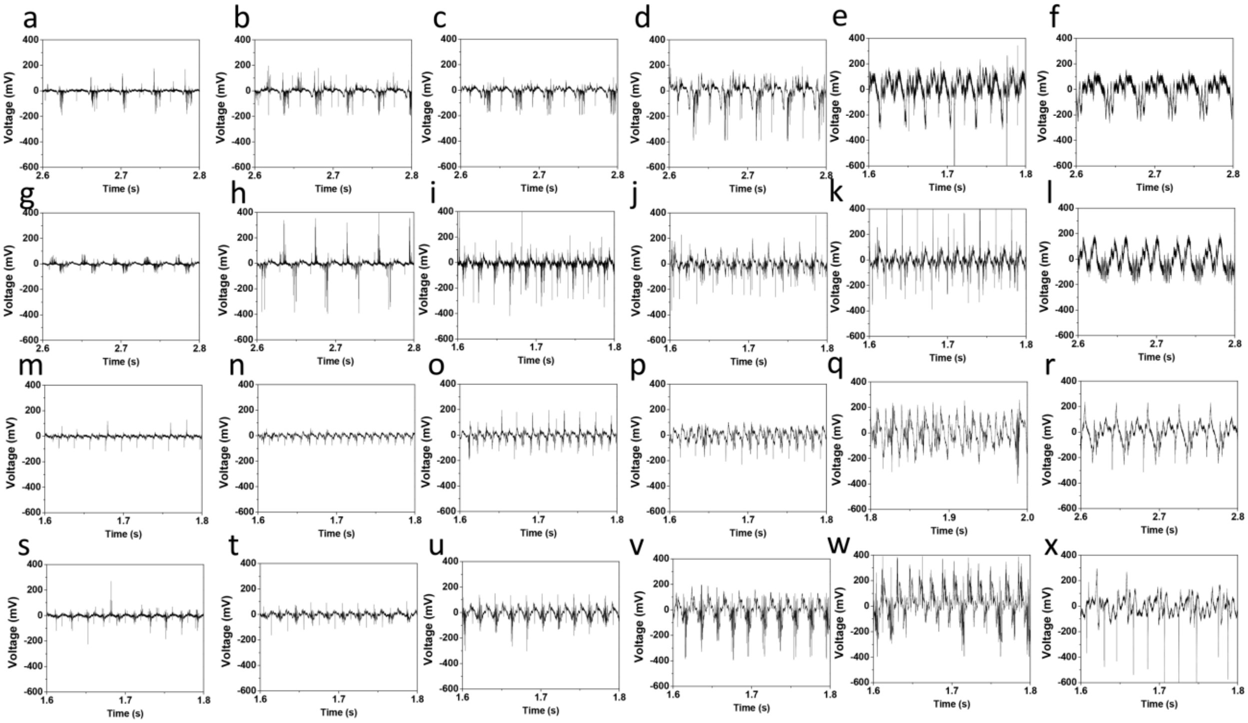

Figure App.A4. Representative voltage generation from electrospun P(VDF-TrFE) nanofiber mats composed of various average fiber diameters across varied total resistances. Voltage output of the mats composed of average fiber diameters of 90 (a-f), 166 (g-l), 242 (m-r), and 859 nm (s-x) under different total circuit resistances of 0.48 (a,g,m,s), 0.91 (b,h,n,t), 1.67 (c,i,o,u), 3.33 (d,j,p,v), 6.88 (e,k,q,w), and 10 MΩ (f,l,r,x).

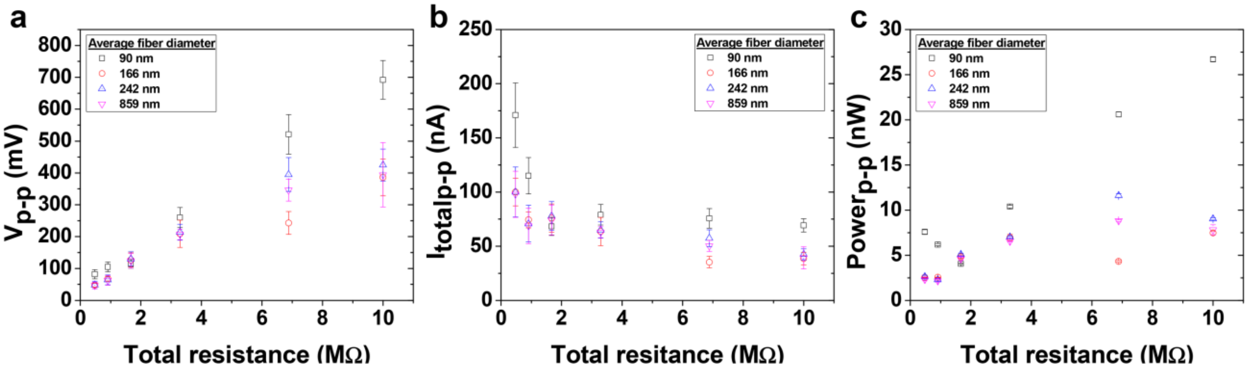

Figure App.A5. (a) Peak-to-peak voltage, (b) total peak-to-peak total current, and (c) peak-to-peak power of electrospun P(VDF-TrFE) nanofiber mats composed of various average fiber diameters. 0.18% of strain was applied at 10 H

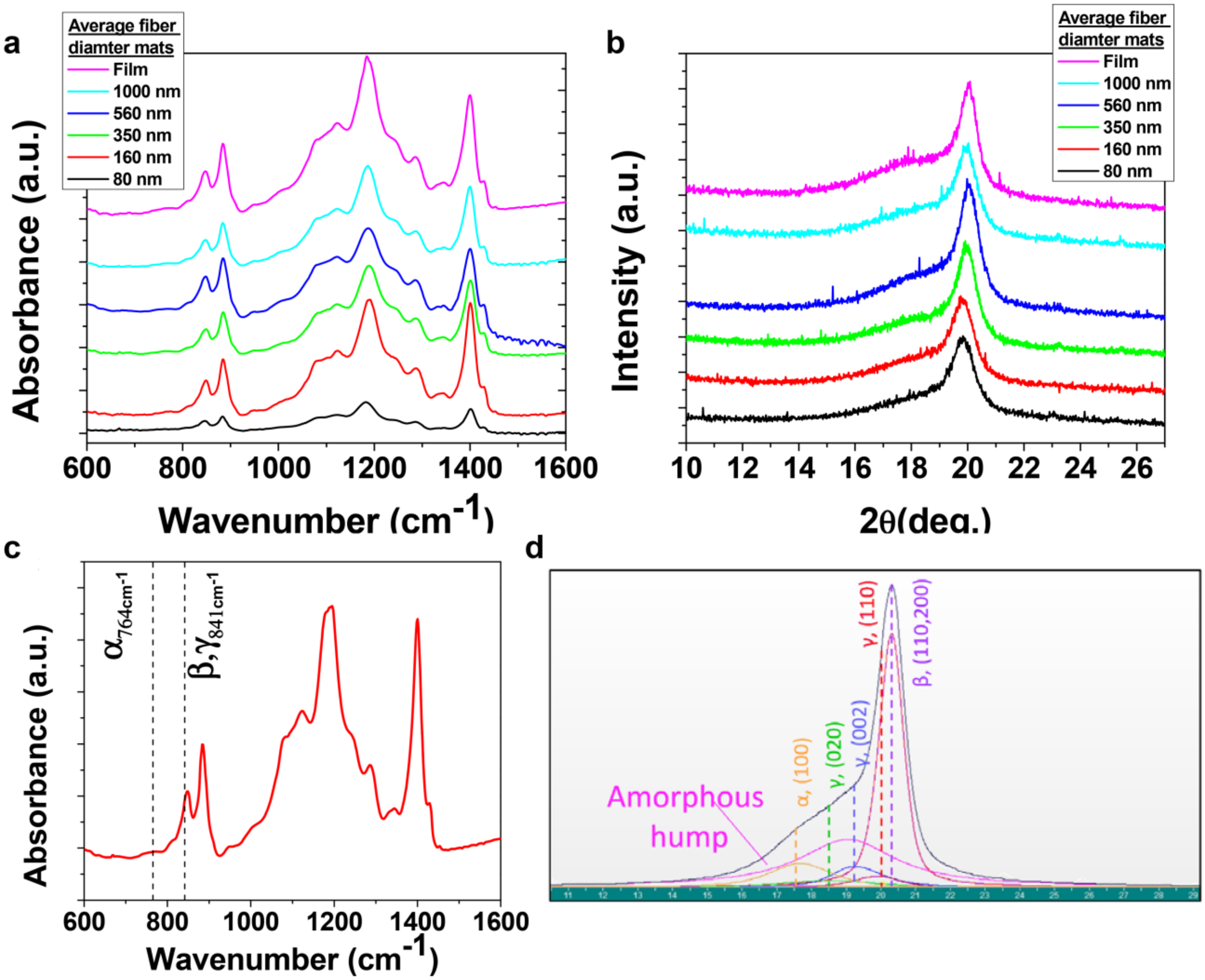

Figure App.A6. FTIR and XRD spectra analysis of electrospun P(VDF-TrFE) nanofibers having various fiber diameters. Representative (a) FTIR and (b) XRD spectra of electrospun P(VDF-TrFE) fibers having different average fiber diameters. Representative spectra of drop casted P(VDF-TrFE) thin film are also shown. (c) A representative FTIR spectrum with peak assignment for the α- and electroactive phases at 764 and 841 cm^{-1}, respectively. (d) An example of peak deconvolution of a representative XRD spectrum.

APPENDIX B. SUPPLEMENTARY INFORMAITON: Transformative Piezoelectric Enhancement of P(VDF-TrFE) Synergistically Driven by Nanoscale Dimensional Reduction and Thermal Treatment

B.1. Optimization of P(VDF-TrFE) electrospinning conditions, tables, and figures

A systematic study of solution tuning including solution conductivity, viscosity, and surface tension was conducted to produce electrospun P(VDF-TrFE) nanofibers with the smallest possible fiber diameter. As a preliminary study, the optimal concentration of salt (pyridinium formate (PF) buffer) to control conductivity of the electrospinning solution was determined; to produce fiber sizes below 100 nm in a DMF/acetone (60/40 vol/vol) solvent system, a maximum of 1.5 wt.% PF, above which electrospraying was exhibited, was determined to increase the conductivity of the solution within an electrospinnable range. Next, to determine optimal factors for viscosity and surface tension, a two-parameter experiment was designed, where the concentration of pyridinium formate (PF) buffer was maintained at 1.5 wt.% in the DMF/acetone solvent system while varying the P(VDF-TrFE) and surfactant (BYK-377)[28] concentrations from 1-2 wt.% and 0.0-0.1 wt.%, respectively. The conductivity of the solutions do not significantly change by varying either P(VDF-TrFE) or BYK-377 concentration. The solution flow rate through a 25-gauge needle at 0.5 ml hr^{-1} and collector distance of 20 cm were kept constant for this and all subsequent experiments, and the applied voltage was adjusted from solution to solution (approx., -15 kV for the solutions tested in this experiment), to maintain the most stable

Taylor cone. The environmental conditions for this and all subsequent experiments were kept at 23 °C and an absolute humidity of 7.6 g m^{-3}. Characterization of the resulting fiber morphology was conducted by SEM (**Figure App. B1a-e**). The fiber diameter as a function of both design parameters shows no distinct trend, mainly due to the lack of fiber formation at low concentrations of P(VDF-TrFE) (**Figure App. B 1f**). Bead density exhibits the expected trend of bead reduction at higher concentrations of P(VDF-TrFE) (**Figure App. B 1g**). Taken together, there is a significant decrease in fiber diameter at the midpoint of each design parameter (i.e., 1.5 wt.% P(VDF-TrFE) and 0.05 wt.% BYK), as well as a significant bead reduction at the same point with an average fiber diameter of 45 nm and bead density of 43,000 beads per mm^2.

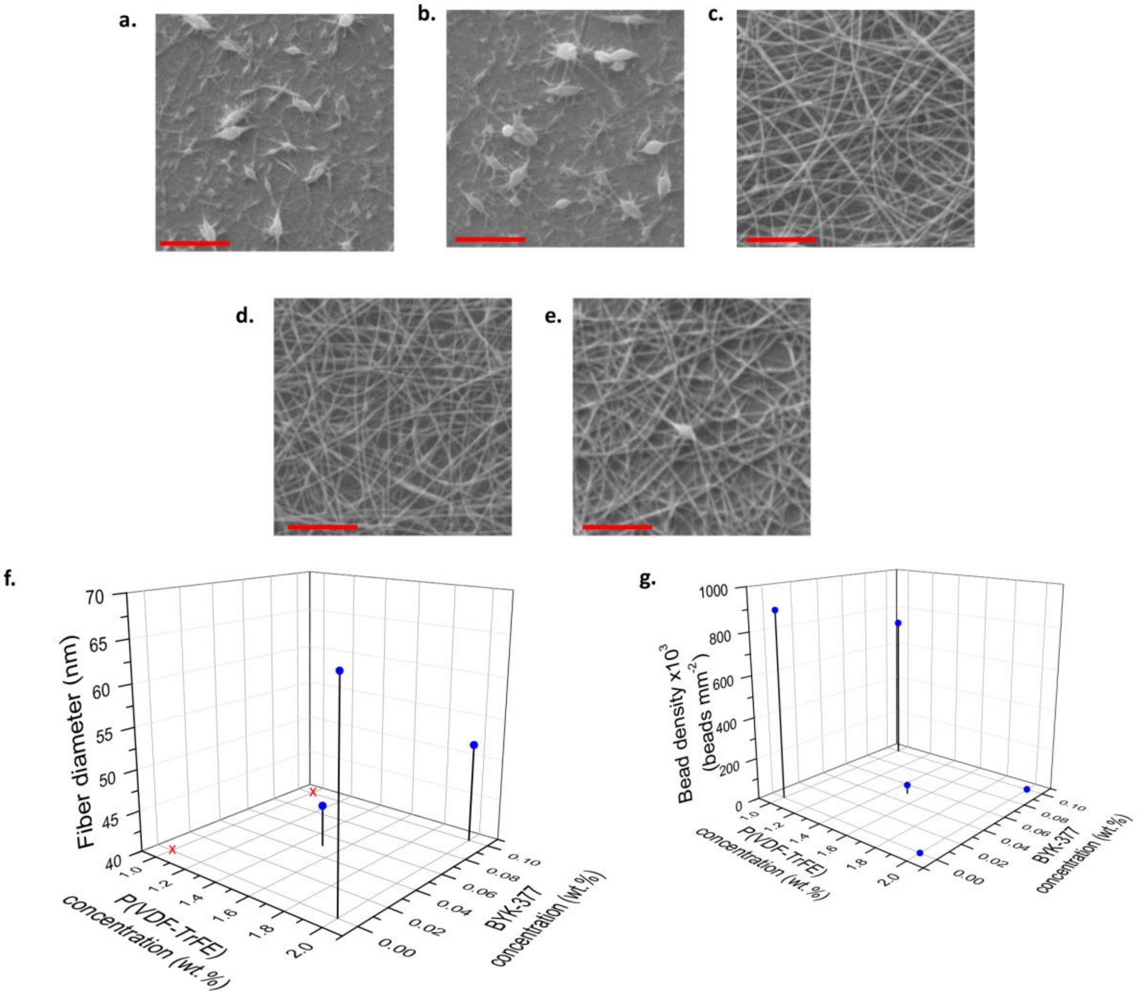

(a-e) Fiber morphologies of corresponding solution from design parameters ((a) 1 wt.% P(VDF-TrFE)/0 wt.% BYK-377, (b) 1/0.1, (c) 2/0, (d) 2/1, and (e) 1.5/0.05 (scale bar = 2 µm)). Quantification of (f) fiber diameter and (g) bead density as a function of design parameters.

Subsequently, a new experiment to tune the proper concentration of P(VDF-TrFE) was conducted with concentrations of 1.5, 1.4, 1.2, 1.1 and 1.0 wt.% with 1.5 wt.% PF in the DMF/acetone solvent system, while maintaining the BYK-377 concentration at 0.05 wt.% determined from the previous experiment. The resulting fiber morphologies are shown in **Figure App. B2a-f** with arrows in **Figure App. B2d-f** indicating the presence of a thin film morphology due to unstable electrospinning and solution droplet deposition. **Figure App. B2g-j** show the fiber diameter distribution and average diameter of each solution except for 1.1 and 1.0 wt.% P(VDF-TrFE) for which thin film formation was observed. **Figure App. B2k** shows the effect of P(VDF-TrFE) concentration on bead density. From these results, 1.3 wt.%, which resulted in 28 nm average diameter fibers with a bead density of 62,300 beads per mm^2 and slight signs of film morphology, was utilized for further optimization in the next experiments.

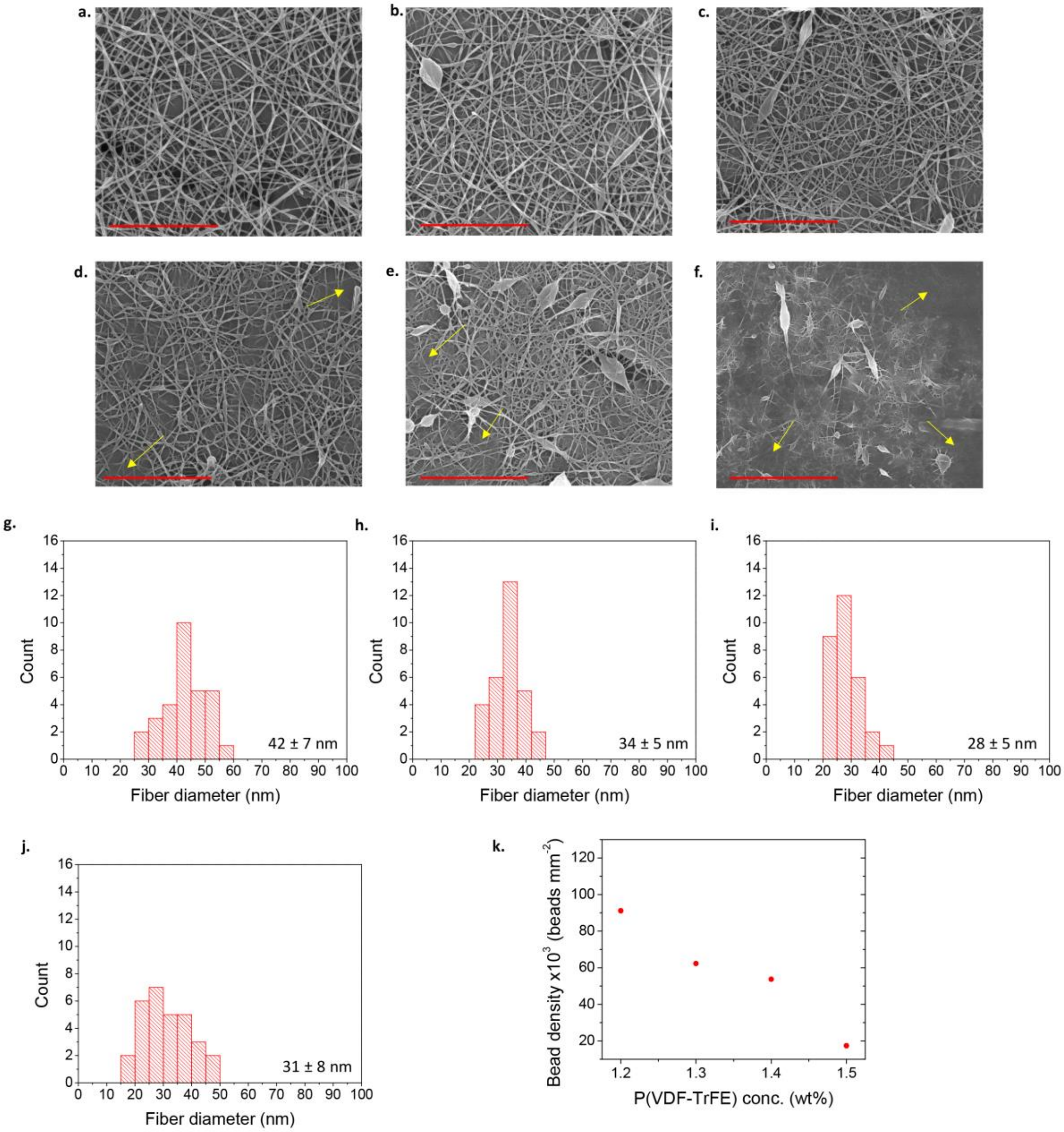

Electrospun P(VDF-TrFE) with various solution concentration between 1.5 and 1.0 wt.% to optimize the synthesis of the smallest fibers without defects. SEM images of (a) 1.5, (b) 1.4, (c) 1.3, (d) 1.2, (e) 1.1, and (f) 1.0 wt.% P(VDF-TrFE) (scale bar = 3 µm).

Corresponding fiber diameter distribution of (g) 1.5, (h) 1.4, (i) 1.3, and (j) 1.2 wt.% P(VDF-TrFE) and bead density as a function of P(VDF-TrFE) concentration (k).

Although it has been shown that utilizing solvents with dielectric constants (ε) of >19 prevents the formation of beads on nanofibers >500 nm, such solutions using solvents with high dielectric values require greater applied voltages to achieve a stable Taylor Cone.[29] The initial solvent system used in this study, composed of DMF (ε=36.7) and acetone (ε=20.7), requires a high and narrow voltage range to maintain a stable Taylor Cone due to the high dielectric constants. The presence of film morphology (**Figure App. B2c**) likely indicates that the solution requires fine adjustments to prevent solution droplet deposition. Tetrahydrofuran (THF) is a partial solvent of PVDF polymers that has a low dielectric constant (ε=7.6) which can potentially stabilize the electrospinning process. **Figure App. B3a** shows the fiber morphology from an electrospun solution of 1.3 wt.% P(VDF-TrFE), 1.5 wt.% PF and 0.05 wt.% BYK-377 in THF, replacing DMF/acetone. The fiber size distribution in **Figure App. B3b** shows that the solution properties still allow for the formation of small fibers even with the low dielectric constant of THF. In spite of no film formation, we observe slight bead formation as well as large agglomerates of polymer, likely due to the partial solubility of P(VDF-TrFE) in THF.

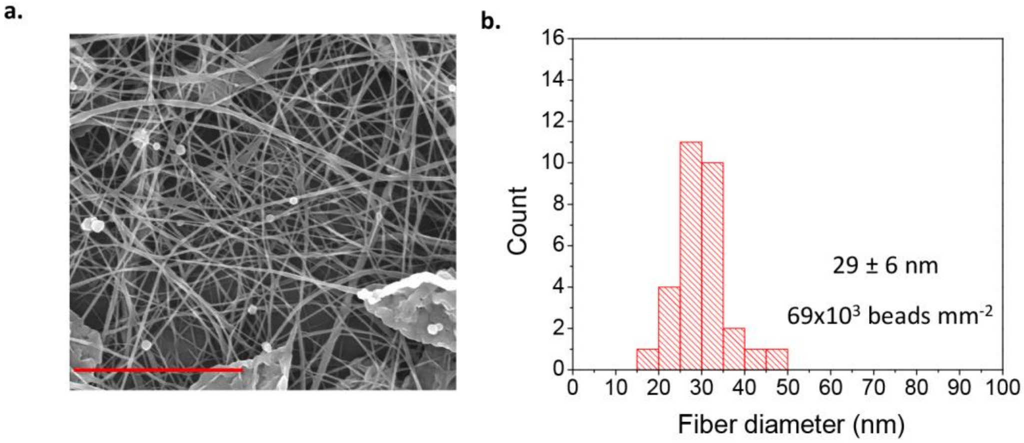

Electrospun P(VDF-TrFE) dissolved in THF. Fiber morphology of electrospun solutions of 1.3 wt.% P(VDF-TrFE) with 1.5 wt.% PF and 0.05 wt.% BYK-377 in (a) THF (scale bar = 3µm) and (b) the resulting fiber distribution.

To increase P(VDF-TrFE) solubility in a THF based solution, we investigated an additive solvent to promote complete dissolution of P(VDF-TrFE) while synthesizing defect-free nanofibers. The use of a Teas solubility graph (**Figure App. B4a**)[30] predicts that utilizing a DMF/THF mixed solvent system drives the solubility of P(VDF-TrFE) closer to the fractional solubility parameters associated with PVDF (assumed to be similar for P(VDF-TrFE). An electrospinning solution in pure DMF with a close match to the solubility parameters of P(VDF-TrFE) resulted in particle deposition likely due to the unstable electrospinning (**Figure App. B4b**). By testing various ratios of DMF/THF, we found that an electrospinning solution of 1.3 wt.% P(VDF-TrFE), 1.5 wt.% PF, 0.05 wt.% BYK-377 in a 50/50 (vol/vol) DMF/THF solvent system produced nanofibers with diameters of 32 ± 5 nm (**Figure App. B4c**), within error of the same solution utilizing pure THF (29 ± 6 nm) (**Figure App. B4d**), without defects. The resulting viscosity, electrical conductivity, and surface tension of the solution were 2.7 cP, 30.9 µS cm^{-1}, and 22.6 dynes cm^{-1}, respectively. From these systematically designed experiments, we achieved the conditions to produce defect-free P(VDF-TrFE) nanofibers in the range of 30 nm diameter.

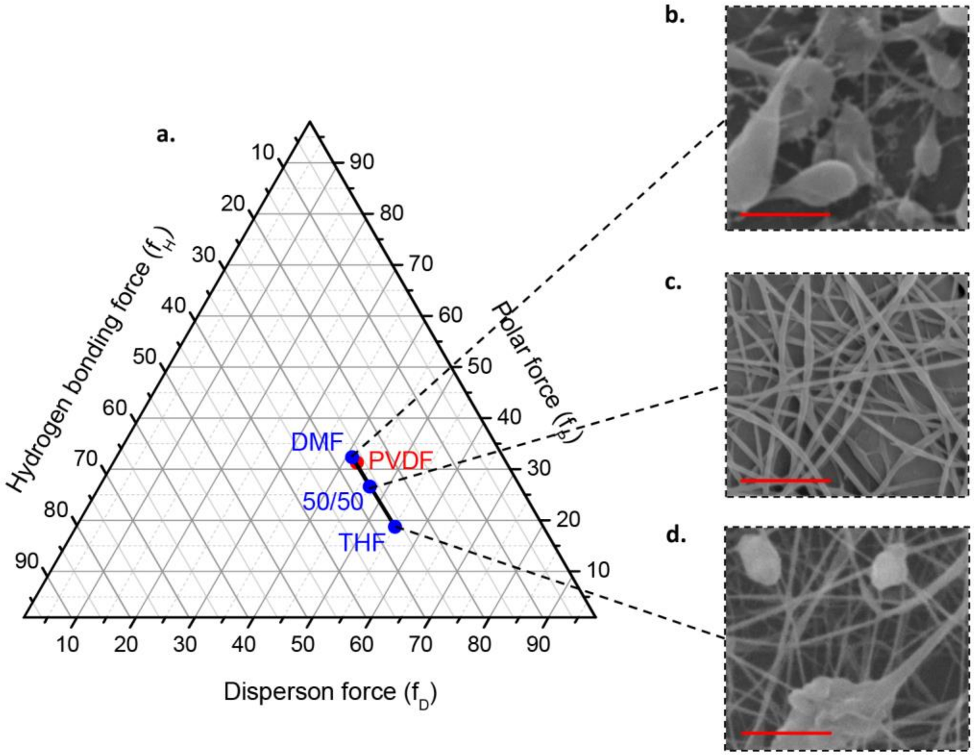

(a) Teas graph showing the relative positions of the fractional solubility parameters of DMF and THF to the parameters of PVDF polymer with the connecting line indicating the path of the solvent mixture ratios. Nanofibers electrospun from 1.3 wt.% P(VDF-TrFE), 1.5 wt.% PF, and 0.05 wt.% BYK-377 in (b) 100% DMF, (c) 50/50 (vol/vol) DMF/THF, and (d) 100% THF solution (Scale bar = 1 μm).

Table S1. Lattice constants of 30 and 90 nm average diameter P(VDF-TrFE) nanofibers with various thermal treatments.

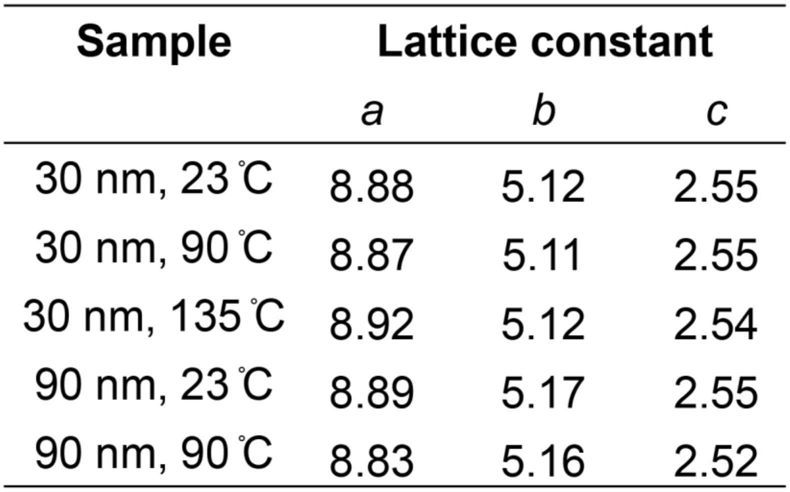

Sample	Lattice constant		
	a	*b*	*c*
30 nm, 23 ℃	8.88	5.12	2.55
30 nm, 90 ℃	8.87	5.11	2.55
30 nm, 135 ℃	8.92	5.12	2.54
90 nm, 23 ℃	8.89	5.17	2.55
90 nm, 90 ℃	8.83	5.16	2.52

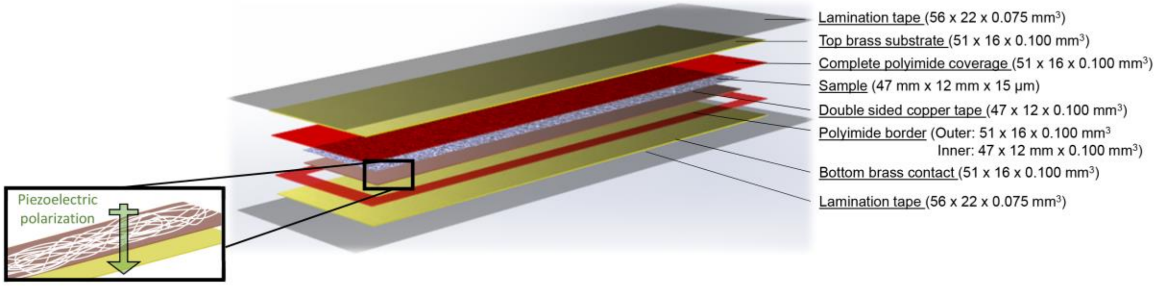

Figure App. B5. A schematic of the cantilever assembly for the measurements of electric outputs from electrospun P(VDF-TrFE) nanofiber mats. The setup was modified from our previous study.[14] A brass substrate (51 x 16 x 0.100 mm^3) was used as the bottom electrical contact as an exposed area of the brass measured 47 x 12 mm^2, whereas polyimide tape was used to seal the rest of the exposed brass substrate around the working area (51 x 16 x 0.100 mm^3). To promote proper fiber adhesion to the bending substrate, a rectangular strip of double sided adhesive copper foil tape with the same dimensions as the electrode area of the brass was used. The fiber mat sample (47 x 12 x 0.015 mm^3) was placed on top of the adhesive copper. A separate brass piece was completely insulated with polyimide tape and placed on top of the bottom assembly to act as the top contact electrode working in capacitive mode. Thin lamination tape was used to seal the structure in a conformal manner and soldered leads were placed on the top and bottom brass pieces to create the final cantilever assembly.

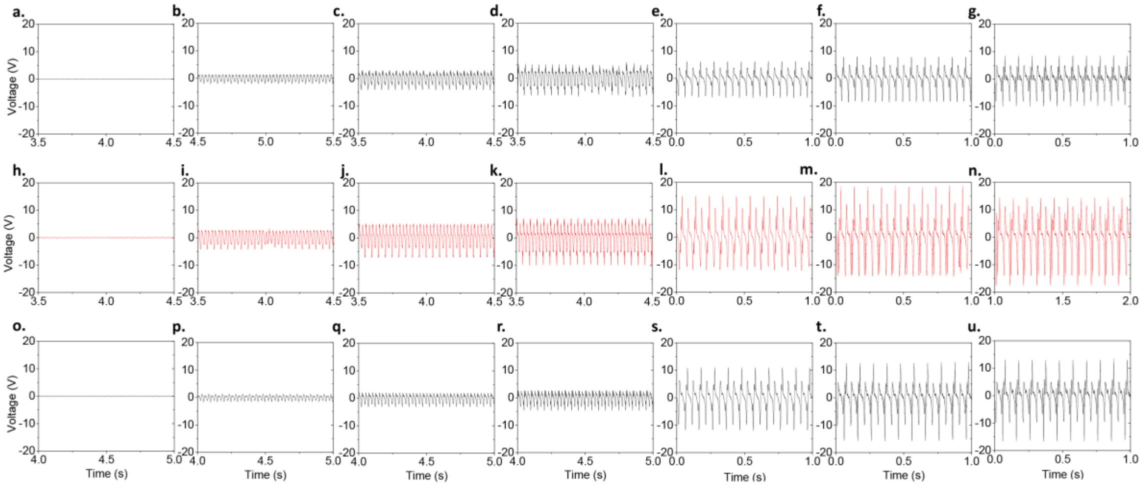

Figure App. B6. Voltage production of nanofiber mat samples. Raw voltage output of 30 nm average fiber diameter mats which were (a-g) thermal-treated at 23 °C, (h-n) 90 °C, and (o-u) 90 nm average fiber diameter mats at 23 °C. These selected plots represent applied strains of (a,h,o) 0.02%, (b,i,p) 0.05%, (c,j,q) 0.09%, (d,k,r) 0.14%, (e,l,s) 0.19%, (f,m,t) 0.22%, and (g,n,u) 0.26%.

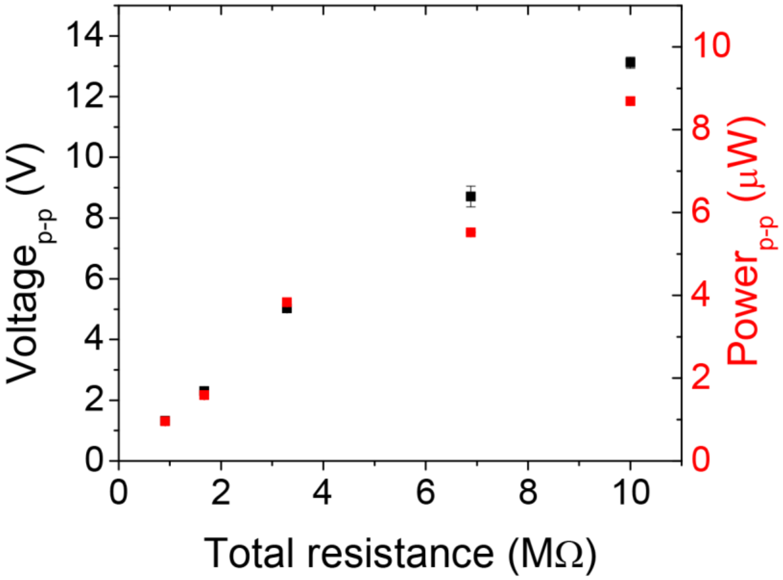

Figure App. B7. Peak-to-peak voltage and power across varying total resistances. The greatest output voltage and power observed at an open circuit (10 MΩ internal resistance) under a moderate applied strain of 0.14%.

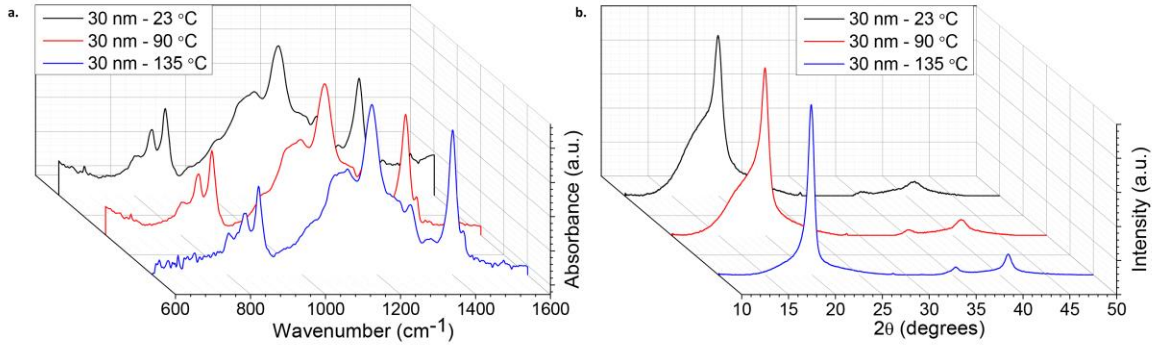

Figure App. B8. (a) FTIR and (b) XRD spectra of electrospun P(VDF-TrFE) mats composed of nanofibers with an average diameter of 30 nm after various heat treatments. The data were used to quantify electroactive phase content and degree of crystallinity.

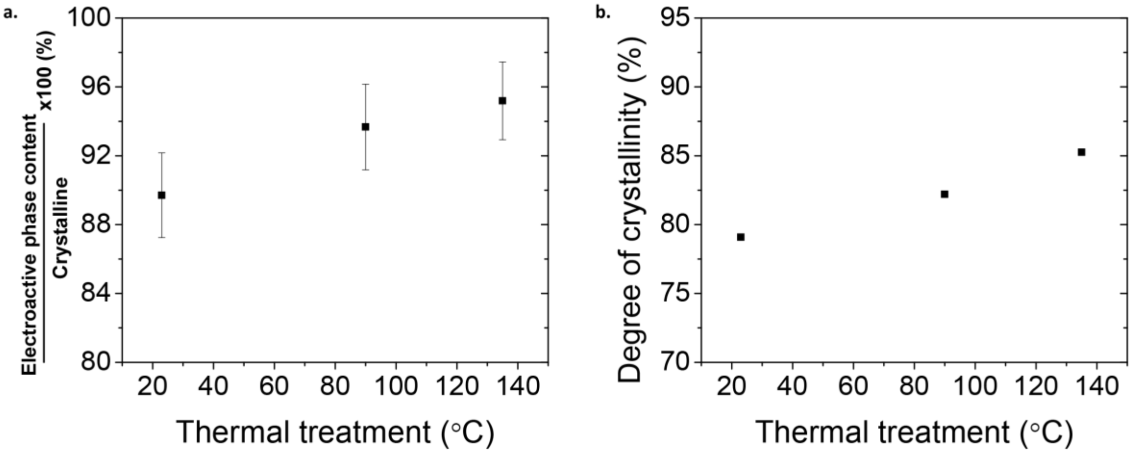

Figure App. B9. (a) Electroactive phase content and (b) degree of crystallinity of electrospun P(VDF-TrFE) mats composed of nanofibers with an average diameter of 30 nm as a function of temperature.

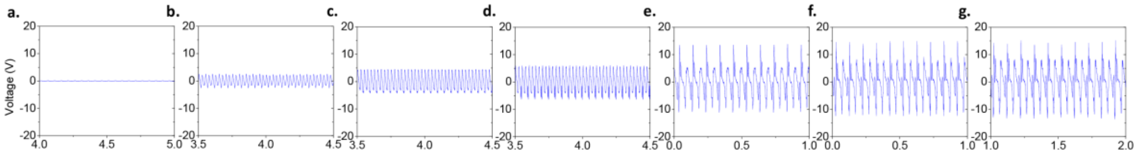

Figure App. B10. Voltage production of 30 nm average fiber diameter mat samples thermal treated at 135℃. These selected plots represent applied strains of (a) 0.02%, (b) 0.05%, (c) 0.09%, (d) 0.14%, (e) 0.19%, (f) 0.22%, and (g) 0.26%

B.2 References

1. M. J. Nalbandian, M. Zhang, J. Sanchez, Y.-H. Choa, D. M. Cwiertny and N. V. Myung, Journal of Molecular Catalysis A: Chemical, 2015, 404, 18-26.

2. C. J. Luo, E. Stride and M. Edirisinghe, Macromolecules, 2012, 45, 4669-4680.

3. C. M. Hansen, Hansen solubility parameters: a user's handbook, CRC press, 2007.

4. G. Ico, A. Showalter, W. Bosze, S. C. Gott, B. S. Kim, M. P. Rao, N. V. Myung and J. Nam, Journal of Materials Chemistry A, 2016, 4, 2293-2304.